



TECHNISCHE
UNIVERSITÄT
WIEN

DISSERTATION

Design of novel achiral and chiral iron(II) pincer complexes

ausgeführt zum Zwecke der Erlangung des akademischen Grades eines Doktors der
technischen Naturwissenschaften unter der Leitung von

Ao. Prof. Dr. Karl Kirchner

Institut für Angewandte Synthesechemie E163

eingereicht an der Technischen Universität Wien

Fakultät für Technische Chemie

von

DI Christian Schröder-Holzhacker

Matr. Nr. 0425085

Schenkendorfsgasse 25/16, 1210 Wien

Wien, am 12.10.2015

U:

Abstract

The first part of this work describes the synthesis of several bidentate and tridentate pincer ligands, based on 2,6-diaminopyridine and 2-aminopyridine, featuring phosphines, sulphides and amines as two-electron donor groups. The preparation is carried out by the reaction of 2,6-diaminopyridine and 2-aminopyridine, respectively, with chlorophosphines PR_2Cl in the presence of a base. The ligands were then modified by selective oxidation of the phosphorous using elemental sulphur or hydrogen peroxide in order to modify coordination properties. Additionally, chiral precursors were used for the synthesis of chlorophosphites PR^*Cl , which lead to the formation of chiral PNP ligands.

In the second and third part, several bidentate complexes were synthesized by the treatment of FeX_2 with 1 or 2 equivs of PN and SN ligands, forming complexes of the overall type $\text{Fe}(\text{PN}^{\text{R}}\text{-Ph})_2\text{X}_2$ for the PN ligands, and, $\text{Fe}(\text{SN}^{\text{R}}\text{-Ph})\text{X}_2$ for the SN ligands, respectively. The behaviour of these complexes was then investigated in solution and solid state by NMR, Mössbauer, mass and magnetic spectroscopy, and the experimental results were compared with DFT calculations.

The fourth part focuses on the synthesis of tridentate PNP pincer complexes with the overall form $\text{Fe}(\text{PNP}^{\text{R}}\text{-}i\text{Pr})\text{X}_2$ and PNN complexes of the type $\text{Fe}(\text{PNN-}i\text{Pr})\text{X}_2$, respectively. Reactivity with carbon monoxide was investigated, leading to the complexes *cis,trans*- $[\text{Fe}(\text{PNP}^{\text{R}}\text{-}i\text{Pr})(\text{CO})\text{X}_2]$ and *trans*- $[\text{Fe}(\text{PNP}^{\text{R}}\text{-}i\text{Pr})(\text{CO})_2\text{X}]^+$, which were characterized by NMR spectroscopy and single crystal XRD.

In the fifth part, TADDOL based PNP pincer ligands were utilized to form chiral complexes of the type $\kappa^2\text{P,N-}[\text{Fe}(\text{PNP-}i\text{Pr/TAD})\text{X}_2]$ and $\kappa^2\text{P,N-}[\text{Fe}(\text{PNP-}i\text{Bu/TAD})\text{X}_2]$. Their behaviour in solution and solid state was investigated by Mössbauer and NMR spectroscopy, showing an equilibrium between κ^2 and κ^3 coordination mode. Furthermore, the reaction with carbon monoxide led to the formation of the complexes $\kappa^3\text{P,N,P-}[\text{Fe}(\text{PNP-}i\text{Pr/TAD})(\text{CO})\text{X}_2]$, which were then unsuccessfully used to form the hydride complex $\kappa^3\text{P,N,P-}[\text{Fe}(\text{PNP-}i\text{Pr/TAD})(\text{H})(\text{CO})\text{Br}]$.

In the last part, PNP-BINEP ligands were treated with FeX_2 to form chiral complexes $\text{Fe}(\text{PNP-}i\text{Pr/BIN})\text{X}_2$. Finally, these complexes reacted with CO and $\text{Na}[(\text{H})\text{BEt}_3]$, leading to the formation of the chiral hydride $\text{Fe}(\text{PNP-}i\text{Pr/BIN})(\text{H})(\text{CO})\text{Br}$, which was then successfully used as catalyst in the homogeneous hydrogenation of ketones to alcohols.

Kurzfassung

Der erste Teil dieser Arbeit beschreibt die Synthese von verschiedenen Bidentat- und Tridentat-Pincer Liganden, basierend auf 2,6-Diaminopyridin und 2-Aminopyridin, welche Phosphine, Sulfide und Amine als 2-Elektron-Donoren bereitstellen. Die Herstellung wird durch die Reaktion von 2,6-Diaminopyridin bzw. 2-Aminopyridin mit Chlorophosphinen PR_2Cl in Gegenwart einer Base durchgeführt. Die Liganden wurden danach durch selektive Oxidation am Phosphor mittels elementarem Schwefel bzw. Wasserstoffperoxid modifiziert um die koordinativen Eigenschaften zu verändern. Zusätzlich wurden chirale Vorstufen für die Synthese von Chlorophosphiten PR_2^+Cl verwendet um chirale PNP Liganden herzustellen.

Im zweiten und dritten Teil werden mehrere Bidentat-Komplexe durch die Umsetzung von FeX_2 mit 1 oder 2 Äquivalenten PN und SN Liganden hergestellt; diese bilden Komplexe mit der allgemeinen Formel $\text{Fe}(\text{PN}^{\text{R}}\text{-Ph})_2\text{X}_2$ für PN Liganden bzw. $\text{Fe}(\text{SN}^{\text{R}}\text{-Ph})\text{X}_2$ für SN Liganden. Das Verhalten dieser Komplexe in Lösung und fester Phase wurde mittels NMR, Mössbauer, Massen- und magnetischer Spektroskopie untersucht und die experimentiellen Ergebnisse mit DFT Berechnungen verglichen.

Der vierte Teil konzentriert sich auf die Synthese von Tridentat-PNP-Pincer Komplexen mit der allgemeinen Formel $\text{Fe}(\text{PNP}^{\text{R}}\text{-}i\text{Pr})\text{X}_2$ bzw. PNN Komplexen des Types $\text{Fe}(\text{PNN-}i\text{Pr})\text{X}_2$. Die Reaktion mit Kohlenmonoxid wurde untersucht, dies führte zur Bildung der Komplexe *cis,trans*- $[\text{Fe}(\text{PNP}^{\text{R}}\text{-}i\text{Pr})(\text{CO})\text{X}_2]$ und *trans*- $[\text{Fe}(\text{PNP}^{\text{R}}\text{-}i\text{Pr})(\text{CO})_2\text{X}]^+$, welche mittels NMR Spektroskopie und Einkristallröntgenstrukturanalyse charakterisiert wurden.

Im fünften Teil wurden PNP-Liganden, basierend auf TADDOL, für die Herstellung von chiralen Komplexen des Types $\kappa^2\text{P,N-}[\text{Fe}(\text{PNP-}i\text{Pr/TAD})\text{X}_2]$ bzw. $\kappa^2\text{P,N-}[\text{Fe}(\text{PNP-}t\text{Bu/TAD})\text{X}_2]$ verwendet. Deren Verhalten in Lösung bzw. fester Phase wurde mittels Mössbauer- und NMR Spektroskopie untersucht; dieses zeigt ein Gleichgewicht zwischen κ^2 und κ^3 -Koordination. Des Weiteren führte die Reaktion dieser Komplexe mit Kohlenmonoxid zur Bildung von $\kappa^3\text{P,N,P-}[\text{Fe}(\text{PNP-}i\text{Pr/TAD})(\text{CO})\text{X}_2]$, welches erfolglos für Synthese eines Hydridkomplexes mit der Form $\kappa^3\text{P,N,P-}[\text{Fe}(\text{PNP-}i\text{Pr/TAD})(\text{H})(\text{CO})\text{Br}]$ verwendet wurde.

Im letzten Teil wurde chirale Komplexe der Form $\text{Fe}(\text{PNP-}i\text{Pr/BIN})\text{X}_2$ durch die Umsetzung von FeX_2 mit PNP-BINEP Liganden hergestellt. Schließlich wurden diese Komplexe nach der Umsetzung mit Kohlenmonoxid und $\text{Na}[(\text{H})\text{BEt}_3]$, was zur Bildung eines chiralen Hydrids $\text{Fe}(\text{PNP-}i\text{Pr/BIN})(\text{H})(\text{CO})\text{Br}$ führte; dieses wurde erfolgreich als Katalysator bei der homogenen Hydrogenierung von Ketonen zu Alkoholen eingesetzt.

Acknowledgments

First, I would like to thank Prof. Karl Kirchner to give me the opportunity to work in his research group and the supervision on this versatile topic. Further, I thank him for performing various DFT calculations and for sharing his motivating enthusiasm in chemistry with me.

I would like to thank Berthold Stöger and Prof Kurt Mereiter for performing single crystal diffraction and for providing good hints for the synthesis of single crystals.

I would like to thank Ernst Pittenauer for measuring ESI-MS of my compounds.

Thanks to Prof. Luis Veiros for performing DFT calculations and Liliana Ferreira for SQUID and Mössbauer measurements.

Thanks to my colleagues Afrooz, Mathias, Matthias, Nikolaus, Özgür, Sara and Sathy, many thanks to Danny and the research group Weinberger for providing coffee breaks and smalltalk.

I would like to thank my friends for sharing their time with me, for providing recreation and for having always somebody to talk to.

Special thanks to my family, especially my parents for the financial and emotional support.

Finally, I would like to thank my beloved Astrid for spending her life time together with me.

Table of content

1	Introduction and scope	1
2	General Part	3
2.1	Phosphines	3
2.2	Pincer ligands	4
2.3	CO Addition	7
2.4	Catalytic hydrogenation	8
3	Results and Discussion	13
3.1	Ligand Synthesis	13
3.1.1	General considerations	13
3.1.2	N-alkylated PNP ligands	15
3.1.3	Chiral PNP ligands	17
3.1.4	Bidentate PN & SN ligands	21
3.1.5	PNN ligands	22
3.1.6	Characterization	23
3.2	PN iron(II) complexes	26
3.2.1	Synthesis	26
3.2.2	Solid state and solution studies	27
3.2.3	Reaction with CO	30
3.2.4	Spin-crossover	32
3.2.5	Mass spectroscopy	37
3.2.6	Calculation of geometry	39
3.3	SN iron(II) complexes	43
3.3.1	Synthesis	43
3.3.2	Solid state studies	43
3.3.3	Solution studies	52
3.4	PNP ^R & PNN iron(II) complexes	55
3.4.1	Synthesis	55
3.4.2	Characterization	57
3.4.3	Reaction with CO	60
3.5	TADDOL-PNP iron(II) complexes	64
3.5.1	Synthesis	64
3.5.2	Solid state studies	64
3.5.3	Solution state studies	68
3.5.4	Reaction with CO and CH ₃ CN	70
3.5.5	Computational studies	75
3.6	BINEP-PNP iron(II) complexes	79
3.6.1	Synthesis	79

3.6.2	Synthesis of chiral hydride	80
3.6.3	Hydrogenation reactions	82
4	Conclusion	84
5	Experimental Section	85
5.1	List of abbreviations	85
5.2	General considerations	86
5.3	Computational Details	88
5.4	Ligand precursors	90
5.5	Ligands	105
5.5.1	PN ligands	105
5.5.2	SN ligands	108
5.5.3	PNP & PNN ligands	111
5.6	Iron(II) complexes	125
5.6.1	PN iron(II) complexes	125
5.6.2	PN/NH ₂ iron(II) complexes	128
5.6.3	SN iron(II) complexes	130
5.6.4	(PN) ₃ iron(II) complexes	134
5.6.5	PNP iron(II) complexes	136
5.6.6	CO & CH ₃ CN iron(II) complexes	143
5.7	Hydrogenation reaction	167
5.8	Crystallographic data	168
6	Bibliography	177

1 Introduction and scope

The design of well-defined ligand systems and the application thereof is one of the most important goals in modern organometallic or inorganic chemistry. Different properties of the resulting transition metal complexes, for example solubility, catalytic activity, selectivity, etc. can be accurately modified and controlled by the characteristics of the ligand system being used. During the last 30 years, a revolutionary new class of ligands – the pincer ligands – are becoming more and more important compared to ordinary monodentates. Pincer ligands, though being first reported already in 1976^[1], remained a mostly unexplored research topic until the late 1990's, when their application in catalysis, molecular recognition and supramolecular chemistry was discovered^[2]. Visible in Figure 1, the number of literature published concerning pincer chemistry per year increased almost exponentially:

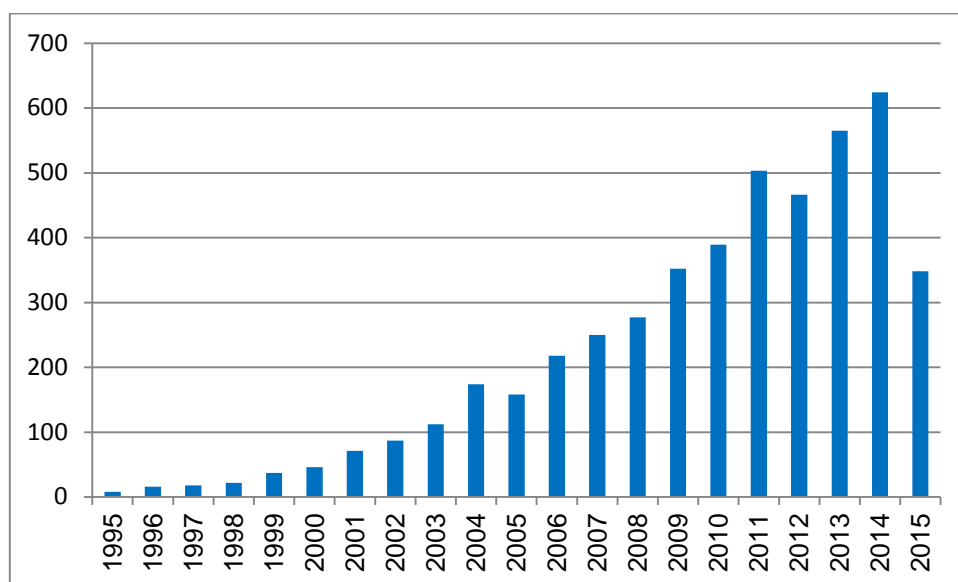
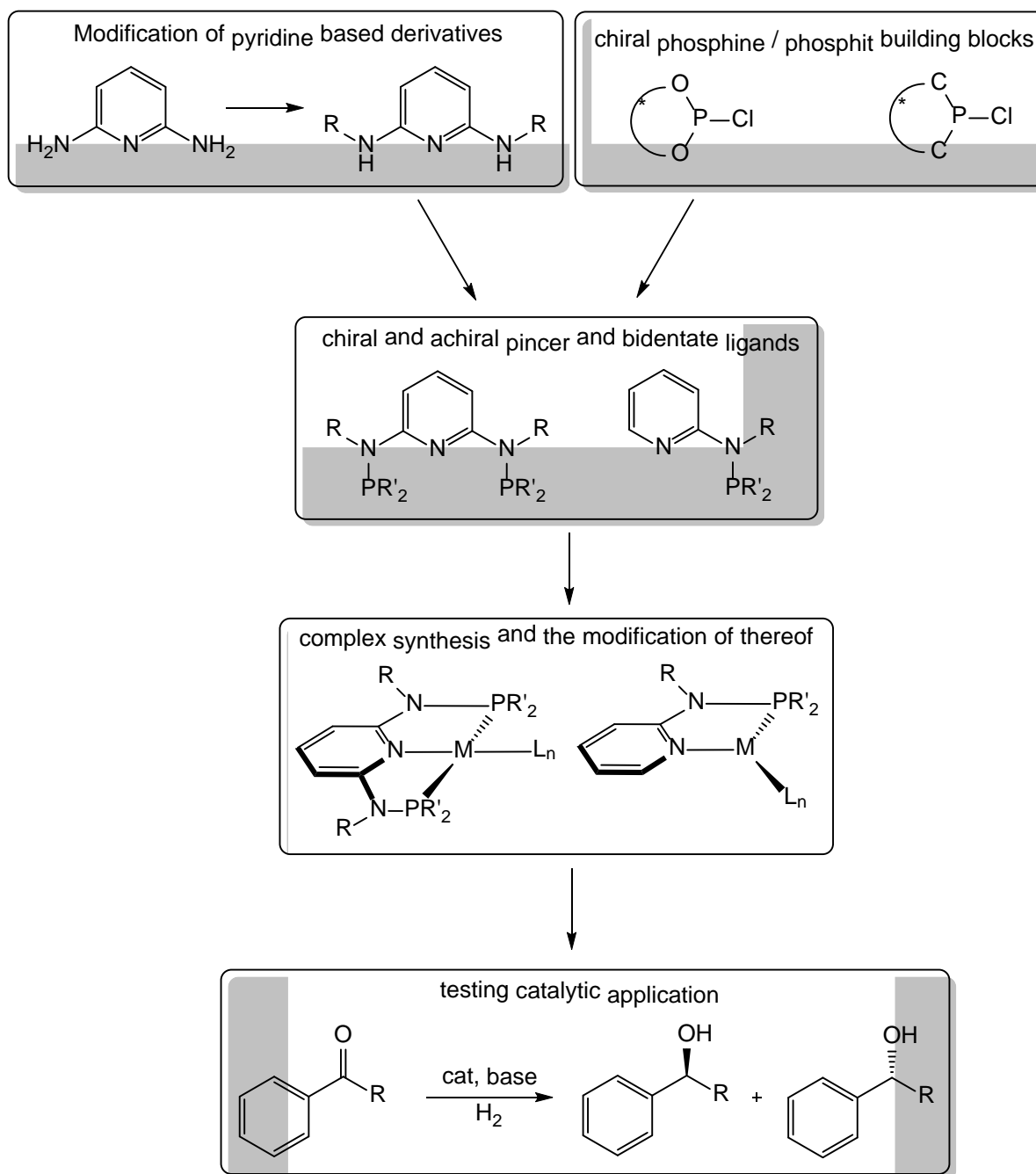


Figure 1. Search results for 'pincer' in SciFinder[®] (as of 01.06.2015).

Despite the high modularity in pincer type ligands, the implementation of chirality for asymmetric catalysis still represents a challenging task. The objectives of this work are depicted in Scheme 1: The first step was the design or modification of pyridine based derivatives, then to synthesize chiral chlorophosphines / chlorophosphites and create new pincer and bidentate ligands. These were used for the formation of iron(II) complexes, which were characterized by means of NMR, IR, Mössbauer, SQUID and MS techniques. Finally, modified complexes were tested for catalytic activity in hydrogenation reactions of ketons.



Scheme 1: Goal of this work.

2 General Part

2.1 Phosphines

Organophosphines, especially tertiary phosphines, play a tremendous role in modern organometallic chemistry, acting as ligands for transition metals in catalytic processes^[3]. They are relatively easy to synthesize, thus, their steric, electronic and stereochemical properties can be altered in a systematic and predictable way over a wide range. Phosphines act as σ -donor/ π -acceptor ligands: they provide electron density by donating their P lone pair to a metal center and interact with filled d-orbitals of the metal via their empty π^* orbitals (Figure 2) The binding manner is similar to that of carbonyl ligands,^[4] where π -backbonding occurs into the ligands empty π^* orbitals.

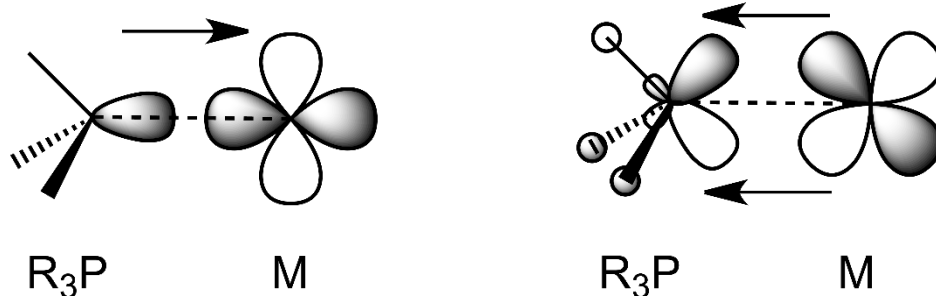


Figure 2: σ -donor / π -acceptor properties of alkylphosphine ligands.

The donor/acceptor properties of phosphines depend on the electronic properties of their substituents: functional groups with electron withdrawing effects will decrease the σ donation while enhancing the π -backbonding, on the other hand substituents with electron donating properties are strengthening the σ -donation bond. This behaviour provides an explanation, why strong σ donors like alkylphosphines increase the electronic density on the metal center, whereas phosphites on the other hand withdraw the electronic density.

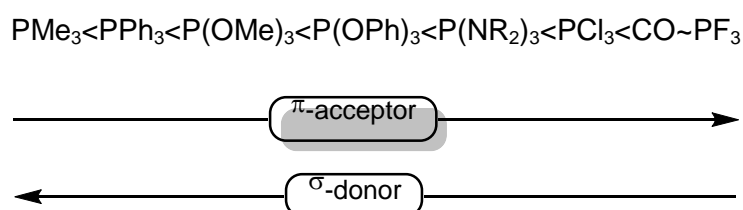


Figure 3: Classification of different phosphines.

Therefore, it is possible to order phosphines according to their σ -donor/ π -acceptor properties (Figure 3). This classification was described and published by Tolman in 1977, in which he also introduced a parameter (Tolman's cone angle Θ) to describe the space occupied by a coordinated phosphine^[5]. The donating/withdrawing properties also affect the basicity of the phosphine. Being a moderately strong Lewis base, depending on the substituents, the pK_a varies between acidic ~ 2.7 (PPh_3) and more basic values ~ 11.4 (PCy_3)^[6].

Another important advantage of phosphine containing ligands is their NMR activity in $^{31}P\{^1H\}$ -NMR spectroscopy. Providing a nucleus with $\frac{1}{2}$ spin, 100% natural occurrence and a relatively high sensitivity, this method is a powerful tool for characterization of ligands, complexes and sometimes giving insight in catalytic mechanisms.

This composition of tuneable steric, electronic, stereochemical and analytical properties make phosphine ligands one of the most used ligands in homogeneous catalysis.

2.2 Pincer Ligands

Pincer ligands are named after their coordination mode to metal centers: they are tridentate ligands featuring an aromatic backbone, bound to two-electron donor groups. The word pincer is derived from the tool, which the ligands resembles. First reported in 1976 by Shaw^[1], the chemistry of pincer ligands and complexes became a vast increasing research field in the past 35 years, including many catalytic applications in homogeneous catalysis^[7], due to their modularity and variability^[2b, 8].

In Figure 4, the general structure of a pincer complex is described: it contains an aromatic backbone and two donor groups (E), which are connected by a spacer (A). The metal center is meridionally coordinated, forming two five-membered rings with a constrained geometry, explaining high thermal stability, though some pincer ligands can be considered to show hemi-labile coordination behaviour.

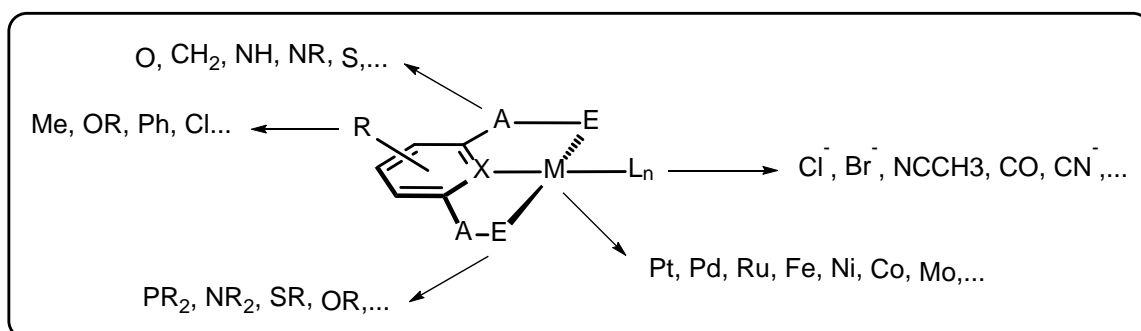


Figure 4: General structure of a tridentate pincer complex.

The *ipso* atom (X) in the aromatic ring usually is N or C, in the latter case the ligand has to be deprotonated before coordination is possible, or sometimes, the C-H bond has *agostic* binding properties, building a three-center two electronic bond^[9]. For the spacer (A) methylene groups (-CH₂-) are very common, by the use of amines (-NH-) or oxygen atoms (-O-) the introduction of the donor groups is simplified. As for the lone pair donors (E), dialkyl amines (NR₂), disubstituted phosphines (PR₂), phosphites (P(OR)₂), thioethers (SR), or N-heterocyclic carbenes (NHC's), etc. are reported in literature. In Figure 5, some different pincer type ligands are shown:

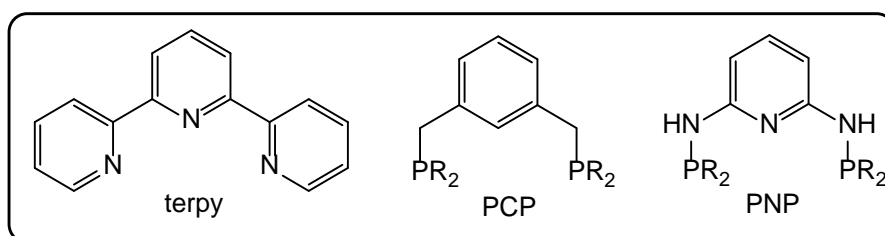
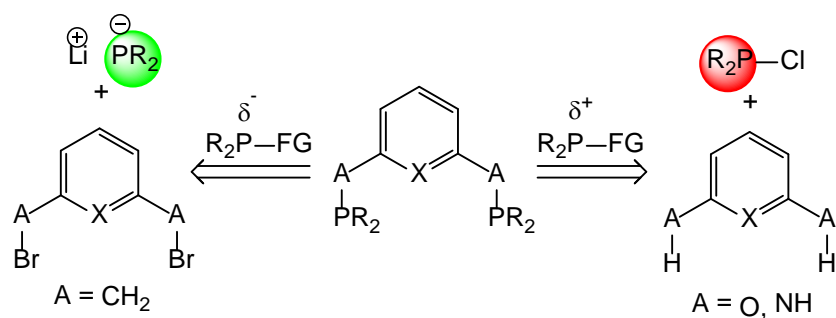


Figure 5: Examples of different pincer type ligands.

The notation of the pincers usually contains the three donor atoms: the PCP binds via carbon and phosphines, the PNP provides two phosphine groups and a pyridine nitrogen, etc. The spacer and the functional group on the phosphines (PR₂) can be mentioned, too. PNP^{NH}-iPr describes a phosphine/pyridine pincer with an amine spacer and two isopropyl groups on the phosphines, for example.

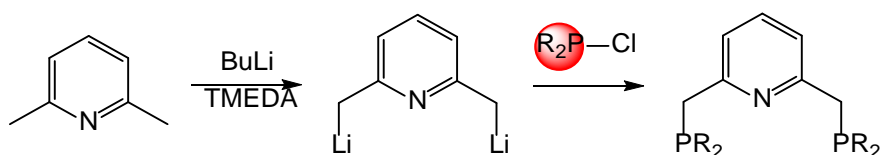
The choice of the spacer group not only influences the steric and electronic properties, but also determines the synthetic strategy for the introduction of the phosphines. In principle, two different synthetic pathways exist, shown in Scheme 2:



Scheme 2: Synthetic pathway for introduction of the phosphines.

- 1) The P-synthon has a negative charge, therefore the functional group of the spacer is positively polarized, the phosphorous precursor is a secondary phosphine, which has to be deprotonated by a strong base (*n*-BuLi, KO*t*Bu). In this case the spacer is typically an alkyl bromide.
- 2) If the P-synthon has a positive charge, as a consequence of this the spacer is negatively polarized. The phosphorous precursor typically is a chlorophosphine or phosphite and the spacer group features a protic hydrogen atom. Depending on the steric properties, this proton can be deprotonated first or the HCl, formed during the reaction has to be scavenged.

However, for 2,6-lutidine as ligand precursor by using the principle of 'Umpolung'^[10], the moderately acidic, benzylic proton can be abstracted, the chlorophosphine is then added^[11] (Scheme 3):



Scheme 3: Ligand synthesis, using 2,6-lutidine as precursor.

Both synthetic pathways have their pros and cons: A wide range of different chlorophosphines are commercial available (though quite expensive) and can be purified by distillation if necessary. Secondary phosphines bear a higher sensitivity towards oxidation and in most cases cannot be purchased, but synthesis of chiral phosphines is much easier via this pathway^[12].

2.3 CO Addition

Carbon Monoxide plays an important role as a key molecule in various fields in modern coordination chemistry. In laboratory and industrial scale productions like hydroformylation reactions^[13], the Monsanto^[14] or Cativa^[15] process, and the Fischer-Tropsch^[16] syntheses, as well as in biological context^[17], the activation of CO by addition to a transition metal complex and the understanding of the resulting binding properties are of high interest. CO shows σ -donor and strong π -acceptor behaviour and is considered to have one of the largest field splitting of ligand field energy levels^[18].

Therefore, in most cases the resulting CO-complexes are low-spin and the carbon-metal bond is thermodynamically stable. However, especially coordinatively unsaturated iron complexes tend to show a great range of reactivity towards CO^[19]:

Visible in Figure 6: Energy profiles of the addition of CO to a coordinatively unsaturated complex in different spin states., the reaction of CO with unsaturated complexes can either lead to addition, in that case forming low-spin complexes, or rejection. The outcome depends strongly on the number (and electronic properties) of the co-ligands, the charge and the geometry of the complex and also on the spin state of the metal. According to the crystal-field theory, the balance between the orbital splitting difference is determined by the balance between the orbital splitting difference (ΔE , HOMO-LUMO gap) and the pairing energy (PE), which is the energetic cost of pairing up two electrons in the same orbital.

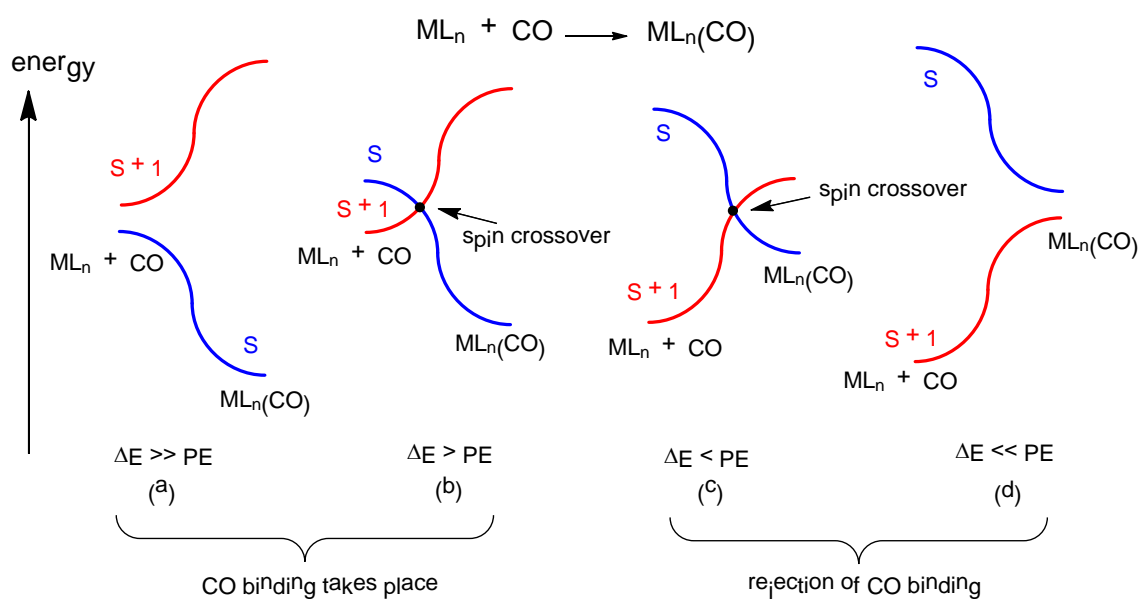


Figure 6: Energy profiles of the addition of CO to a coordinatively unsaturated complex in different spin states.

If $\Delta E > PE$, low-spin complexes are favoured, hence addition will take place, while for $\Delta E < PE$ the high spin configuration will be favoured:

Case (a) is typical for 2nd and 3rd row transition metals: the system is more stable in the saturated configuration, starting at a low spin state and the addition of CO is an exothermic reaction.

Case (b) resembles the addition of CO to 1st row transition metals: The unsaturated complex is usually in a high spin state, the spin state change occurs at the minimum energy crossing point (MECP) and the low spin product is energetically stabilized by pairing two electrons, meaning that the HOMO-LUMO gap is still larger than the pairing energy.

Case (c) & (d): The overall reaction is thermodynamically disfavoured, therefore CO addition will be rejected.

2.4 Catalytic hydrogenation

One of the most important fields in organometallic chemistry is the homogeneous catalytic hydrogenation, using transition metal complexes as catalysts. Almost as important as the reduction of C=C bonds is the hydrogenation of C=O bonds, especially due to their prochirality, the reduction of ketons to secondary alcohols represents an elegant method to introduce chirality into certain substrates^[20].

Also, the advantages of homogeneous compared to heterogeneous systems is their high catalytic activity, reaching turn over numbers (TON) up to 10^5 at a high turn-over frequency (TOF) even at room temperature, leading to exceedingly low catalyst loading^[21], their selectivity to target functional groups and their activity at low hydrogen pressure.

In principle, two different methods exist, distinguished by the hydrogen source: the direct hydrogenation with gaseous H_2 ^[22] or transfer hydrogenation^[23] from a hydrogen donor molecule, usually isopropanol. Though for lab scale reactions the design and application of transfer hydrogenation catalysts might be easier compared to hydrogenation systems, the latter is clearly preferred by industry^[20]. Extensively described by Morris^[24], the catalytic mechanism can be inner sphere, meaning the substrate molecule coordinates to the metal centre during reaction, or outer sphere, where reduction takes place without direct binding between substrate and complex. In addition to that, the ligand can be involved in the catalytic

cycle, mainly enhancing the substrate's coordination or by featuring acidic protons, which are deprotonated/reprotonated^[2f, 25].

Certainly, Noyori's approach in 1980 to introduce phosphine based ligands providing axial chirality with a BINOL backbone was a breakthrough, as shown in Figure 7, exceeding excellent enantioselectivity up to 95 % ee:

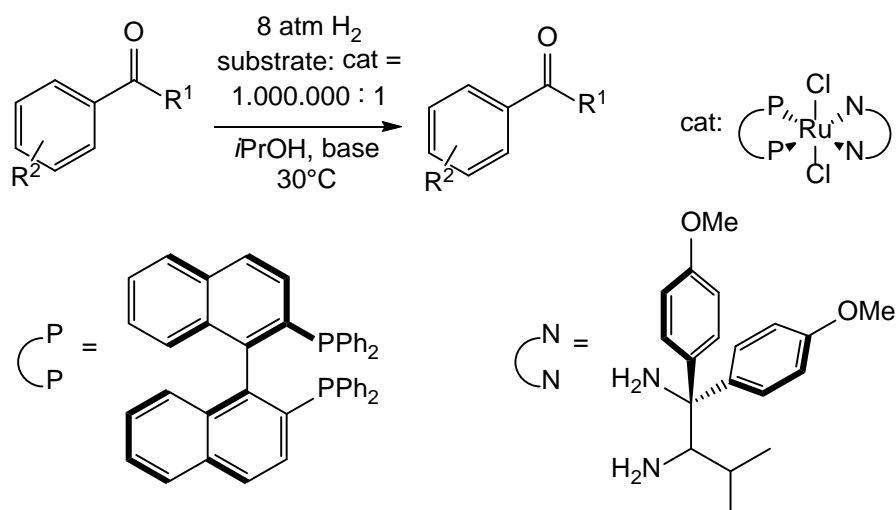


Figure 7: Noyori's BINAP based Ru(II) catalyst.

Usually, for noble transition metals, the energy barrier between two oxidation states can be considered to be relatively small, facilitating oxidative addition. This is particularly important for a certain type of hydrogenation reaction, which often takes place in Ru/Rh catalysed reductions. This catalysis is believed to work with an inner sphere mechanism without involvement of the ligand, therefore the dihydrogen splitting happens in a homolytic pathway by oxidative addition and reductive elimination, flipping the metal's oxidation state, in the case of Ru, between +II and 0 (Figure 8):

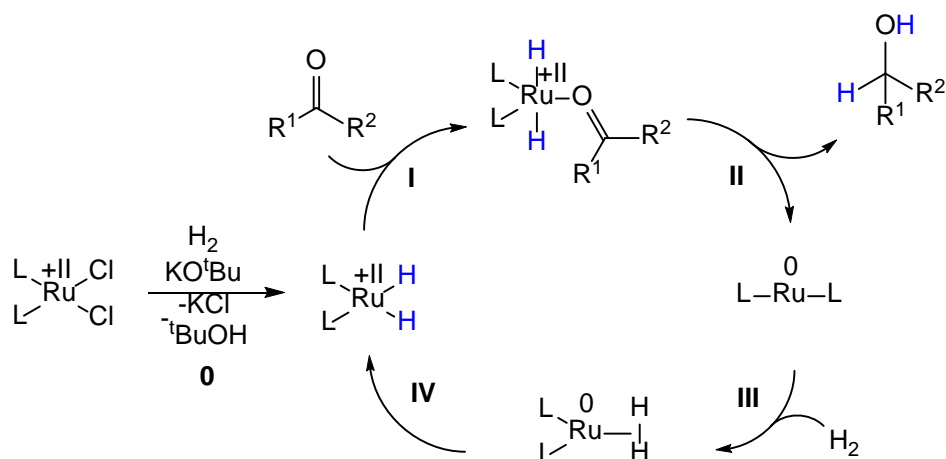


Figure 8: Catalytic mechanism, providing change in oxidation state.

- 0:** In the first step, the catalyst has to be activated by addition of a base, in order to create an open coordination site. The complex then reacts with H_2 and the alcoholate to form a dihydride species and the corresponding alcohol. In the activation step, the H-H bond is heterolytically cleaved.
- I:** The substrate coordinates to the dihydride complex, the oxidation state is not changed.
- II:** The substrate is reduced by insertion of one of the hydrides, the other is formally oxidized to a proton while elimination occurs to form the alcoholic product. By this reductive elimination the oxidation state of the metal centre is reduced, in this case forming a Ru(0) complex.
- III:** This highly coordinatively unsaturated complex reacts with H_2 , first by side-on coordination, forming a dihydrogen complex.
- IV:** The H-H bond is homolytically cleaved by oxidative addition to the Ru metal centre, changing the oxidation state to +II.

However, the ‘traditional’ transition metals Ru, Rh, Pt, Ir, etc. used in homogeneous catalysis do feature some disadvantages: they are expensive, rare and some have to be considered to be toxic. Therefore, recently attempts have been made to use non-toxic and cheap transition metals instead, and especially iron seems to be a promising possibility^[26].

Being a 1st row transition metal, the energy barrier between +II and the highly unstable oxidation state +IV is fairly high, oxidative addition of a substrate is not possible. Instead, H_2

splitting occurs heterolytically^[27] and the ligand has to be directly involved in the reaction. As a consequence, complex synthesis for iron catalysts bears some challenging tasks. Ligands have to feature strong splitting donors like phosphines and/or CO in order to maintain a low spin state during catalysis. Furthermore, a high electronic density has to be provided to insure stability of the hydride and an acidic proton for heterolytic H₂-splitting is necessary.

In Figure 9, different examples of iron based catalysts are displayed. PNP^{NH} or PNP^{CH}₂-type complexes by Milstein and our working group are potent catalysts for hydrogenations^[2f, 25] of ketons, Morris' type is used for asymmetric transfer hydrogenations^[24, 28] and Guan reported iron catalysed hydrosilylations^[29].

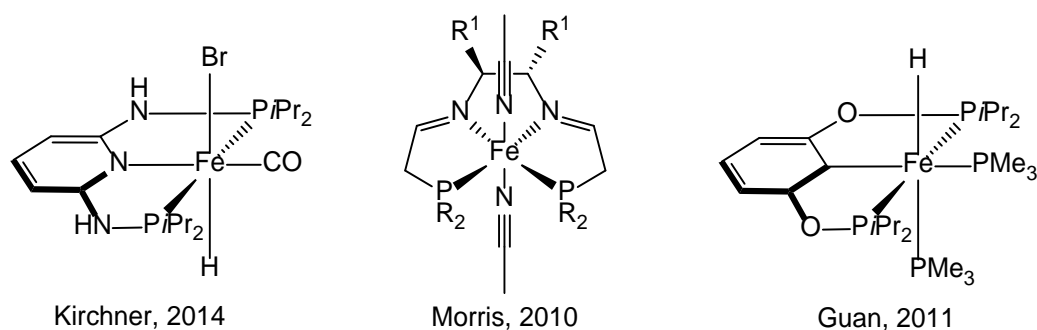


Figure 9: Recent developed Fe-based complexes used as catalysts.

Due to the impossibility of oxidative addition, the proposed catalytic pathway differs from that of noble metal catalysts (Figure 10):

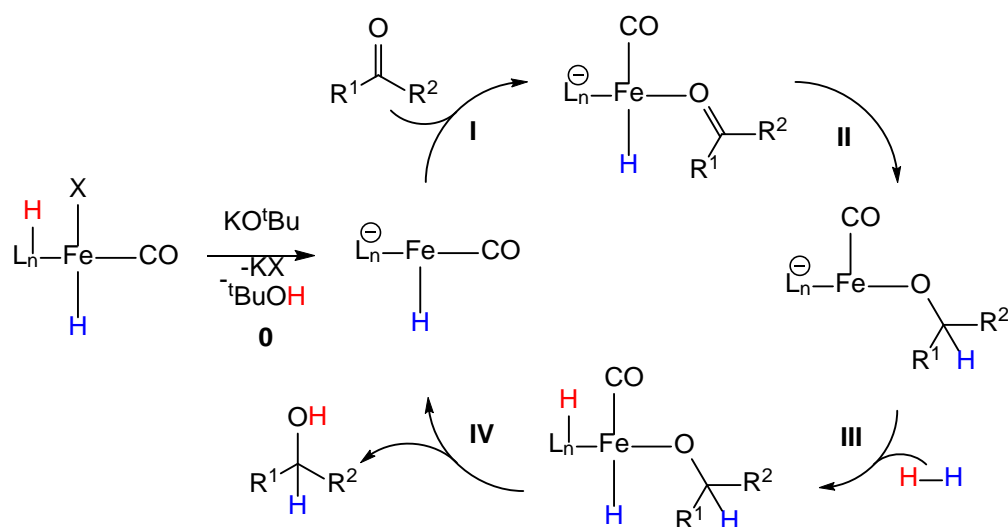


Figure 10: Catalytic mechanism with involvement of the ligand.

- 0:** In the first step, the catalyst has to be activated by addition of a base. The halide is abstracted and the ligand deprotonated, forming an open coordination site
- I:** The substrate coordinates to the coordinatively unsaturated complex.
- II:** The substrate is reduced by migration of the hydride to the positive polarized carbon, forming again an open coordination site.
- III:** Dihydrogen is added and heterolytically cleaved; therefore, formally a proton and a hydride are formed. The hydride binds to the positively charged metal centre, the protons reprotonates (the solvent may be involved in the proton transfer) the ligand.
- IV:** The product is cleaved by protonation, simultaneously deprotonating the ligand and forming an open coordination site.

Recently, this proposed catalytic cycle has been discussed a lot^[25, 27a, 30]. Certainly, the importance of an alcoholic solvent for stabilizing open coordination sites and for proton transfer has been proven by experiment. But on the other hand the reprotonation of the ligand, reported in step III, still is of speculative nature. It is also conceivable, that the formed proton is abstracted externally by the alcoholate in solution. In addition to that, the cleavage in step IV might be an exchange reaction between the product and the alcoholic solvent.

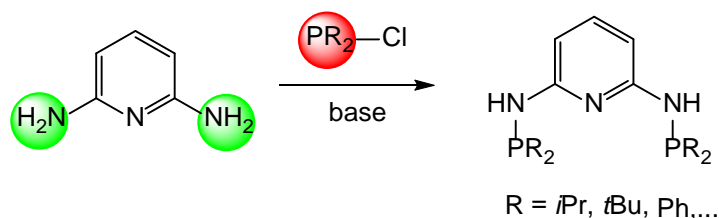
3 Results and Discussion

3.1 Ligand synthesis

3.1.1 General considerations

A lot of different pincer ligands systems are known in literature, as described in 2.2. Originally featuring a CH₂ spacer group, the synthesis of pyridine based pincer ligands has two major drawbacks: the organic precursors are not commercially available or expensive and the necessary secondary phosphine is highly sensitive towards oxidation.

In order to avoid those disadvantages, a new pyridine backbone pincer system was invented by our group in 2006^[31]. Based on 2,6-diaminopyridine and derivatives, the phosphine is connected to the aromatic backbone by an amine spacer. This P-N bond is established by nucleophilic substitution on the phosphorous by condensing HCl and scavenging by a base. Depending on the steric and electronic properties of the phosphine, the amine can/must be deprotonated first. This is particularly the case for *t*Bu groups or bulky phosphites.



Scheme 4: Ligand synthesis of PNP^{NH} ligands.

This reaction usually is carried out in aprotic and dry solvents (toluene, THF) under inert conditions at elevated temperature up to 80°C. Treatment of 1 equiv. 2,6-diaminopyridine with 2 equiv. chlorophosphine in the presence of an excess of Et₃N leads to the desired product in yields >90 % and high purity.

In the last 8 years, many different ligands have been synthesized and published by our group³², featuring alkyl and aryl phosphines, and chiral and achiral phosphites or phosphoramidites, respectively (Figure 11):

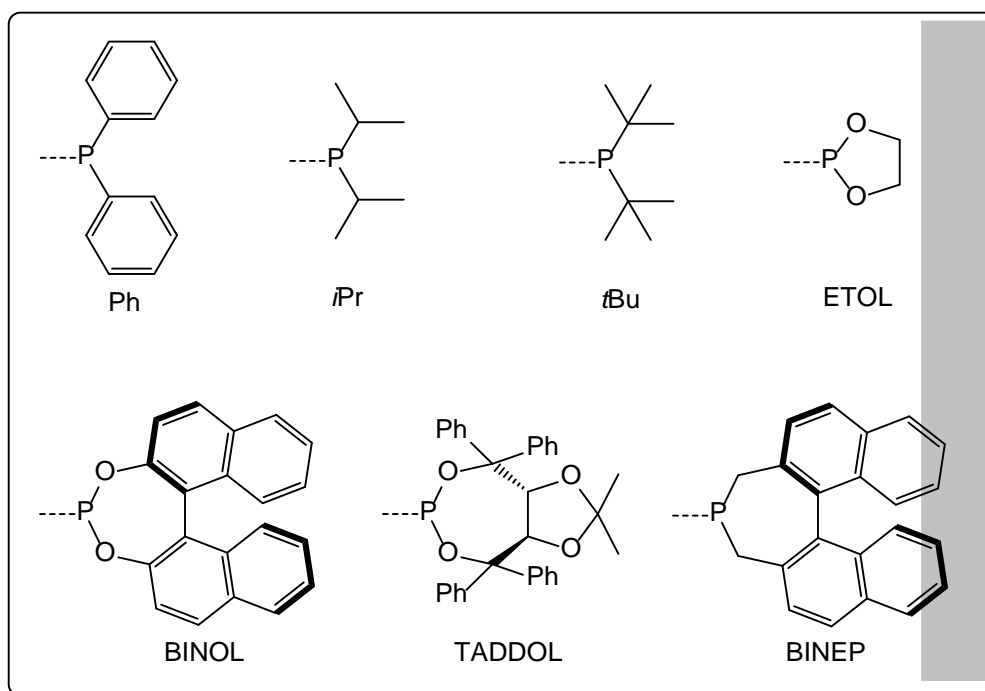
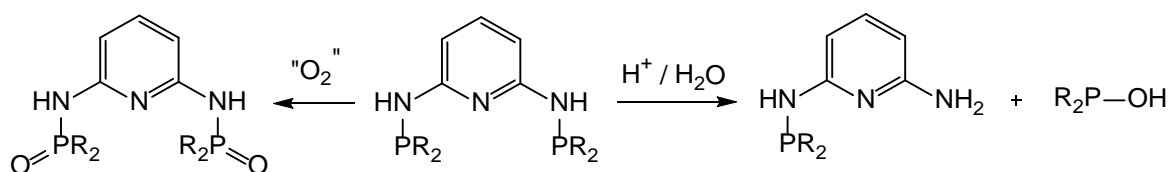


Figure 11: Several different PNP ligands.

Though the aminophosphines are synthesized by a simple substitution reaction and a wide range of different chlorophosphines / phosphites can be used, the NH-spacer system has one important disadvantage, compared to CH₂ linked phosphines: the P-N bond can be easily cleaved by hydrolysis under acidic or strongly basic conditions in the presence of water, thus, the free phosphine is sensitive towards oxidation, shown in Scheme 5:

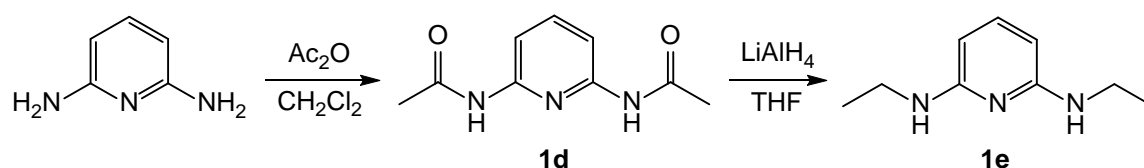


Scheme 5: Hydrolysis and oxidation of PNP ligands.

The application of PNP^{NH}-ligands in iron^[2e, 31], molybdenum^[32b], tungsten^[32a] and noble transition metals has been reported in literature, and the deprotonation of the acidic NH-functionality has been proven to be active in the activation of H₂^[33].

3.1.2 N-alkylated PNP ligands

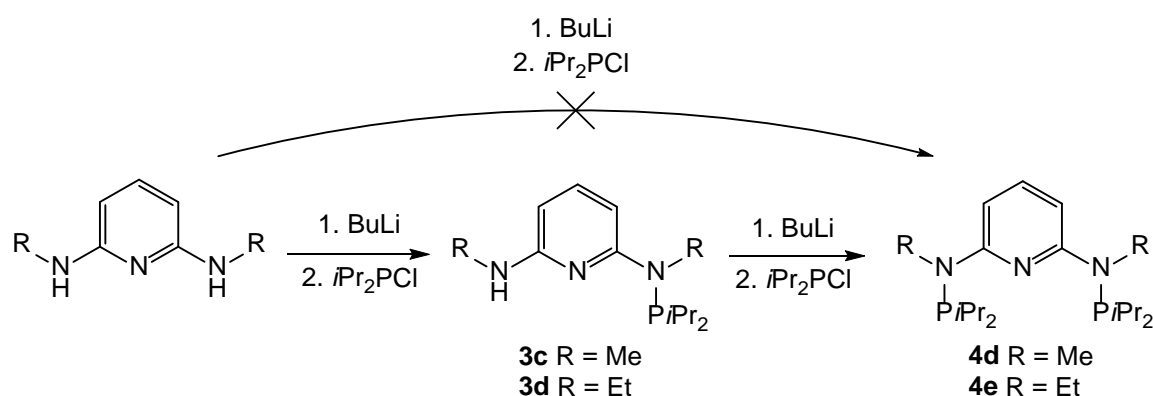
Though the deprotonation/reprotonation was proved by ^1H and ^2H -NMR experiments and single-crystal XRD, the importance of the acidic NH was discussed, especially the possible different outcome if the reaction site was blocked by an alkyl group. The synthetic route to $\text{PNP}^{\text{R-}i\text{Pr}}$ ligands has already been published in 2006^[31]. The corresponding pyridine precursors can be accessed by acylation and reduction by LiAlH_4 in excellent yields (>85 %) and high purity after purification via bulb-to-bulb distillation (Scheme 6):



Scheme 6: Alkylation of 2,6-diaminopyridine.

The corresponding N^2, N^6 -dimethylpyridine-2,6-diamine is synthesized by the reaction of methyl amine and 2,6-dibromopyridine in a microwave vial^[34].

Because double deprotonation of both protons cannot be done simultaneously, the amino groups have to be phosphorylated stepwise. The synthesis can be carried out in a one-pot reaction, however, the overall yield and purity of the ligands is increased if workup is done after the first step (Scheme 7):



Scheme 7: Phosphorylation of N-alkylated 2-aminopyridines.

Despite of already being reported, this synthesis could first not be repeated. Care was taken to control stoichiometry and temperature, but in the first tries seemed to lead mainly to

hydrolysed and P-P coupling products. In fact, the desired product has been successfully synthesized, but was overseen in $^{31}\text{P}\{^1\text{H}\}$ -NMR due to its broad signal (Figure 12):

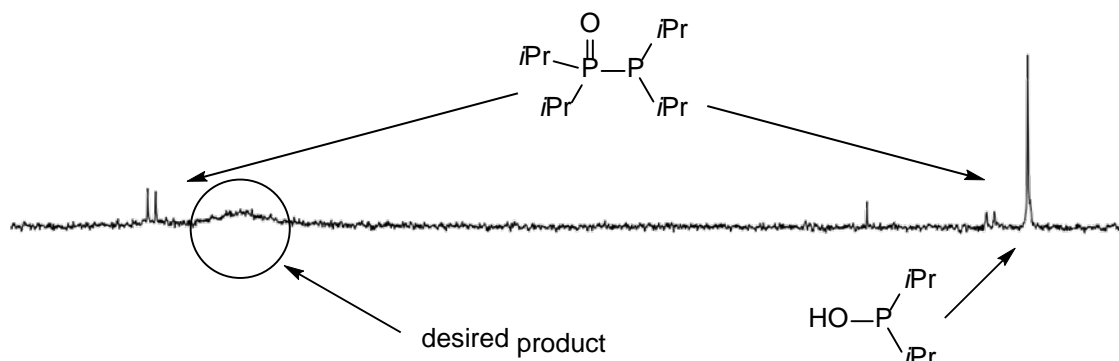
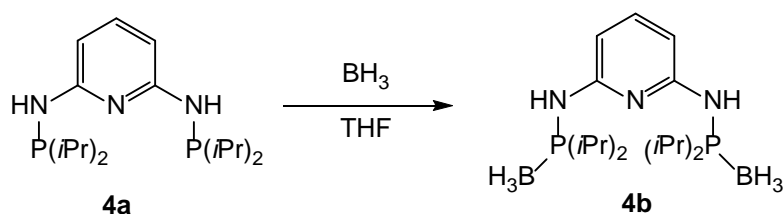


Figure 12: $^{31}\text{P}\{^1\text{H}\}$ -NMR reaction spectrum of **3c**, showing the reaction of N^2,N^6 -diethylpyridine-2,6-diamine and $\text{P}(\text{iPr})_2\text{Cl}$.

So a different approach was developed: to alkylate the amine functionality after phosphorylation. Starting at PNP-*iPr* **4a**, the phosphine group has to be protected first in order to avoid reaction with the alkylation reagent, which would take place otherwise. Transformation of the phosphine to the phosphine oxide or thiophosphine was successful, as these are known protection groups, but all attempts for deprotection either failed or lead to cleavage of the P-N bond under acidic conditions.

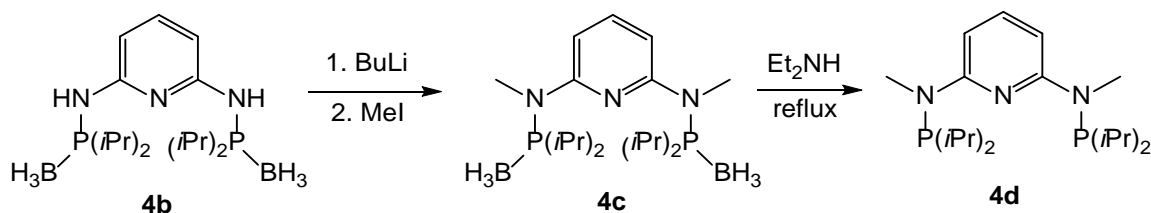
Another protecting group for phosphines known in literature is borane BH_3 ^[12, 35], commercial available as 1.0 M solution in THF. Protection is achieved by dissolving the phosphine ligand in THF and adding the borane solution in small excess (2.50 eq), depicted in Scheme 8, in quantitative yield:



Scheme 8: BH_3 protection of PNP-*iPr*.

The alkylation is carried out after deprotonation of the acidic proton: *n*-BuLi is used for selective deprotonation and methyl iodide acts as the alkylation reagent. At ambient

temperature the pyridine nitrogen is not alkylated, leading to the desired product in acceptable yield (63%). Due to the basicity of the *i*Pr-phosphine, the deprotonation has to be performed by refluxing in Et₂NH, depicted in Scheme 9.



Scheme 9: Alkylation of BH₃-protected PNP-*i*Pr ligand.

The ligand PNP^{Me}-*i*Pr was isolated as yellow oil, containing small amounts of impurities of unreacted starting materials, but can be recrystallized in hot acetonitrile to obtain it as white solid. For the compound PNP^{Et}-*i*Pr, recrystallization is not possible due to its low melting point, therefore it was purified by flash chromatography, which is a possible method of purification for almost every synthesized ligand. To avoid P-N bond cleavage, the silica gel has to be conditioned with Et₃N foregoing.

3.1.3 Chiral PNP ligands

Already in 2006, Benito-Garagorri used tartaric acid derivatives and ephedrine as key molecules for the implementation of chirality. Generally, the use of diols has to be recognized as THE method to access chiral phosphines, as the chiral pool provides plenty of them in multiple gram or even kilogram scale^[36]. Forming a five membered dioxaphospholane by reaction of tartaric esters and PCl₃, chiral phosphite PNP ligands were produced and the catalytic application in coupling reactions has been tested^[2e].

Despite their modular synthesis, the tartaric acid based phosphite contains an ester functionality, bearing low stability under basic conditions in protic solvents, making application in hydrogenation or transfer hydrogenation reactions impossible.

In the search for alternative chiral diols, either commercial available or accessible by trivial synthesis in multiple gram scale, BINOL (1,1'-Bi-2-naphthol) and TADDOL (2,2-Dimethyl- $\alpha,\alpha,\alpha',\alpha'$ -tetraphenyl-dioxolan-4,5-dimethanol) were taken into consideration. The first one, BINOL, has already been reported by our group for being utilized in PNP and PCP ligands^[31].

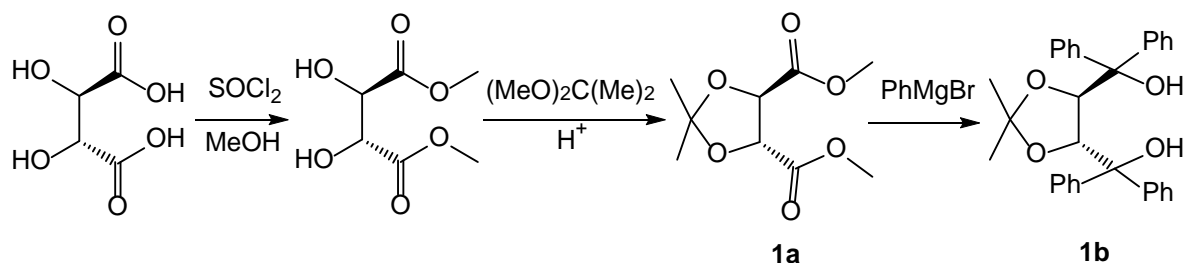
^{37]}, but the thermal stability was found to be very low; decomposition was observed during synthesis even at r.t.

First reported by Seebach in the early 1990's^[38], TADDOL is used as a chiral auxiliary for the asymmetric reduction of ketons^[39] and modified Sharpless epoxidations^[40] in stoichiometric reactions, and transition metal catalysed coupling reactions as chiral backbones in phosphoramidite ligands^[2c, 41]. So far, TADDOL based ligands have not been reported regarding iron complexes.

The synthesis of TADDOL is well known in literature^[41-42], starting directly from L-tartaric acid, or from commercial available L-dimethyl tartrate (Scheme 10).

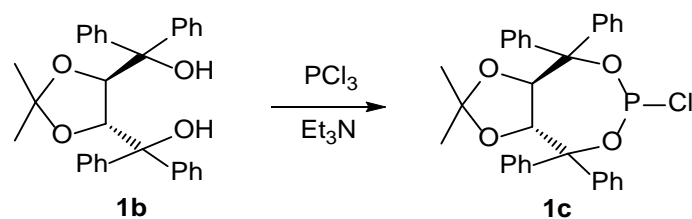
- 1) methylation by SOCl_2 in methanol
- 2) protection of the hydroxy groups by 2,2-dimethoxy propane
- 3) reduction by Grignard reaction

The first 2 steps were carried out in quantitative yield, the overall yield after purification was >70 %:



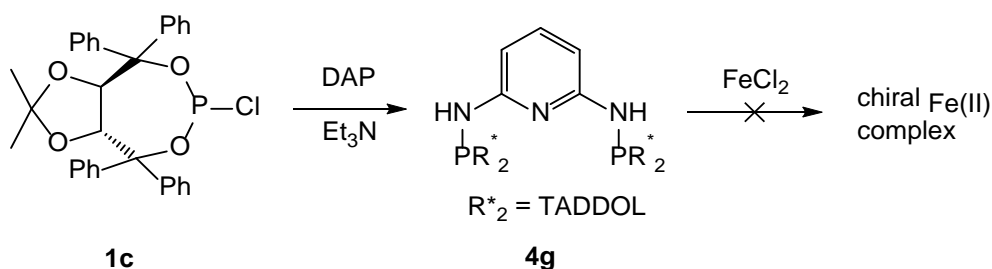
Scheme 10: TADDOL synthesis.

The next step, the phosphorylation by the reaction of TADDOL with PCl_3 in the presence of Et_3N was synthesized in dry toluene at 60°C , leading to the chlorophosphite in moderate yield (50-60 %) but high purity (Scheme 11). Reported in literature^[41], this compound is usually not isolated, but precipitation by addition of *n*-hexane proved to be an excellent way for purification.



Scheme 11: Phosphorylation of TADDOL.

2,6-diaminopyridine was then treated with **1c** in the presence of excess of Et_3N and the ligand PNP-TAD **4g** was obtained in sufficient yield and purity. However, this ligand showed exceeded sensitivity compared to PNP-*i*Pr and the following complexation reaction with FeCl_2 was not successful, as depicted in Scheme 12, but a green κ^2/κ^3 -complex was formed instead.

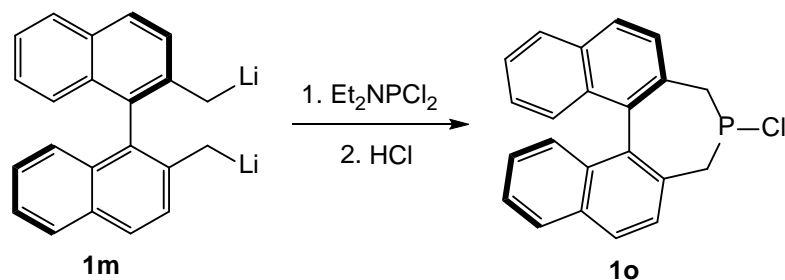


Scheme 12: Synthesis of PNP-TAD (**4g**) and unsuccessful complexation reaction.

This bonding behaviour has already been reported by our group: when treated with FeCl_2 , two PNP-Ph ligands directly form an octahedral κ^2/κ^3 -complex, regardless on the stoichiometry^[43].

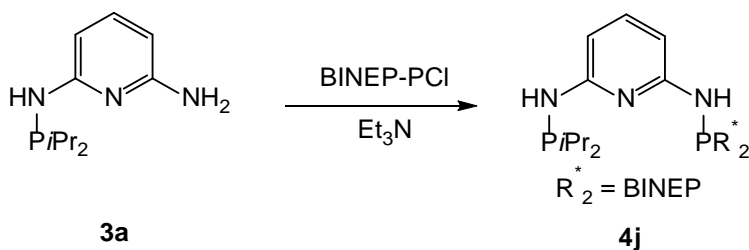
In order to avoid this, the symmetric ligand design was reconsidered. If one phosphorous donor atom furnishes electronic density and a moderately steric effect, and the other donor atom contains chirality, the complexation should be made possible. The mono-substituted PN/ NH_2 -*i*Pr **3a** is synthesized by reaction of excessive 2,6-diaminopyridine and $\text{P}i\text{Pr}_2\text{Cl}$ in the presence of Et_3N in moderate yield (61 %) and has to be purified by flash chromatography to remove unreacted starting material and the by-product PNP-*i*Pr **4a**.

The precursor was then used for the reaction with the chiral chlorophosphite TAD-PCl **1c** (Scheme 13):



Scheme 15: Synthesis of BINEP-PCI (**1o**).

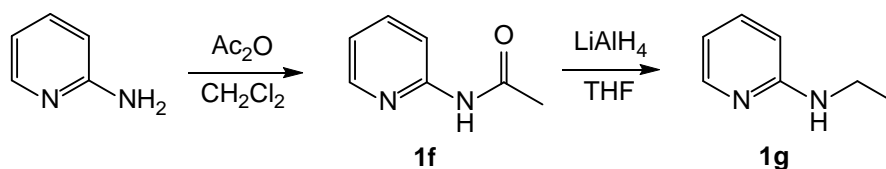
The chiral chlorophosphine **1o** was then used to form the chiral ligand PNP-*i*Pr/BIN **4j**, analogously to the TADDOL based PNP ligands, shown in Scheme 16:



Scheme 16: Synthesis of PNP-*i*Pr/BIN (**4j**).

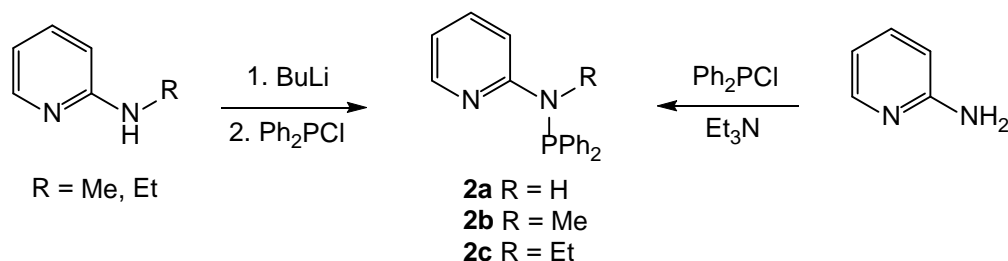
3.1.4 Bidentate PN & SN ligands

Analogously to the tridentate ligands, different diphenylphosphine bidentates have been synthesized^[45]. The 2-aminopyridine precursors were either purchased or, the 2-ethylamino pyridine produced via 2-step synthesis, respectively (Scheme 17):



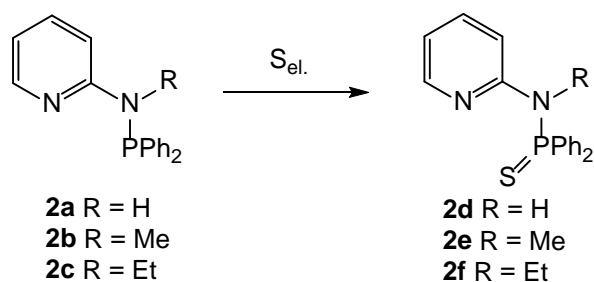
Scheme 17: Alkylation of 2-aminopyridine.

The phosphorylation was carried out in the same method; the secondary phosphine has to be deprotonated first (Scheme 18):



Scheme 18: Ligand synthesis of PN-Ph (**2a-c**) ligands.

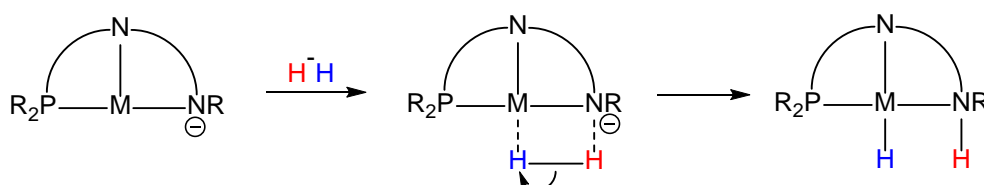
The resulting PN ligands have then been selectively oxidized by elemental sulphur^[46], in order to alter the donor properties (Scheme 19):



Scheme 19: Selective oxidation of PN ligands by elemental sulphur.

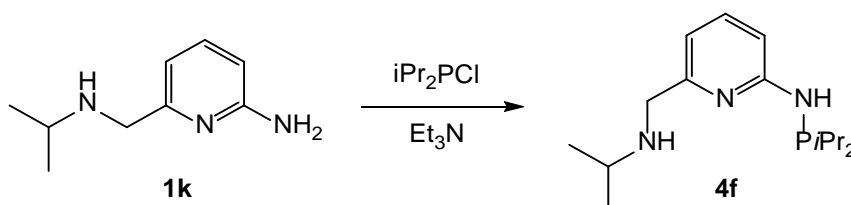
3.1.5 PNN ligand

The impotency of the NH functionality in PNP ligands has already been described. Used by Morris^[24] for his catalytic systems, a direct coordination of the nitrogen to the metal centre facilitates the H₂-splitting, leading to higher turn-over numbers or making the reaction possible in aprotic solvents, since no proton transfer takes place (Scheme 20):



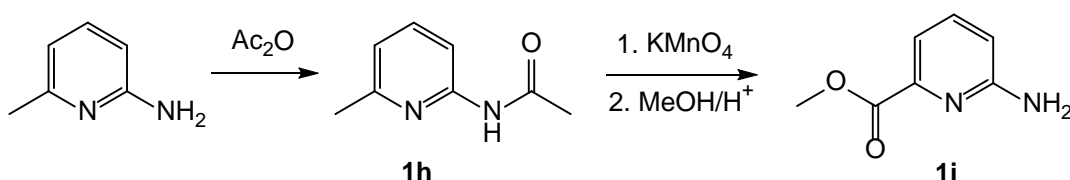
Scheme 20: Heterolytic H₂ splitting by coordinated NH ligand.

The synthetic pathway to form such a ligand was challenging. Milstein's route^[47], starting at 2,6-bis(chloromethyl)pyridine did not work with primary amines, leading to mixtures of different phosphines or amines. Finally it was possible to synthesize the amine **1k** which was selectively phosphorylated on the aromatic NH₂ group to form the PNN-*i*Pr ligand **4f** (Scheme 21):



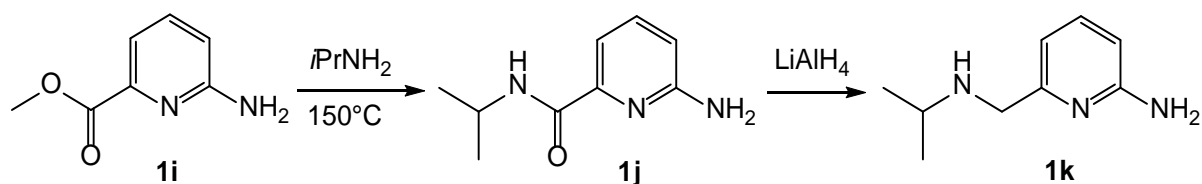
Scheme 21: Phosphorylation of amine **1k**.

The successful synthetic route is shown in the following schemes. The key step is the selective oxidation of the methyl group by KMnO₄. Since this reagent can lead to total oxidation of the substrate, it has to be converted to the amide first, in order to withdraw electronic density from the aromatic ring, therefore avoid total oxidation^[48]. The amide is then cleaved by the addition of methanol/sulphuric acid, forming the ester simultaneously in moderate yield (39%).



Scheme 22: Selective oxidation of the methyl group.

Next, the ester **1i** is quantitatively transformed into the amide **1j** by neat reaction in isopropyl amine in a pressure tube at 150°C for 4 h. This amide is then reduced by LiAlH₄ to form the desired amine **1k**.



Scheme 23: Amidation and reduction of the ester **1i**.

3.1.6 Characterization

The ligands **2a-f**, **3a-d** and **4a-j** were characterized using ¹H, ³¹P and ¹³C {¹H}-NMR. The formation of the ligands can be observed by ³¹P{¹H}-NMR and by the NH-signal in ¹H-NMR, as this proton shows a doublet with a distinct coupling constant ²J_{PH} in the range of 10 Hz, depending on the PR₂ group. Also, a significant shift can be observed for the pyridine protons. In 2,6-diaminopyridine the py⁴ appears at ~7 ppm, while in phosphorylated ligands this signal is shifted up to 7.50 ppm. The py³ and py⁵ protons are equal in for the symmetric PNP ligands and appear as a duple, while in the asymmetric substituted ligands **4h-j** the py³ and py⁵ protons give a separated signals.

In ¹³C{¹H}-NMR, the pyridine or phenyl signals usually are coupled to the phosphorous, but depending on the type of phosphine, those J_{CP} coupling constants can be significantly different. For example, the ¹J_{CP} for the ph¹ signal in PN^R-Ph ligands are usually in the range of 10 Hz, whereas for the SN^R-Ph the very same coupling constant is below the limit of detection.

The exact assignments, especially for ¹³C{¹H} -NMR, were confirmed by ¹H-COSY, HMBC (¹H-¹³C) and HSQC (¹H-¹³C) experiments. Interestingly, for the HMBC, the pyridine nitrogen facilitates ⁴J_{CH} cross peaks and in rare cases even ⁵J_{CH} signals were visible.

In Table 1, the ³¹P{¹H}-NMR shifts of all ligands are listed and the coupling constants of NH or NCH_x signals are compared. Noteworthy in the ³¹P-NMR shifts are the signals for the N-alkylated ligands **3c**, **3d**, **4d** and **4e**; the peaks are particularly broad. This can be explained by the increased electronic density surrounding the P-N bond. In the case of the boronated ligands **4b** and **4c**, the ³¹P-NMR signals should appear as broad quartets, however only broad multiplets were detected, regardless on the resolution or frequency, as this ³¹P{¹H}-

NMR experiment was performed with the same outcome at a frequency of 162 MHz and 101 MHz for $^{31}\text{P}\{^1\text{H}\}$, respectively.

Ligand		³¹ P{ ¹ H}-NMR		¹ H-NMR: NH or N-CH _x signal		
		shift [ppm]	signal	shift [ppm]	signal	J _{PH} [Hz]
2a	PN-Ph	25.9	s	5.31	d	8.4
2b	PN ^{Me} -Ph	50.9	s	2.97	d	1.6
2c	PN ^{Et} -Ph	49.5	s	3.61	dq	2.4
2d	SN-Ph	51.4	s	6.71	bs	-
2e	SN ^{Me} -Ph	64.8	s	3.15	d	10.7
2f	SN ^{Et} -Ph	64.1	s	3.79	dq	14.0
3a	PN/NH ₂ - <i>i</i> Pr	47.4	s	4.40	d	47.4
3b	PN/NH ₂ - <i>t</i> Bu	58.2	s	4.67	d	11.0
3c	PN/N ^{Me} H- <i>i</i> Pr	70.0	bs	2.82	d	5.1
3d	PN/N ^{Et} H- <i>i</i> Pr	78.8	bs	3.62	dq	6.7
4a	PNP- <i>i</i> Pr	47.6	s	4.24	d	11.1
4b	PNP- <i>i</i> Pr x(BH ₃) ₂	76.6	m	4.65	d	7.6
4c	PNP ^{Me} - <i>i</i> Pr x(BH ₃) ₂	94.0	m	3.17	d	7.9
4d	PNP ^{Me} - <i>i</i> Pr	69.5	bs	3.04	d	2.3
4e	PNP ^{Et} - <i>i</i> Pr	78.8	bs	3.65	dq	6.7
4f	PNN- <i>i</i> Pr	48.4	s	4.68	d	10.9
4g	PNP-TAD	134.0	s	5.50	d	3.9
4h	PNP- <i>i</i> Pr/TAD	47.9 (<i>i</i> Pr)	s	4.43 (<i>i</i> Pr)	d	11.2
		134.6 (TAD)	s	5.67 (TAD)	d	4.3
4i	PNP- <i>t</i> Bu/TAD	58.6 (<i>t</i> Bu)	s	4.67 (<i>t</i> Bu)	d	11.2
		132.4 (TAD)	s	5.55	d	2.4
4j	PNP- <i>i</i> Pr/BIN	48.6 (<i>i</i> Pr)	s	4.08 (<i>i</i> Pr)	d	10.7
		48.1 (BIN)	s	4.31 (BIN)	d	10.9

Table 1: ³¹P, ¹H NH, NCH_x shifts and J_{PH} coupling constants thereof.

The compounds **3a**, **3b**, **4h** and **4i** were also characterized by high-res MS spectroscopy, confirming the purity and chemical composition, depicted in Table 2. The TADDOL based ligands showed small impurities, which were identified as the oxidized species. As the ³¹P NMR gave no evidence of such impurities, these were either generated during preparation or measurement.

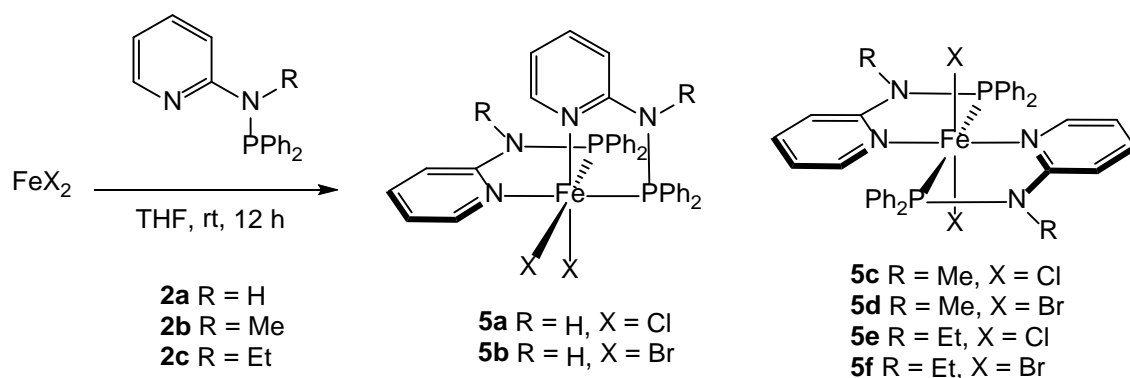
Ligand		ESI-HRMS (m/z), [M+H] ⁺	
		calculated	found
3a	PN/NH ₂ - <i>i</i> Pr	226.1468	226.1453
3b	PN/NH ₂ - <i>t</i> Bu	254.1786	254.1788
4h	PNP- <i>i</i> Pr/TAD	720.3115	720.3113
4i	PNP- <i>t</i> Bu/TAD	748.3428	748.3427

Table 2: ESI-HRMS of compounds **3a**, **3b**, **4h** and **4i**.

3.2 PN iron(II) complexes^[45]

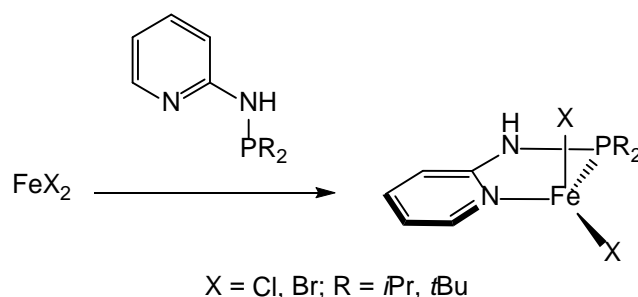
3.2.1 Synthesis

In sharp contrast to reactions with the bulky ligands PN-*i*Pr and PN-*t*Bu^[46a], treatment of anhydrous FeCl₂ or FeBr₂ with 2 equiv of the PN ligands PN-Ph (**2a**), PN^{Me}-Ph (**2b**) and PN^{Et}-Ph (**2c**) in THF at room temperature for 12 h afforded pale yellow octahedral complexes of the general formula Fe(PN^R-Ph)₂X₂ in yields between 77 and 92% isolated yields (Scheme 24). The formation of these complexes is independent of whether 1 or 2 equivs of ligands are used. However, in the first case substantial amounts of FeX₂ remained unreacted.



Scheme 24: Synthesis of Fe(PN^R-Ph)₂X₂ complexes.

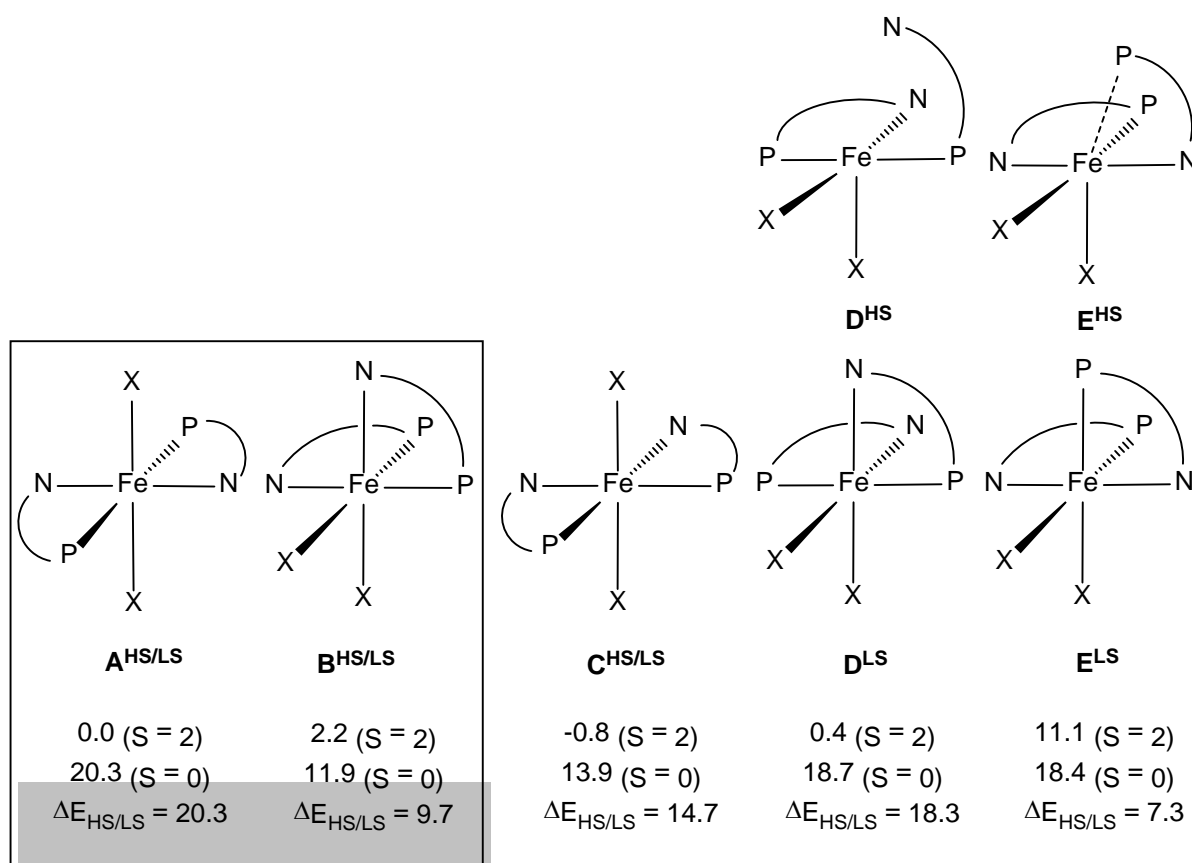
There was no evidence for the formation of tetra-coordinate Fe(PN^R-Ph)₂X₂ as in the case of the more electron donating and bulkier PN-*i*Pr and PN-*t*Bu ligands (Scheme 25).



Scheme 25: Coordination of PN-*i*Pr and PN-*t*Bu with FeX₂^[46a].

3.2.2 Solid state and solution studies

In the solid state all complexes are thermally stable if air is excluded. In solution **5a** and **5b** turned out to be highly unstable forming different decomposition products depending on the solvent (*vide infra*). On the other hand, **5c-5f** are stable in most common solvents such as CH₃OH, THF, CH₂Cl₂ and CH₃CN for several days without showing any noticeable decomposition. In fact, even single crystals suitable for X-ray diffraction measurements could be grown for **5c**. This behaviour clearly suggests that **5a** and **5b** are structurally different from **5c-5f**. It has to be kept in mind that for complexes of the general formula Fe(PN^R-Ph)₂X₂ in principle five different coordination isomers are conceivable as illustrated in Scheme 26:



Scheme 26: DFT calculated geometries and electronic energies in kcal/mol for X = Cl and PN = PN-Ph (**2a**).

The molecular structure of Fe(PN^{Me}-Ph)₂Cl₂ (**5c**), depicted in Figure 13, reveals that all Cl, P and N atoms are in *trans* position to one another. Accordingly, in the case of complexes bearing the PN^{Me}-Ph (**2b**) or PN^{Et}-Ph (**2c**) ligand isomer **A** in its high spin form is the thermodynamically most stable species. This finding is also supported by DFT calculations (*vide infra*).

In order to establish the nature of the isomer formed in the case of complexes **5a** and **5b** featuring the PN-Ph ligand (**2a**), reactivity studies in different solvents were carried out. Additionally, a variety of measurements including SQUID magnetometry, ^{57}Fe Mössbauer spectroscopy, UV/VIS, Raman, ESI-MS as well as DFT calculations were performed.

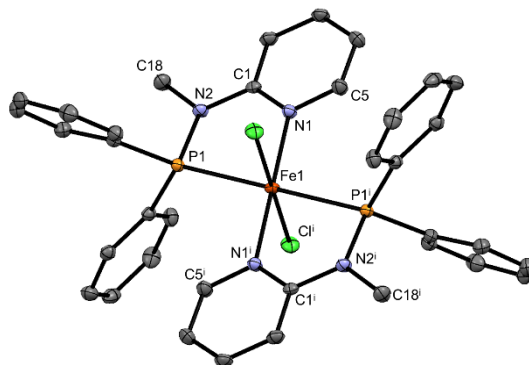
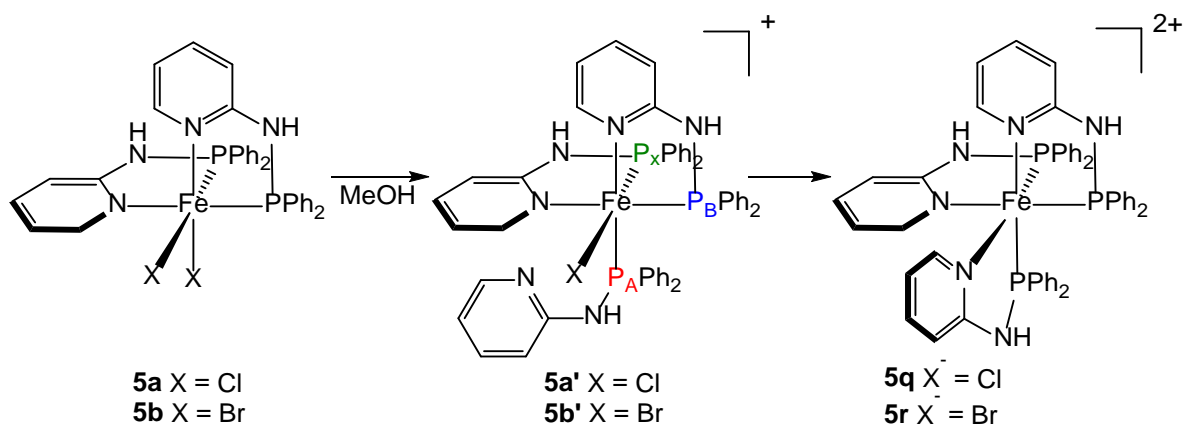


Figure 13: Structural view of *trans*- $\text{Fe}(\text{PN}^{\text{Me}}\text{-Ph})_2\text{Cl}_2$ (**5c**) showing 50% thermal ellipsoids (H atoms and solvent molecules omitted for clarity). Selected bond lengths (Å) and bond angles (°): Fe1–N1 2.1910(13), Fe1–P1 2.6046(4), Fe1–Cl1 2.3637(4), P1–N2 1.7195(14), N2–C18 1.469(2), N2–C1 1.394(2), N1–Fe1–P1 75.80(4), N1–Fe1–P1i 104.20(4), N1–Fe1–Cl1 88.67(4), N1–Fe1–Cl1i 91.33(4), P1–Fe1–Cl1 94.83(1), P1–Fe1–Cl1i 85.17(1), Cl1–Fe1–Cl1i = P1–Fe–P1i = N1–Fe1–N1i = 180.00.

Due to the instability of **5a** and **5b** in solution as well as the paramagnetic nature of complexes **5a-5f**, bearing basically aromatic protons and carbon atoms, ^1H -NMR spectra exhibited only very broad and featureless signals and were thus not very informative. $^{13}\text{C}\{^1\text{H}^{491}\text{H}\}$ -NMR signals could not be detected at all.

In CH_3OH complexes **5a** and **5b** are substitutionally labile and undergo rearrangement reactions to yield the diamagnetic dicationic *tris*-PN-Ph complex $[\text{Fe}(\text{PN-Ph})_3]^{2+}$ (**5q**, **5r**) together with free ligand PN-Ph, the paramagnetic tetrahaloferrate anion FeX_4^{2-} and intractable paramagnetic materials. Monitoring of this reaction by $^{31}\text{P}\{^1\text{H}\}$ -NMR spectroscopy revealed that this reaction proceeds *via* the intermediates *cis*- P,N - $[\text{Fe}(\kappa^2\text{-}P,N\text{-PN}^{\text{H}}\text{-Ph})_2(\kappa^1\text{-}P\text{-PN}^{\text{H}}\text{-Ph})(\text{X})]^+$ where one PN ligand is coordinated in in $\kappa^1\text{-}P$ -fashion (Scheme 27).



Scheme 27: Reaction of $\text{Fe}(\text{PN-Ph})_2\text{X}_2$ in MeOH.

This reaction involves an intermolecular ligand transfer between two $\text{Fe}(\text{PN-Ph})_2\text{X}_2$ complexes and is complete within about 15 minutes at room temperature. In the $^{31}\text{P}\{^1\text{H}\}$ -NMR spectra (measured at a 600 MHz NMR spectrometer), intermediate **5a'** displays an ABX pattern providing further evidence for a *cis-Cl,P,N*-structure of the starting materials **5a** and **5b**, depicted in Figure 14.

Intermediate **5b'** still exhibits a simpler A_2X spin system ($\delta_{\text{A}} \approx \delta_{\text{B}}$). The rational synthesis of the complexes **5q** and **5r** can be achieved in 90% isolated yield by reacting anhydrous FeX_2 with 3 equivs of PN-Ph **2a** in CH_3OH .

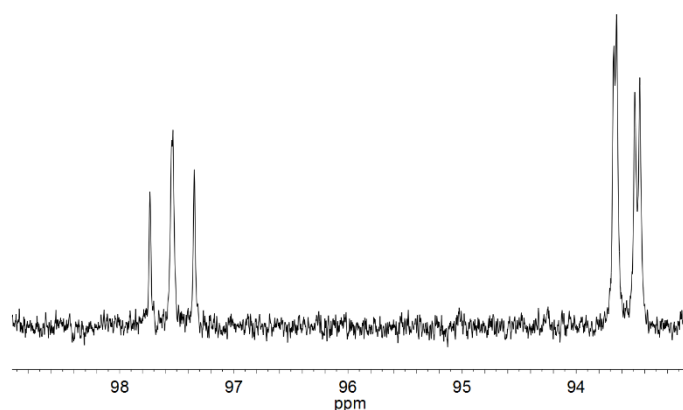


Figure 14: $^{31}\text{P}\{^1\text{H}\}$ -NMR spectra measured at 243 Mhz, monitoring the reaction of $\text{Fe}(\text{PN-Ph})_2\text{Cl}_2$ (**5a**) in CD_3OD .

This complex gives rise to a singlet in the $^{31}\text{P}\{^1\text{H}\}$ -NMR spectrum at 104.5 ppm indicating that all P and N atoms, respectively, are *cis* to one another. The structure of **5r** was unequivocally established by X-ray crystallography. A structural view is depicted in Figure 15 with selected bond distances given in the caption. This coordination behavior was only observed in the

case of the $\text{Fe}(\text{PN-Ph})_2\text{X}_2$ complexes **5a** and **5b**, whereas the complexes featuring the ligands $\text{PN}^{\text{Me}}\text{-Ph}$ (**2b**) or $\text{PN}^{\text{Et}}\text{-Ph}$ (**2c**) showed no lability in solution or reactivity with CH_3CN .

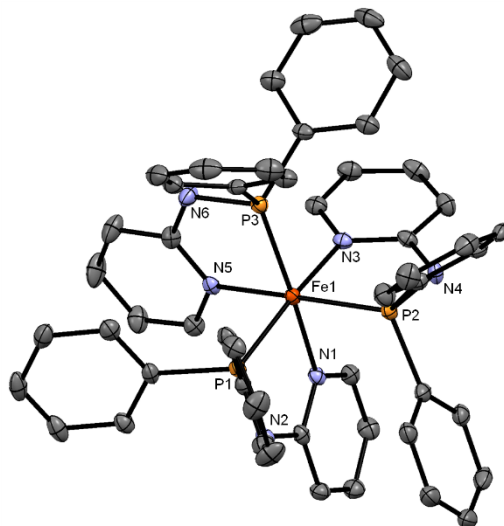


Figure 15: Structural view of *cis*- $[\text{Fe}(\text{PN-Ph})_3]\text{Br}_2$ (**5r**) showing 50% thermal ellipsoids (H atoms and solvent molecules omitted for clarity). Selected bond lengths (Å) and bond angles (°): Fe1–N1 2.042(2), Fe1–N3 2.048(2), Fe1–N5 2.058(2), Fe1–P1 2.2396(7), Fe1–P2 2.2546(8), Fe1–P3 2.2401(7), P1–N2 1.697(2), P2–N4 1.684(2), P3–N6 1.679(2), N1–Fe1–P1 83.44(6), N3–Fe1–P2 83.16(6), N5–Fe1–P3 82.72(6), N1–Fe1–N3 90.43(8), N1–Fe1–N5 89.33(8), N3–Fe1–N5 90.01(8), P1–Fe1–P2 102.40(3), P1–Fe1–P3 98.54(3), P2–Fe1–P3 100.63(3), N1–Fe1–P3 171.53(7), N3–Fe1–P1 171.43(6), N5–Fe1–P2 172.18(6).

3.2.3 Reaction with CO

Though coordinatively saturated, the complexes **5a-5f** do react with carbon monoxide, which is indicated by a change of colour from bright yellow to dark violet, forming the cationic compounds of the general formula $[\text{Fe}(\text{PN}^{\text{R}}\text{-Ph})_2\text{COX}]^+$. The solubility of the PN-Ph containing complexes was exceedingly low in common solvents and, additionally, a mixture of products was detected. The complexes featuring the $\text{PN}^{\text{Me}}\text{-Ph}$ and $\text{PN}^{\text{Et}}\text{-Ph}$ ligands of the formula $[\text{Fe}(\text{PN}^{\text{R}}\text{-Ph})_2\text{COX}]\text{X}$ could not be isolated directly, because CO was released when the solvent was evaporated, forming starting material. In the presence of a halide scavenger NaBF_4 or AgBF_4 the stable complexes **7a-7d** were formed.

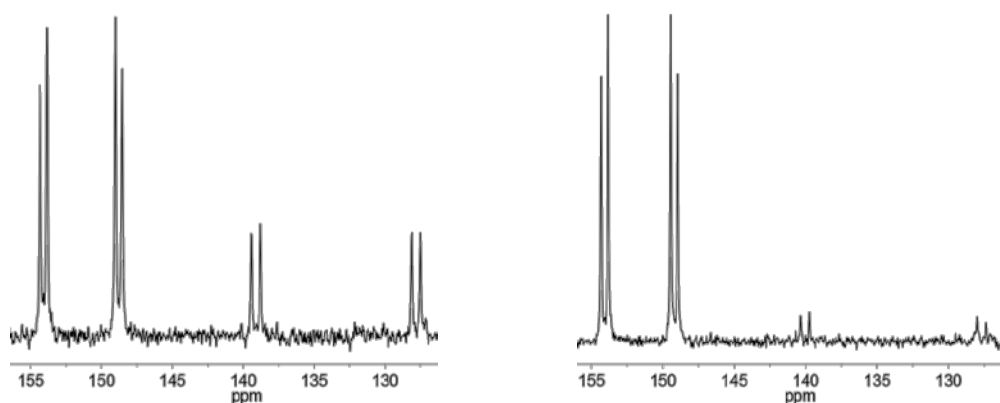
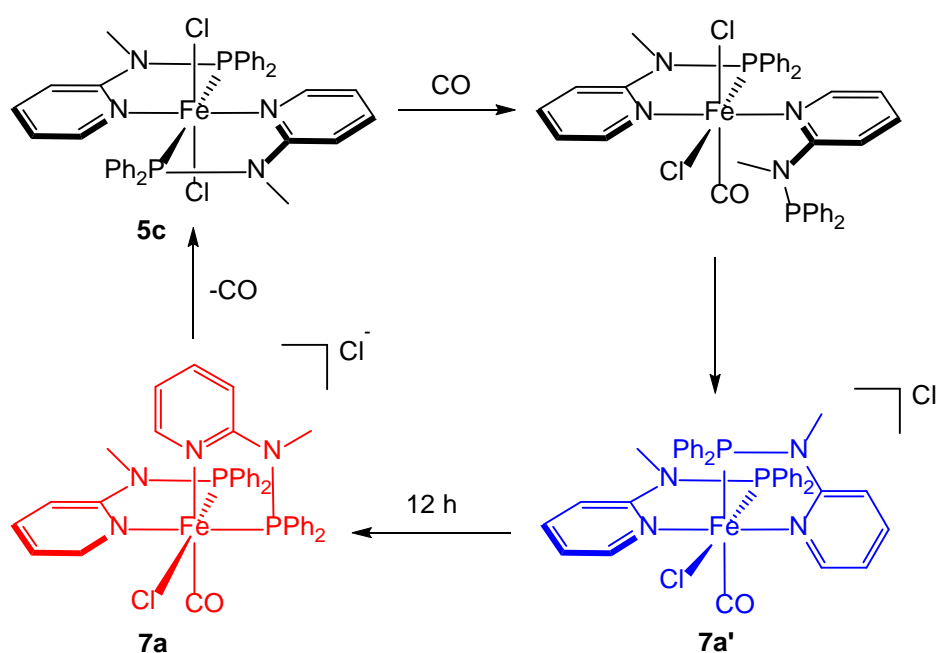


Figure 16: ^{31}P -NMR spectra of $\text{Fe}(\text{PN}^{\text{Me}}\text{-Ph})_2\text{Cl}_2$ (**5c**) after treatment with CO, showing the isomerization progress after 2 h (left) and 12 h (right).

The coordination reaction was monitored by $^{31}\text{P}\{^1\text{H}\}$ -NMR spectroscopy, showing an isomerization at room temperature in the form of two sets of AB spin systems with coupling constants $^2J_{\text{PP}} \approx 47$ Hz, indicating *cis*-conformation of the two P atoms (Figure 16). In a further investigation, the experiment was repeated at -80°C and $^{31}\text{P}\{^1\text{H}\}$ -NMR followed, keeping the sample at low temperature. The spectrum showed a non-coordinated P atom at 39.7 ppm leading to the assumption, that the metal-phosphine bond of one ligand is cleaved, therefore creating an open coordination site. Upon reaching room temperature, this singlet disappeared while simultaneously the intensity of the AB spin system increased (Scheme 28):



Scheme 28: Coordination of CO to $\text{Fe}(\text{PN}^{\text{Me}}\text{-Ph})_2\text{Cl}_2$ (**5c**), followed by isomerization.

The complexes **7a-7d** were isolated as pink to red solids and characterized by ^1H , $^{31}\text{P}\{^1\text{H}\}$, $^{13}\text{C}\{^1\text{H}\}$ -NMR and IR spectroscopy. $^{13}\text{C}\{^1\text{H}\}$ -NMR showed distinguished signals for each pyridine carbon of the two ligands, the N-Me group in **7a** or **7b** is seen as a doublet with a $^2J_{\text{CP}}$ of 4-6 Hz, the N-Et group in **7c** and **7d** appear as singlets. In the IR spectrum the CO band is a broad signal between 1970 and 1980 cm^{-1} .

3.2.4 Spin-crossover

Upon cooling to 77 K, the colour of complexes **5a** and **5b** changed from pale yellow to dark violet, suggesting possible high-spin/low-spin transitions. In agreement with this observation, the UV/Vis spectrum of **5a** and **5b** in the solid state at 293 K did not show any absorption in the visible range, while at 123 K these complexes exhibit two band at 562 and 690 nm and 565 and 716 nm, respectively (Figure 17).

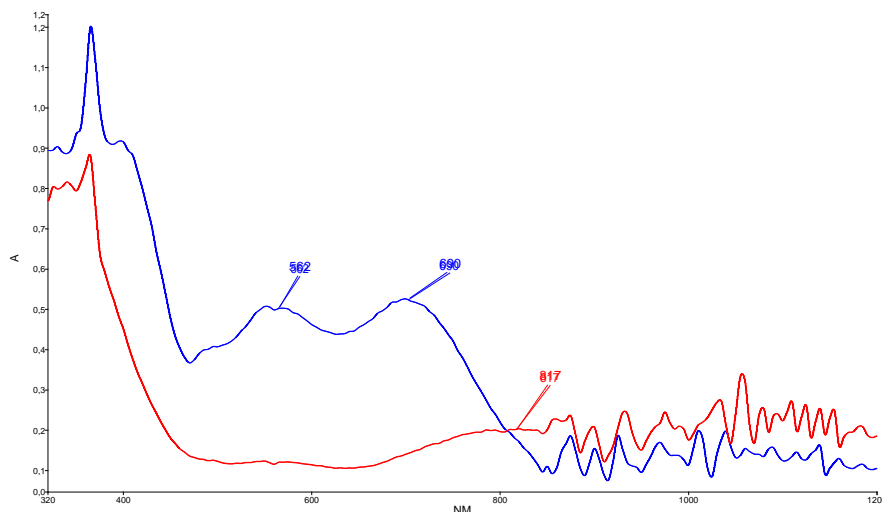


Figure 17: Experimental UV/Vis spectra of $\text{Fe}(\text{PN-Ph})_2\text{Cl}_2$ (**5a**) at 123 K (blue) and 293 K (red).

On the other hand, all other complexes did not change their colour at low temperature again suggesting that the structures of **5a** and **5b** are significantly different from those of **5c-5f**.

The magnetic properties of the compounds **5a-5d** were studied by SQUID magnetometry and ^{57}Fe Mössbauer spectroscopy. The temperature dependent magnetic behaviour of complexes **5a** and **5b** (Figure 18), in agreement with the colour changes, shows that both

compounds exhibit a thermal and almost spin transition (ST) with $\chi_m T$ values near $3.0 \text{ cm}^3 \text{ mol}^{-1} \text{ K}$ at 300 K consistent with HS Fe(II), and $\chi_m T$ values below $0.4 \text{ cm}^3 \text{ mol}^{-1} \text{ K}$ at 10 K, corresponding to a high fraction of LS Fe(II) and a residual content of HS Fe(II), as confirmed by Mössbauer spectra. Both samples were measured on cooling and warming sequences displaying gradual spin transitions without thermal hysteresis, maintaining the low temperature LS Fe(II) fraction up to approximately 125 K (**5a**) or 150 K (**5b**). At those temperatures the population of the HS state gradually increases, achieving full conversion over a temperature range of 125 K (**5a**) or 150 K (**5b**). The ST temperatures, $T_{1/2}$, can be assumed as 185 K for **5a** and 22 K for **5b** (Figure 18).

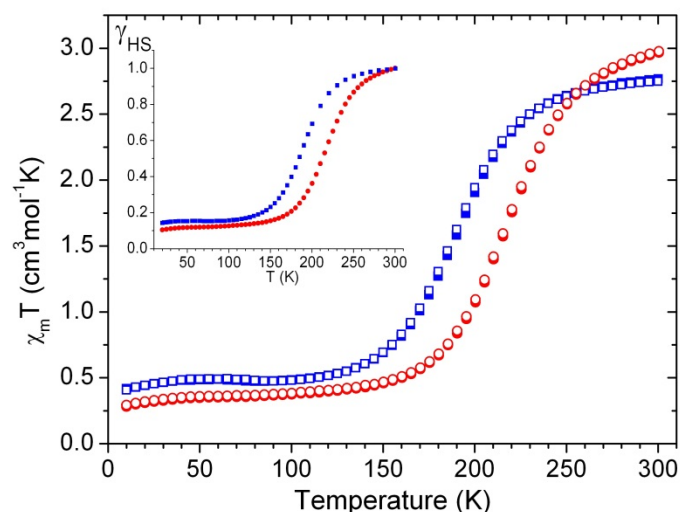


Figure 18: Temperature dependence of $\chi_m T$ for $\text{Fe}(\text{PN-Ph})_2\text{Cl}_2$ (**5a**) (blue squares) and $\text{Fe}(\text{PN-Ph})_2\text{Br}_2$ (**5b**) (red circles) upon cooling (solid symbols) and warming (open symbols). The inset shows the temperature variation of the HS Fe(II) mole fraction for both compounds, assuming that at 300 K there is only HS.

These first order spin transitions, somewhat gradual, not complete at low temperatures and displaying no thermal hysteresis, are more likely to be associated to weak intermolecular cooperative effects, without structural phase transitions^[49-50]. Although hydrogen-bonded networks can induce cooperative interactions, and their existence cannot be discarded in the presence of the PN-Ph ligand, they should be relatively weak since the complexes are neutral and there is no charge assistance^[49].

⁵⁷Fe Mössbauer results are in good agreement with magnetization data, as can be seen from Figure 26 and Table 3. At room temperature only one quadrupole doublet characteristic of HS Fe(II) with isomer shift values (δ) of $0.87(1) \text{ mm s}^{-1}$ and quadrupole splitting values (ΔE_Q) around $3.1(1) \text{ mm s}^{-1}$ are detected for both complexes **5a** and **5b**. A second quadrupole

doublet attributed to LS Fe(II) appears and its fraction increases as the temperature decreases. At 78 K the hyperfine parameters $\delta = 0.48(1) \text{ mm s}^{-1}$ and $\Delta E_Q \approx 1.0(1) \text{ mm s}^{-1}$ confirm the LS state of Fe(II) with relative fractions of 87% for the Cl compound and 92% for the Br one, assuming the same Debye-Waller factor for LS and HS species. According to the magnetization data, the HS fraction existing at this temperature should remain until 10 K.

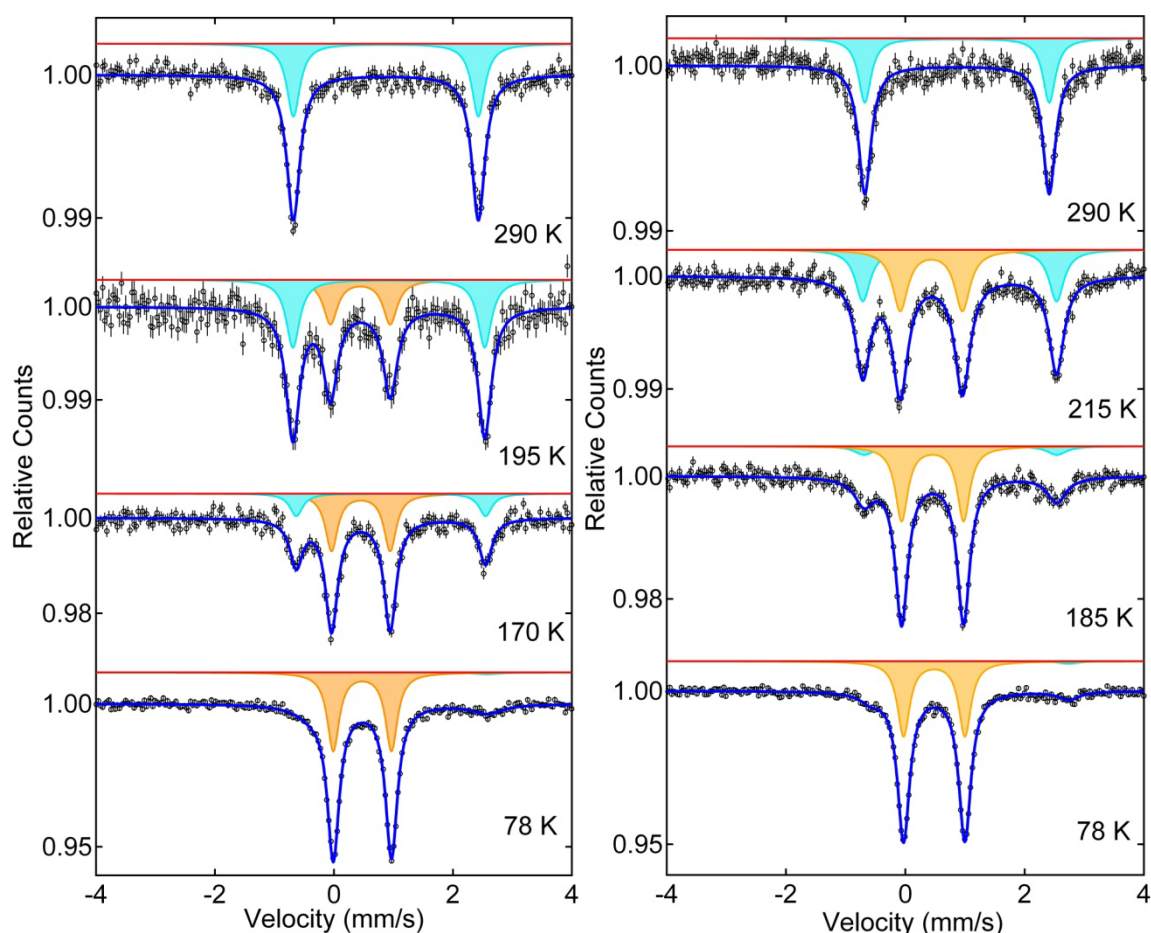


Figure 19: Temperature dependence of ^{57}Fe Mössbauer spectra of $\text{Fe}(\text{PN-Ph})_2\text{Cl}_2$ (**5a**) (left) and $\text{Fe}(\text{PN-Ph})_2\text{Br}_2$ (**5b**) (right).

Compound	T (K)	δ (mm s^{-1})	ΔE_Q (mm.s^{-1})	Γ (mm s^{-1})	I (%)	Fe(II) site
$\text{Fe}(\text{PN-Ph})_2\text{Cl}_2$ (5a)	290	0.87(1)	3.11(1)	0.27(1)	100	HS
	195	0.92(1)	3.22(1)	0.28(2)	58.5	HS
		0.44(1)	1.00(1)	0.29(2)	41.5	LS
	170	0.96(1)	3.18(1)	0.26(2)	30.4	HS
		0.45(1)	0.99(1)	0.25(1)	69.6	LS
	78	1.10(3)	2.95(5)	0.63(9)	13.3	HS
		0.48(1)	0.98(1)	0.24(1)	86.7	LS

	290	0.87(1)	3.09(1)	0.26(1)	100	HS
	215	0.91(1)	3.25(1)	0.30(1)	44.8	HS
Fe(PN-Ph) ₂ Br ₂		0.44(1)	1.04(1)	0.31(1)	55.2	LS
(5b)	185	0.92(1)	3.23(3)	0.39(4)	20.9	HS
		0.46(1)	1.04(1)	0.26(1)	79.1	LS
	78	1.08(2)	3.32(4)	0.41(7)	8.5	HS
		0.48(1)	1.03(1)	0.25(1)	91.5	LS

Table 3: Estimated hyperfine parameters from the ⁵⁷Fe Mössbauer spectra of Fe(PN-Ph)₂Cl₂ (**5a**) and Fe(PN-Ph)₂Br₂ (**5b**) collected at different temperatures. δ – isomer shift; ΔE_Q – quadrupole splitting; Γ – FWHM line width; I – relative area with uncertainties < 2%.

The thermal variation of the inverse molar magnetic susceptibility and of $\chi_m T$ for complexes **5c** and **5d** is shown in Figure 20. Upon replacement of the NH moiety by a NMe unit the spin transition completely vanishes, indicating an increased energy difference between the HS and LS forms in the 2b and 3b complexes when compared with 2a and 3a ones. The thermal variation of χ_m^{-1} is well described by a modified Curie law ($\chi_m = C_m/T+K$, where C_m is the molar Curie constant and K is a temperature independent constant). Iron effective magnetic moments of 5.0(1) and 5.1(1) μ_B were extracted from the C_m values of the Cl and Br complexes, respectively, in good agreement with the effective magnetic moment of HS Fe(II) in the spin-only approximation (4.9 μ_B).

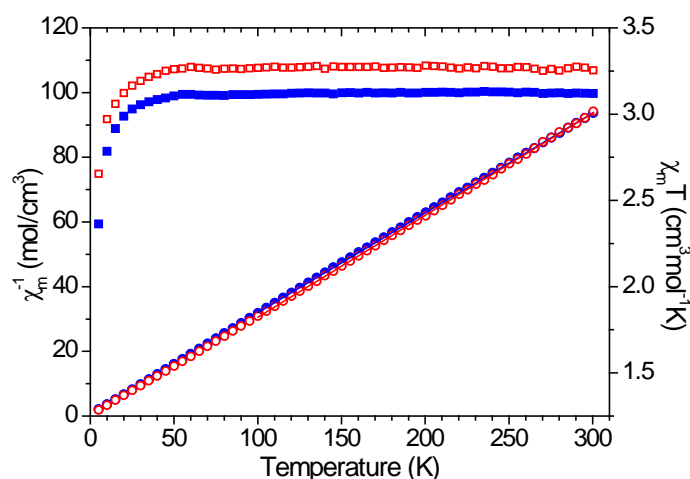


Figure 20: Temperature dependence of the inverse molar susceptibility (circles) and of $\chi_m T$ (squares) for Fe(PN^{Me}-Ph)₂Cl₂ (**5c**) (solid symbols) and Fe(PN^{Me}-Ph)₂Br₂ (**5d**) (open symbols). The straight lines correspond to Curie law fittings to the experimental data.

⁵⁷Fe Mössbauer spectra collected at room temperature for **5c** and **5d** also agree with magnetization data since only one iron site (quadrupole doublet) with hyperfine parameters

characteristics of HS Fe(II) is observed: $\delta = 0.85(1)$ and $0.88(1)$ mm/s and $\Delta E_Q = 3.04(1)$ and $3.14(1)$ mm/s for the Cl and Br complexes, respectively (Figure 21, Table 4). Comparing room temperature hyperfine parameters obtained for all octahedral compounds, it is clear that the substitution of the NH moiety by a NMe unit does neither change significantly the s-electron density at the iron nuclei (related with δ) nor the quadrupole splitting values. This latter parameter depends on the electric field gradient (EFG) surrounding the Fe nuclei with two contributing sources: the lattice (charges in a non-cubic symmetry) surrounding the Mössbauer probe and the iron valence electrons. As similar values were obtained for *trans* and *cis* complexes and rather different values were obtained for the *cis* compound in high and low spin states, it can be deduced that the main contribution for the EFG comes from the iron valence electrons.

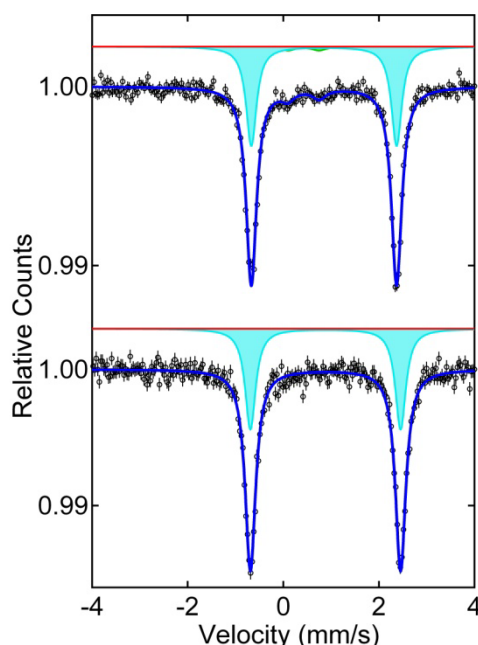


Figure 21: ^{57}Fe Mössbauer spectra of $\text{Fe}(\text{PN-Ph})_2\text{Cl}_2$ (**5a**) (top) and $\text{Fe}(\text{PN-Ph})_2\text{Br}_2$ (**5b**) (bottom) collected at 290 K.

Compound	δ (mm s $^{-1}$)	ΔE_Q (mm s $^{-1}$)	Γ (mm.s $^{-1}$)	Fe(II) site
$\text{Fe}(\text{PN}^{\text{Me}}\text{-Ph})_2\text{Cl}_2$ (5c)	0.85(1)	3.04(1)	0.26(1)	HS ^a
$\text{Fe}(\text{PN}^{\text{Me}}\text{-Ph})_2\text{Br}_2$ (5d)	0.88(1)	3.14(1)	0.27(1)	HS

Table 4: Estimated hyperfine parameters from the ^{57}Fe Mössbauer spectra of $\text{Fe}(\text{PN}^{\text{Me}}\text{-Ph})_2\text{Cl}_2$ (**5c**) and $\text{Fe}(\text{PN}^{\text{Me}}\text{-Ph})_2\text{Br}_2$ (**5d**) collected at different temperatures. δ – isomer shift; ΔE_Q – quadrupole splitting; Γ – FWHM line width. ^a A small impurity due to oxidation during Mössbauer sample preparation is also present.

The ^{57}Fe Mössbauer parameters were calculated for the isomer **B** of complex **5a** with a DFT approach (using ORCA^[51] and two basis sets, b1 and b2, see Experimental details). The electronic density at the nucleus (ρ) was converted in isomer shifts (δ), using the method of Neese^[52] and the quadrupole splitting was obtained directly. The isomer shifts are 0.835 (HS) and 0.611 (LS) mm/s with the b1 basis, and 0.736 and 0.515 mm/s, respectively with the better b2 basis set. The quadrupole splittings were calculated as 0.579, 3.009 (b1) and 0.579, 3.026 (b2) mm/s, for LS and HS, respectively. Both are good estimates of the experimental parameters. The same calculation (b1) for isomer **C** led to similar isomer shifts (0.830 and 0.631 mm/s, for HS and LS), and quadrupole splitting for the LS isomer (0.620 mm/s). However, the quadrupole splitting for the HS room temperature species is calculated as 2.398 mm/s, very far from the experimental value. This suggests that isomer **B** is the most likely species to be present in the solid.

3.2.5 Mass spectroscopy

Moreover, complexes **5a**, **5b**, **5c**, **5d**, **5q** and **5r** were also investigated by means of ESI-MS (Table 5). Solutions of those complexes in CH_3OH in the presence of NaX ($X = \text{Cl}, \text{Br}$) were subjected to ESI-MS analysis in the positive ion mode. By means of the called 'soft ionization' technique ESI at atmospheric pressure, the most abundant signals are observed at m/z is 647.10, 675.23, 691.05, and 719.08, respectively, which correspond to the cationic complexes $[\text{Fe}(\text{PN}^{\text{R}}\text{-Ph})_2\text{X}]^+$ ($[\text{M-X}]^+$), where one halide ligand is dissociated. Further abundant fragments are $[\text{M-X-HX}]^+$ (only for **5a** and **5b**), $[\text{M-X-5a}]^+$ and $[\text{M-X-5b}]^+$. Representative corresponding positive ion ESI full scan mass and MS/MS (low energy CID) spectra of **5c** are depicted in Figure 22. Furthermore in the inset of Figure 22 (**A**) the isotopic pattern of $[\text{M-Br}]^+$ ion is compared with the theoretical pattern, which turned out to correlate quite well.

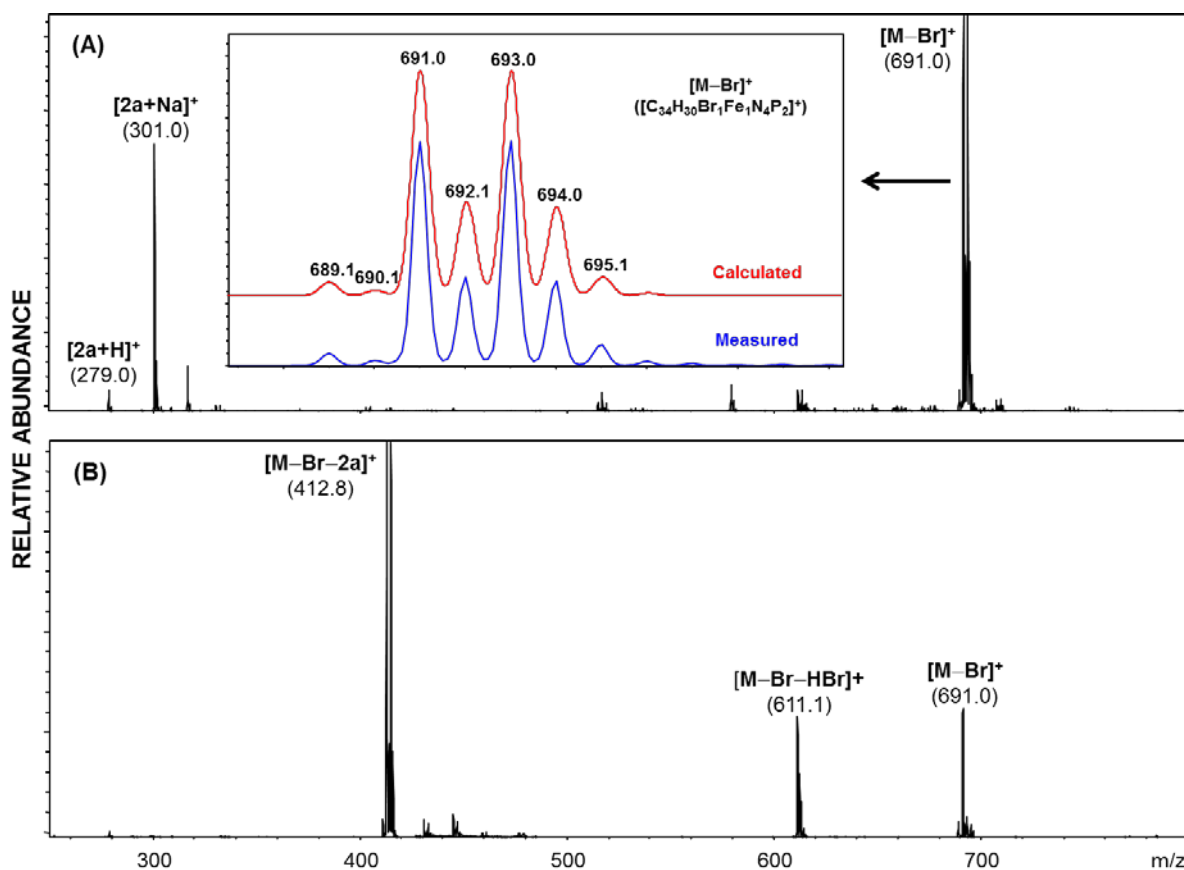


Figure 22: Positive-ion ESI full scan mass spectrum of Fe(PN-Ph)₂Br₂ (**3a**) (**A**) and corresponding MS/MS (low energy CID)-spectrum of *in-source*-generated [M-Br]⁺ precursor ion (m/z 691.0) (**B**). Inset shows the calculated and measured isotopic pattern of [M-Br]⁺. In both spectra only signals containing the Fe-isotope of highest abundance (⁵⁶Fe) are annotated.

Compound	Elemental composition/ Molecular weight ^a	Elemental composition	Elemental composition
5a	C ₃₄ H ₃₀ Cl ₂ Fe ₁ N ₄ P ₂ 682.07	C ₃₄ H ₃₀ Cl ₁ Fe ₁ N ₄ P ₂ [M-Cl] ⁺ = 647.10	C ₃₄ H ₂₉ Fe ₁ N ₄ P ₂ [M-Cl-HCl] ⁺ = 611.12 C ₁₇ H ₁₅ Cl ₁ Fe ₁ N ₁ P ₁ [M-Cl- 2a] ⁺ = 369.00
5c	C ₃₆ H ₃₄ Cl ₂ Fe ₁ N ₄ P ₂ 710.10	C ₃₆ H ₃₄ Cl ₁ Fe ₁ N ₄ P ₂ [M-Cl] ⁺ = 675.13	C ₁₈ H ₁₇ Cl ₁ Fe ₁ N ₁ P ₁ [M-Cl- 2b] ⁺ = 383.02
5b	C ₃₄ H ₃₀ Br ₂ Fe ₁ N ₄ P ₂ 769.97	C ₃₄ H ₃₀ Br ₁ Fe ₁ N ₄ P ₂ [M-Br] ⁺ = 691.05	C ₃₄ H ₂₉ Fe ₁ N ₄ P ₂ [M-Br-HBr] ⁺ = 611.12 C ₁₇ H ₁₅ Br ₁ Fe ₁ N ₁ P ₁ [M-Br- 2a] ⁺ = 412.95
5d	C ₃₆ H ₃₄ Br ₂ Fe ₁ N ₄ P ₂ 798.00	C ₃₆ H ₃₄ Br ₁ Fe ₁ N ₄ P ₂ [M-Br] ⁺ = 719.08	C ₁₈ H ₁₇ Br ₁ Fe ₁ N ₁ P ₁ [M-Br- 2b] ⁺ = 426.97
5q	C ₅₁ H ₄₅ Cl ₂ Fe ₁ N ₆ P ₃ 960.16	C ₅₁ H ₄₄ Fe ₁ N ₆ P ₃ [M-Cl-HCl] ⁺ = 889.22	C ₃₄ H ₂₉ Fe ₁ N ₄ P ₂ [M-Cl-HCl- 2a] ⁺ = 611.12
5r	C ₅₁ H ₄₅ Br ₂ Fe ₁ N ₆ P ₃ 1048.06	C ₅₁ H ₄₄ Fe ₁ N ₆ P ₃ [M-Br-HBr] ⁺ = 889.22	C ₃₄ H ₂₉ Fe ₁ N ₄ P ₂ [M-Br-HBr- 2a] ⁺ = 611.12

Table 5: Elemental compositions of the neutral compounds **5a**, **5b**, **5c**, **5d**, **5q**, **5r** and calculated m/z values of [M-X]⁺ (compounds **5a**, **5b**, **5c** and **5d**), [M-X-HX]⁺ (compounds **5a**, **5b**, **5c**, **5d**, **5q** and **5r**) and [M-X-HX-**5a/b**]⁺ ions (compounds **5a**, **5b**, **5c**, **5d**, **5q** and **5r**; X = Cl, Br). ^a Mass calculations are based on the lowest mass chlorine (³⁵Cl) and bromine isotope (⁷⁹Br), respectively, and the most abundant iron isotope (⁵⁶Fe).

3.2.6 Calculation of geometry

The geometries and energies (in kcal/mol) of all possible isomers of **5a** and **5b** in two different spin states (S = 2 and S = 0) were determined by means of DFT/OPBE calculations (Scheme 26, electronic energies shown for all isomers of **5a**). Isomer **A^{HS}** was used as reference point for all calculations. Stable minima in both S = 2 and S = 0 spin states could be obtained for all five isomers.

In all cases the quintet ground state (S = 2) is thermodynamically more stable and the energies of isomers **A^{HS}**-**D^{HS}** are very similar ranging from -0.8 to 2.2 kcal/mol, while **E^{HS}** is less stable than **A^{HS}** by 11.1 kcal/mol. All of these four isomers are possible high spin species. It is interesting to note, however, that isomers **D^{HS}** and **E^{HS}** are structurally significantly different from the other isomers. These complexes are five coordinate species adopting a distorted square pyramidal geometry. While in **D^{HS}** one pyridine moiety is no longer coordinated to the iron center (the Fe-N_{py} distance is 3.86 Å), in **E^{HS}** one phosphine moiety is weakly bound with a Fe-P bond distance of 3.10 Å. In fact, isomer **D^{HS}** strongly

resembles five coordinate PNP pincer complexes of the type $[\text{Fe}(\text{PNP})\text{Cl}_2]$ which form stable HS complexes with a quintet ground state that show no spin crossover^[53].

The corresponding singlet ground states $\mathbf{A}^{\text{LS}}-\mathbf{E}^{\text{LS}}$, all with an octahedral geometry, are less stable than the corresponding HS states. The energy differences between HS and LS spin states ($\Delta E_{\text{HS/LS}}$) of isomers **A-E** are 20.3, 9.7, 14.7, 18.3, and 7.3 kcal/mol. It is, thus, reasonable that at low temperatures no spin-crossover takes place in the case of isomer **A**, which displays a very high energy difference. Accordingly, a HS/LS crossover is more likely to take place in the case of **B** and to a lesser extent of **C** where (i) the HS species has low energy and (ii) $\Delta E_{\text{HS/LS}}$ is small. In contrast, spin transitions in **D** and **E** would be associated with severe structural changes, e.g., changes of both geometry and coordination number (Scheme 26), which appear to be unlikely to occur in the solid state and are not suggested by any experimental data. The high-spin state exhibits typically longer metal ligand bonds, since the partially occupied e_g^* states are metal-ligand anti-bonding. In the present case of the $\text{Fe}(\text{PN}^{\text{R}}\text{-Ph})_2\text{X}_2$ complexes this effect is very pronounced for the Fe-P and Fe-N bonds (for instance, Fe-N1 shortens from 2.388 to 1.967 Å, and Fe-P1 from 2.529 to 2.151 Å) but modest for the Fe-Cl bonds (Table 6). There are several literature examples of octahedral Fe(II) diphosphine complexes of the types $\text{Fe}(\text{PP})_2\text{X}_2$ (PP = *cis*-1,2-bis(diphenylphosphino)ethylene, X = Cl, Br) where the Fe-P bonds are abnormally long in the quintet ground state^[54]. Based on these calculations, we propose that **2a** and **3a** adopt a *cis*-Cl,P,N-geometry (**B**). The structures of the HS and LS isomers of **B** are shown in Figure 9. However, a *cis*-P,N-*trans*-Cl arrangement (**C**) cannot be conclusively ruled out.

complexes	spin state	Fe-P	Fe-N	Fe-Cl
5b	HS	2.605	2.191	2.364
$[\text{Fe}(\text{PP})_2\text{Cl}_2]$	HS	2.584		2.363
$[\text{Fe}(\text{PP})_2\text{Cl}_2]$	LS	2.301		2.329
A ^{HS}	HS	2.687	2.325	2.332
A ^{LS}	LS	2.253	2.012	2.313
B ^{HS}	HS	2.612	2.397	2.350
B ^{LS}	LS	2.159	2.033	2.337
5q	LS	2.245	2.049	
5r	LS	2.215	2.020	

Table 6: Mean Fe-P, Fe-N_{py}, and Fe-Cl bond lengths (Å) for complexes **5b**, *trans*- $\text{Fe}(\text{PP})_2\text{Cl}_2$ (PP = *cis*-1,2-bis(diphenylphosphino)ethylene)^[54], **A**^{HS}, **A**^{LS}, **B**^{HS}, **B**^{LS}, **5q** and **5r**.

As was shown above, the Mössbauer parameters calculated for isomer **B** of complex **5a** are in good agreement with those determined experimentally for the HS and the LS species, contrary to isomer **C**. Since there is a pronounced colour change from pale yellow to dark violet, we also calculated the electronic spectrum of the two spin states of isomers **B** and **C** of complex **5a**. The high spin forms exhibit very weak absorptions in the visible, with the bands at 392.7 nm (**B**) or 368.7 nm (**C**) representing the beginning of the UV strong absorptions, and both are consistent with the pale colour of the complex. On the other hand, the spectra of the low spin forms are dominated by the strong absorptions at 545.5 nm (**B**) or 559.8 nm (**C**), with another weaker one (684.5 nm) for **B** and two weaker ones (647.0 and 709.1 nm) for **C**. The agreement between calculated and experimental spectra (562 and 690 nm) is slightly better for isomer **B** reinforcing the idea that it corresponds to the observed isomer of **5a**.

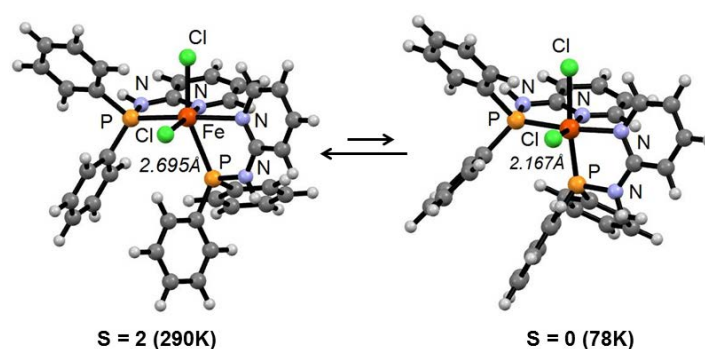


Figure 23: Optimized geometries of *cis-Cl,P,N-Fe(PN-Ph)₂Cl₂* (**B**) in spin states $S = 2$ (**B**^{HS}, left) and $S = 0$ (**B**^{LS}, right). Selected bond lengths (Å) for **B**^{HS}: Fe–P1 2.529, Fe–P2 2.695, Fe–N1 2.388, Fe–N2 2.406, Fe–Cl1 2.379, Fe–Cl2 2.320. **B**^{LS}: Fe–P1 2.151, Fe–P2 2.167, Fe–N1 1.967, Fe–N2 2.098, Fe–Cl1 2.351, Fe–Cl2 2.322.

To get further evidence for the above suggested *cis*-configuration, vibrational spectroscopy (FIR, Raman) was performed. While the Raman spectra did not reveal characteristic vibrations allowing a distinction between the different isomers, in the FIR characteristic bands associated with Fe–Cl and Cl–Fe–Cl vibrations could be identified (Figure 24 and Figure 25). In the theoretically obtained FIR of the *cis*-isomer **B**^{HS} two characteristic Fe–Cl stretching vibrations are found at 252 and 276 cm⁻¹, whereas for the *trans*-isomer **C**^{HS} vibrations at 141 and 298 cm⁻¹ are observed which are assignable to the Cl–Fe–Cl bending mode and the asymmetric Cl–Fe–Cl stretching frequency, respectively. In the experimentally obtained spectrum, despite of the weak signals, the two expected bands for the *cis*-product are observed at 253 and 278 cm⁻¹, while the characteristic asymmetric Cl–Fe–Cl stretching mode expected for **C**^{HS} (and **A**^{HS}) is missing. Thus, the experimental FIR data seem to support the

cis-configuration, as the respective spectral features in the two *trans* isomers are missing. One has to keep in mind however that the experimental IR and Raman spectra are obtained for bulk solid samples, while the calculated spectra correspond to single isolated molecules in the gas-phase.

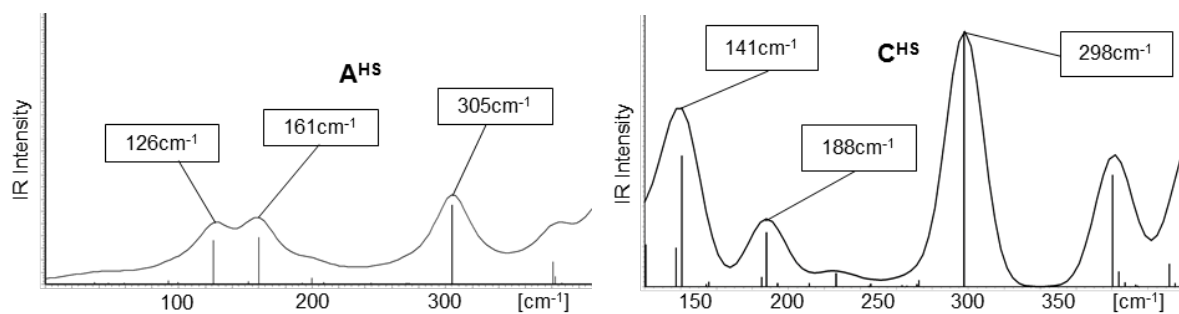


Figure 24: Calculated FIR spectra for **A^{HS}** (left) and **C^{HS}** (right).

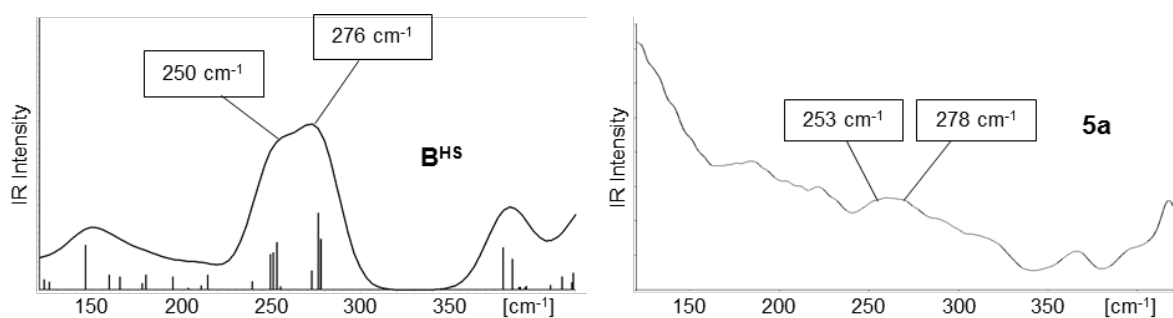
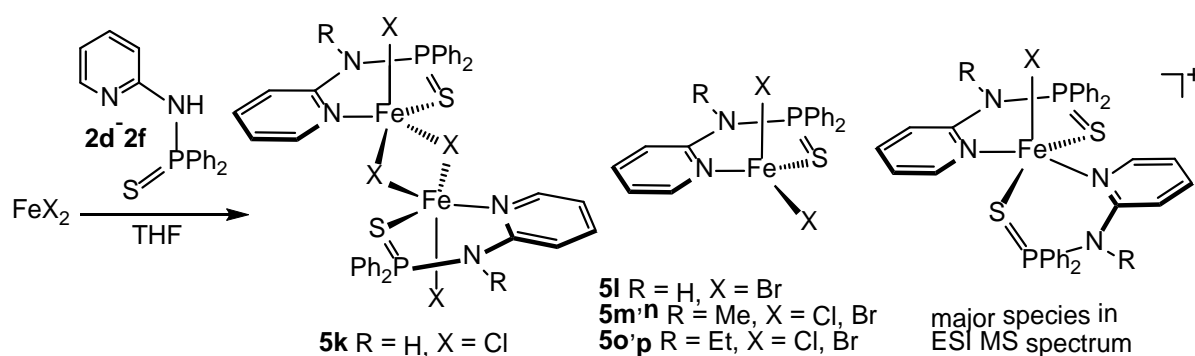


Figure 25: Calculated (**B^{HS}**, left) and experimental (**5a**, right) FIR spectra.

3.3 SN iron(II) complexes^[55]

3.3.1 Synthesis

Treatment of anhydrous FeX_2 ($\text{X} = \text{Cl}, \text{Br}$) with 1 equiv of the $\text{SN}^{\text{R}}\text{-Ph}$ ligands SN-Ph (**2d**), $\text{SN}^{\text{R}}\text{-Ph}$ (**2e**) and $\text{SN}^{\text{Et}}\text{-Ph}$ (**2f**) in THF or MeOH at room temperature afforded the coordinatively unsaturated complexes of the general stoichiometry $\text{Fe}(\text{SN}^{\text{R}}\text{-Ph})\text{X}_2$ (**5l-p**) in 76 to 85% isolated yields (Scheme 29). These reactions were independent of whether 1 or 2 equivs were used.



Scheme 29: Reaction of FeX_2 with bidentate $\text{SN}^{\text{R}}\text{-Ph}$ ligands based on 2-aminopyridine

Cationic pentacoordinate $[\text{Fe}(\text{SN}^{\text{R}}\text{-Ph})_2\text{X}]^+$ complexes bearing two SN ligands could not be prepared, despite the fact that these species were the most prominent fragments in the ESI MS spectra. Interestingly, the related $[\text{Fe}(\text{ON-}i\text{Pr})_2\text{X}]^+$ complexes bearing *N*-(2-pyridyl)aminodiisopropylphosphine oxide ligands were obtained in high yields^[46a]. All SN complexes are thermally robust white to pale yellow solids that are moderately air sensitive both in the solid state and in solution.

3.3.2 Solid state studies

Due to the paramagnetic nature and the poor solubility of all complexes, bearing basically aromatic proton and carbon atoms; $^1\text{H-NMR}$ spectra exhibited only very broad and featureless signals and were not very informative, while $^{13}\text{C}\{^1\text{H}\}$ and $^{31}\text{P}\{^1\text{H}\}$ -NMR signals could not be detected at all. The solid state structures of all complexes have been determined by X-ray crystallography. Their molecular structures are depicted in Figure 26-

Figure 31. Except for the dimeric complex $[\text{Fe}(\text{SN-Ph})(\mu\text{-Cl})(\text{Cl})]_2$ (**5k**), the complexes **5l-p** are monomeric and contain Fe in relatively uniform coordination figures of modestly distorted tetrahedral shape with mean bond lengths of Fe–Cl = 2.249 Å (**5m**, **5o**), Fe–Br = 2.394 Å (**5l**, **5n**, **5p**), Fe–S = 2.378 Å (**5l**, **5n**, **5p**) and Fe–N 2.125 Å (**5l**, **5n**, **5p**).

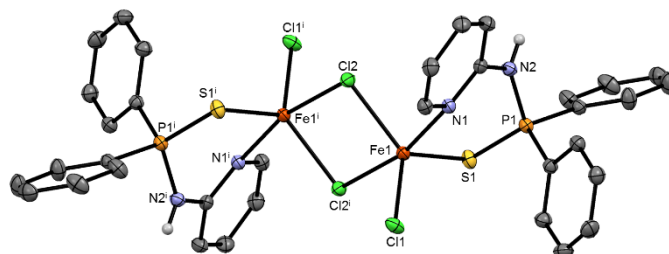


Figure 26: Structural view of $[\text{Fe}(\text{SN-Ph})_2(\mu\text{-Cl})\text{Cl}]_2$ (**5k**) showing 50% thermal ellipsoids (most H atoms and solvent molecules omitted for clarity). Selected bond lengths (Å) and bond angles (°): Fe1–N1 2.2669(12), Fe1–S1 2.3830(4), Fe1–Cl1 2.2794(4), Fe1–Cl2 2.3611(4), Fe1–Cl2ⁱ 2.6049(4), P1–N2 1.6735(12), P1–S1 1.9877(5), N1–Fe1–S1 98.22(3), N1–Fe1–Cl1 95.71(3), N1–Fe1–Cl2 84.07(3), N1–Fe1–Cl2ⁱ 167.23(3), S1–Fe1–Cl1 114.61(2), S1–Fe1–Cl2 117.65(2), S1–Fe1–Cl2ⁱ 86.54(1), Cl1–Fe1–Cl2 127.21(2), Cl1–Fe1–Cl2ⁱ 93.02(1), Cl2–Fe1–Cl2ⁱ 83.23(1), N2–P1–S1 114.31(5), P1–S1–Fe1 97.45(2).

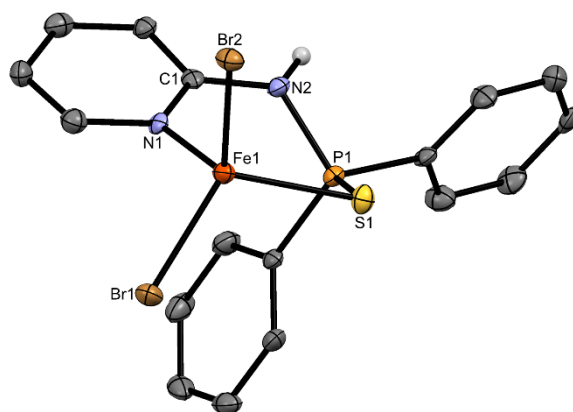


Figure 27: Structural view of $\text{Fe}(\text{SN-Ph})\text{Br}_2$ (**5l**) showing 50% thermal ellipsoids (most H atoms and solvent molecules omitted for clarity). Selected bond lengths (Å) and bond angles (°): Fe1–N1 2.1126(10), Fe1–S1 2.3693(4), Fe1–Br1 2.3748(2), Fe1–Br2 2.4193(2), P1–N2 1.6763(10), P1–S1 1.9869(4), N1–Fe1–S1 106.03(3), N1–Fe1–Br1 106.77(3), N1–Fe1–Br2 105.50(3), S1–Fe1–Br1 114.518(11), S1–Fe1–Br2 107.792(10), Br1–Fe1–Br2 115.430(8), N2–P1–S1 114.11(4), P1–S1–Fe1 93.121(15).

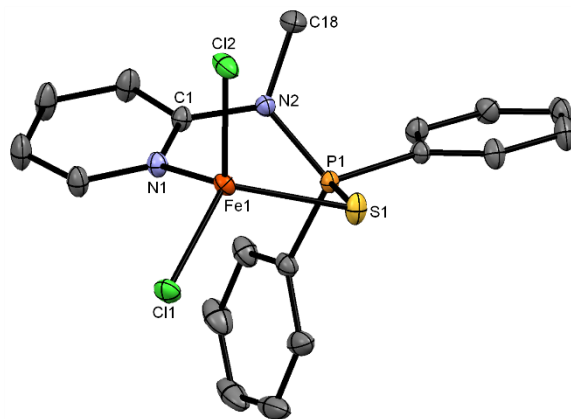


Figure 28: Structural view of Fe(SN^{Me}-Ph)Cl₂ (**5m**) showing 50% thermal ellipsoids (H atoms and solvent molecules omitted for clarity). Selected bond lengths (Å) and bond angles (°): Fe1–N1 2.1259(15), Fe1–S1 2.3782(5), Fe1–Cl1 2.2476(5), Fe1–Cl2 2.2484(5), P1–N2 1.6698(15), P1–S1 1.9846(6), N2–C18 1.475(2), N1–Fe1–S1 102.04(4), N1–Fe1–Cl1 106.03(4), N1–Fe1–Cl2 105.61(5), S1–Fe1–Cl1 114.56(2), S1–Fe1–Cl2 108.29(2), Cl1–Fe1–Cl2 118.56(2), N2–P1–S1 116.30(6), P1–S1–Fe1 95.77(2).

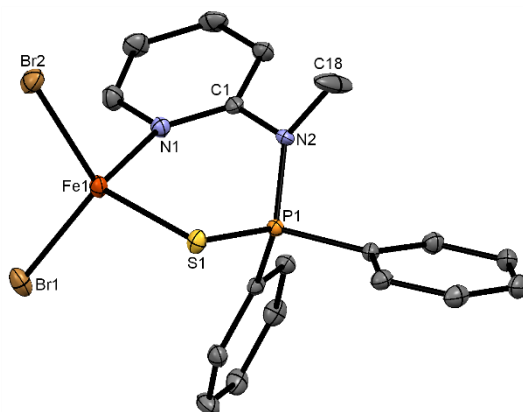


Figure 29: Structural view of Fe(SN^{Me}-Ph)Br₂ (**5n**) showing 50% thermal ellipsoids (H atoms and solvent molecules omitted for clarity). Selected bond lengths (Å) and bond angles (°): Fe1–N1 2.1309(17), Fe1–S1 2.3947(6), Fe1–Br1 2.3964(4), Fe1–Br2 2.3885(4), P1–N2 1.6716(17), P1–S1 1.9877(7), N2–C18 1.465(3), N1–Fe1–S1 104.49(5), N1–Fe1–Br1 107.00(5), N1–Fe1–Br2 100.48(5), S1–Fe1–Br1 112.89(2), S1–Fe1–Br2 113.34(2), Br1–Fe1–Br2 116.80(2), N2–P1–S1 114.81(6), P1–S1–Fe1 91.35(2).

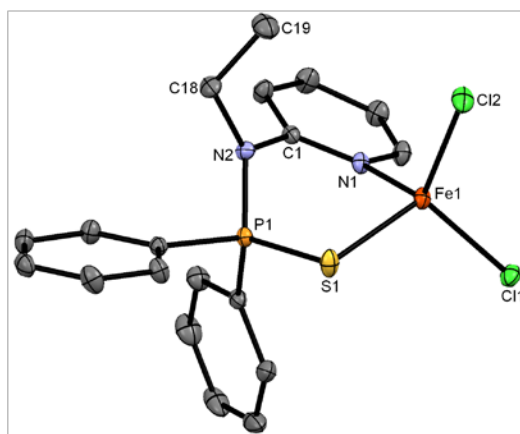


Figure 30: Structural view of $\text{Fe}(\text{SN}^{\text{Et}}\text{-Ph})\text{Cl}_2$ (**5o**) showing 50% thermal ellipsoids (H atoms and solvent molecules omitted for clarity). Selected bond lengths (Å) and bond angles (°): Fe1–N1 2.1284(13), Fe1–S1 2.3733(4), Fe1–Cl1 2.2564(4), Fe1–Cl2 2.2448(4), P1–N2 1.6664(12), P1–S1 1.9870(5), N2–C18 1.491(2), N1–Fe1–S1 101.49(4), N1–Fe1–Cl1 104.74(3), N1–Fe1–Cl2 110.95(4), S1–Fe1–Cl1 112.21(2), S1–Fe1–Cl2 109.76(2), Cl1–Fe1–Cl2 116.54(2), N2–P1–S1 115.91(5), P1–S1–Fe1 96.25(2).

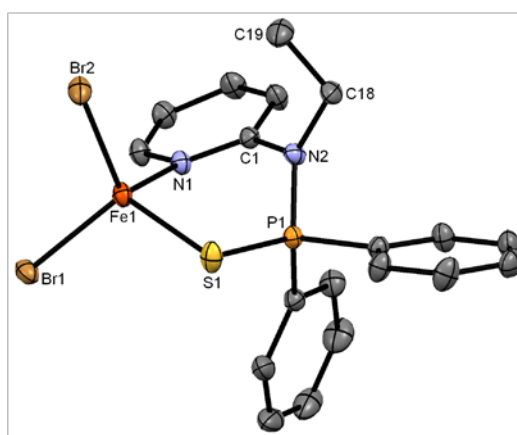


Figure 31: Structural view of $\text{Fe}(\text{SN}^{\text{Et}}\text{-Ph})\text{Br}_2$ (**5p**) showing 50% thermal ellipsoids (H atoms and solvent molecules omitted for clarity). Selected bond lengths (Å) and bond angles (°): Fe1–N1 2.1270(11), Fe1–S1 2.3732(4), Fe1–Br1 2.3954(2), Fe1–Br2 2.3868(2), P1–N2 1.6659(11), P1–S1 1.9879(5), N2–C18 1.4904(16), N1–Fe–S1 102.48(3), N1–Fe1–Br1 105.38(3), N1–Fe1–Br2 110.50(3), S1–Fe1–Br1 113.44(1), S1–Fe1–Br2 110.58(1), Br1–Fe1–Br2 113.72(1), N2–P1–S1 115.74(4), P1–S1–Fe1 95.61(2).

The two Fe–halogen bonds in each tetrahedron show only marginal differences in length, at most 0.044 Å in **5i**. The tetrahedral bond angles about Fe vary between 100.5 and 118.6°, where the low end values concern mostly the angle S–Fe–N while the high end values represent Cl1–Fe–Cl2 (116.5 – 118.6°) or Br1–Fe–Br2 (113.7 – 116.8°). The six-membered chelate rings -Fe–S1–P–N2–C1–N1- of the five complexes display relatively uniform distorted twist-boat conformations with N1 and P1 as the boat ends (e.g. Fig. 2). Iron is always located significantly above the mean-plane of the pyridine ring, by 0.44 to 0.67 Å in **5n** and **5m**, phosphorus is always located distinctly below this plane, by 0.83 to 1.17 Å in **5n**

and **5o**, and sulfur lies in the vicinity of this plane (0.02 to 0.49 Å). Due to this conformation are the bonds Fe–(Cl₂,Br₂) and P1–C12 (to phenyl ring 2) approximately antiparallel to each other and steeply inclined to the pyridine ring. All these outlined geometric features of the complexes **5l**, **5m**, **5n**, **5o** and **5p** agree qualitatively with the findings for Fe(SN-*i*Pr)Cl₂ and Fe(SN-*i*Pr)Br₂ reported previously^[46a] (mean values for the last two complexes are: Fe–Cl = 2.270 Å, Fe–Br = 2.408 Å, Fe–S = 2.369 Å, Fe–N = 2.120 Å). Only one more systematic difference between compounds with unsubstituted N₂ (**5l** and the two *i*Pr containing complexes) and those with methyl or ethyl substituted N₂ is that the chelate ring bond angle at N₂ ranges from 125 to 130° for the first group while it ranges from 119 to 122° for the second group.

As shown in Figure 1, the complex [Fe(SN^H-Ph)(μ-Cl)(Cl)]₂ (**5k**) is a centrosymmetric dimer, in sharp contrast to its monomeric Br analogue **5l**. By dimerization via an additional Fe–Cl bond the iron atom in **5k** switches from a tetrahedral to a distorted trigonal bipyramidal five-coordination with Cl1, Cl2 and S1 as the equatorial ligands to Fe and with N1 and Cl2ⁱ (centrosymmetric equivalent of Cl2) as the axial ligands. The bond lengths to the equatorial ligands, measuring Fe–Cl1 2.279 Å, Fe–Cl2 2.361 Å and Fe–S1 2.383 Å, are a little longer than in the tetrahedral complexes **5l**, **5n** and **5p**. The corresponding bond angles of Cl1–Fe–Cl2 127.2°, Cl1–Fe–S1 114.6° and Cl2–Fe–S1 117.7° give a sum of 359.5° and Fe is displaced by 0.099 Å from the plane of the Cl1–Cl2–S1 triangle toward the axial ligand N1. The axial ligands N1 and Cl2ⁱ have bond lengths significantly larger than in tetrahedral complexes, namely Fe–N1 2.267 Å and Fe–Cl2ⁱ 2.605 Å, and show an interligand angle of 167.2°. Dimerization of dichloroiron(II) complexes with chelating N,N'-ligands is known in the literature^[56], where the crystal structures of two FeCl₂ complexes with N-(2,6-diisopropylphenyl)-1-(2-pyridyl)ethanimine ligands are reported, one monomeric complex with a tetrahedral FeCl₂(N,N') coordination and one dimeric [FeCl₂(N,N')]₂ complex with a trigonal bipyramidal coordination (CSD refcodes KEDLAH and KEDLOV^[57]), both isostructural with two corresponding CoCl₂ complexes. Other pairs of analogous monomeric and dimeric dihalogenide complexes of iron with N,N ligands are represented by CSD refcodes PUXRAQ/PUXROQ, VIRWID/VIRWAV, and NEMMOP/NEMNAW.

Despite their relatively low formal electronic count neither the tetrahedral 14e⁻ complexes Fe(SN^R-Ph)X₂ nor the dimeric 16e⁻ complex [Fe(SN-Ph)(μ-Cl)(Cl)]₂ reacted with CO. The same behavior was observed recently for complexes Fe(SN-*i*Pr)X₂ (X = Cl, Br)^[46a].

The magnetic properties of compounds [Fe(SN-Ph)(μ-Cl)(Cl)]₂ (**5k**), Fe(SN-Ph)Br₂ (**5l**), Fe(SN^{Et}-Ph)Cl₂ (**5o**) and Fe(SN^{Et}-Ph)Br₂ (**5p**) were studied by SQUID magnetometry and Mössbauer spectroscopy. Their magnetic behaviour can be seen in Figure 32 and Figure 33. The iron effective magnetic moments extracted from a Curie law fitting to inverse molar

susceptibility data were $5.0(1) \mu_B$ for both **5k** and **5l** and $5.0(1)$ and $5.1(1) \mu_B$ for **5o** and **5p**, respectively, clearly indicating the HS state for Fe(II) ions.

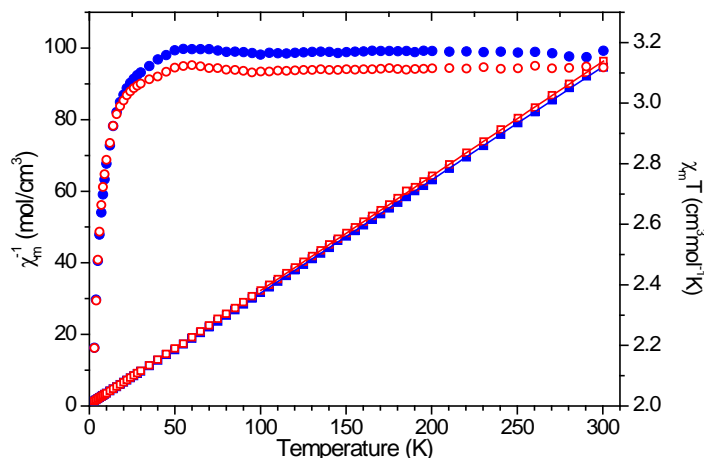


Figure 32: Temperature dependence of the inverse molar susceptibility (squares) and of $\chi_m T$ (circles) of $[\text{Fe}(\text{SN}^{\text{H}}\text{-Ph})(\mu\text{-Cl})_2(\text{Cl})_2]$ (**5k**) (solid symbols) and $\text{Fe}(\text{SN-Ph})\text{Br}_2$ (**5l**) (open symbols). The straight lines are Curie law fittings to the experimental data.

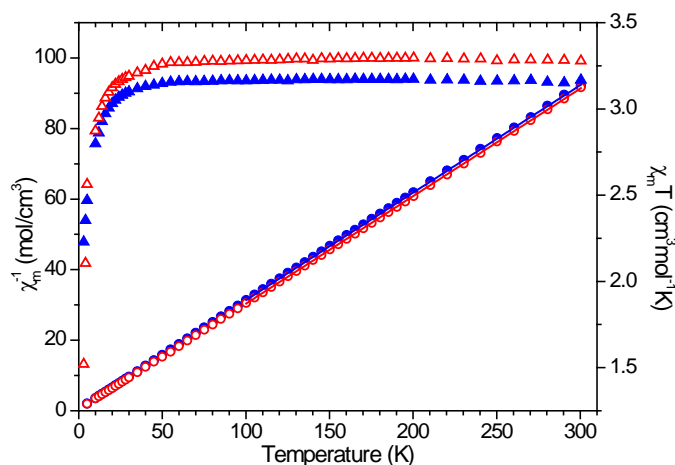


Figure 33: Temperature dependence of the inverse molecular susceptibility (circles) and of $\chi_m T$ (triangles) of $\text{Fe}(\text{SN}^{\text{Et}}\text{-Ph})\text{Cl}_2$ (**5o**) (solid symbols) and $\text{Fe}(\text{SN}^{\text{Et}}\text{-Ph})\text{Br}_2$ (**5p**) (open symbols). The straight lines correspond to Curie law fittings to the experimental data.

The Mössbauer spectra of the four compounds were collected at 78 K. The results are in good agreement with magnetization data, as can be seen from Table 7. Although containing a small Fe(III) impurity (central doublet in Figure 34 and Figure 35, with $\delta \approx 0.46$ mm/s and $\Delta E_Q \approx 0.70$ mm/s and fractions below 20%), which can be explained by oxidation during the sample preparation and/or the measurement, all spectra confirm the exclusive presence of HS Fe(II). In spite of the expected differences in the hyperfine parameters of the Cl and Br

derivatives, the proximity of IS and QS values for **5k** (dimer) and **5l** (monomer) complexes is quite surprising and was not expected.

Compound	δ (mm s ⁻¹)		ΔE_Q (mm s ⁻¹)	
	Exp.	Calcd.	Exp.	Calcd.
[Fe ₂ (SN ^H -Ph) ₂ (μ -Cl) ₂ (Cl) ₂] (5k)	0.881(1)	0.847/0.848	3.080(2)	2.808/2.837
[Fe(SN ^H -Ph)(Cl) ₂] (5k')		0.804		2.787
[Fe(SN ^H -Ph)(Br) ₂] (5l)	0.855(1)	0.795	3.282(2)	2.917
[Fe(SN ^{Et} -Ph)(Cl) ₂] (5o)	0.899(1)		3.008(1)	
[Fe(SN ^{Et} -Ph)(Br) ₂] (5p)	0.877(1)		3.259(2)	
[Fe(PN ^H - <i>i</i> Pr)Cl ₂] ^a	0.680(2)		2.871(4)	
[Fe(SN ^H - <i>i</i> Pr)(Cl) ₂] ^a	0.796(2)		2.998(4)	
[Fe(SeN ^H - <i>i</i> Pr)Cl ₂] ^a	0.790(2)		2.996(5)	
[Fe(ON ^H - <i>i</i> Pr) ₂ (Cl)] ⁺ ^a	1.049(2)		2.008(4)	
[Fe(ON ^H - <i>i</i> Pr) ₂ (Br)] ⁺ ^a	1.029(3)		2.583(7)	

Table 7: Estimated hyperfine parameters from the ⁵⁷Fe Mössbauer spectra of **5k**, **5l**, **5o**, **5p** collected at 78 K and comparison between **5k'**, Fe(PN-*i*Pr)Cl₂, Fe(SN-*i*Pr)Cl₂, Fe(SeN-*i*Pr)Cl₂, [Fe(ON-*i*Pr)₂Cl]⁺ and [Fe(ON-*i*Pr)₂Br]⁺. δ – isomer shift ; ΔE_Q – quadrupole splitting ; ^a Reference^[46a], measured at room temperature.

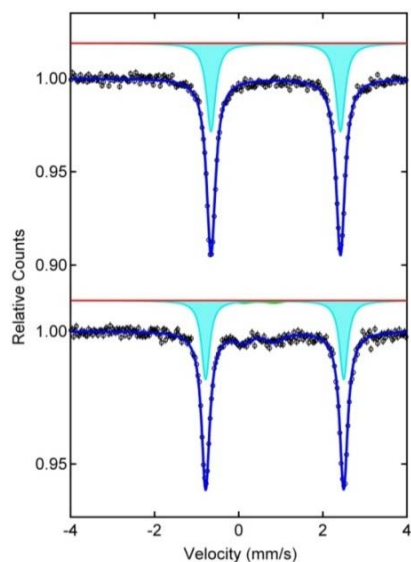


Figure 34: ⁵⁷Fe Mössbauer spectra [Fe(SN-Ph)(μ -Cl)(Cl)₂] (**5k**) (top) and Fe(SN-Ph)Br₂ (**5l**) (bottom) collected at 78 K.

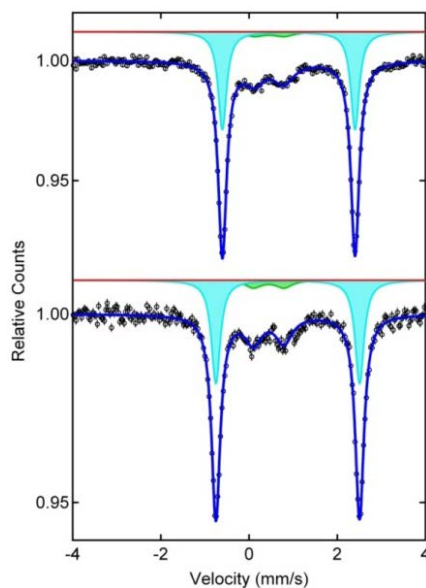


Figure 35: ^{57}Fe Mössbauer spectra $\text{Fe}(\text{SN}^{\text{Et}}\text{-Ph})\text{Cl}_2$ (**5o**) (top) and $\text{Fe}(\text{SN}^{\text{Et}}\text{-Ph})\text{Br}_2$ (**5p**) (bottom) collected at 78 K.

The Mössbauer parameters were calculated for complexes $[\text{Fe}(\text{SN-Ph})(\mu\text{-Cl})\text{Cl}]_2$ (**5k**), $\text{Fe}(\text{SN-Ph})\text{Cl}_2$ (**5k'**) and $\text{Fe}(\text{SN-Ph})\text{Br}_2$ (**5l**) with a DFT approach (using ORCA^[51] and two basis sets, b1 and b2). The structure of **5k**, **5k'** and **5l** were optimized by means of DFT/B3LYP calculations and are depicted in Figure 36 for **5k** and **5k'**. In agreement with experimental findings, the dimeric complex **5k** is more stable than the corresponding unobserved monomeric complex **5k'** by 18.4 kcal/mol (dimerization energy).

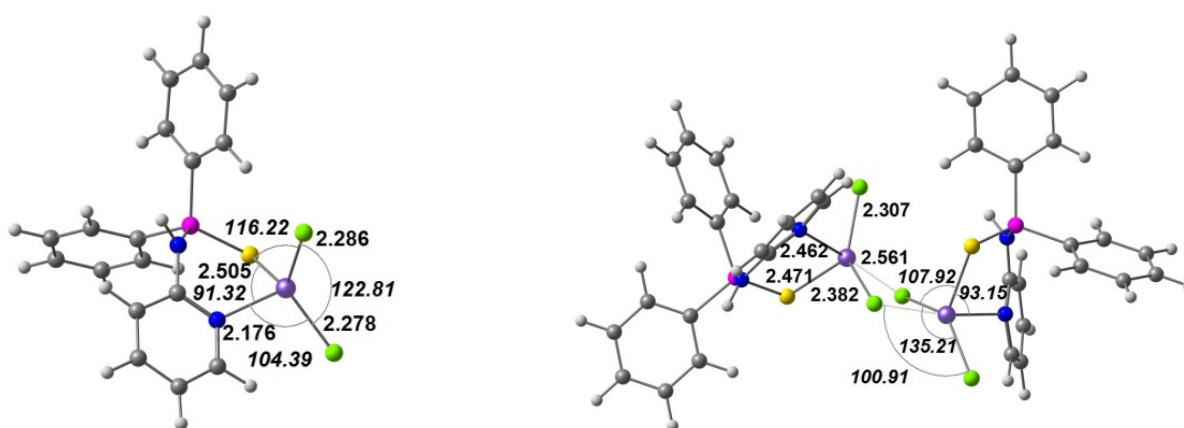


Figure 36: DFT calculated structures of $\text{Fe}(\text{SN-Ph})\text{Cl}_2$ (**5k'**, left) and $[\text{Fe}(\text{SN-Ph})(\mu\text{-Cl})(\text{Cl})]_2$ (**5k**, right), with relevant distances and angles.

The electronic density at the nucleus (ρ) was converted in isomer shifts (δ), using the approach of Neese^[52a] and the quadrupole splitting was obtained directly. The values

calculated for **5k** and **5l** with the b1 basis set are shown in Table 7, and they reproduce quite well the experimental ones (the values for **5k** are the average for the two iron(II) centers). The calculated IS for the mononuclear Fe(SN-Ph)Cl₂ (**5k'**) is 0.804 mm/s, for the two iron atoms) to have no doubt that the powder measured sample was also dimeric, as observed by single crystal XRD. As previously reported^[46a], for the same coordination, Br QS values are higher for the Br derivatives (the calculated QS for the Cl monomer **5k'** is 2.787 mm/s). This is usually assigned to a larger distortion in the local Fe geometry associated with the larger Br ion size. Both IS and QS values determined for complexes **5o** and **5p** follow these trends.

IS values often decrease with coordination number, which is not the case here, since tetrahedral **5o** has a slightly higher IS value (0.90 mm/s) than pentacoordinate **5k** (0.88 mm/s). Furthermore, QS values normally increase with lattice distortion and here similar values are found for the QS parameter of **5k** and **5o** compounds. Calculated values allow us to compare tetrahedral **5k'** and binuclear pentacoordinate **5k**, with IS of 0.804 and 0.847/0.848 mm/s, respectively, and they follow the expected trend (tetrahedral is lower). Again, examination of calculated QS values shows 2.787 for tetrahedral **5k'** and 2.808/2.837 mm/s for pentacoordinate **5k**, the highest value being observed for the more distorted pentacoordinate **5k**. We cannot compare directly **5k** and **5o**. The remaining question concerns the proximity between the IS and QS of the monomeric **5k'** and dimeric **5k**.

The two structures shown in Figure 36 allow a better comparison between the monomeric and the dimeric complexes. In particular, in **5k**, the fifth bond around Fe is a very long one (2.561 Å as shown in Figure 36 and 2.611 Å in the second unit, the complex is asymmetric). A long distance (2.6049 Å) has also been determined by X-ray diffraction Figure 26. The S-Fe-N angle changes only from 91.32 in **5k'** to 93.15 in **5k**. Other angles also display small changes. We can thus consider that the formation of such an asymmetric dimer results in a slightly small perturbation on the coordination geometry of Fe(II) and the Mössbauer parameters do not change very significantly. Taking into account the temperature in the previous study of the tetrahedral complexes Fe(EN-*i*Pr)Cl₂ (E = P, S and Se), and the effect of temperature on IS values, the IS of all complexes can be considered similar (Table 7), and thus, no difference on the electron density at the iron nuclei are observed when *i*Pr at the phosphine is substituted by Ph.

3.3.3 Solution studies

Compound	Elemental composition/ molecular weight (M) ^a	Elemental composition / precursor ions ^a	Elemental composition / product ions ^a
5k	C ₃₄ H ₃₀ Cl ₄ Fe ₂ N ₄ P ₂ S ₂ 871.88	C ₃₄ H ₃₀ Cl ₃ Fe ₂ N ₄ P ₂ S ₂ [M-Cl] ⁺ = 836.91	C ₃₄ H ₂₉ Cl ₂ Fe ₂ N ₄ P ₂ S ₂ [M-Cl-HCl] ⁺ = 800.94
			C ₃₄ H ₂₈ Cl ₁ Fe ₂ N ₄ P ₂ S ₂ [M-Cl-2HCl] ⁺ = 764.96
			C ₃₄ H ₃₀ Cl ₁ Fe ₁ N ₄ P ₂ S ₂ [M-Cl-FeCl ₂] ⁺ = 711.04
			C ₃₄ H ₂₉ Fe ₁ N ₄ P ₂ S ₂ [M-Cl-FeCl ₂ -HCl] ⁺ = 675.07
	C ₃₄ H ₃₀ Cl ₁ Fe ₁ N ₄ P ₂ S ₂ [M-Cl-FeCl ₂] ⁺ = 711.04	C ₃₄ H ₂₉ Fe ₁ N ₄ P ₂ S ₂ [M-Cl-FeCl ₂ -HCl] ⁺ = 675.07	
	C ₃₄ H ₂₉ Fe ₁ N ₄ P ₂ S ₂ [M-Cl-FeCl ₂ -HCl] ⁺ = 675.07	-	
5l	C ₁₇ H ₁₅ Br ₂ Fe ₁ N ₂ P ₁ S ₁ 523.84	C ₃₄ H ₃₀ Br ₁ Fe ₁ N ₄ P ₂ S ₂ [M+1a-Br] ⁺ = 754.99	C ₃₄ H ₂₉ Fe ₁ N ₄ P ₂ S ₂ [M+1a-Br-HBr] ⁺ = 675.07
		C ₃₄ H ₂₉ Fe ₁ N ₄ P ₂ S ₂ [M+1a-Br-HBr] ⁺ = 675.07	-
		C ₁₇ H ₁₅ Br ₂ Fe ₁ N ₂ P ₁ S ₁ Na ₁ [M+Na] ⁺ = 546.83	C ₁₇ H ₁₅ N ₂ P ₁ S ₁ Na ₁ [1b+Na] ⁺ = 333.06
5m	C ₁₈ H ₁₇ Cl ₂ Fe ₁ N ₂ P ₁ S ₁ 449.96	C ₃₆ H ₃₄ Cl ₁ Fe ₁ N ₄ P ₂ S ₂ [M+1b-Cl] ⁺ = 739.07	C ₁₈ H ₁₇ Cl ₁ Fe ₁ N ₂ P ₁ S ₁ [M-Cl] ⁺ = 414.99
		C ₁₈ H ₁₇ Cl ₂ Fe ₁ N ₂ P ₁ S ₁ Na ₁ [M+Na] ⁺ = 472.95	C ₁₈ H ₁₇ N ₂ P ₁ S ₁ Na ₁ [1b+Na] ⁺ = 347.07
		C ₁₈ H ₁₇ Cl ₁ Fe ₁ N ₂ P ₁ S ₁ [M-Cl] ⁺ = 414.99	-
5n	C ₁₈ H ₁₇ Br ₂ Fe ₁ N ₂ P ₁ S ₁ 537.86	C ₃₆ H ₃₄ Br ₁ Fe ₁ N ₄ P ₂ S ₂ [M+1b-Br] ⁺ = 783.02	C ₁₈ H ₁₇ Br ₁ Fe ₁ N ₂ P ₁ S ₁ [M-Br] ⁺ = 458.94
		C ₁₈ H ₁₇ Br ₂ Fe ₁ N ₂ P ₁ S ₁ Na ₁ [M+Na] ⁺ = 560.85	C ₁₈ H ₁₇ Br ₁ Fe ₁ N ₂ P ₁ S ₁ [M-Br] ⁺ = 458.94
			C ₁₈ H ₁₇ N ₂ P ₁ S ₁ Na ₁ [1b+Na] ⁺ = 347.07
		C ₁₈ H ₁₇ Br ₁ Fe ₁ N ₂ P ₁ S ₁ [M-Br] ⁺ = 458.94	-
5o	C ₁₉ H ₁₉ Cl ₂ Fe ₁ N ₂ P ₁ S ₁ 464.98	C ₃₈ H ₃₈ Cl ₁ Fe ₁ N ₄ P ₂ S ₂ [M+1c-Cl] ⁺ = 767.11	C ₁₉ H ₁₉ Cl ₁ Fe ₁ N ₂ P ₁ S ₁ [M-Cl] ⁺ = 429.01
		C ₁₉ H ₁₉ Cl ₂ Fe ₁ N ₂ P ₁ S ₁ Na ₁ [M+Na] ⁺ = 486.96	C ₁₉ H ₁₉ N ₂ P ₁ S ₁ Na ₁ [1c+Na] ⁺ = 361.09
5p	C ₁₉ H ₁₉ Br ₂ Fe ₁ N ₂ P ₁ S ₁ 551.87	C ₃₈ H ₃₈ Br ₂ Fe ₁ N ₄ P ₂ S ₂ Na ₁ [M+1c+Na] ⁺ = 912.96	C ₁₉ H ₁₉ Br ₂ Fe ₁ N ₂ P ₁ S ₁ Na ₁ [M+Na] ⁺ = 574.86
		C ₃₈ H ₃₈ Br ₁ Fe ₁ N ₄ P ₂ S ₂ [M+1c-Br] ⁺ = 811.05	C ₁₉ H ₁₉ Br ₁ Fe ₁ N ₂ P ₁ S ₁ [M-Br] ⁺ = 472.95
		C ₁₉ H ₁₉ Br ₂ Fe ₁ N ₂ P ₁ S ₁ Na ₁ [M+Na] ⁺ = 574.86	C ₁₉ H ₁₉ Br ₁ Fe ₁ N ₂ P ₁ S ₁ [M-Br] ⁺ = 472.95
			C ₁₉ H ₁₉ N ₂ P ₁ S ₁ Na ₁ [1c+Na] ⁺ = 361.09
		C ₁₉ H ₁₉ Br ₁ Fe ₁ N ₂ P ₁ S ₁ [M-Br] ⁺ = 472.95	-

Table 8: elemental compositions of the neutral compounds **5k-5p** and calculated m/z values of observed precursor ions and corresponding prominent product (fragment) ions. ^a Mass calculations are based on the lowest mass of chlorine (³⁵Cl) and bromine isotope (⁷⁹Br), respectively, and the most abundant iron isotope (⁵⁶Fe).

Because of the ease of transferring solution-phase ions to the gas phase at atmospheric pressure for identification or further reactions, electrospray ionization mass spectrometry (ESI-MS) has become increasingly popular as a mechanistic tool for studying short-lived reactive intermediates in inorganic and organometallic reactions. Therefore, all complexes were investigated by means of ESI-MS (Table 8). Solutions of these complexes in *i*PrOH and/or MeOH in the presence of NaX (X = Cl, Br) were subjected to ESI-MS analysis in the positive ion mode.

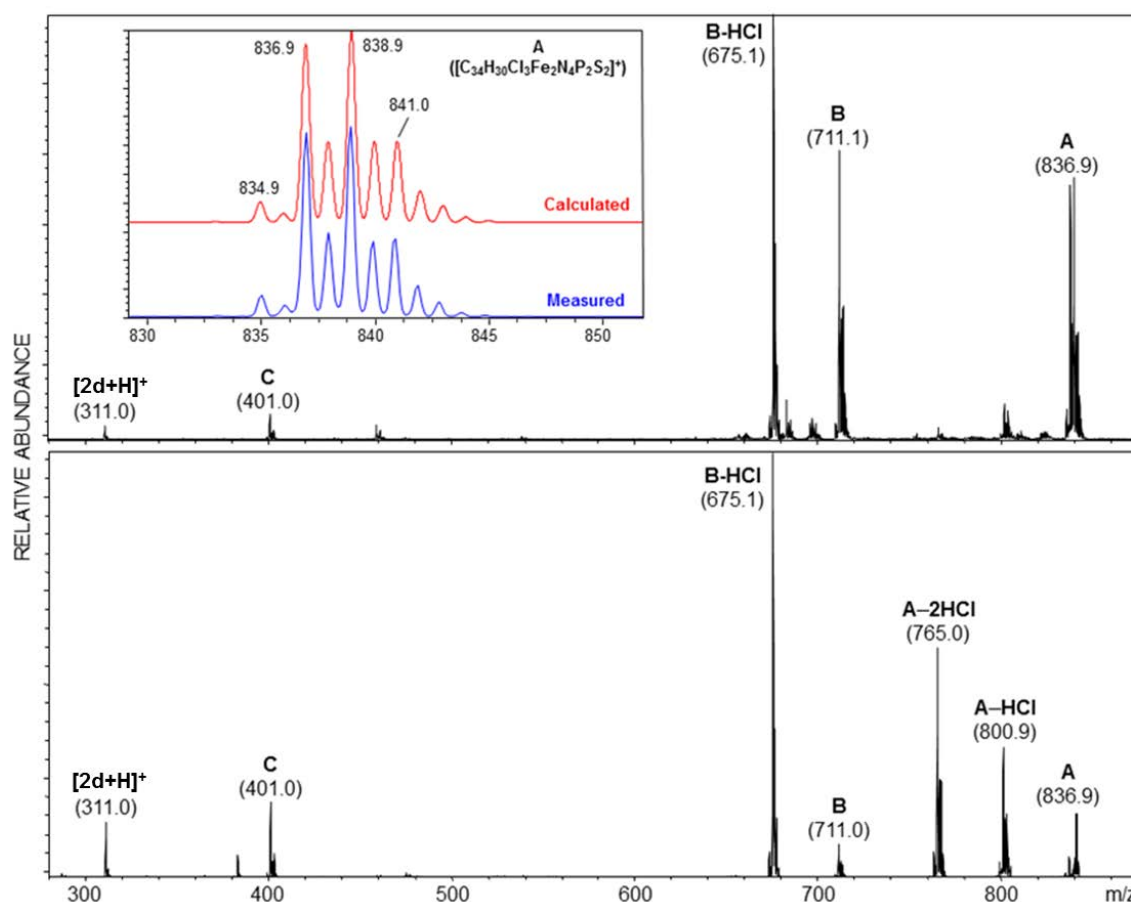
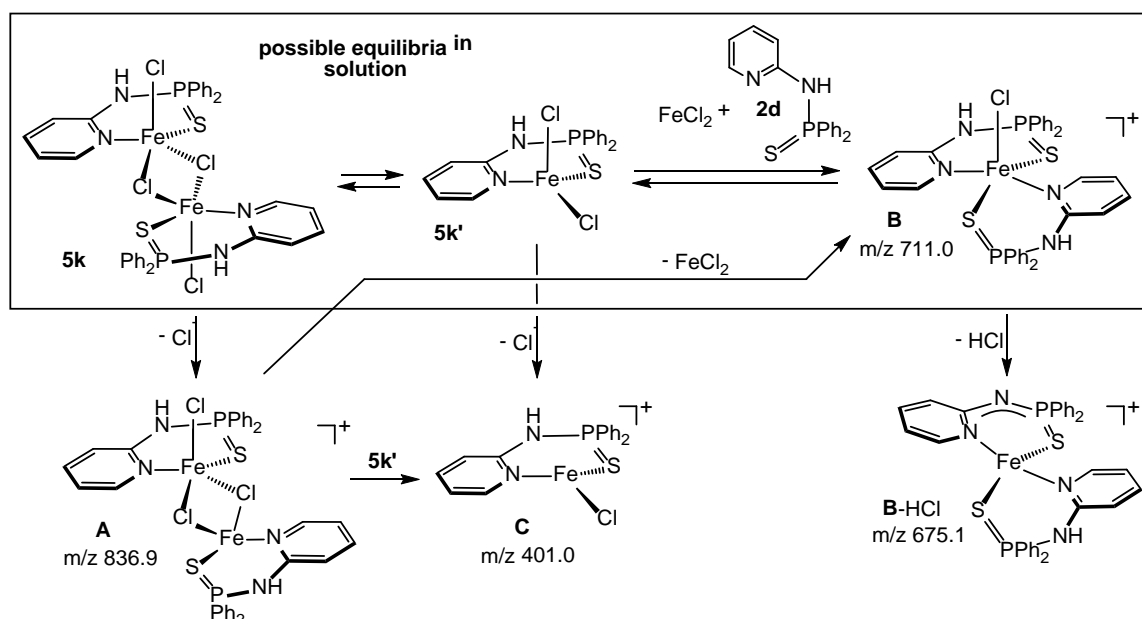


Figure 37: Positive ion ESI full scan mass spectrum of $[\text{Fe}(\text{SN-Ph})(\mu\text{-Cl})\text{Cl}]_2$ (**5k**) in *i*PrOH (top) and corresponding MS/MS (low energy CID) spectrum of in source generated $[\text{Fe}_2(\text{SN-Ph})_2(\mu\text{-Cl})_2\text{Cl}]^+$ (**A**) precursor ions (bottom). Inset shows the calculated and measured isotopic pattern of **A**. Only signals containing the Fe isotopes of highest abundance (^{56}Fe) and the Cl isotope of lowest mass (^{35}Cl) are annotated.

Under the so-called ‘soft ionization’ conditions in the electrospray source, the ESI mass spectrum of $[\text{Fe}(\text{SN-Ph})(\mu\text{-Cl})\text{Cl}]_2$ (**5k**) shows prominent peaks at m/z 836.9, 711.0, 675.1, 401.0 and 311.0 assignable to the dinuclear species $[\text{Fe}_2(\text{SN-Ph})_2(\mu\text{-Cl})_2\text{Cl}]^+$ (**A**), the mononuclear species $[\text{Fe}(\text{SN-Ph})_2\text{Cl}]^+$ (**B**), $[\text{Fe}(\text{SN-Ph})(\text{SN}^{\text{H}}\text{-Ph})]^+$ (**B-HCl**), and $[\text{Fe}(\text{SN-Ph})\text{Cl}]^+$ (**C**) together with the protonated SN-Ph ligand (**2d**), respectively (Figure 37 and

Scheme 30). Complexes **A** and **C**, respectively, result from loss of one chloride ligand in **5k** and **5k'**. The formation of **B** (solvated) FeCl_2 , and free ligand **2d** are in equilibrium with one another. The fragmentation of the selected $[\text{Fe}_2(\text{SN-Ph})_2(\mu\text{-Cl})_2\text{Cl}]^+$ ion (**A**) with m/z 836.9 by low energy collision-induced dissociation (CID) in an ion trap analyser resulted in the formation of ions with m/z 801.9 and 765.0 due to stepwise HCl loss (**A-HCl**, **A-2Cl**). Additionally, the known fragment ions **B**, **B-HCl**, **C**, and protonated **1a** were observed. From the CID spectrum of **A** it is apparent that in this particular case $[\text{Fe}(\text{SN-Ph})_2\text{Cl}]^+$ (**B**) originates exclusively from **A** upon liberation of FeCl_2 (Scheme 30).



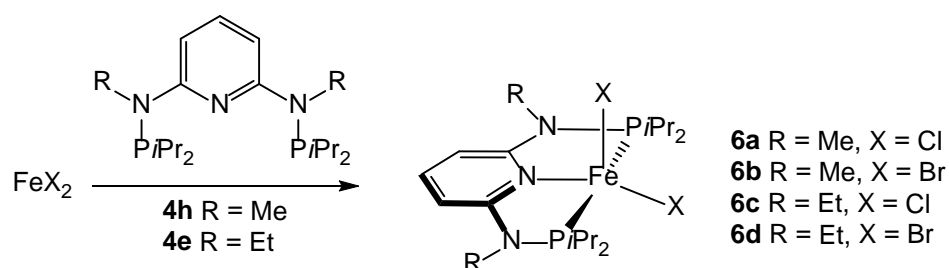
Scheme 30: Reactions in solution and fragmentation pathways of $[\text{Fe}(\text{SN-Ph})(\mu\text{-Cl})(\text{Cl})]_2$ (**5k**) in *i*PrOH as established by ESI MS.

In the case of all other complexes there was no evidence of a dimeric species. The ESI mass spectrometric analysis gave rise to the typical fragments $[\text{Fe}(\text{SN}^{\text{R}}\text{-Ph})_2\text{X}]^+$ (type **B**) and, in the case of **5l**, $[\text{Fe}(\text{SN-Ph})(\text{SN}^{\text{H}}\text{-Ph})]^+$ (type **B-HCl**) together with peaks of $[\text{Fe}(\text{SN}^{\text{R}}\text{-Ph})\text{X}]^+$ (type **C**) and the sodiated ligands $\text{SN}^{\text{R}}\text{-Ph}$ (**2d-f**) were found. For comparison, the ESI mass spectrum of $\text{Fe}(\text{SN-}i\text{Pr})\text{Cl}_2$ ^[46a] in *i*PrOH was recorded exhibiting the same fragmentation pattern as for complexes $[\text{Fe}(\text{SN}^{\text{R}}\text{-Ph})_2\text{X}]^+$. There was again no evidence of the presence of a dimeric complex in the gas phase.

3.4 PNP^R & PNN iron(II) complexes

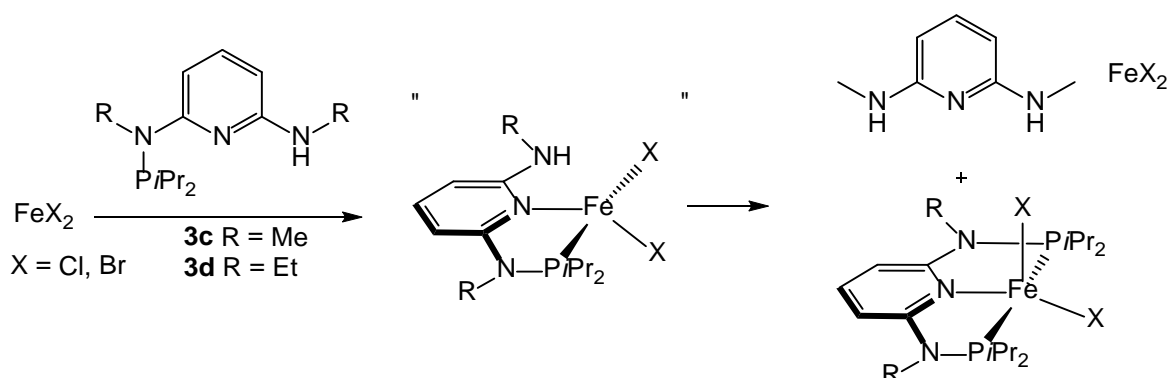
3.4.1 Synthesis

Treatment of anhydrous FeX₂ (X = Cl, Br) with 1 equiv of the ligands in THF at room temperature afforded complexes of the general type Fe(PNP^R-iPr)X₂ (Scheme 31), analogously to prior results^[53]. The 4 complexes were isolated as bright yellow solids, thermodynamically stable if air and moisture is excluded.



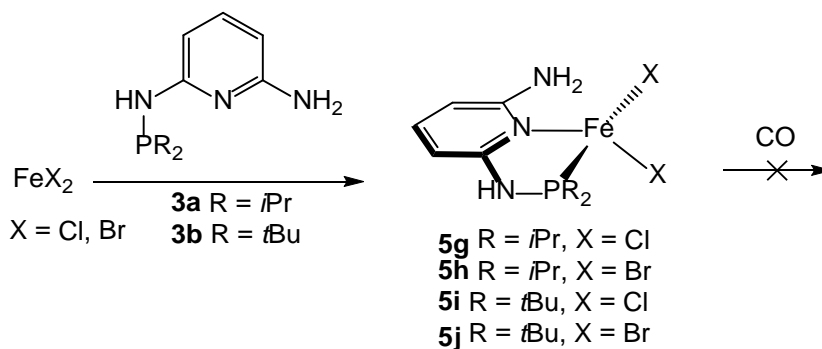
Scheme 31: Reaction of FeX₂ with PNP^R-iPr ligands

The ligand precursors **3c** and **3d** were also used for complexation reactions, but the resulting complex was could not be isolated due to isomerization of the κ^2 -coordinated complex to the κ^3 P,N,P compounds in solution. The products were identified by ¹H-NMR spectroscopy, after the insoluble, inorganic residue was removed by filtration, depicted in Scheme 32:



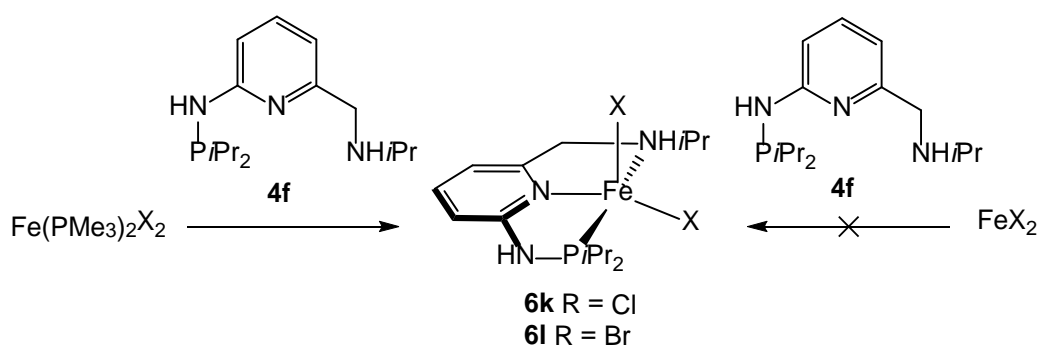
Scheme 32: Reaction of FeX₂ with **3c** and **3d**, followed by isomerization.

On the other hand, complexation was successful with the ligand precursors PN/NH₂-*i*Pr (**3a**) and PN/NH₂-*t*Bu (**3b**). Reaction with FeX₂ resulted in complexes of the type Fe(κ^2P,N -PN/NH₂-R)Cl₂ (Scheme 33).



Scheme 33: Synthesis of the complexes Fe(κ^2P,N -PN/NH₂-R)X₂.

PNN-type complexes with the general formula Fe(PNN-*i*Pr)X₂ (X = Cl, Br) were synthesized by the reaction of ligand **4f** with the iron(II) precursor Fe(PMe₃)₂Cl₂ and Fe(PMe₃)₂Br₂, which is synthesized by treatment of PMe₃ with the iron halides in CH₂Cl₂^[58]. Fe(P(OMe)₃)₃X₂ can be used as a cheaper alternative. The analogue reaction of ligand **4f** with FeCl₂ or FeBr₂ did not lead to the desired product, possibly forming polymeric, insoluble Fe(PNN-*i*Pr)_xX_y, including inseparable inorganic materials, regardless on the stoichiometry.



Scheme 34: Synthesis of complexes Fe(PNN-*i*Pr)Cl₂ (**6k**) and Fe(PNN-*i*Pr)Br₂ (**6l**).

The compounds **5g-j**, **6k** and **6l**, respectively, were obtained as bright yellow stable solids. Further experiments were performed, but the coordinatively unsaturated complexes failed to react with other ligands or substrates, even CO addition was rejected. Also the reaction of

the ligands **3a**, **3b** and **4f** with the carbonyl precursors $\text{Fe}(\text{CO})_4\text{X}_2$ was carried out, but no defined product could be isolated.

3.4.2 Characterization

Single crystals suitable for XRD were grown of the complexes **5g**, **6a**, **6b**, **6d**, **6k** and **6l**, though showing paramagnetic behaviour, it was possible to characterize the complexes **6a-d** by ^1H -NMR spectroscopy.

In Figure 38, the ^1H -NMR spectra of the complex $\text{Fe}(\text{PNP}^{\text{Me}}\text{-}i\text{Pr})\text{Cl}_2$ (**6a**) is shown. The signals typically appear as broad singlets, lack of coupling splitting and the chemical shift depends on the position relative to the paramagnetic centre. The isopropyl CH protons are typically shifted up to 190 ppm, the methyl signals appear between 0 – 30 ppm, the aromatic pyridine signals $\text{py}^{3,5}$ are chemically equivalent and can be seen as a sharp singlet at 60 – 80 ppm. The *para* pyridine proton features a high-field shift at -20 ppm. $^{31}\text{P}\{^1\text{H}\}$ and $^{13}\text{C}\{^1\text{H}\}$ -NMR spectra were not successfully recorded.

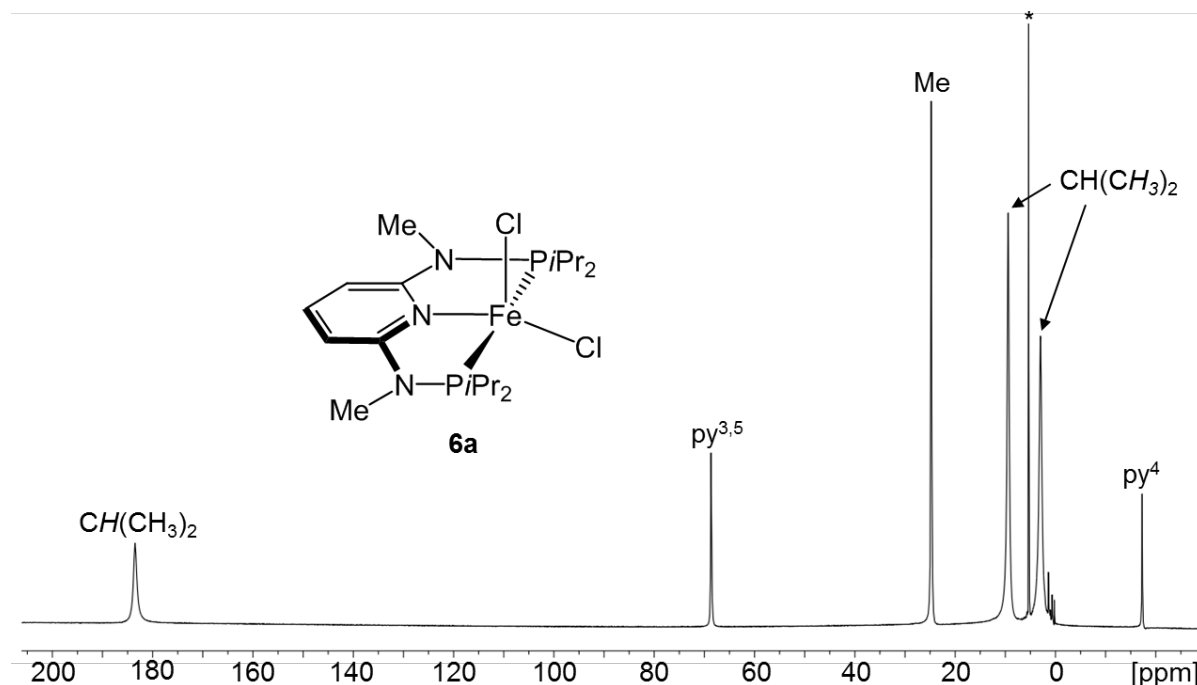


Figure 38: ^1H -NMR spectra of $\text{Fe}(\text{PNP}^{\text{Me}}\text{-}i\text{Pr})\text{Cl}_2$ (**6a**) in CD_2Cl_2 (*).

The molecular structure of the compounds **5g**, **6a**, **6c**, **6d**, **6k** and **6l** are depicted in Figure 39-Figure 50Figure 18Figure 52. Compound **5g** adopts a distorted tetrahedral geometry, the complexes **6a**, **6c**, **6d**, **6k** and **6l** are of distorted trigonal bipyramidal shape.

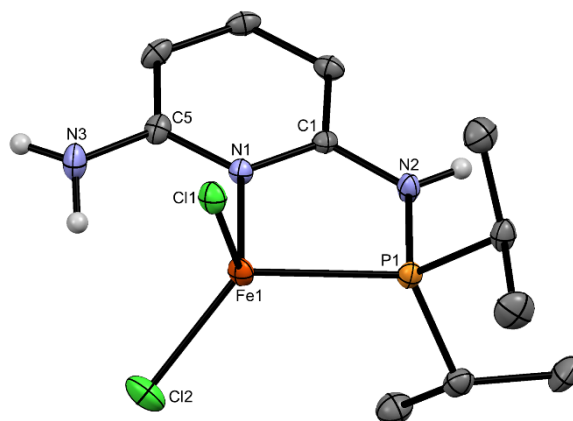


Figure 39: Structural view of $\text{Fe}(\text{PN}/\text{NH}_2\text{-}i\text{Pr})\text{Cl}_2$ (**5g**) showing 50% thermal ellipsoids (H atoms and solvent molecules omitted for clarity). Only one of the two crystallographically independent complexes is shown. Selected bond lengths (Å) and bond angles (°): Fe1–Cl1 2.2740(4), Fe1–Cl2 2.2369(4), Fe1–P1 2.4038(5), Fe1–N1 2.106(1), P1–N2 1.690(1), Cl1–Fe1–Cl2 118.81(2), Cl1–Fe1–P1 112.18(2), Cl1–Fe1–N1 111.19(3), Cl2–Fe1–P1 119.91, Cl2–Fe1–N1 106.74, Cl1–Fe1–P1–N2 104.95(5), Cl2–Fe1–P1–N2 108.43(5).

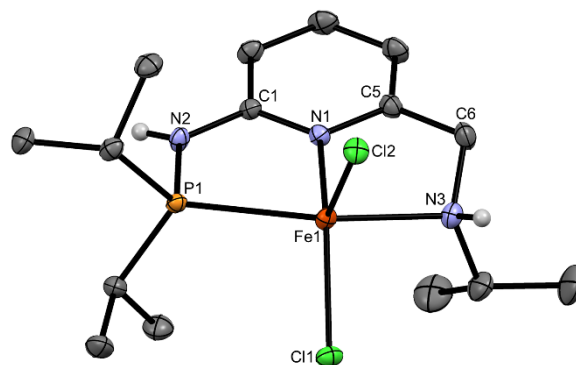


Figure 40: Structural view of $\text{Fe}(\text{PNN-}i\text{Pr})\text{Cl}_2$ (**6k**) showing 50% thermal ellipsoids (most H atoms and solvent molecules omitted for clarity). Selected bond lengths (Å) and bond angles (°): Fe1–Cl1 2.3461(4), Fe1–Cl2 2.3292(3), Fe1–P1 2.5158(4), Fe1–N1 2.140(1), Fe1–N3 2.215(1), Cl1–Fe1–Cl2 105.76(1), Cl1–Fe1–P1 98.92(1), Cl1–Fe1–N1 143.29(3), Cl1–Fe1–N3 94.39(3), Cl2–Fe1–P1 106.44(1), Cl2–Fe1–N1 110.39(3), Cl2–Fe1–N3 94.13(3), Cl1–Fe1–P1–N2 140.82(4).

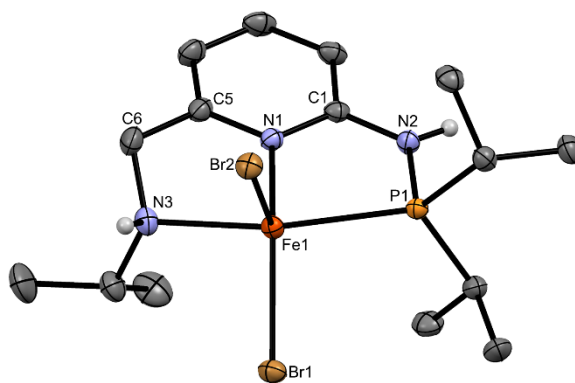


Figure 41: Structural view of $\text{Fe}(\text{PNN-}i\text{Pr})\text{Br}_2$ (**6I**) showing 50% thermal ellipsoids (most H atoms and solvent molecules omitted for clarity). Selected bond lengths (Å) and bond angles (°): Br1–Fe1 2.4792(3), Br2–Fe1 2.4771(2), Fe1–P1 2.5154(4), Fe1–N1 2.135(1), Fe1–N3 2.217(1), Br1–Fe1–Br2 104.76(1), Br1–Fe1–P1 99.13(1), Br1–Fe1–N1 144.34(3), Br1–Fe1–N3 95.02(4), Br2–Fe1–P1 106.19(1), Br2–Fe1–N1 110.33(3), Br2–Fe1–N3 93.08(4), Br1–Fe1–P1–N2 141.06(4), Br2–Fe1–P1–N2 110.56(4).

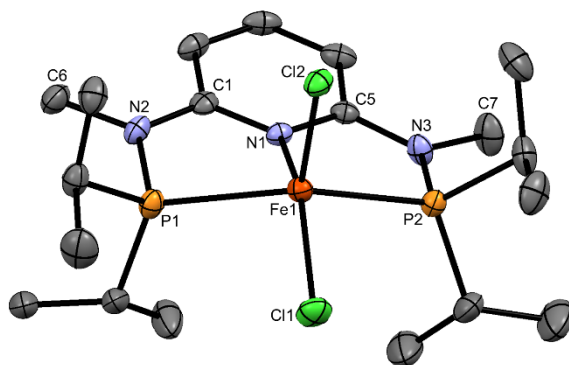


Figure 42: Structural view of $\text{Fe}(\text{PNP}^{\text{Me}}-i\text{Pr})\text{Cl}_2$ (**6a**) showing 50% thermal ellipsoids (H atoms and solvent molecules omitted for clarity). Selected bond lengths (Å) and bond angles (°): Fe1–Cl1 2.301(1), Fe1–Cl2 2.347(1), Fe1–P1 2.464(1), Fe1–P2 2.443(1), Fe1–N1 2.289(3), Cl1–Fe1–Cl2 106.70(4), Cl1–Fe1–P2 104.13(4), Cl1–Fe1–P1 108.39(4), Cl1–Fe1–N1 107.81(7), Cl2–Fe1–P1 96.47(4), Cl2–Fe1–P2 94.43(4), Cl2–Fe1–N1 145.46(8), Cl1–Fe1–P2–N3 97.7(1), Cl2–Fe1–P2–N3 153.8(1).

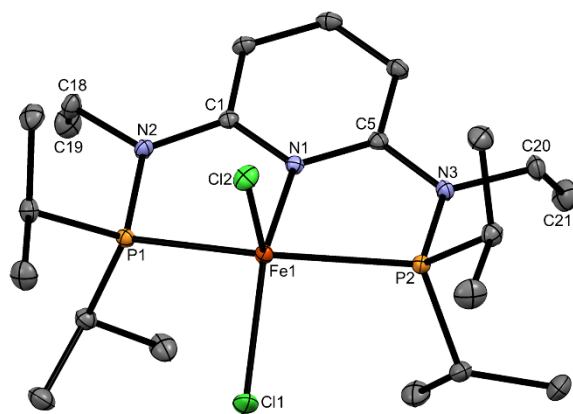


Figure 43: Structural view of $\text{Fe}(\text{PNP}^{\text{Et-}i\text{Pr}})\text{Cl}_2$ (**6c**) showing 50% thermal ellipsoids (H atoms and solvent molecules omitted for clarity). Selected bond lengths (Å) and bond angles (°): Fe1–Cl1 2.301(1), Fe1–Cl2 2.347(1), Fe1–P1 2.464(1), Fe1–P2 2.443(1), Fe1–N1 2.289(3), Cl1–Fe1–Cl2 106.70(4), Cl1–Fe1–P1 108.39(4), Cl1–Fe1–P2 104.13(4), Cl1–Fe1–N1 107.81(7), P1–Fe1–P2 140.89(4), Cl1–Fe1–P1–N2 82.4(1), Cl1–Fe1–P2–N3 97.7(1).

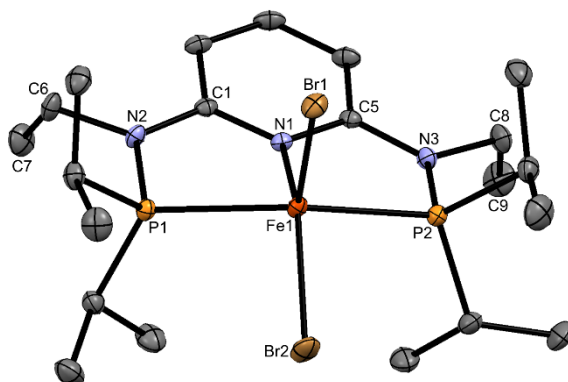
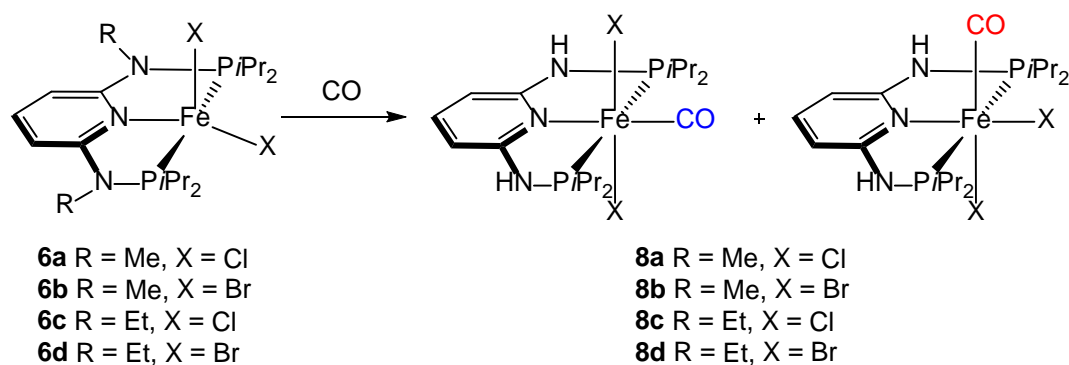


Figure 44: Structural view of $\text{Fe}(\text{PNP}^{\text{Et-}i\text{Pr}})\text{Br}_2$ (**6d**) showing 50% thermal ellipsoids (H atoms and solvent molecules omitted for clarity). Selected bond lengths (Å) and bond angles (°): Br1–Fe1 2.4463(3), Br2–Fe1 2.5071(3), Fe1–P1 2.4389(4), Fe1–P2 2.4363(4), Fe1–N1 2.267(1), Br1–Fe1–Br2 105.47(1), Br1–Fe1–P1 104.01(1), Br1–Fe1–P2 103.94(1), Br1–Fe1–N1 111.86(3), Br2–Fe1–P1 95.85(1), Br2–Fe1–P2 94.64(1), Br2–Fe1–N1 142.67(3), Br1–Fe1–P1–N2 93.41(4), Br2–Fe1–P2–N3 148.45(4).

3.4.3 Reaction with CO

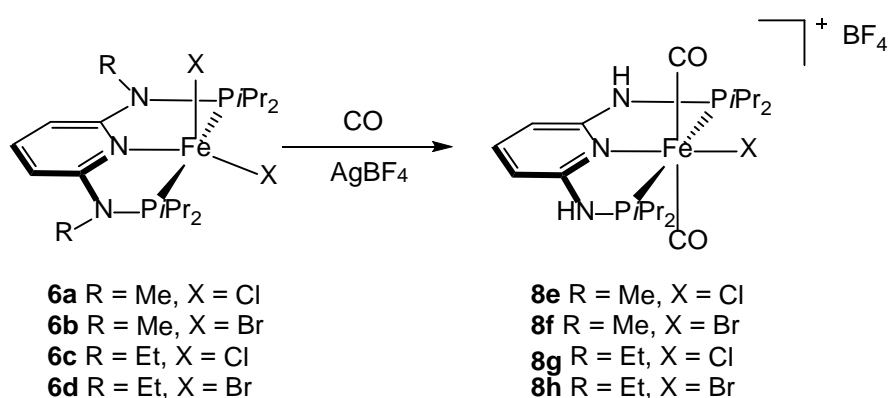
Complexes **6a-d** showed reactivity with CO analogue to prior results^[46a, 53], yielding in diamagnetic complexes of the general type $\text{Fe}(\text{PNP}^{\text{R-}i\text{Pr}})(\text{CO})\text{X}_2$ (**8a-d**) (Scheme 35). However, in contrast to the complex $\text{Fe}(\text{PNP-}i\text{Pr})\text{Cl}_2$, compounds **6a-d** remained unreacted in the solid state, even after 24 h under CO atmosphere. In solution, in dependency on the solvent and the halide, a mixture of the *cis/trans* isomers, and, in the case of bromide complexes **6b** and **6d**, small amounts of $[\text{Fe}(\text{PNP}^{\text{R-}i\text{Pr}})(\text{CO})\text{Br}]^+$ were formed.



Scheme 35: Reaction of $\text{Fe}(\text{PNP}^{\text{R}}\text{-iPr})\text{X}_2$ (**6a-d**) with CO, forming *cis/trans*- $\text{Fe}(\text{PNP}^{\text{R}}\text{-iPr})(\text{CO})\text{X}_2$

The CO-complexes have been isolated, but release CO under reduced pressure and over time slowly even in solid state. For complex **8a**, the solubility of the two isomers was investigated. In dry acetone, the *trans* complex was significantly less soluble, therefore it was isolated by filtration. Surprisingly, in $^{31}\text{P}\{^1\text{H}\}$ -NMR spectra observed, using CD_2Cl_2 as solvent, again the *cis* isomer was formed by isomerization, and the ratio was found to be exactly the same as in the prior formed mixture. This indicates an active equilibrium between the *cis* and the *trans* form, depending on the solvent.

Treatment of **6a-d** with 1 equiv of AgBF_4 in THF under CO atmosphere resulted in the formation of diamagnetic, octahedral cationic complexes $[\text{Fe}(\text{PNP}^{\text{R}}\text{-iPr})(\text{CO})_2\text{X}]\text{BF}_4$. The complexes were isolated in good yields (73-79%) as air stable, orange to red solids (Scheme 36).



Scheme 36: Synthesis of complexes $[\text{Fe}(\text{PNP}^{\text{R}}\text{-iPr})(\text{CO})_2\text{X}]\text{BF}_4$ (**8e-8h**).

The complexes **8a-h** were characterized by ^1H , $^{31}\text{P}\{^1\text{H}\}$, $^{13}\text{C}\{^1\text{H}\}$ -NMR and IR spectroscopy. The CO signal appears as triplet in the $^{13}\text{C}\{^1\text{H}\}$ -NMR spectra at a chemical shift of 212 ppm

and a $^2J_{CP}$ of 25 Hz for the $\text{Fe}(\text{PNP}^{\text{R-}i\text{Pr}})\text{X}_2$, and 225 ppm with a $^2J_{CP}$ of 22 Hz for $[\text{Fe}(\text{PNP}^{\text{R-}i\text{Pr}})(\text{CO})_2\text{X}]^+$, respectively. The CO band appears as a broad band at 1950 cm^{-1} for the mono-CO compounds and at 2000 cm^{-1} for the cationic complexes. The molecular structures of the complexes $[\text{Fe}(\text{PNP}^{\text{R-}i\text{Pr}})(\text{CO})_2\text{X}]\text{BF}_4$ (**8e-h**) are shown in Figure 45-Figure 48. The average C-O bond length is 1.13 \AA , the Fe-C-O angle differs from the stretched 180° to $174\text{-}177^\circ$, compared to free CO with a bond length of 1.06 \AA (solid state).

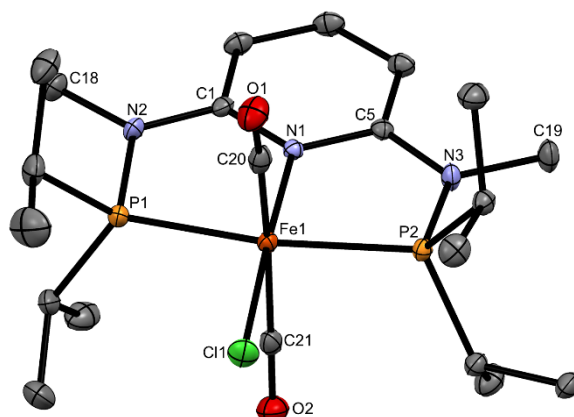


Figure 45: Structural view of $[\text{Fe}(\text{PNP}^{\text{Me-}i\text{Pr}})(\text{CO})_2\text{Cl}]\text{BF}_4$ (**8e**) showing 50% thermal ellipsoids (H atoms, BF_4^- and solvent molecules omitted for clarity). Selected bond lengths (\AA) and bond angles ($^\circ$): Fe1–Cl1 2.3008(5), Fe1–P1 2.2507(4), Fe1–P2 2.2455(4), Fe1–N1 1.976(1), Fe1–C20 1.818(1), Fe1–C21 1.819(1), Cl1–Fe1–P1 97.58(2), Cl1–Fe1–P2 93.99(2), Cl1–Fe1–N1 177.78(4), C20–Fe1–C21 168.71(7), Fe1–C20–O1 174.02, Fe1–C21–O2 173.76, Cl1–Fe1–P1–N2 176.63(4), Cl1–Fe1–P2–N3 174.93(4).

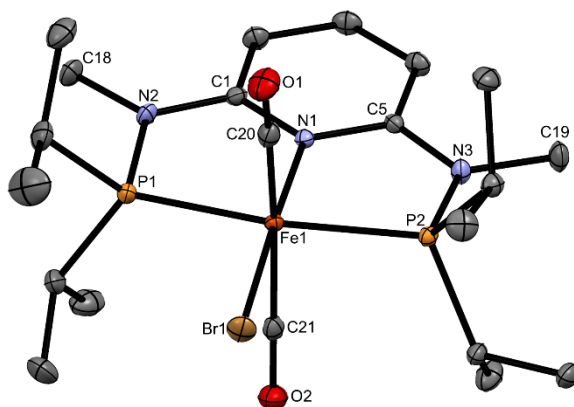


Figure 46: Structural view of $[\text{Fe}(\text{PNP}^{\text{Me-}i\text{Pr}})(\text{CO})_2\text{Br}]\text{BF}_4$ (**8f**) showing 50% thermal ellipsoids (H atoms, BF_4^- and solvent molecules omitted for clarity). Selected bond lengths (\AA) and bond angles ($^\circ$): Fe1–Br1 2.4423(3), Fe1–P1 2.533(4), Fe1–P2 2.2487(4), Fe1–N1 1.980(1), Fe1–C20 1.825(1), Fe1–C21 1.818(1), Br1–Fe1–P1 97.57(1), Br1–Fe1–P2 94.30(1), Br1–Fe1–N1 178.14(3), C20–Fe1–C21 167.60(6), Fe1–C20–O1 174.58, Fe1–C21–O2 174.50, Br1–Fe1–P1–N2 176.78(4), Br1–Fe1–P2–N3 175.63(4).

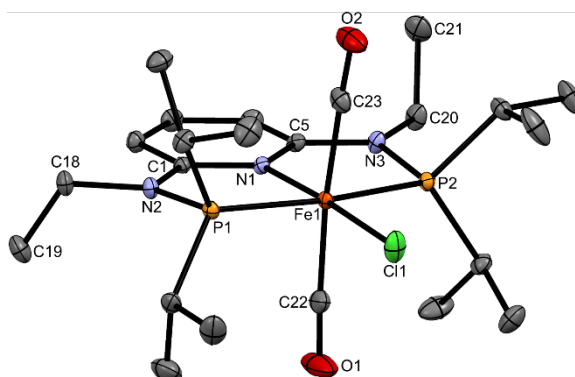


Figure 47: Structural view of $[\text{Fe}(\text{PNP}^{\text{Et}}\text{-}i\text{Pr})(\text{CO})_2\text{Cl}]\text{BF}_4$ (**8g**) showing 50% thermal ellipsoids (H atoms, BF_4^- and solvent molecules omitted for clarity). Selected bond lengths (Å) and bond angles ($^\circ$): Fe1–Cl1 2.3034(3), Fe1–P1 2.2494(3), Fe1–P2 2.2598(3), Fe1–N1 1.9713(7), Fe1–C22 1.813(1), Fe1–C23 1.8316(9), Cl1–Fe1–P1 92.87(1), Cl1–Fe1–P2 97.99(1), Cl1–Fe1–N1 176.60(2), C22–Fe1–C23 174.40(4), Fe1–C22–O1 176.16, Fe1–C23–O2 178.03, Cl1–Fe1–P1–N2 173.17(3), Cl1–Fe1–P2–N3 176.84(3).

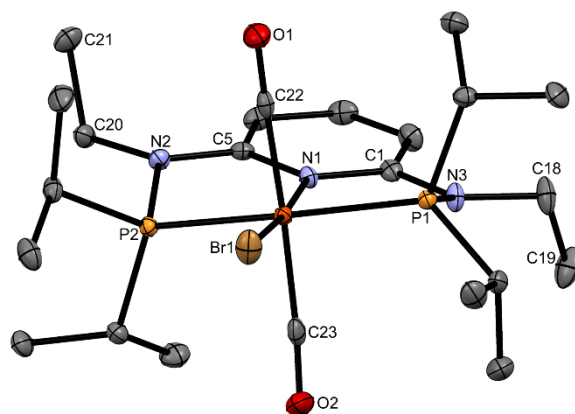


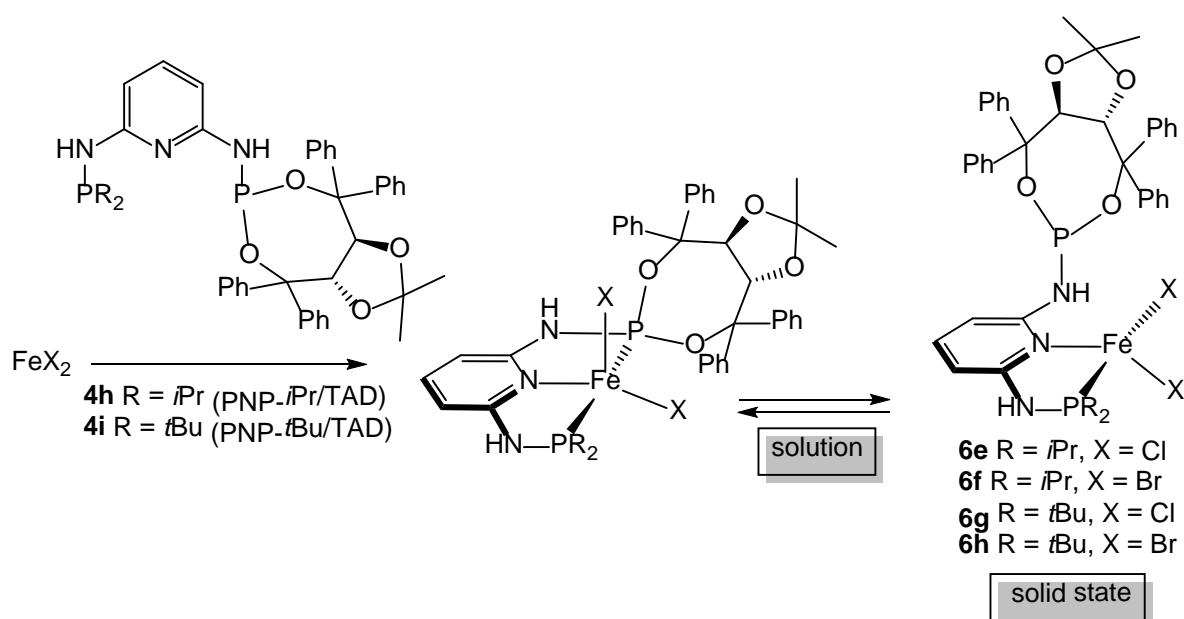
Figure 48: Structural view of $[\text{Fe}(\text{PNP}^{\text{Et}}\text{-}i\text{Pr})(\text{CO})_2\text{Br}]\text{BF}_4$ (**8h**) showing 50% thermal ellipsoids (H atoms, BF_4^- and solvent molecules omitted for clarity). Selected bond lengths (Å) and bond angles ($^\circ$): Fe1–Br1 2.4457(3), Fe1–P1 2.539(5), Fe1–P2 2.2452(5), Fe1–N1 1.983(2), Fe1–C22 1.825(2), Fe1–C23 1.818(2), Br1–Fe1–P1 97.51(1), Br1–Fe1–P2 97.03(2), Br1–Fe1–N1 174.03(5), C20–Fe1–C21 168.60(8), Fe1–C20–O1 176.72, Fe1–C21–O2 174.20, Br1–Fe1–P1–N3 169.63(6), Br1–Fe1–P2–N2 153.28(6).

Complex **8e** was used in order to show the different reactivity between $[\text{Fe}(\text{PNP-}i\text{Pr})(\text{CO})_2\text{Cl}]^+$ and $[\text{Fe}(\text{PNP}^{\text{Me}}\text{-}i\text{Pr})(\text{CO})_2\text{Cl}]^+$ for the heterolytic cleavage of H_2 ^[33].

3.5 TADDOL-PNP iron(II) complexes^[59]

3.5.1 Synthesis

Treatment of anhydrous FeCl_2 with 1 equiv of the PNP ligands PNP-*i*Pr/TAD (**4h**) and PNP-*t*Bu/TAD (**4i**) in THF at room temperature afforded coordinatively unsaturated complexes of the general formula $\text{Fe}(\text{PNP-}i\text{Pr/TAD})\text{X}_2$ (**6e**: X = Cl, **6f**: X = Br) and $\text{Fe}(\text{PNP-}t\text{Bu/TAD})\text{X}_2$ (**6g**: X = Cl, **6h**: X = Br) in up to 89% isolated yield. All 4 complexes are thermally robust yellow solids that are air sensitive in the solid state and particularly in solution (Scheme 37).



Scheme 37: Synthesis of $\text{Fe}(\text{PNP-R/TAD})\text{X}_2$ (**6e-6h**) – solution vs. solid state behaviour.

3.5.2 Solid state studies

In the solid state, the complexes were characterized by elemental analysis, SQUID and Mössbauer spectroscopy. In addition, the molecular structure of **6f** and **6g** were determined by X-ray crystallography. Structural views of **6f** and **6g** are depicted in Figure 49 and Figure 50 with selected bond distances and angles given in the captions. Surprisingly, these complexes adopt a distorted tetrahedral geometry with the PNP ligands coordinated in κ^2P,N -fashion rather than in the typical *meridional* κ^3P,N,P -coordination mode. Such a coordination mode is unexpected and unusual for pyridine based PNP pincer ligands in particular when taking into account that these complexes are coordinatively unsaturated $14e^-$ species.

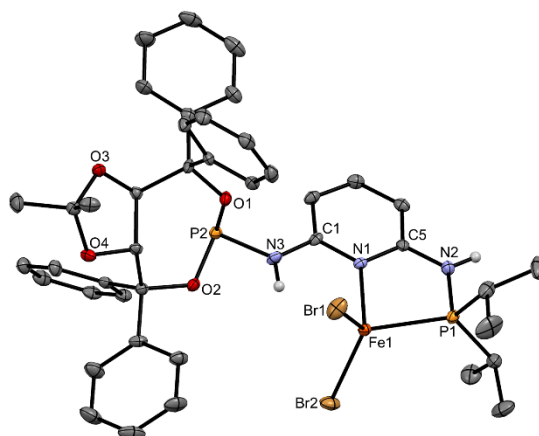


Figure 49: Structural view of showing $\text{Fe}(\kappa^2 P,N\text{-PNP-}i\text{Pr/TAD})\text{Br}_2$ (**6f**) 50% thermal ellipsoids (most H atoms and solvent molecules omitted for clarity). Only one of the two crystallographically independent complexes is shown. Selected bond lengths (Å) and bond angles (°): Fe1–Br1 2.3571(5), Fe1–Br2 2.3785(5), Fe1–P1 2.3776(8), Fe1–N1 2.125(2), N1–Fe1–P1 81.37(6), Br1–Fe1–Br2 117.78(2).

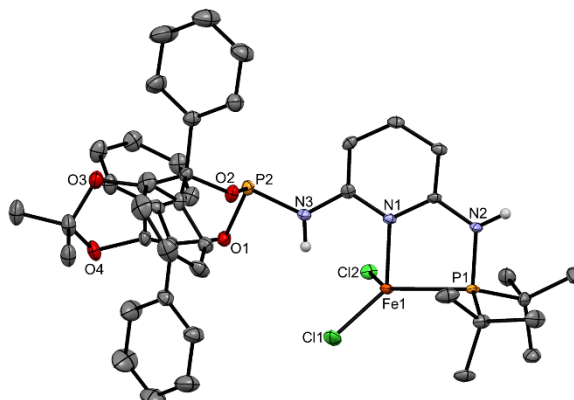


Figure 50: Structural view of showing $\text{Fe}(\kappa^2 P,N\text{-PNP-}t\text{Bu/TAD})\text{Cl}_2$ (**6g**) 50% thermal ellipsoids (most H atoms and solvent molecules omitted for clarity). Selected bond lengths (Å) and bond angles (°): Fe1–Cl1 2.2389(8), Fe1–Cl2 2.2453(8), Fe1–P1 2.4150(8), Fe1–N1 2.120(2), N1–Fe1–P1 80.43(5), Cl1–Fe1–Cl2 115.70(3).

The magnetic properties of **6e**, **6f**, **6g** and **6h** were investigated by means of SQUID magnetometry and Mössbauer spectroscopy. Magnetic moments of $\mu_{\text{eff}} = 4.95(1)$, $4.98(1)$, $4.97(1)$ and $5.00(1)$ μ_{B} for the complexes were derived from the temperature dependence of the inverse molar magnetic susceptibility, which was well described by a Curie law above 10 K (four unpaired electrons). These values are in good agreement with the effective magnetic moment of HS Fe(II) in the spin only approximation ($4.9 \mu_{\text{B}}$). The thermal variation of the inverse molar magnetic susceptibility and of $\chi_{\text{m}}T$ for all complexes is shown in Figure 51. Mössbauer spectroscopy of these complexes at 78 K showed isomer shifts (IS) of 0.76–0.79 mm/s and large quadrupole splittings (QS) in the range 2.93–3.22 mm/s (Table 9 and Figure 52). All spectra confirm the exclusive presence of HS Fe(II), with higher isomer shifts and

lower quadrupole splittings for the Cl complexes in comparison with the Br ones as was also the case for related Fe SN-complexes.

complex	T (K)	IS (mm/s)	QS (mm/s)	Fe(II)	geometry
Fe(κ^2P,N -PNP- <i>i</i> Pr,TAD)Cl ₂ (6e)	78	0.78(1)	2.93(1)	HS	tetrahedral
Fe(κ^2P,N -PNP- <i>i</i> Pr,TAD)Br ₂ (6f)	78	0.76(1)	3.14(1)	HS	tetrahedral
Fe(κ^2P,N -PNP- <i>t</i> Bu,TAD)Cl ₂ (6g)	78	0.79(1)	3.06(1)	HS	tetrahedral
Fe(κ^2P,N -PNP- <i>t</i> Bu,TAD)Br ₂ (6h)	78	0.77(1)	3.22(1)	HS	tetrahedral
<i>trans</i> -Fe(κ^3P,N,P -PNP- <i>i</i> Pr,TAD)(CO)Br ₂ (8j)	78	0.23(1)	1.19(1)	LS	octahedral
Fe(κ^3P,N,P -PNP- <i>i</i> Pr)Cl ₂ ^a	298	0.80(1)	2.56(1)	HS	square pyramidal
Fe(κ^2P,N -PN- <i>i</i> Pr)Cl ₂ ^b	298	0.680(2)	2.871(4)	HS	tetrahedral
Fe(κ^3N,N,N - ^{<i>i</i>} PrPDI)Cl ₂ ^c	80	0.89	2.40	HS	square pyramidal
Fe(κ^3N,N,N -HN{CH ₂ CH ₂ (P <i>i</i> Pr ₂)}Cl ₂ ^d	80	0.86	2.89	HS	square pyramidal
Fe(κ^3N,N,N -HN{CH ₂ CH ₂ (PCy ₂)}Cl ₂ ^d	80	0.86	2.98	HS	square pyramidal
Fe(κ^3N,N,N -HN{CH ₂ CH ₂ (P <i>t</i> Bu ₂)}Cl ₂ ^d	80	0.99	2.69	HS	square pyramidal
<i>trans</i> -Fe(κ^3P,N,P -PNP- <i>i</i> Pr)(CO)Cl ₂ ^a	298	0.15(1)	1.56(1)	LS	octahedral
<i>cis</i> -Fe(κ^3P,N,P -PNP- <i>i</i> Pr)(CO)Cl ₂ ^a	298	0.13(1)	1.09(1)	LS	octahedral

Table 9: Estimated hyperfine parameters from the ⁵⁷Fe Mössbauer spectra of **6e**, **6f**, **6g**, **6h** and **8j** collected at 78 K and related Fe(II) complexes. IS: isomer shift, QS: quadrupole splitting. ^a Reference^[53], PNP-*i*Pr = *N,N*-bis(diisopropylphosphino)-2,6-diaminopyridine. ^b Reference^[46a], PN-*i*Pr = *N*-diisopropylphosphino-2-aminopyridine, ^c Reference^[60], ^{*i*}PrPDI = 2,6-(2,6-*i*Pr₂C₆H₃N=CCH₃)₂C₅H₃N, ^d Reference^[61].

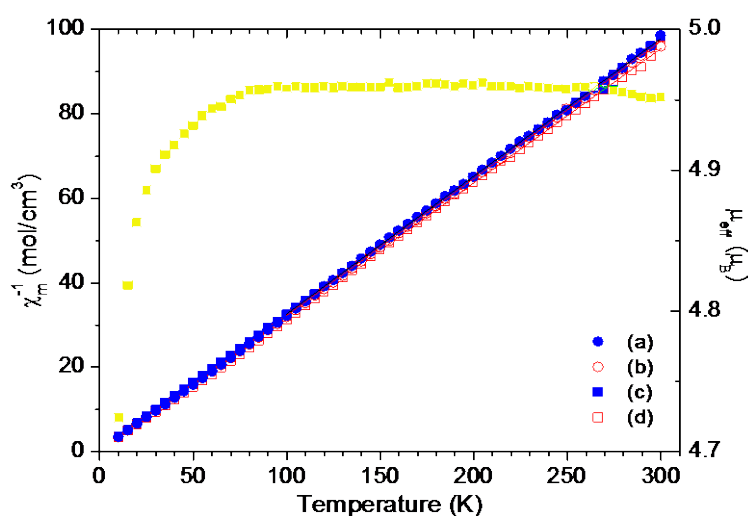


Figure 51: Temperature dependence of the inverse molar susceptibility of (a) Fe(κ^2P,N -PNP-*i*Pr,TAD)Cl₂ (**6e**), (b) Fe(κ^2P,N -PNP-*i*Pr/TAD)Br₂ (**6f**), (c) Fe(κ^2P,N -PNP-*t*Bu/TAD)Cl₂ (**6g**), and (d) Fe(κ^2P,N -PNP-*t*Bu/TAD)Br₂ (**6h**), and of the effective magnetic moment of the **6g** compound. The straight lines correspond to Curie law fittings to the experimental data.

As can be seen from Table 9, the isomer shift and quadrupole splitting values are different from those observed for high-spin Fe(II) complexes with similar ligands but different geometries. When compared to compounds with square pyramidal coordination, it can be noticed that all tetrahedral complexes exhibit lower IS and higher QS values^[53].

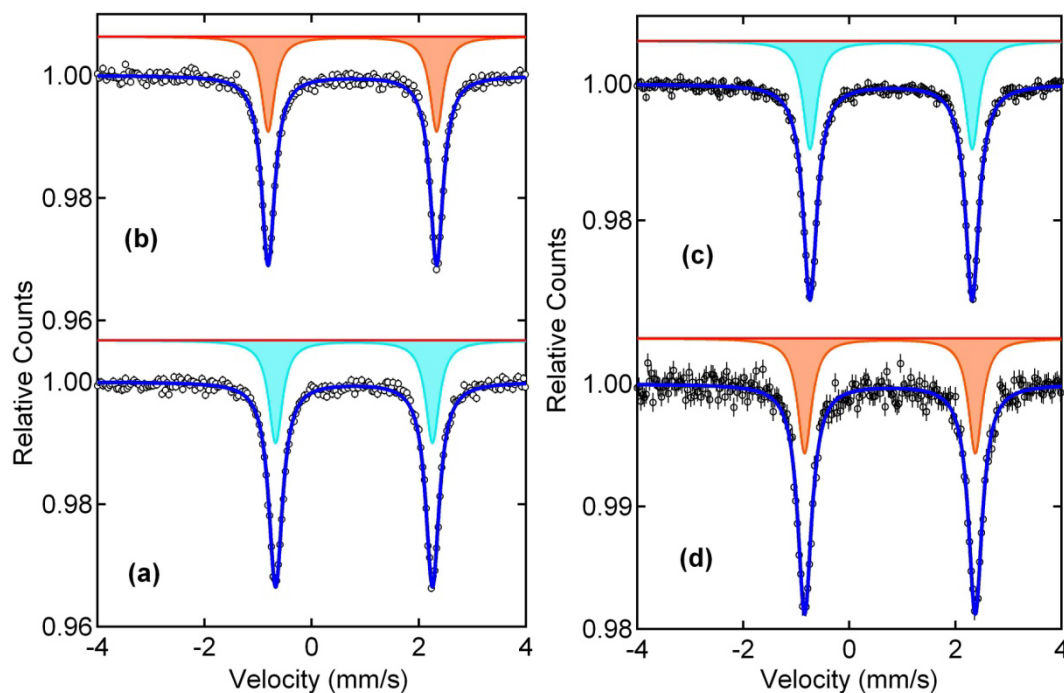


Figure 52: ^{57}Fe Mössbauer spectra of (a) $\text{Fe}(\kappa^2P,N\text{-}i\text{Pr/TAD})\text{Cl}_2$ (**6e**), (b) $\text{Fe}(\kappa^2P,N\text{-}i\text{Pr/TAD})\text{Br}_2$ (**6f**), (c) $\text{Fe}(\kappa^2P,N\text{-}t\text{Bu/TAD})\text{Cl}_2$ (**6g**) and (d) $\text{Fe}(\kappa^2P,N\text{-}t\text{Bu/TAD})\text{Br}_2$ (**6h**) collected at 78 K.

Additionally, complex $\text{Fe}(\kappa^2P,N\text{-PNP-}i\text{Pr/TAD})\text{Br}_2$ (**6f**) was investigated by powder XRD, in order to perform a phase analysis. Depicted in Figure 53, the pattern shows a good fitting between the calculated (red) and measured (blue) reflexes, meaning that complex **6f** crystallizes only in κ^2 -coordination.

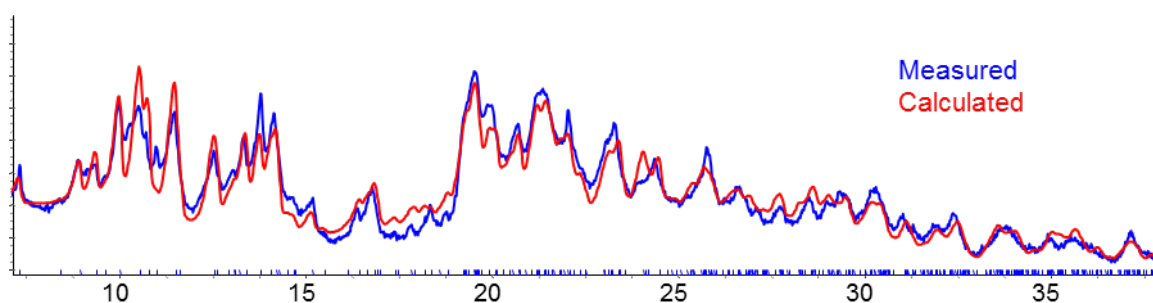


Figure 53: Powder XRD pattern of $\text{Fe}(\kappa^2P,N\text{-PNP-}i\text{Pr/TAD})\text{Br}_2$ (**6f**).

3.5.3 Solution studies

While the solid state structures of complexes **6e**, **6f**, **6g** and **6h** could be unequivocally established, due to the paramagnetic and complex nature of these compounds, the situation in solution turned out to be more difficult. It is not obvious whether these complexes are four or five coordinate containing κ^2P,N - or κ^3P,N,P -bond PNP ligands, respectively, or whether both species are present and, if this is the case, whether these are in equilibrium with one another. Accordingly, several experiments were performed to provide information on the solution structure and behaviour of **6e**, **6f**, **6g** and **6h**.

ESI-MS studies (in the positive ion mode) of complexes **6e**, **6f**, **6g** and **6h** in $\text{CH}_3\text{CN}/\text{CH}_3\text{OH}$ (9/1) solutions revealed that these complexes remain largely intact and fragments of the sodiated complexes of $\text{Fe}(\text{PNP-R/TAD})\text{X}_2$ ($[\text{M}+\text{Na}]^+$) were observed at m/z 868.2, 886.1, 892.2, and 984.1, respectively. Further abundant fragments are $[\text{M}-\text{X}]^+$ (**6e**, **6g**, **6h**), $[\text{M}-\text{X}+\text{CH}_3\text{OH}]^+$ (**6e**, **6g**), and $[\text{M}-\text{X}-\text{HX}+\text{CH}_3\text{OH}]^+$ (**6g**) revealing the high affinity of CH_3OH towards these Fe(II) complexes. A representative positive ion ESI full scan mass spectra of **6f** is depicted in Figure 54. In the inset, the isotopic pattern of the $[\text{M}+\text{Na}]^+$ ion is compared with the theoretical pattern, which turned out to correlate quite well.

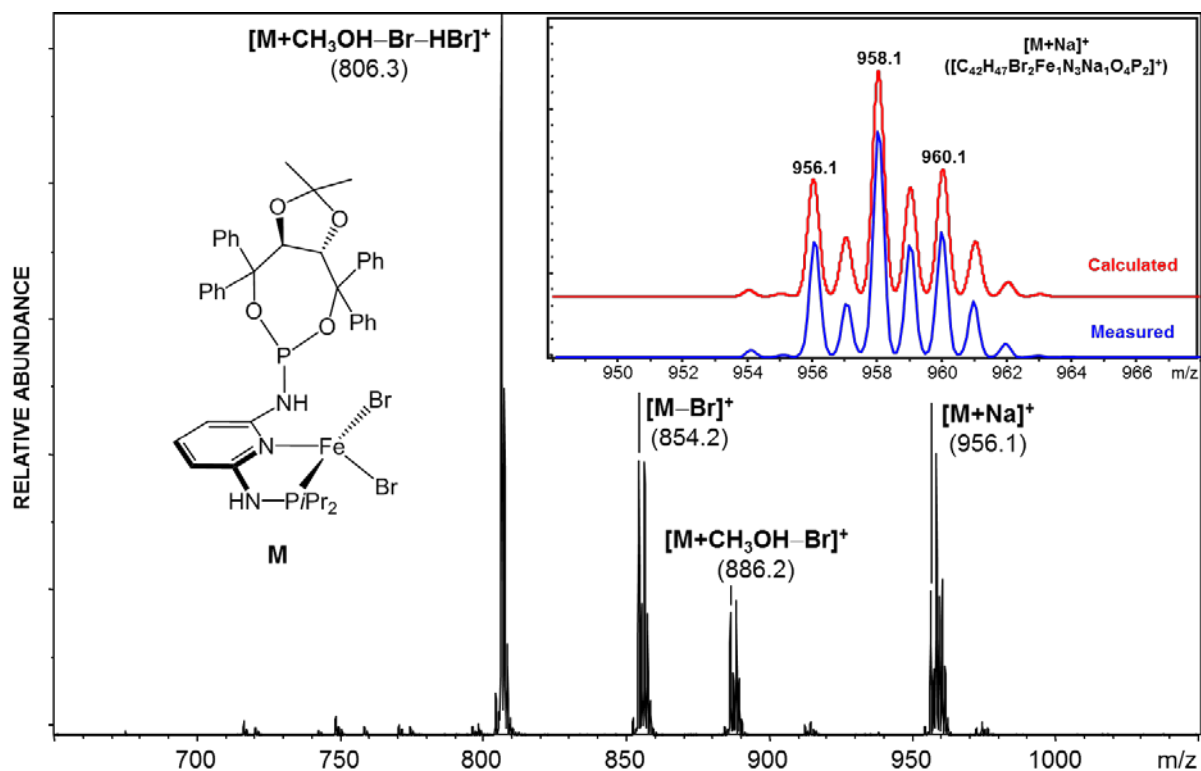
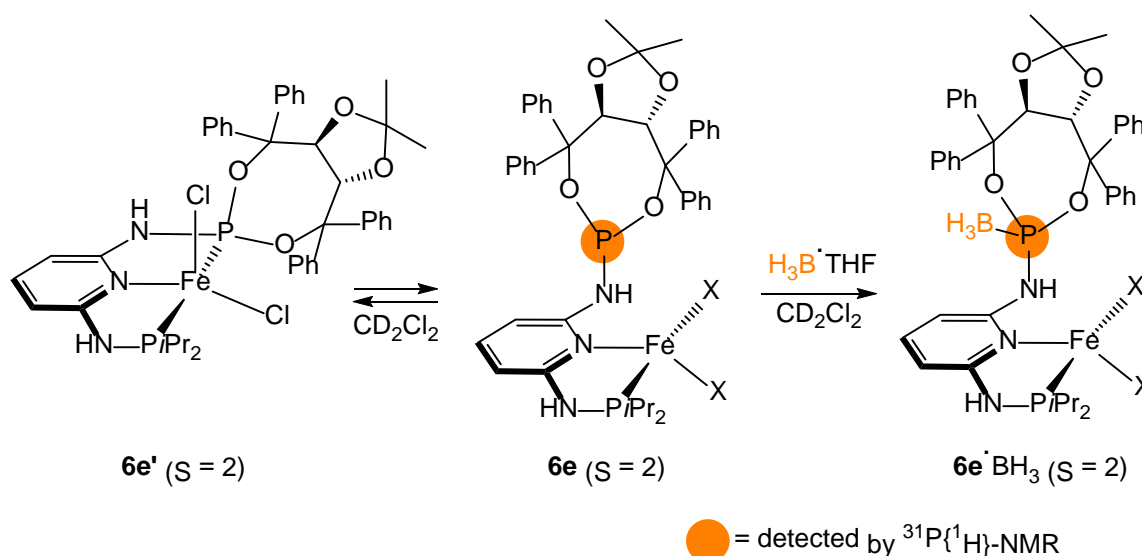


Figure 54: Positive ion ESI full scan mass spectrum of $\text{Fe}(\text{PNP-}iPr/\text{TAD})\text{Br}_2$ (**6f**) in $\text{CH}_3\text{OH}/\text{CH}_3\text{CN}$ (9/1). Inset shows the calculated and measured isotopic pattern of the sodiated complex $\text{Fe}(\text{PNP-}$

*i*Pr/TAD)Br₂ ([M+Na]⁺). Only signals containing the Fe isotopes of highest abundance (⁵⁶Fe) are annotated.

All complexes display large paramagnetic shifted ¹H and ¹³C{¹H}-NMR solution spectra with broad and featureless signals which, due to the complexity of the PNP ligands, were not assignable and thus not informative. Interestingly, while at room temperature no ³¹P{¹H}-NMR signals could be detected, at -50°C complexes **6e**, **6f**, **6g** and **6h** exhibit a broad signal at about 126 ppm, assignable to the non-coordinated TAD arm of the κ²*P,N*-bond PNP-R/TAD ligands (*cf* 134.6 and 132.4 ppm for the free ligands **4h** and **4i**). This observation clearly points to an equilibrium between κ²*P,N*- and κ³*P,N,P*-bound species, i.e., the PNP-R/TAD ligand is hemilabile, which is also supported by DFT calculations (*vide infra*). Related solution equilibria were proposed for the pincer complex Fe(PONOP-*t*Bu)Cl₂ bearing the bulky *bis*-phosphite PONOP-*t*Bu ligand^[62]. Moreover, addition of BH₃·THF to a solution of **6e** in CD₂Cl₂ leads to boronation of the pendant TAD arm shifting the equilibrium towards the four-coordinate complex Feκ²*P,N*-PNP-*i*Pr/TAD^{BH₃})Cl₂ (**6e**·BH₃) (Scheme 38). ³¹P{¹H}-NMR spectra of these studies are shown in Figure 55.



Scheme 38: Solution equilibria and boronation of Fe(κ²*P,N*-PNP-*i*Pr/TAD)Cl₂ (**6e**) with BH₃·THF in CD₂Cl₂.

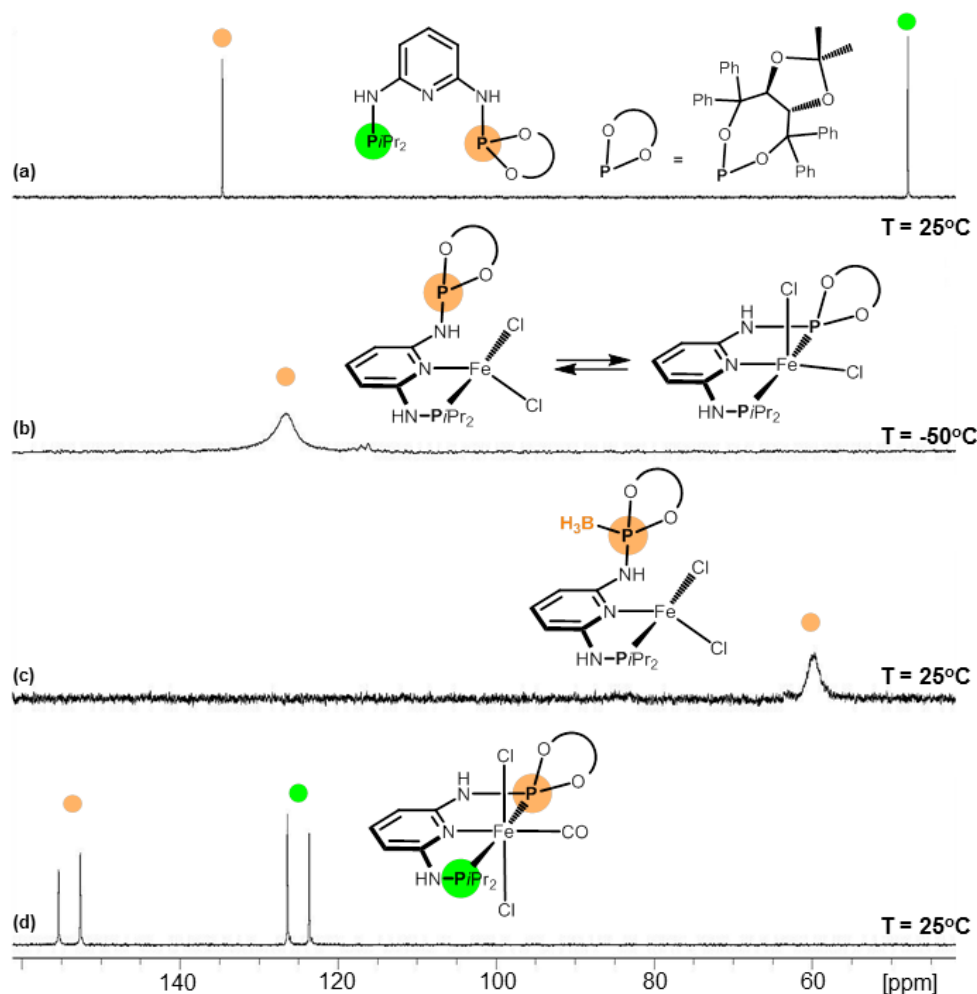


Figure 55: $^{31}\text{P}\{^1\text{H}\}$ -NMR spectra of (a) PNP-*i*Pr/TAD (**4h**), (b) $\text{Fe}(\kappa^2\text{-P,N-PNP-}i\text{Pr/TAD})\text{Cl}_2$ (**6e**), (c) $\text{Fe}(\kappa^2\text{-P,N-PNP}^{\text{BH}_3}\text{-}i\text{Pr/TAD})\text{Cl}_2$ (**6e-BH}_3**), (d) *trans*- $\text{Fe}(\text{P,N,P-PNP-}i\text{Pr/TAD})(\text{CO})\text{Cl}_2$ (**8i**) in CD_2Cl_2 (spectra of (b) and (c) are referenced internally to PPh_3 set to -5.6 ppm).

3.5.4 Reaction with CO and CH_3CN

When CO was bubbled into acetone solutions of **6e** and **6f** for a few minutes, an immediate colour change from pale yellow to violet and blue, respectively, was observed due to formation of *trans*- $\text{Fe}(\kappa^3\text{-P,N,P-PNP-}i\text{Pr/TAD})(\text{CO})\text{Cl}_2$ (**8i**) and *trans*- $\text{Fe}(\kappa^3\text{-P,N,P-PNP-}i\text{Pr/TAD})(\text{CO})\text{Br}_2$ (**8j**) (Scheme 39). Pure crystalline materials had to be obtained by diffusion of *n*-pentane into a THF solution of **8i** and **8j**, respectively, since evaporation of the solvent resulted in rapid CO loss and reformation of **6e** and **6f**. In the case of the bulkier *t*Bu complexes **6g** and **6h**, no CO addition was observed. The same behaviour was found for $\text{Fe}(\text{PNP-}t\text{Bu})\text{X}_2$. Noteworthy, in the solid state none of the tetrahedral complexes underwent CO addition, in contrast to the reactions of the five coordinate complexes $\text{Fe}(\text{PNP-}i\text{Pr})\text{X}_2$

reported previously^[63]. Complexes **8i** and **8j** were fully characterized by ¹H, ¹³C{¹H} and ³¹P{¹H}-NMR spectroscopy. The ³¹P{¹H}-NMR spectra give rise to two doublets centered at 154.0/125.0 and 161.6/125.2 ppm, respectively, with large ²J_{PP} coupling constants of 278 and 261 Hz which are consistent with a *trans*-P,P configuration (Figure 55, (d)). In the ¹³C{¹H}-NMR spectra the CO ligands exhibit a single low-intensity doublet of doublet resonance at 220.3 and 222.5 ppm. Complexes **8i** and **8j** give rise to one band at 1986 and 1980 cm⁻¹ in the IR spectrum (*cf* 2143 cm⁻¹ in free CO). For comparison, in *trans*-Fe(PNP-*i*Pr)(CO)Cl₂ and *trans*-Fe(PNP-*i*Pr)(CO)Br₂ the CO-stretching frequency is observed at 1956 cm⁻¹, indicating that PNP-*i*Pr/TAD is a weaker donor than PNP-*i*Pr.

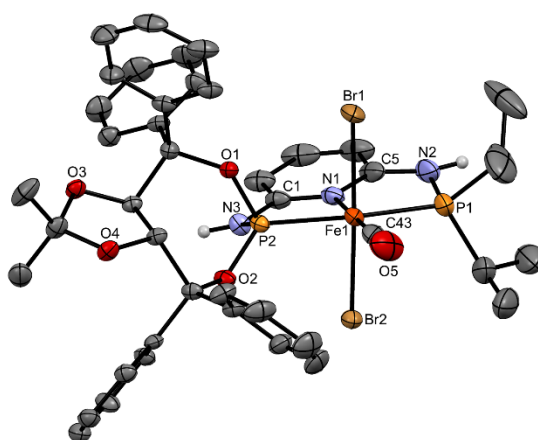


Figure 56: Structural view of showing Fe(κ^3P,N,P -PNP-*i*Pr/TAD)(CO)Br₂ (**8j**) 50% thermal ellipsoids (most H atoms and solvent molecules omitted for clarity). Selected bond lengths (Å) and bond angles (°): Fe1–Br1 2.4508(9), Fe1–Br2 2.4482(8), Fe1–C43 1.766(4), Fe1–P1 2.258(1), Fe1–P2 2.201(1), Fe1–N1 1.996(3), P1–Fe1–P2 163.91(4), N1–Fe1–C43 179.3(1), Br1–Fe1–Br2 177.33(2).

Heating solid samples of **8i** and **8j** leads to regeneration of complexes Fe(κ^2P,N -PNP-*i*Pr/TAD)Cl₂ (**6e**) and Fe(κ^2P,N -PNP-*i*Pr/TAD)Br₂ (**6f**). However, loss of CO is slow with about 80% conversion after 2h. The Mössbauer spectra of the complex **8j** before and after being partially decarbonylated (by heating at 100°C for 1h and 2h under vacuum) are shown in Figure 57. The spectrum of **8j** is well fitted to a quadrupole doublet with IS = 0.23(1) mm/s and QS = 1.19(1) mm/s assignable to a typical low spin Fe(II) complex in a symmetric octahedral environment. The isomer shift decrease observed from **6f** to **8j** is explained by the HS-LS change induced by the reaction with CO. Accordingly, the decrease in the quadrupole splitting values is explained by the much less asymmetric environment of Fe(II) in six coordination (**8j**) than in four coordination (**6f**).

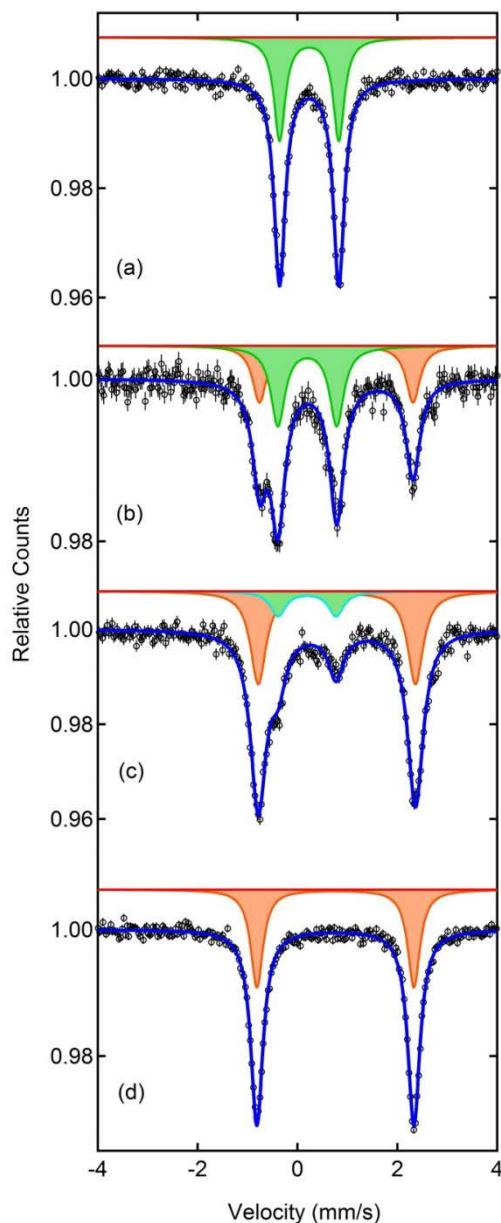
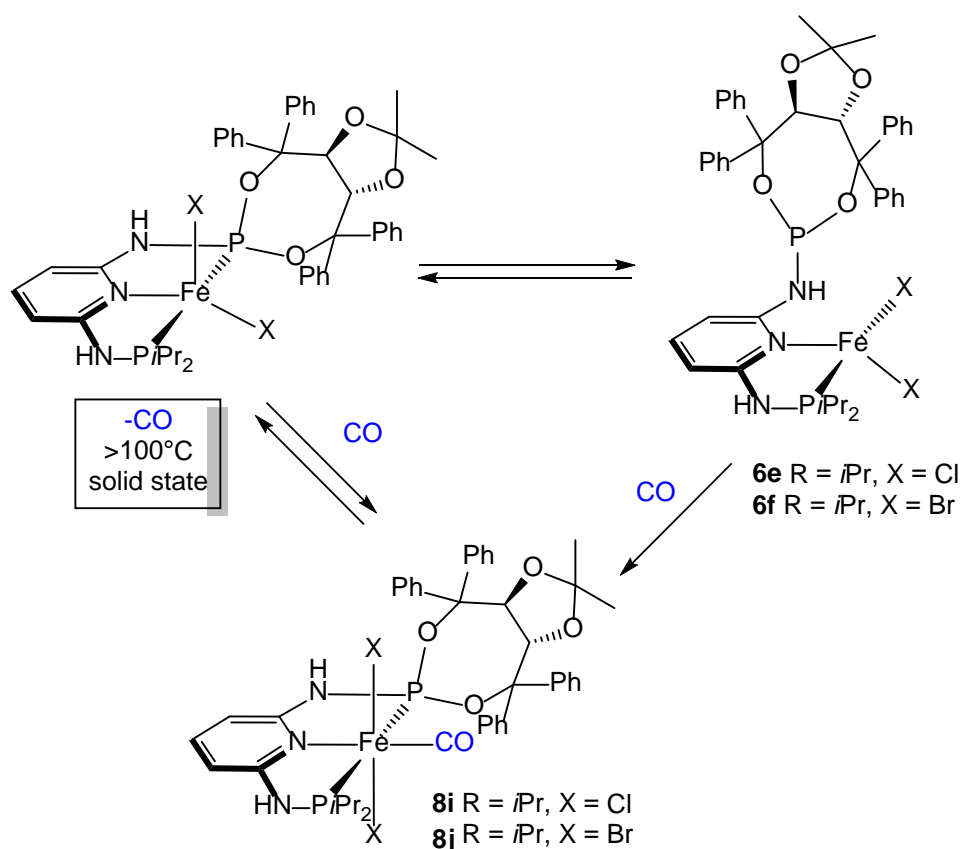


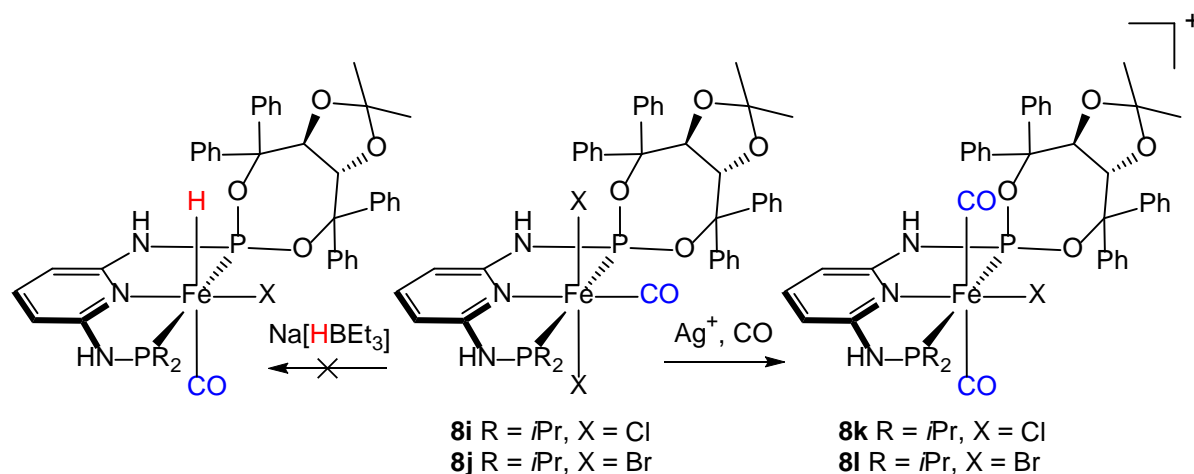
Figure 57: ^{57}Fe Mössbauer spectra collected at 78 K of (a) $\text{trans-Fe}(\kappa^3P,N\text{-PNP-}i\text{Pr/TAD})(\text{CO})\text{Br}_2$ (**8j**), (b) and (c) $\text{trans-Fe}(\kappa^3P,N\text{-PNP-}i\text{Pr/TAD})(\text{CO})\text{Br}_2$ (**8j**) after heating for 1h and 2h at 100°C under vacuum, respectively, and (d) $\text{Fe}(\kappa^3P,N\text{-PNP-}i\text{Pr/TAD})\text{Br}_2$ (**6f**).

When compared with the hyperfine parameters of **8j** spectrum (Table 9), it can be deduced that 60% and 21% of this contribution remains unreacted in the 1h and 2h annealed samples, respectively. A second doublet appears in these partially decarbonylated samples, displaying hyperfine parameters of $IS = 0.78(1)$ mm/s, $QS = 3.07(2)$ mm/s and $IS = 0.79(1)$ mm/s, $QS = 3.15(1)$ mm/s, for the 1h and 2h annealed samples, respectively. As can be seen from Table 9, the isomer shifts and quadrupole splitting values of $\text{Fe}(\kappa^2P,N\text{-PNP-}i\text{Pr/TAD})\text{Br}_2$ (**6f**), indicating that at higher temperatures the CO release in the solid state does not induce the formation of the pentacoordinated $\text{Fe}(\kappa^3P,N,P\text{-PNP-}i\text{Pr/TAD})\text{Br}_2$ complex.



Scheme 39: Reaction of $\text{Fe}(\text{PNP-}i\text{Pr/TAD})\text{X}_2$ (**6e**, **6f**) with CO in solution forming *trans*- $\text{Fe}(\kappa^3\text{P,N,P-PNP-}i\text{Pr/TAD})(\text{CO})\text{X}_2$ (**8i**, **8j**).

Treatment of **6e** and **6f** or **8i** and **8j**, respectively, with 1 equiv AgSbF_6 in THF in the presence of CO at room temperature afforded selectively the cationic complexes *trans*- $[\text{Fe}(\kappa^3\text{P,N,P-PNP-}i\text{Pr/TAD})(\text{CO})_2\text{X}]^+$ (**8k**, **8l**), in 80 and 81% isolated yields (Scheme 40). These complexes are thermally robust red solids that are air stable both in the solid state and in solution for several days. In the $^{13}\text{C}\{^1\text{H}\}$ -NMR spectrum the two CO ligands are chemically and magnetically not equivalent thus giving rise to two low intensity doublet of doublet resonances centered at about 207 ppm. In the IR spectrum the CO ligands exhibit only one band at 2026 and 2021 cm^{-1} for the mutually *trans* CO ligands which can be assigned to the asymmetric CO stretching frequency. The symmetric CO stretching band is IR inactive and thus not observed.



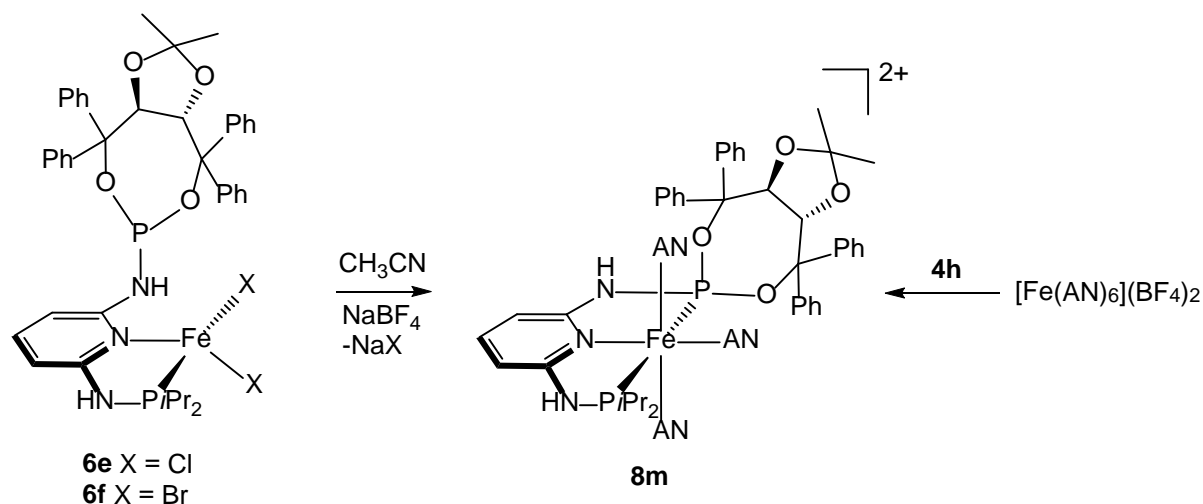
Scheme 40: Reaction of $\text{Fe}(\kappa^3P,N,P\text{-}i\text{Pr/TAD})(\text{CO})\text{X}_2$ (**8i**, **8j**) with CO in the presence of Ag^+ forming $\text{trans-Fe}(\kappa^3P,N,P\text{-PNP-}i\text{Pr/TAD})(\text{CO})_2\text{X}]^+$ (**8k**, **8l**) and attempted reaction with $\text{Na}[\text{HBEt}_3]$.

Since the hydride complex $\text{Fe}(\text{PNP-}i\text{Pr})(\text{CO})(\text{H})\text{Br}$ turned out to be an efficient hydrogenation catalyst for both ketones and aldehydes^[25], it was attempted to prepare chiral hydride complexes of the type $\text{Fe}(\kappa^3P,N,P\text{-PNP-}i\text{Pr/TAD})(\text{CO})(\text{H})\text{X}$ following an established procedure. However, treatment of **8i** or **8j** with $\text{Na}[\text{HBEt}_3]$ lead to decomposition and the only tractable product could be isolated were the free PNP ligands.

Finally, the reaction of the complexes **6e-h** with CH_3CN was investigated. Upon dissolving the complexes in deuterated acetonitrile, $^{31}\text{P}\{^1\text{H}\}$ -NMR spectra were measured. While the more bulky complexes featuring the PNP-*t*Bu/TAD ligands did not show any reaction, therefore no phosphorous signal could be detected, the complexes **6e** and **6f** were transformed to the cationic diamagnetic complexes with the formula $[\text{Fe}(\kappa^3P,N,P\text{-PNP-}i\text{Pr/TAD})]\text{X}_2$ (Scheme 41). This reaction was found to be fully reversible, evaporation of the solvent lead to starting material. In order to isolate the product complex, the counter ion was exchanged by the addition of NaBF_4 . Alternatively, treatment of iron precursor $[\text{Fe}(\text{AN})_6](\text{BF}_4)_2$ with 1 equiv PNP-*i*Pr/TAD (**4h**) afforded the identical complex in comparable yield as orange air sensitive solid. Analogously, the same reaction with the PNP-*t*Bu/TAD ligand (**4i**) did not yield in the product but only free PNP ligand was found in NMR spectra.

The compound was characterized by ^1H , $^{31}\text{P}\{^1\text{H}\}$ and $^{13}\text{C}\{^1\text{H}\}$ -NMR. Lability of the AN ligands was visible in ^1H -NMR, since an exchange between the coordinated CH_3CN and solvent CD_3CN was observed by a decreased signal for the coordinated AN. In $^{31}\text{P}\{^1\text{H}\}$ -NMR spectra two sets of doublets were visible, displaying a characteristic large $^2J_{\text{PP}}$ coupling constant of 243.6 Hz, giving rise to a *trans* configuration. The doublets are centred at 154.1 and 114.8 ppm for the TAD and *i*Pr arm, respectively. Interestingly, the halide ligands proved to be much more labile than compared to the $\text{Fe}(\text{PNP-}i\text{Pr})\text{X}_2$ complexes where the chloride

complex $\text{Fe}(\text{PNP-}i\text{Pr})\text{Cl}_2$ showed no reaction with CH_3CN , and the analogue bromide complex still featured high-spin starting material in considerable amount.



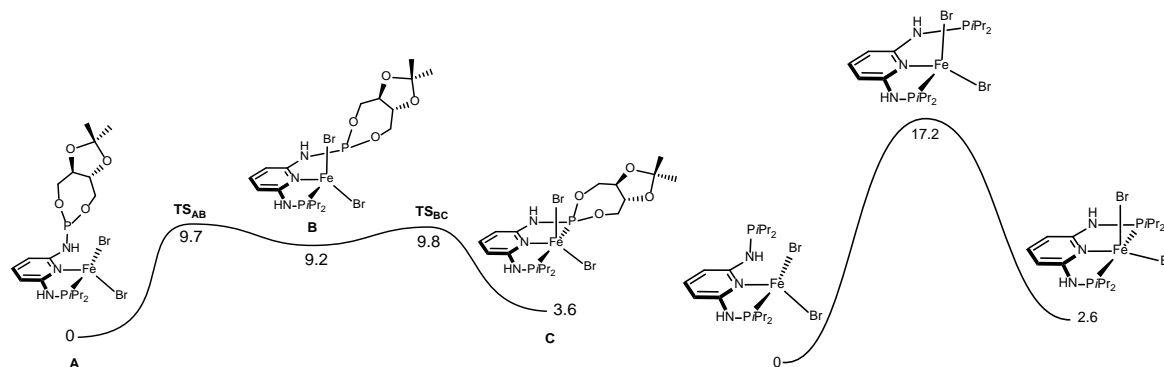
Scheme 41: Reaction of complexes **6e** and **6f** with CH_3CN .

3.5.5 Computational studies

The change in coordination of the PNP ligand from a κ^2P,N to a κ^3P,N,P mode was investigated by means of DFT calculations^[64], using a model of complex **6f** ($R = i\text{Pr}$, $X = \text{Br}$) with a simplified TADDOL moiety (TAD'). In the model the phenyl groups were replaced by H-atoms for computational expediency. The energy profile for the rearrangement between the four-coordinated complex with a κ^2P,N -PNP ligand (**A**) and the pentacoordinated species with a κ^3P,N,P -PNP ligand (**C**) is shown in Scheme 42.

The mechanism for the coordination of the second P-atom in $\text{Fe}(\text{PNP-}i\text{Pr/TAD}')\text{Br}_2$ comprises two steps. The first is re-orientation of the pendant arm of the PNP ligand in the reactant, with rotation along the $\text{C}_{\text{py}}\text{-N}_{\text{NH}}$ bond. In the second step, the P-atom coordinates the metal. The overall process has an energy barrier of 9.8 kcal/mol (corresponding to **TS_{BC}**) and indicates a facile process that should occur easily at room temperature. This is in agreement with $^{31}\text{P}\{^1\text{H}\}$ -NMR studies (Figure 55). Since the five-coordinated isomer **C** is only 3.6 kcal/mol less stable than the initial complex **A**, the profile in Scheme 42 suggests that an equilibrium between the two forms may occur in solution. Importantly, the performance of the model used in the calculations was tested through the comparison of the stability difference

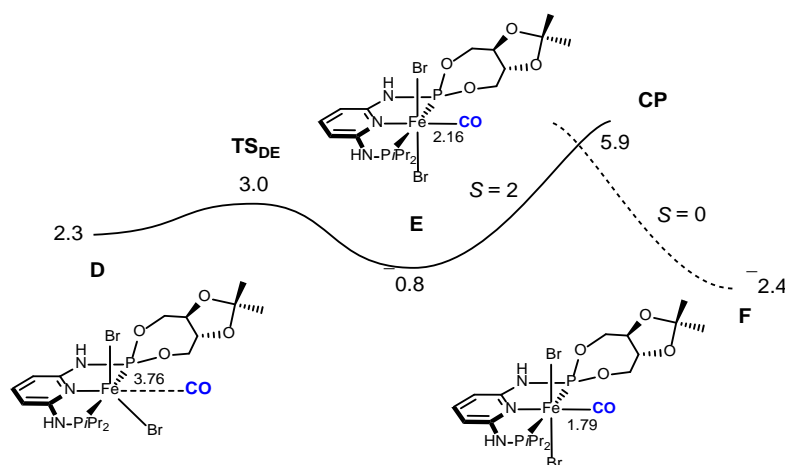
obtained for the two isomers calculated with the real species, that is, with full TADDOL fragments in the PNP ligands.



Scheme 42: Energy profile (kcal/mol) for the rearrangement between κ^2P,N and κ^3P,N,P in $\text{Fe}(\text{PNP-}i\text{Pr/TAD})\text{Br}_2$ and comparison with $\text{Fe}(\text{PNP-}i\text{Pr})\text{Br}_2$

The results indicate that the four-coordinated species is more stable than its five-coordinated counterpart by 2.8 kcal/mol, a value that is only 0.8 kcal/mol smaller than the one obtained with the simplified model and validates the use of that model in the calculations. For comparison, the equilibrium between $\text{Fe}(\kappa^3P,N,P\text{-PNP-}i\text{Pr})\text{Br}_2$ and $\text{Fe}(\kappa^2P,N\text{-PNP-}i\text{Pr})\text{Br}_2$ was also investigated (Scheme 42). This process proceeds via a single step but with a single step but with a considerably higher barrier of 17.2 kcal/mol and agrees with the fact experimentally no $\text{Fe}(\kappa^2P,N\text{-PNP-}i\text{Pr})\text{Br}_2$ complex was detected. These results may also suggest that the hemilability of the PNP-R/TAD ligands is not due to steric but electronic reasons.

The energy profile calculated for CO addition to the five-coordinated complex $\text{Fe}(\kappa^3P,N,P\text{-PNP-}i\text{Pr/TAD}')\text{Br}_2$ is represented in Scheme 43. The first step of the mechanism occurs in the spin quintet ($S = 2$) potential energy surface (PES). Starting point is the pair of reactants **D**, *i.e.*, the five-coordinated complex and one CO molecule. From **D** CO addition occurs in a single step going through a rather early transition state (**TS_{DE}**) with a long Fe-C_{CO} bond distance (3.01 Å) indicating that CO coordination is only starting once that transition state is reached.



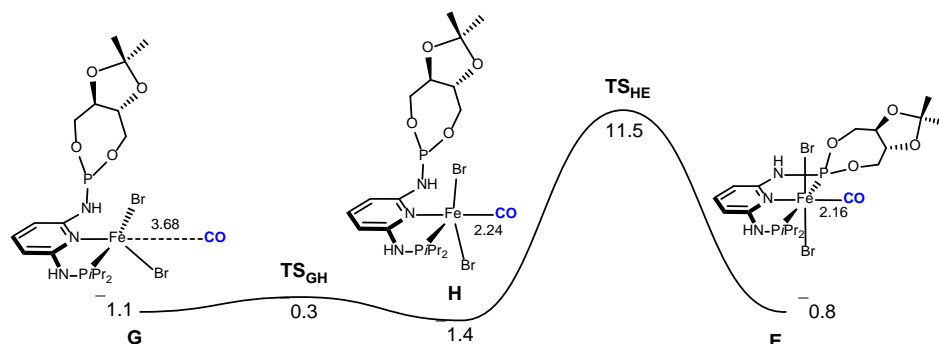
Scheme 43: Energy profile (kcal/mol) for the reaction of CO addition to $\text{Fe}(\kappa^3P,N,P\text{-}i\text{Pr/TAD})\text{Br}_2$. The energy values are referred to **A** and the Fe-C_{CO} distances (Å) are indicated. The full curve corresponds to the $S = 2$ potential energy surface (PES), and the dashed curve corresponds to the $S = 0$ PES.

In the resulting intermediate **E** CO coordination is established with a Fe-C_{CO} distance of 2.16 Å. This step is thermodynamically favorable ($\Delta E = -3.1$ kcal/mol) and has a negligible barrier of 0.7 kcal/mol. Since the product of the reaction is the low spin ($S = 0$) CO adduct **F**, there must be a spin change from the quintet to the singlet spin PES in the last step of the mechanism. In other words, this is a “spin forbidden” or “non-adiabatic” reaction and, thus, the change between PES occurs through a minimum-energy crossing point (MECP). In the MECP both the geometry and the energy of the molecules are the same in the two PES. Once that point is reached along the reaction coordinate there is a given probability for the system to change spin state and hop from one spin state to the other, completing the “spin-forbidden” reaction. Accordingly, in the last step of the mechanism depicted in Scheme 7, the high spin CO complex, **E** ($S = 2$), changes to its low spin isomer, **F** ($S = 0$), through a crossing point (**CP**) that has an intermediate geometry between the two CO species. The moderate energy barrier associated with the spin exchange (6.7 kcal/mol) reflects the small geometry modifications associated with this step. The final product **F** is 2.4 kcal/mol more stable than the initial reagent, the four-coordinated species $[\text{Fe}(\kappa^2P,N\text{-PNP-}i\text{Pr,TAD}')\text{Br}_2]$ (**A**).

From the two profiles it becomes clear that the most difficult process along the path is coordination of the second P-atom of the PNP ligand, rather than CO addition or spin change. In fact, the highest barrier along the entire mechanism is associated with TS_{BC} , *i.e.*, the step corresponding to the coordination of the dangling P-atom, from **B** to **C** (see Scheme 40).

An alternative mechanism is CO addition to the four coordinated complex $\text{Fe}(\kappa^2P,N\text{-PNP-}i\text{Pr/TAD}')\text{Br}_2$ followed by a subsequent change in the coordination mode of the PNP ligand

from κ^2P,N to κ^3P,N,P with coordination of the free P-atom. The energy profile for this process is depicted in Scheme 44.



Scheme 44: Energy profile (kcal/mol) for the reaction of CO addition to $\text{Fe}(\kappa^2P,N\text{-PNP-}i\text{Pr/TAD})\text{Br}_2$ followed by exchange of the coordination of the pincer ligand from κ^2P,N to κ^3P,N,P . The energy values are referred to **A**, and the Fe-C_{CO} distances (\AA) are indicated.

The mechanism starts with a pair of non-interacting reactants **G**, the CO molecule and the $\text{Fe}(\kappa^2P,N\text{-PNP-}i\text{Pr,TAD}')\text{Br}_2$ complex. In the first step there is CO addition and formation of a five-coordinated CO complex **H** that maintains the PNP dangling arm existing in the initial complex. A rather long Fe-C_{CO} distance of 2.80 \AA in the corresponding transition state (**TS_{GH}**) indicates that CO coordination is just beginning when **TS_{GH}** is reached along the reaction coordinate. This step occurs with a very small barrier of only 0.8 kcal/mol and the intermediate **H** formed is only 0.3 kcal/mol more stable than the initial reagents. In the second step of the mechanism, from **H** to **E**, there is coordination of the P-atom of the PNP ligand, originating the high spin six-coordinated CO complex. Coordination of the P-atom in the CO species occurs in a single step, from **H** to **E**, through the transition state **TS_{HE}**. In **TS_{HE}**, formation of the new Fe-P bond is still far from complete, as indicated by a distance of 3.64 \AA , which is 1.08 \AA longer than the coordination distance in **E**. This step is practically thermoneutral ($\Delta E = 0.6$ kcal/mol) and the corresponding barrier (12.9 kcal/mol) is the highest of that path.

In the first mechanism, coordination of the loose P-atom of the pincer ligand, with the corresponding change from κ^2P,N to κ^3P,N,P occurs first and it is followed by CO addition. This path corresponds to the profiles represented in Scheme 42, and its highest barrier is 9.8 kcal/mol. In the second path, the order of the processes is reversed. First there is addition of CO to the four-coordinated complex with $\kappa^2P,N\text{-PNP}$, and only then occurs coordination of the free P-atom. The highest barrier obtained for this case, associated with the P-

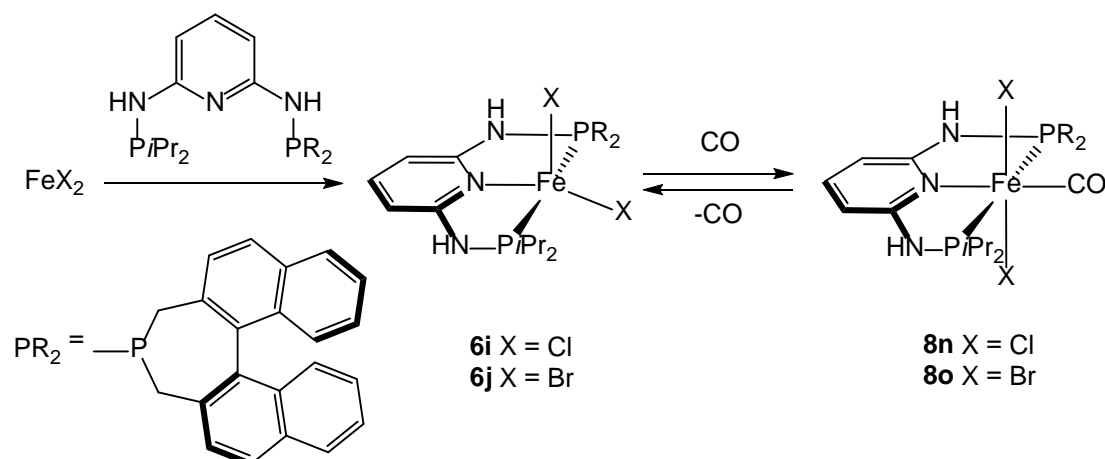
coordination step (**TS_{HE}** in Scheme 9), is 12.9 kcal/mol and slightly higher by 3.1 kcal/mol than the barrier associated with the first mechanism. Therefore, the first mechanism should be slightly favored.

This trend is supported by the fact that, despite their relatively low formal electron count, the related four coordinate complexes $\text{Fe}(\kappa^2 P, N\text{-PN-}i\text{Pr})\text{X}_2$ ($\text{PN-}i\text{Pr} = N\text{-diisopropylphosphino-2-aminopyridine}$) did not react with CO at ambient temperature^[46a], while pentacoordinate complexes $\text{Fe}(\kappa^3 P, N, P\text{-PNP-}i\text{Pr})\text{X}_2$ readily added CO to give octahedral complexes of the type $\text{Fe}(\kappa^3 P, N, P\text{-PNP-}i\text{Pr})(\text{CO})\text{X}_2$. In general, the outcome of a CO addition to high spin iron(II) complexes depends on the geometry and coordination number, the key factor being the overall ligand field of the ensemble of ligands in the reactant. Accordingly, the lower the coordination number the less likely CO addition will take place and reactions will be disfavoured^[19].

3.6 BINEP-PNP iron(II) complexes

3.6.1 Synthesis

BINEP complexes were prepared analogously to $\text{Fe}(\text{PNP}^R\text{-}i\text{Pr})\text{X}_2$ complexes by treatment of FeX_2 ($\text{X} = \text{Cl}, \text{Br}$) with the chiral ligand PNP-*i*Pr/BIN (**4j**) (Scheme 45). The complexes $\text{Fe}(\text{PNP-}i\text{Pr}/\text{BIN})\text{Cl}_2$ (**6i**) and $\text{Fe}(\text{PNP-}i\text{Pr}/\text{BIN})\text{Br}_2$ (**6j**) were isolated as bright yellow powder in good yields (84-87%) and are sensitive to air/moisture, especially in solution. Characterization by ¹H-NMR-spectroscopy was carried out, but no essential information could be obtained due to the paramagnetic behaviour of the complexes **6i** and **6j**.



Scheme 45: Synthesis of $\text{Fe}(\text{PNP-}i\text{Pr})\text{Cl}_2$ (**6i**), $\text{Fe}(\text{PNP-}i\text{Pr}/\text{BIN})\text{Br}_2$ (**8j**) and the reversible addition of CO.

In order to reduce costs during optimization of synthetic parameters, the ligand synthesis and complexation reaction was first performed with the racemic substrate. While it was possible to grow single crystals, suitable for XRD analysis, all attempts failed for the chiral complexes. Therefore in Figure 58, the molecular structure of the *racemic* product is depicted, which is also indicated by the space group $I4_1/a$. The bond lengths and angles are similar to other $\text{Fe}(\text{PNP})\text{X}_2$ complexes.

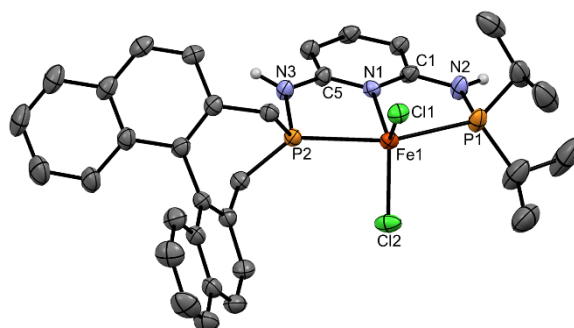
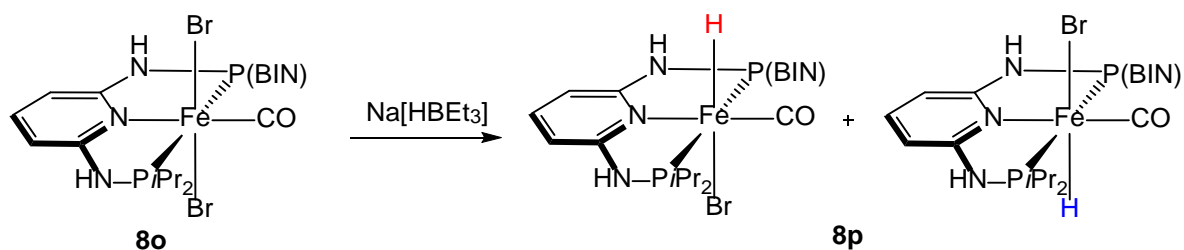


Figure 58: Structural view of showing *rac*- $\text{Fe}(\text{PNP-}i\text{Pr}/\text{BIN})\text{Cl}_2$ (**6i**) 50% thermal ellipsoids (most H atoms and solvents molecules omitted for clarity). Selected bond (\AA) and bond angles ($^\circ$): Fe1–Cl1 2.3057(8), Fe1–Cl2 2.3366(9), Fe1–P1 2.4853(9), Fe1–P2 2.5150(9), Fe1–N1 2.141(2), Cl1–Fe1–Cl2 130.99(3), Cl1–Fe1–P1 97.69(3), Cl2–Fe1–P2 92.32(3), P1–Fe1–P2 159.16(3), Cl1–Fe1–P1–N2 130.5(1), Cl2–Fe1–P1–N2 97.0(1).

3.6.2 Synthesis of chiral hydride

Depicted in Scheme 45, the coordinatively unsaturated complexes **6i** and **6j** react with CO to form the diamagnetic, octahedral complexes $\text{Fe}(\text{PNP-}i\text{Pr}/\text{BIN})\text{COCl}_2$ (**8n**) and $\text{Fe}(\text{PNP-}i\text{Pr}/\text{BIN})\text{COBr}_2$ (**8o**), respectively. Isolation of the pure CO-complexes was however not possible, since the compounds slowly released CO when the solvent was evaporated, forming again starting material. Therefore, the complexes were synthesized *in situ* by bubbling CO for 3 min in a solution of **6i** or **6j**.



Scheme 46: Synthesis of chiral hydride species Fe(PNP-*i*Pr/BIN)(H)(CO)Br (**8p**).

The obtained deep blue solutions were then directly used for the next step, the exchange of one halide to form the hydride species by addition of Na[HB(Et)₃] in small excess (Scheme 46). Though the synthetic parameters are already known and published by our group^[25], the outcome was somehow different. A considerable amount of free ligand was found in ³¹P{¹H}-NMR spectra, the yield was significantly low (40-50%) and decomposition slowly takes place in solution, regardless of the solvent. Due to this difficulties, the complete purification and characterization was not successful. Nevertheless, the product was identified by ¹H-NMR in the high field region, where the hydride-signal was to be expected, shown in Figure 59:

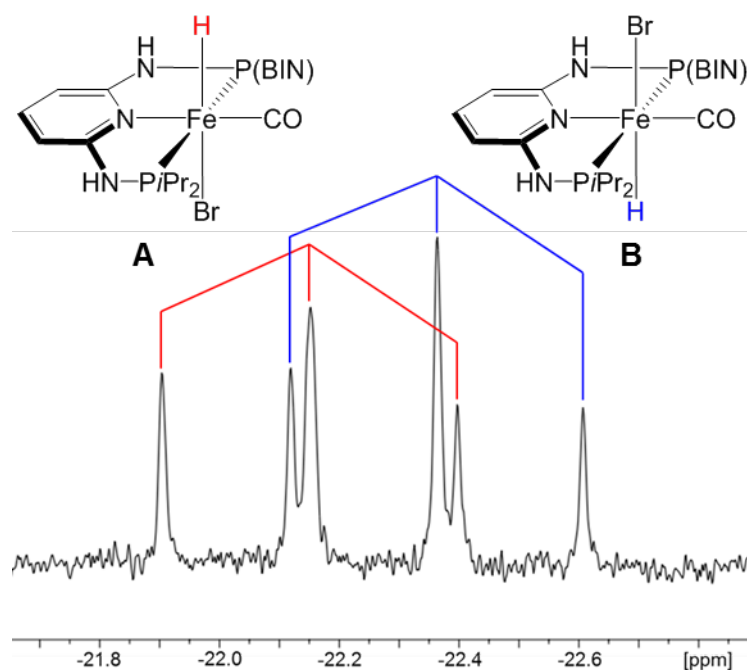


Figure 59: ¹H-NMR spectra of Fe(PNP-*i*Pr/BIN)(H)(CO)Br (**8p**) in MeOD, showing 2 isomers.

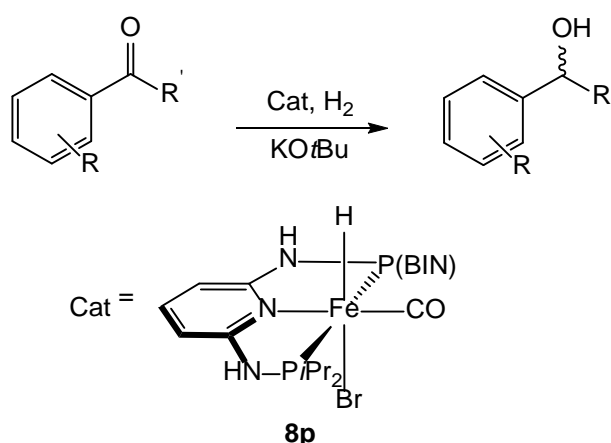
Two diastereomers are formed, depending on which halide is exchanged. The hydride of isomer **A** (red) has a chemical shift of -22.15 ppm and appears as a triplet with a ²J_{PH} of 61.6 Hz, whereas isomer **B** is shifted to -22.36 ppm with a ²J_{PH} of 61.1 Hz. Since the two phosphorus atoms are not chemically equivalent, a doublet on doublet (dd) signal would be

expected, which in this case is merged into a triplet, because of the similarity of the two coupling constants.

Despite of the impure state and the diastereomer mixture of the hydride complex, it was tested for activity in hydrogenation reactions of several prochiral ketons.

3.6.3 Hydrogenation reactions

The iron(II) hydride complex $\text{Fe}(\text{PNP-}i\text{Pr}/\text{BIN})(\text{H})\text{COBr}$ (**8p**) was used as a catalyst in the hydrogenation reaction to reduce ketons to secondary alcohols (Scheme 47) Since the catalyst could yet not be isolated as a clean product, only preliminary tests have been made.



Scheme 47: Catalytic hydrogenation of ketons, using $\text{Fe}(\text{PNP-}i\text{Pr}/\text{BIN})(\text{H})\text{COBr}$ (**8p**) as catalyst.

Using 2 μmol of substrate (acetophenon, 4-fluoroacetophenon, 4-bromoacetophenon, 4-chloroacetophenon and 2-(1-)naphthylacetophenon), 1 mol% catalyst, 2 mol% KOtBu , 2mL EtOH , the reaction mixture was stirred for 18 h at r.t. under 5 bar H_2 atmosphere. After the designated reaction time, the catalyst and insoluble inorganic materials were removed via filtration over a small pad of silica. The rate of conversion was measured by $^1\text{H-NMR}$ and $^{19}\text{F-NMR}$ -spectroscopy, respectively.

The results are depicted in Table 10. It should be noted, that the experiments have to be considered as a preliminary test for the overall activity of the specific catalyst. The experiments have not been repeated yet and the number of substrates, including their diversity of functional groups has been kept small. Additionally, the enantiomeric access has

not been determined yet, and the question can be raised, if one enantiomeric alcohol will be preferably formed at all, since the catalyst contains two diastereomers is almost 50:50 rate.

However, the catalyst shows acceptable activity in the reduction of these 5 substrates with rates of conversion up to >99%, indicating that in further experiments the catalyst loadings can be reduced significantly.

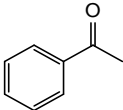
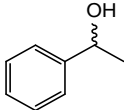
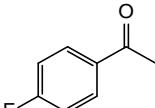
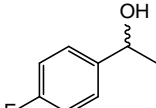
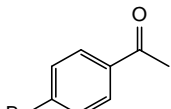
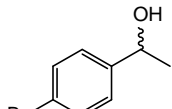
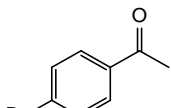
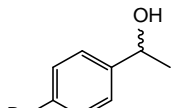
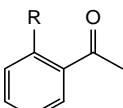
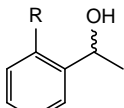
entry	substrate	product	conversion [%]
1			89
2			96
3			>99
4			>99
5			>99

Table 10: iron catalyzed hydrogenation of ketones (entry 5: R = naphthyl).

4 Conclusion

To conclude, several new PN, SN and PNP ligands based on 2,6-diaminopyridine and 2-aminopyridine were synthesized and characterized. The treatment of FeX_2 with these ligands lead to the formation of PN, SN and PNP complexes, showing different coordination modes and reactivity with CO in solution compared to solid state.

In the case of PN bidentate complexes, the coordination behaviour has a huge dependency on the NH functionality of the ligand, undergoing a change in spin state when temperature is decreased for the compounds $\text{Fe}(\text{PN-Ph})_2\text{X}_2$ (**5a**, **5b**), whereas complexes $\text{Fe}(\text{PN}^{\text{R}}\text{-Ph})_2\text{X}_2$ (**5c-5f**) maintained high-spin.

Tridentate complexes of the type $\text{Fe}(\text{PNP}^{\text{R}}\text{-}i\text{Pr})\text{X}_2$ were successfully synthesized and the reaction with CO in solid state and solution was tested. While in solid state the complexes did not show any reaction, in solution the complexes $\text{Fe}(\text{PNP}^{\text{R}}\text{-}i\text{Pr})(\text{CO})\text{X}_2$ (**8a-8d**) were formed and, additionally, cationic complexes $[\text{Fe}(\text{PNP}^{\text{R}}\text{-}i\text{Pr})(\text{CO})_2\text{X}]^+$ (**8e-8h**) were isolated in the presence of a halide scavenger.

For the TADDOL based complexes $\text{Fe}(\text{PNP-}i\text{Pr/TAD})\text{X}_2$ (**6e**, **6f**) and $\text{Fe}(\text{PNP-}i\text{Bu/TAD})\text{X}_2$ (**6g**, **6h**) an equilibrium between κ^3 and κ^2 coordination mode was investigated by NMR and Mössbauer spectroscopy, the CO complexes $\text{Fe}(\text{PNP-}i\text{P/TAD})(\text{CO})\text{X}_2$ were characterized and isolated. Additionally, the CO complex was used for the unsuccessful attempt to synthesize the chiral hydride $\text{Fe}(\text{PNP-}i\text{Pr/TAD})(\text{H})(\text{CO})\text{Br}$.

Finally, chiral complexes containing BINEP-based phosphine PNP ligands were synthesized. After the reaction with CO and $\text{Na}[(\text{H})\text{BEt}_3]$, the hydride species $\text{Fe}(\text{PNP-}i\text{Pr/BIN})(\text{H})(\text{CO})\text{Br}$ was successfully formed and used as catalyst in the homogeneous hydrogenation of ketones to alcohols. Even though the complexes proved to be an active catalyst system, further experiments have to be performed, especially the enantiomeric excess has to be measured on several substrates.

5 Experimental section

5.1 List of abbreviations

AN	acetonitrile
BIN/BINEP	4,5-dihydro-3 <i>H</i> -dinaphtho[2,1- <i>c</i> :1',2'- <i>e</i>]phosphepine
BINOL	1,1'-bi-2-naphthol
<i>n</i> -BuLi	<i>n</i> -buthyllithium
<i>t</i> Bu	tert-butyl
cat	Catalyst
CO	carbon monoxide
Cy	cyclohexyl
MC	methylene chloride
DAP	2,6-diaminopyridine
DMSO	dimethyl sulfoxide
EE	ethyl acetate
Et	ethyl
EtOH	ethanol
ETOL	ethane-1,2-diol
HOMO	highest occupied molecular orbital
LUMO	lowest unoccupied molecular orbital
Me	methyl
MS	mass spectroscopy
Ph	phenyl
<i>i</i> Pr	isopropyl
PE	petrol ether
RT	room temperature
TAD/TADDOL	((4 <i>R</i> ,5 <i>R</i>)-2,2-dimethyl-1,3-dioxolane-4,5-diyl)bis(diphenylmethanol)
THF	tetrahydrofurane
TMEDA	N,N,N',N'-tetramethylethylenediamine
TOF	turn over frequency
TON	turn over number
XRD	X-ray diffraction

5.2 General Considerations

All manipulations were performed under an inert atmosphere of argon by using Schlenk techniques. The solvents were purified according to standard procedures^[65]. The deuterated solvents were purchased from Aldrich and dried over 4 Å molecular sieves.

NMR-spectroscopy

^1H , $^{13}\text{C}\{^1\text{H}\}$ and $^{31}\text{P}\{^{661}\text{H}\}$ NMR spectra were recorded on Bruker AVANCE-250, AVANCE 400 and AVANCE DRX 600 spectrometers. ^1H and $^{13}\text{C}\{^1\text{H}\}$ NMR spectra were referenced internally to residual protio-solvent, and solvent resonances, respectively, and are reported relative to tetramethylsilane ($\delta = 0$ ppm). $^{31}\text{P}\{^1\text{H}\}$ NMR spectra were referenced externally to H_3PO_4 (85%) ($\delta = 0$ ppm).

Magnetization & Mössbauer measurements

Magnetization measurements as a function of temperature were performed on powder samples using SQUID magnetometer (Quantum Design MPMS). The curves were obtained under 0.1 T, for temperatures ranging from 10 to 300 K, using cooling and warming sequences with a temperature variation rate of 1 K per minute waiting time at each measurement temperature. The molar susceptibility values (χ_m) were corrected for diamagnetism of the constituent atoms using Pascal constants.

The ^{57}Fe Mössbauer spectra were recorded in transmission mode at several temperatures between room temperature and 78 K using a conventional constant acceleration spectrometer and a 50mCi ^{57}Co source in a Rh matrix. The low temperature measurements were performed using a liquid nitrogen flow cryostat with a temperature stability of ± 0.5 K. The velocity scale was calibrated using an α -Fe foil. The spectra were fitted to Lorentzian lines using the WinNormos software program, and the isomer shifts reported are relative to metallic α -Fe at room temperature.

Mass spectroscopy

All mass spectrometric measurements were performed on an Esquire 3000^{puls} 3D-quadrupole ion trap mass spectrometer (Bruker Daltonics, Bremen, Germany) in positive-ion mode electrospray ionization (ESI-MS). Mass calibration was done with a commercial mixture

of perfluorinated trialkyl-triazines (ES Tuning Mix, Agilent Technologies, Santa Clara, CA, USA). All analytes were dissolved in methanol 'hypergrade for LC-MS Lichrosolv' quality (Merck, Darmstadt, Germany) to a concentration of roughly 1 mg/mL and doped with sodium chloride or sodium bromide (Merck, Darmstadt, Germany) to avoid dissociation of both halogen substituents from the iron cation promoting the corresponding $[M-X]^+$ ion formation ($X = Cl, Br$) as previously described for molybdenum and titanium complexes^[32c, 67]. Direct infusion experiments were carried out using a Cole Parmer model 74900 syringe pump (Cole Parmer instruments, Vernon Hills, IL, USA) at a flow rate of 2 μ L/min. Full scan and MS/MS scans were measured in the range M/z 100-1100 with the target mass set to m/z 1000. Further experimental conditions include: drying gas temperature: 150°C, capillary voltage: -4 kV; skimmer voltage: 40 V; octapole and lens voltages: according to the target mass set. Helium was used as buffer gas for full scans and as collision gas for MS/MS scans in the low energy CID (collision induced dissociation) mode. The activation and fragmentation width for tandem mass spectrometric (MS/MS) experiments was set to 6 Da to cover the main isotope cluster for fragmentation. The corresponding fragmentation amplitude ranged from 0.4 to 0.6 V in order to keep a low abundant precursor ion intensity in the resulting MS/MS spectrum. As precursor ions for tandem mass spectrometric experiments the ions $[M-X]^+$ could be selected as precursor ions. All mass calculations are based on the lowest mass (i.e. most abundant) iron isotope (^{56}Fe -isotope). Mass spectra and tandem spectra were averaged during data acquisition time of 1 to 2 min and one analytical scan consisted of five successive micro scans resulting in 50 and 100 analytical scans, respectively, for the final mass spectrum or MS/MS spectrum.

IR & Raman spectroscopy

Raman spectra were collected on a Horiba Jobin Yvon Micro-Raman spectrometer (LabRam 800 HR) equipped with an integral Olympus BX 41 microscope (20f objective) and a Peltier-cooled CCD detector, using the 632.8 nm line of a He-Ne laser (1.5 mW) for excitation. A 600 line grating was used for obtaining the Raman spectrum. The Raman-Stokes spectra were recorded in the 4000–200 cm^{-1} range of Raman shifts at 1.3 cm^{-1} spectral resolution; $\tilde{\nu}$ in cm^{-1} ; relative intensities are given in % of the most intense peak. The spectrograph was calibrated using a Si-wafer at 520 cm^{-1} Raman-shift. Far IR spectra were recorded within the range 700 cm^{-1} to 100 cm^{-1} on a Perkin-Elmer 400 FIR FTIR spectrometer, equipped with a Pike Technologies GladiATR using a diamond crystal plate. Electronic spectra of the undiluted powder samples have been measured using a Perkin Elmer Lambda 900 UV-VIS-NIR spectrometer equipped with a thermostatable powder sample holder in diffuse reflection

geometry (Praying Mantis accessory®) between 335 nm and 1200 nm within the temperature range of 123 K and 298 K.

X-ray crystallography

X-ray data were collected at $T = 100$ K on a Bruker Kappa APEX-2 CCD diffractometer using graphite monochromated Mo-K α radiation ($\lambda = 0.71073$ Å) and φ - and ω -scan frames covering complete spheres of the reciprocal space with $\theta_{\max} = 30^\circ$. Corrections for absorption and $\lambda/2$ effects were applied using program SADABS^[68]. After structure solution with program SHELXS97 refinement on F^2 was carried out with program SHELXL97^[69]. Non-hydrogen atoms were refined anisotropically. Hydrogen atoms were placed in calculated positions and thereafter treated as riding. Prior to final refinement disordered solvent molecules were removed with procedure SQUEEZE of program PLATON^[70]. The powder X-ray diffraction measurements were carried out on a Panalytical X'Pert diffractometer in Bragg-Brentano geometry using Cu K $\alpha_{1,2}$ radiation, an X'Celerator linear detector with a Ni-filter, sample spinning and $2\theta = 5$ -70°, $T = 298$ K.

5.3 Computational Details

Calculations were performed using the GAUSSIAN 09 software package^[71], and the OPBE^[72] functional without symmetry constraints. This functional was shown to perform well in mechanistic studies of spin forbidden reactions in related Fe systems^[73]. It has to be noted however that while DFT is very successful at predicting geometries of both high-spin and low-spin complexes, obtaining the correct ground state represents a major challenge since GGA (generalized gradient approximation) functionals (e.g., OPBE, PBE) tend to favour the low-spin-states, while the hybrid functionals (e.g., B3LYP, PBE0) artificially favour the high-spin states^[74]. For example, the energy difference^[74] between the HS and LS states of *cis*-Cl,P,N-Fe(PN-Ph)₂Cl₂ (**B**) is 4.5 kcal/mol when calculated with PBE^[75] changing to 24.1 kcal/mol with PBE0^[76] and to 18.4 kcal/mol, if B3LYP^[64, 77] is employed. With the exception of the PBE functional, data in all cases the HS state is more stable than LS state which is in agreement with the experimental data. The optimized geometries were obtained with the Stuttgart/Dresden ECP (SDD) basis set^[78] to describe the electrons of the iron atom. For all other atoms a standard 6-31g** basis set was employed^[79]. Frequency calculations were performed to confirm the nature of the stationary points yielding no imaginary frequency for

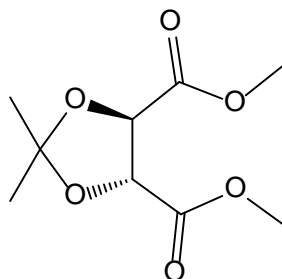
the minima. Transition state optimizations were performed with the Synchronous Transit-Guided Quasi-Newton Method (STQN) developed by Schlegel *et al.*^[80], following a thorough search of the Potential Energy Surfaces (PES). Each transition state was further confirmed by following its vibrational mode downhill on both sides, and obtaining the minima presented on the energy profiles.

TD-DFT^[81] calculations were performed to obtain the UV/Vis spectra using the formalism implemented on Gaussian 09. The OPBE functional was found to reproduce experimental spectra more reliable than other tested (CAM, B3LYP). The basis set was the same as for geometry optimization, with one added f polarization function^[82].

Mössbauer parameters (quadrupole splitting – ΔE_Q – and isomer shift – δ) were evaluated by performing single point calculations at the B3LYP^[74a] level of theory with the ORCA software (Version 2.9.0)^[51], on the optimized geometries. The value for ΔE_Q is directly given by the program, while the isomer shift was evaluated from the electron density at the Fe nucleus using the approach of Neese^[52]. Fe was described by the triply polarized core properties basis set CP(PPP)^[83] and the other atoms by the SV(P) basis set^[84] with the inner s-functions uncontracted, the auxiliary basis set SV/J^[85] as also used for these calculations (basis set b1). For the Fe atom, an enhanced integration grid was used, and the overall integration accuracy was increased to 7^[52]. Taking into account the results of a recent benchmark study^[86] about the prediction of ⁵⁷Fe-Mössbauer parameters by DFT, we also calculated both Mössbauer parameters, ΔE_Q and δ , with the Partridge-1 basis set^[87] for Fe and cc-pVDZ basis set^[88] for the other atoms (basis set b2).

5.4 Ligand precursors

Dimethyl (4*R*, 5*R*)-2,2-dimethyl-1,3-dioxolane-4,5-dicarboxylate (1a)



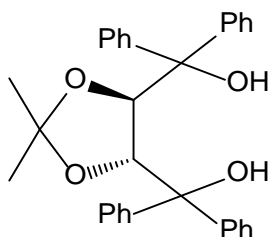
Dimethyl tartrate (1.00 eq; 86.73 mmol; 15.45 g), dimethoxy propane (1.50 eq; 130.09 mmol; 13.55 g) and *p*-toluenesulfonic acid (0.01 eq; 0.87 mmol; 165 mg) was refluxed for 12 h in 300 mL cyclohexane, while the methanol was removed by a Dean-Starck apparatus. After cooling to r.t. the mixture was quenched with 5 g NaHCO₃ and 200 mL water was added. The aqueous phase was extracted with 3x 50 mL EE, the combined organic phases washed with 50 mL brine, dried over Na₂SO₄, filtered and the solvent was removed under reduced pressure. The product was isolated as a yellow oil and was used without further purification for the next step. It can be purified by distillation.

Yield: 18.21 g (96%) yellow oil

¹H-NMR (δ, CDCl₃, 20 °C): 4.76 (s, 2H, CH), 3.77 (s, 6H, COOCH₃), 1.44 (s, 6H, C(CH₃)₂).

¹³C{¹H}-NMR (δ, CDCl₃, 20 °C): 170.00 (s, COOCH₃), 113.77 (s, C(CH₃)₂), 76.91 (s, CH), 52.71 (s, COOCH₃), 26.22 (s, C(CH₃)₂).

(4*R*, 5*R*)-2,2-dimethyl-1,3-dioxolane-4,5-diyl)bis(diphenylmethanol) ≡ TADDOL (1b**)**



Magnesium (8.00 eq; 347.67 mmol; 8.45 g) was suspended in 20 mL dry THF under inert conditions, and a few drops of bromobenzene (8.00 eq; 347.67 mmol; 54.59 g) were added to start the Grignard reaction. The exothermic reaction was carefully diluted with 250 mL THF and bromobenzene was added dropwise. After refluxing for 3 h, **1a** (1.00 eq; 43.46 mmol; 9.48 g) was added at 0°C, then the reaction was refluxed for 12 h. The solution was cooled to 0°C and quenched carefully with 150 mL water, followed by 150 mL sat. NH₄Cl solution. The aqueous phase was extracted with 3x 75 mL Et₂O, the combined organic phases washed with 50 mL brine, dried over Na₂SO₄, filtered and the solvent was removed under reduced pressure. The yellow oil was recrystallized out of hot CH₃CN, the isolated white crystals dissolved in 150 mL toluene and evaporated to dryness, to remove CH₃CN.

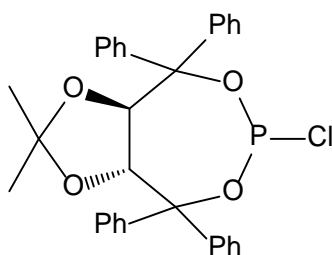
Yield: 16.77 g (83%) white powder

¹H-NMR (δ, CDCl₃, 20°C): 7.56-7.53 (m, 4H, ph), 7.35-7.26 (m, 16H, ph), 4.61 (s, 2H, CH), 4.07 (s, 2H, OH), 1.05 (s, 6H, CH₃).

¹³C{¹H}-NMR (δ, CDCl₃, 20°C):

145.91 (s, ph¹), 142.65 (s, ph¹), 128.60 (s, ph), 128.12 (s, ph), 127.60 (s, ph), 127.26 (s, ph), 109.53 (s, C(CH₃)₂), 80.89 (s, CH), 78.14 (s, C(ph)₂), 27.12 (s, CH₃).

(3aR, 8aR)-6-chloro-2,2-dimethyl-4,4,8,8-tetraphenyltetrahydro-[1,3]dioxolo[4,5-e][1,3,2]dioxaphosphine \equiv TAD-PCI (1c)



1b (1.00 eq; 10.42 mmol; 4.86 g) was dissolved in 150 mL toluene with Et₃N (2.50 eq; 26.04 mmol; 3.6 mL) and cooled to 0°C. PCl₃ (1.10 eq; 11.46 mmol; 1.0 mL) was added slowly via syringe. The reaction was stirred at 60°C for 1 h, half of the solvent was removed under reduced pressure and the remaining mixture filtered over pre-dried Celite[®] under inert conditions. The solvent was removed by evaporation, the resulting yellow oil was treated with 100 mL *n*-pentane, whereby the product precipitated as white solid. After isolation by filtration it was washed with 20 mL *n*-pentane and dried under vacuum.

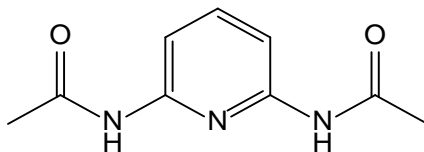
Yield: 3.48 g (63%) white solid

¹H-NMR (δ, CDCl₃, 20°C): 7.71-7.48 (m, 6H, ph), 7.48-7.15 (m, 14H, ph), 5.82 (d, ³J_{HH} = 8.1 Hz, 1H, CH), 5.11 (d, ³J_{HH} = 8.1 Hz, 1H, CH), 0.86 (s, 3H, CH₃), 0.49 (s, 3H, CH₃).

¹³C{¹H}-NMR (δ, CDCl₃, 20°C): 144.72 (s, ph¹), 144.12 (s, ph¹), 140.51 (s, ph¹), 139.94 (s, ph¹), 128.87 (s, ph), 128.70 (s, ph), 128.34 (s, ph), 128.06 (s, ph), 127.98 (s, ph), 127.57 (s, ph), 127.35 (s, ph), 127.12 (s, ph), 126.95 (s, ph), 114.22 (s, C(CH₃)₂), 91.00 (d, ²J_{CP} = 14.3 Hz, C(ph)₂), 88.97 (d, ²J_{CP} = 11.3 Hz, C(ph)₂), 81.62 (d, ³J_{CP} = 6.6 Hz, CH), 79.20 (d, ³J_{CP} = 6.3 Hz, CH), 26.84 (s, CH₃), 26.23 (s, CH₃).

³¹P{¹H}-NMR (δ, CDCl₃, 20°C): 148.0.

***N*²,*N*⁶-(pyridine-2,6-diyl)diacetamid (1d)**



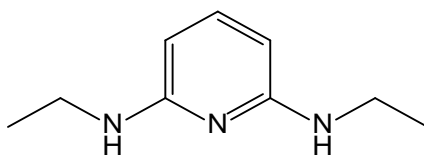
Pyridine-2,6-diamine (1.00 eq; 99.41 mmol; 10.85 g) was suspended in 200 mL dry CH₂Cl₂ and cooled to 0°C. Acetic anhydride (2.10 eq; 208.77 mmol; 19.8 mL) was added and the reaction mixture was refluxed for 2 h. After quenching with 10 mL water, the solvent was evaporated. The product was purified by recrystallization out of a saturated solution in refluxing CH₂Cl₂/MeOH 15:1. The solubility of the bright yellow solid is exceptionally low.

Yield: 15.98 g (83%) bright yellow solid

¹H-NMR (δ, d₆-Aceton, 20°C): 9.09 (s, 2H, NH), 7.82 (d, ³J_{HH} = 7.9 Hz, 2H, py^{3,5}), 7.64 (t, ³J_{HH} = 8.0 Hz, 1H, py⁴), 2.09 (s, 6H, COCH₃).

¹³C{¹H}-NMR (δ, d₆-Aceton, 20°C): 168.64 (s, CO), 150.60 (s, py^{2,6}), 139.81 (s, py⁴), 108.42 (s, py^{3,5}), 23.41 (s, CH₃).

*N*²,*N*⁶-diethylpyridin-2,6-diamine (**1e**)



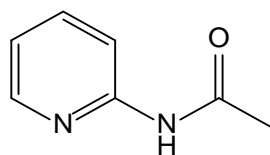
1d (1.00 eq; 59.68 mmol; 11.53 g) was suspended in 300 mL dry THF under inert conditions and cooled to 0°C. LiAlH₄ (2.50 eq; 149.20 mmol; 2.4 M; 62.2 mL) was added carefully, whereby the colour changed to yellow and a precipitate was formed. After slowly warming to reflux temperature, the mixture was stirred for 12 h to achieve complete conversion. The reaction was quenched with aqueous THF at 0°C and filtered through a frit to remove inorganic salts. The solvent was evaporated, the remaining yellow oil was dissolved in 100 mL water and extracted with 3x 100 mL CH₂Cl₂. The combined organic phases were washed with 50 mL brine, dried over Na₂SO₄, filtered and evaporated. The crude product was purified by bulb-to-bulb distillation (≈ 1 mbar; 160°C).

Yield: 7.76 g (79%) colourless, O₂-sensitive oil

¹H-NMR (δ, CDCl₃, 20°C): 7.24 (t, ³J_{HH} = 7.9 Hz, 1H, py⁴), 5.70 (d, ³J_{HH} = 7.9 Hz, 2H, py^{3,5}), 4.18 (s, 2H, NH), 3.22 (m, 4H, CH₂CH₃), 1.21 (t, ³J_{HH} = 7.2 Hz, 6H, CH₂CH₃).

¹³C{¹H}-NMR (δ, CDCl₃, 20°C): 158.32 (s, py^{2,6}), 137.37 (s, py⁴), 94.27 (s, py^{3,5}), 36.92 (s, CH₂CH₃), 14.96 (s, CH₂CH₃).

***N*-(pyridine-2-yl)acetamid (1f)**



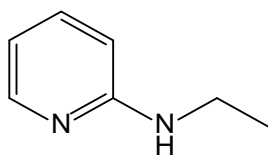
2-Aminopyridine (1.00 eq; 37.51 mmol; 3.53 g) was dissolved in 70 mL dry CH₂Cl₂ and cooled to 0°C. Acetic anhydride (1.20 eq; 45.01 mmol; 4.3 mL) was added and the reaction was refluxed for 4 h, by then all substrate was consumed (maintained by DC). The reaction was quenched with 10 mL water and the solvent was removed under reduced pressure. The remaining yellow solid was resolved in 100 mL sat. NaHCO₃ solution and extracted with 4x 50 mL. The organic phase was washed with 50 mL brine, dried over Na₂SO₄, filtered and the solvent was removed under vacuum.

Yield: 4.68 g (92%) white solid

¹H-NMR (δ, CDCl₃, 20°C): 9.02 (s, 1H, NH), 8.28 (m, 1H, py⁶), 8.28 (d, ³J_{HH} = 8.2 Hz, 1H, py³) 7.73 (m, 1H, py⁴), 6.06 (m, 1H, py⁵), 2.22 (s, 3H, OCH₃).

¹³C{¹H}-NMR (δ, CDCl₃, 20°C): 168.88 (s, CONH), 151.71 (s, py²), 147.52 (s, py⁶), 138.51 (s, py⁴), 119.69 (s, py⁵), 114.34 (s, py³), 24.66 (s, COCH₃).

N-ethylpyridin-2-amine (1g)



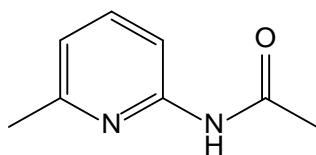
1f (1.00 eq; 46.49 mmol; 6.33 g) was dissolved in 200 mL dry THF under inert conditions and cooled to 0°C. LiAlH₄ (1.10 eq; 51.14 mmol; 2.4 M; 21.3 mL) was added carefully via syringe to the solution, whereby the colour changed to yellow. The reaction was slowly warmed to reflux temperature and stirred for 12 h. After carefully quenching the mixture with aqueous THF, the suspension was filtered to remove inorganic salts and the solvent was evaporated. The yellow oil was resolved in 100 mL water and extracted with 3x 100 mL CH₂Cl₂. The combined organic phases were washed with 50 mL brine, dried over Na₂SO₄, filtered and the solvent was removed under reduced pressure. The product was purified by bulb-to-bulb distillation.

Yield: 4.68 g (82%) yellow, O₂-sensitive oil

¹H-NMR (δ, CDCl₃, 20°C): 8.03 (d, ³J_{HH} = 4.5 Hz, 1H, py⁶), 7.36 (m, 1H, py⁴), 6.50 (m, 1H, py⁵), 6.32 (d, ³J_{HH} = 8.4 Hz, 1H, py³), 4.53 (s, 1H, NH), 3.24 (m, 2H, CH₂CH₃), 1.20 (t, ³J_{HH} = 7.19, 3H, CH₂CH₃).

¹³C{¹H}-NMR (δ, CDCl₃, 20°C): 158.85 (s, py²), 148.15 (s, py⁶), 137.36 (s, py⁴), 112.61 (s, py⁵), 106.33 (s, py³), 36.85 (s, CH₂CH₃), 14.83 (s, CH₂CH₃).

***N*-(6-methylpyridine-2-yl)acetamide (1h)**



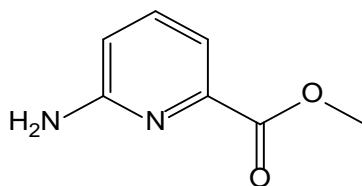
6-Methylpyridine-2-amine (1.00 eq; 167.28 mmol; 18.09 g) was dissolved in 300 mL dry CH_2Cl_2 and cooled to 0°C . Acetic anhydride (1.20 eq; 200.73 mmol; 19.0 mL) was added and the reaction was refluxed for 3 h (maintained by DC). 10 mL water was added and the solvent was evaporated to dryness. The remaining solid was resolved in 200 mL sat. NaHCO_3 solution and extracted with 3x 100 mL CH_2Cl_2 . The combined organic phases were washed with 50 mL brine, dried over Na_2SO_4 , filtered and evaporated.

Yield: 20.13 g (80%) bright yellow solid

$^1\text{H-NMR}$ (δ , CDCl_3 , 20°C): 8.63 (s, 1H, NH), 7.98 (d, $^3J_{\text{HH}} = 8.1$ Hz, 1H, py³), 7.57 (t, $^3J_{\text{HH}} = 7.9$ Hz, 1H, py⁴), 6.87 (d, $^3J_{\text{HH}} = 7.5$ Hz, 1H, py⁵), 2.43 (s, 3H, CH_3), 2.15 (s, 3H, COCH_3).

$^{13}\text{C}\{^1\text{H}\}$ -NMR (δ , CDCl_3 , 20°C): 168.77 (s, CONH), 156.59 (s, py²), 150.78 (s, py⁶), 138.66 (s, py⁴), 119.17 (s, py⁵), 111.00 (s, py³), 24.53 (s, COCH_3), 23.92 (s, CH_3).

Methyl-6-aminopicolinate (1i)



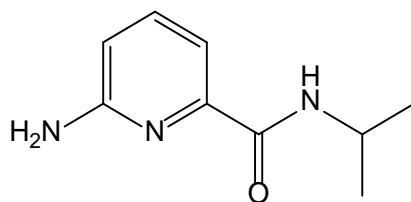
1h (1.00 eq; 124.52 mmol; 18.70 g) and KH_2PO_4 (2.00 eq; 249.03 mmol; 33.89 g) were dissolved in 500 mL water and warmed to 80°C. KMnO_4 (2.50 eq; 311.29 mmol; 49.19 g) was added in small portions during 1 h in a ratio, that the temperature did not exceed 90°C. The solution was stirred further at 80°C, until the violet colour completely vanished. Insoluble inorganic materials (MnO_2) were removed by filtration over Celite[®] and the clear solution was extracted with 3x 100 mL CH_2Cl_2 to regain unreacted educts. The aqueous solution was concentrated under reduced pressure, followed by addition of 100 mL toluene and removing the solvent again by evaporation. This protocol was repeated twice with 100 mL MeOH. The white solid was then dissolved in 200 mL MeOH, 20 mL H_2SO_4 was added and the mixture was refluxed for 24 h. After evaporation of the solvent, the oily suspension was added 100 mL EE and slowly neutralized with sat. NaHCO_3 solution. The aqueous phase was extracted with 3x 100 mL EE, the combined phases dried with 50 mL brine, dried over Na_2SO_4 , filtered and concentrated under vacuum.

Yield: 7.35 g (39%) yellow solid

$^1\text{H-NMR}$ (δ , CDCl_3 , 20°C): 7.54 (t, $^3J_{\text{HH}} = 7.7$ Hz, 1H, py⁴), 7.47 (d, $^3J_{\text{HH}} = 7.3$ Hz, 1H, py³), 6.66 (d, $^3J_{\text{HH}} = 7.8$ Hz, 1H, py⁵), 4.85 (s, 2H, NH), 3.93 (s, 3H, CH₃).

$^{13}\text{C}\{^1\text{H}\}\text{-NMR}$ (δ , CDCl_3 , 20°C): 165.98 (s, COOMe), 158.37 (s, 158.41, py⁶), 146.07 (s, py²), 138.28 (s, py⁴), 115.65 (s, py³), 112.77 (s, py⁵), 52.69 (s, OCH₃).

6-Amino-*N*-isopropylpicolinamide (1j)



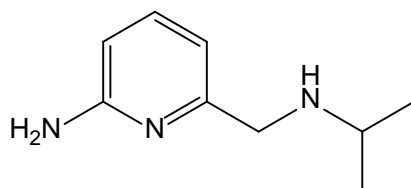
1i (1.00 eq; 22.32 mmol; 4.00 g) was stirred in isopropyl amine (>10.00 eq; ~20 mL) in a microwave vial at 150°C for 4 h. The suspension was dissolved in 50 mL toluene and all volatile compounds were removed by evaporation. The yellow product was dried for 1 h under vacuum.

Yield: quantitative, yellow solid

¹H-NMR (δ, CDCl₃, 20°C): 7.73 (s, 1H, CONH), 7.53 (m, 2H, py^{3,4}), 6.60 (m, 1H, py⁵), 4.59 (s, 2H, NH₂), 4.27-4.14 (m, 1H, CH(CH₃)₂), 1.30 (d, ³J_{HH} = 6.6 Hz, 6H, CH(CH₃)₂).

¹³C{¹H}-NMR (δ, CDCl₃, 20°C): 163.65 (s, CONH), 157.05 (s, py⁶), 148.40 (s, py²), 138.79 (s, py⁴), 112.58 (s, py³), 111.49 (s, py⁵), 41.18 (s, CH(CH₃)₂), 22.78 (s, CH(CH₃)₂).

6-((isopropylamino)methyl)pyridine-2-amine (1k)



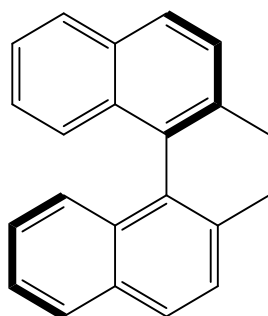
1j (1.00 eq; 17.78 mmol; 3.19 g) was dissolved in 100 mL dry THF and cooled to 0°C. LiAlH₄ (3.50 eq; 62.24 mmol; 2.4 M; 26.0 mL) was added slowly and the mixture was refluxed for 48 h. After carefully quenching at 0°C with 40 mL NaOH solution (10%) the suspension was filtered and the solvent was removed under reduced pressure. The residue was dissolved in 100 mL water and extracted with 4x 100 mL CH₂Cl₂. The combined organic phases were washed with 50 mL brine dried over Na₂SO₄, filtered and concentrated under vacuum. The product was purified via bulb-to-bulb distillation.

Yield: 1.50 g (55%) white solid

¹H-NMR (δ, CDCl₃, 20°C): 7.38 (t, ³J_{HH} = 7.7 Hz, 1H, py⁴), 6.64 (d, ³J_{HH} = 7.3 Hz, 1H, py⁵), 6.37 (d, ³J_{HH} = 8.1 Hz, 1H, py³), 4.42 (s, 2H, NH₂), 3.73 (s, 2H, CH₂), 2.86 (hept, ³J_{HH} = 6.2 Hz, 1H, CH(CH₃)₂), 1.89 (s, 1H, NH), 1.12 (d, ³J_{HH} = 6.3 Hz, 6H, CH(CH₃)₂).

¹³C{¹H}-NMR (δ, CDCl₃, 20°C): 158.42 (s, py²), 158.12 (s, py⁶), 138.10 (s, py⁴), 112.34 (s, py⁵), 106.69 (s, py³), 52.79 (s, CH₂), 48.34 (s, CH(CH₃)₂), 22.94 (s, CH(CH₃)₂).

(1*R*)-2,2'-dimethyl-1,1'-binaphthalene (11)



(1*R*)-[1,1'-Binaphthalene]-2,2'-diol (1.00 eq; 18.54 mmol; 5.31 g) was dissolved in 100 mL CH₂Cl₂ and pyridine (4.00 eq; 74.16 mmol; 6.0 mL) was added. The solution was cooled to 0°C and Tf₂O (2.20 eq; 40.79 mmol; 6.9 mL) was added slowly via syringe. After stirring at r.t. for 12 h, the reaction was quenched by addition of 20 mL HCl (5 %) and evaporated to dryness. The oily residue was redissolved in 150 mL EE and washed with 100 mL HCl (5 %), the aqueous phase extracted with 100 mL EE. The combined organic phases were washed with 100 mL sat. NaHCO₃ solution, 50 mL brine, dried over Na₂SO₄, filtered and evaporated. The crude product was transferred to a small pad of silica and eluted with 300 mL CH₂Cl₂. The solvent was removed under reduced pressure and the white powder was isolated.

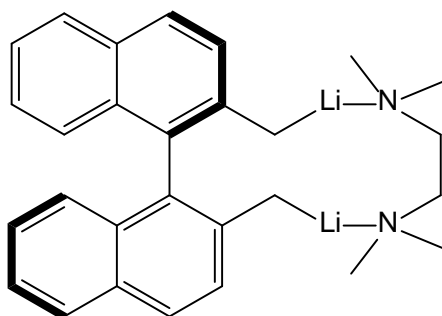
Binol-bistriflate was suspended with Ni(dppp)Cl₂ (0.05 eq; 0.93 mmol; 502 mg) in 150 mL Et₂O and cooled to 0°C. MeMgBr (6.00 eq; 111.24 mmol; 3.0 M; 37.0 mL) was added and the reaction was refluxed for 24 h. After quenching by addition of 100 mL water at 0°C, 20 mL HCl (conc.) was added and stirred for 1 h. The aqueous phase was extracted with 2x 100 mL Et₂O, the combined organic phases washed with 100 mL sat. NaHCO₃ solution, 50 mL brine, dried over Na₂SO₄, filtered and evaporated to dryness. The crude product was purified by flash chromatography, using silica gel and PE/EE 3:1 as eluent.

Yield: 5.00 g (96%) white solid

¹H-NMR (δ, CDCl₃, 20°C): 7.99 – 7.90 (m, 4H, ph^{4,5}), 7.57 (d, ³J_{HH} = 8.4 Hz, 2H, ph³), 7.45 (t, ³J_{HH} = 7.4 Hz, 2H, ph⁶), 7.29 – 7.23 (m, 2H, ph⁷), 7.13 (d, ³J_{HH} = 8.5 Hz, 2H, ph⁸), 2.11 (s, 6H, CH₃).

¹³C{¹H}-NMR (δ, CDCl₃, 20°C): 135.18 (s, ph¹), 134.33 (s, ph²), 132.82 (s, ph⁸), 132.27 (s, ph⁴), 128.79 (s, ph³), 127.99 (s, ph⁵), 127.49 (s, ph⁴), 126.15 (s, ph⁷), 125.70 (s, ph⁸), 124.95 (s, ph⁶), 20.10 (s, CH₃).

(1*R*)-2,2'-dimethyl-1,1'-binaphthalene, Li₂-TMEDA adduct (1m)

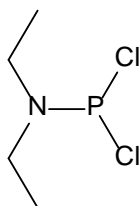


n-BuLi (2.50 eq; 64.98 mmol; 26.0 mL) was transferred to a schlenk flask, evaporated, the remaining oil dissolved in 75 mL Et₂O and cooled to -10°C. **1I** (1.00 eq; 25.99 mmol; 7.34 g) in 30 mL Et₂O was added and the orange solution was allowed to reach r.t. TMEDA (2.50 eq; 64.98 mmol; 9.8 mL) was added and the reaction was stirred at r.t. for 36 h. After addition of 20 mL *n*-pentane, the solution was cooled to 0°C and filtered under inert conditions. The red-brownish powder was washed with 2x 20 mL *n*-pentane and dried under vacuum for 1 h.

The product was used without further purification for the following reaction. The red powder has to be handled in a glove box and ignites under air.

Yield: 9.81 g (92%) red-brownish powder

1,1-dichloro-*N,N*-diethylphosphanamine (1n)



PCl_3 (1.00 eq; 96.71 mmol; 13.28 g) was dissolved in 300 mL toluene and cooled to 0°C . Diethyl amine (2.00 eq; 193.42 mmol; 14.15 g) was added slowly, whereupon a cloudy precipitate formed. The suspension was warmed to 60°C and stirred for 1 h, filtered at r.t. over a small pad of celite and the solvent was removed under reduced pressure. The crude product was purified by distillation (30 mbar, 83°C).

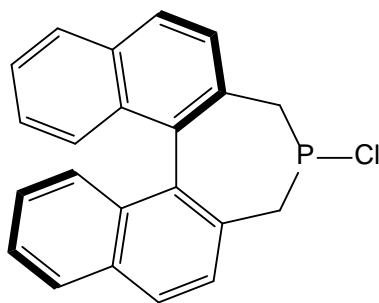
Yield: 12.03 g (72%) colourless liquid

$^1\text{H-NMR}$ (δ , CDCl_3 , 20°C): 3.37 (dq, $^3J_{\text{HH}} = 7.1$ Hz, $^3J_{\text{PH}} = 14.2$ Hz, 4H, NCH_2CH_3), 1.21 (t, $^3J_{\text{HH}} = 7.1$ Hz, 6H, CH_3).

$^{13}\text{C}\{^1\text{H}\}\text{-NMR}$ (δ , CDCl_3 , 20°C): 41.68 (d, $^2J_{\text{CP}} = 22.9$ Hz, NCH_2CH_3), 14.10 (d, $^3J_{\text{CP}} = 4.8$ Hz, NCH_2CH_3).

$^{31}\text{P}\{^1\text{H}\}\text{-NMR}$ (δ , CDCl_3 , 20°C): 162.4.

(1*R*)-4-chloro-4,5-dihydro-3*H*-dinaphto[2,1-*c*:1',2'-*e*]phosphepine \equiv BINEP-PCl (1o**)**



1m (1.00 eq; 23.83 mmol; 9.78 g) was dissolved in 300 mL toluene and cooled to 0°C. **1n** (1.10 eq; 26.21 mmol; 4.56 g) was added, whereupon the colour changed from dark red to yellow. The reaction was stirred at r.t. for 12 h and filtered. Dry HCl gas was bubbled through the solution for 30 min, followed by a steady stream of argon. The white precipitate was filtered over a small pad of Celite[®] and washed thoroughly with 2x 30 mL toluene. The solvent was removed under reduced pressure, the product was precipitated by addition of 100 mL *n*-pentane. The white solid was collected by filtration and dried under vacuum for 2 h.

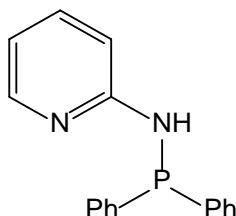
Yield: 3.89 g (47%) beige solid

³¹P{¹H}-NMR (δ , CDCl₃, 20°C): 114.6.

5.5 Ligands

5.5.1 PN ligands

N-(diphenylphosphanyl)pyridin-2-amin \equiv PN-Ph (2a)



2-Aminopyridine (1.00 eq; 21.25 mmol; 2.00 g) was suspended with Et_3N (1.50 eq; 31.87 mmol; 4.4 mL) in 150 mL toluene and cooled to 0°C . PPh_2Cl (1.05 eq; 22.31 mmol; 6.21 g) was added slowly and the reaction was stirred at 80°C for 12 h. The solution was filtered over a small pad of Celite[®] and the solvent was removed under reduced pressure. The product crystallized as bright yellow solid. It can be purified via chromatography using silica gel (conditioned with 5 Vol% Et_3N) and 1:1:1 PE/EE/MC as eluent.

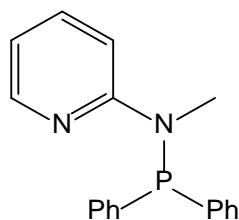
Yield: 5.28 g (89%)

$^1\text{H-NMR}$ (δ , CDCl_3 , 20°C): 8.00 (ddd; $^3J_{\text{HH}} = 5.0$ Hz, $^5J_{\text{PH}} = 1.8$ Hz, $^4J_{\text{HH}} = 0.8$ Hz, 1H, py⁶), 7.44 – 7.35 (m, 5H, ph^{2,6}, py⁴), 7.32 – 7.24 (m, 6H, ph^{3,4,5}), 6.95 (ddvt, $^3J_{\text{HH}} = 8.4$ Hz, $^4J_{\text{PH}} = 1.7$ Hz, $^4J_{\text{HH}} = 0.9$ Hz, 1H, py³), 6.62 (ddd, $^3J_{\text{HH}} = 7.2$ Hz, $^3J_{\text{HH}} = 5.0$ Hz, $^4J_{\text{HH}} = 0.9$ Hz, 1H, py⁵), 5.31 (d, $^2J_{\text{PH}} = 8.4$ Hz, 1H, NH).

$^{13}\text{C}\{^1\text{H}\}$ -NMR (δ , CDCl_3 , 20°C): 158.54 (d, $^2J_{\text{CP}} = 20.6$ Hz, py²), 148.27 (d, $^4J_{\text{CP}} = 1.4$ Hz, py⁶), 139.58 (d, $^1J_{\text{CP}} = 11.4$ Hz, ph¹), 137.81 (d, $^4J_{\text{CP}} = 2.1$ Hz, py⁴), 131.28 (d, $^2J_{\text{CP}} = 20.9$ Hz, ph^{2,6}), 129.27 (s, ph⁴), 128.60 (d, $^3J_{\text{CP}} = 6.7$ Hz, ph^{3,5}), 115.10 (s, py⁵), 108.86 (d, $^3J_{\text{CP}} = 15.2$ Hz, py³).

$^{31}\text{P}\{^1\text{H}\}$ -NMR (δ , CDCl_3 , 20°C): 25.9.

***N*-(diphenylphosphanyl)-*N*-methylpyridin-2-amin \equiv PN^{Me}-Ph (2b)**



N-methylpyridin-2-amine (1.00 eq; 36.43 mmol; 4.23 g) was dissolved in 100 mL toluene and cooled down to 0°C. *n*-BuLi (1.05 eq; 38.25 mmol; 2.5 M; 16.5 mL) was added slowly via syringe, whereby the colour of the solution changed from yellow to bright red. After stirring at r.t. for 2 h, the solution was again cooled down to 0°C, PPh₂Cl (1.05 eq; 38.25 mmol; 8.81 g) was added and the reaction was stirred 12 h at 80°C for complete conversion. The mixture was quenched with 50 mL sat. NaHCO₃ solution, the organic phase was washed with 50 mL brine, dried over Na₂SO₄, filtered and the solvent was removed under reduced pressure. The yellow residue was purified via flash chromatography, using silica gel (conditioned with 5 Vol% Et₃N) and 3:1 PE/EE as eluent.

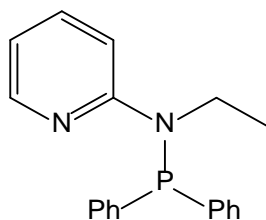
Yield: 8.89 g (78%) white solid

¹H-NMR (δ, CDCl₃, 20°C): 8.29 (ddd, ³J_{HH} = 5.0 Hz, ⁴J_{HH} = 1.9 Hz, ⁵J_{PH} = 0.8 Hz, 1H, py⁶), 7.55 (ddd, ³J_{HH} = 8.9 Hz, ³J_{HH} = 7.1 Hz, ⁴J_{HH} = 2.0 Hz, 1H, py⁴), 7.49 – 7.41 (m, 11H, ph, py³), 6.78 (ddd, ³J_{HH} = 7.0 Hz, ³J_{HH} = 5.0 Hz, ⁴J_{HH} = 0.9 Hz, 1H, py⁵), 2.97 (d, ³J_{PH} = 1.6 Hz, 3H, NCH₃).

¹³C{¹H}-NMR (δ, CDCl₃, 20°C): 161.33 (d, ²J_{CP} = 27.1 Hz, py²), 147.66 (d, ⁴J_{CP} = 1.8 Hz, py⁶), 137.05 (d, ⁴J_{CP} = 3.1 Hz, py⁴), 136.67 (d, ¹J_{CP} = 14.9 Hz, ph¹), 132.00 (d, ²J_{CP} = 20.5 Hz, ph^{2,6}), 129.02 (s, ph⁴), 128.53 (d, ³J_{CP} = 5.8 Hz, ph^{3,5}), 114.67 (d, ⁵J_{CP} = 1.0 Hz, py⁵), 110.63 (d, ³J_{CP} = 21.6 Hz, py³), 34.21 (d, ²J_{CP} = 8.6 Hz, NCH₃).

³¹P{¹H}-NMR (δ, CDCl₃, 20°C): 50.9.

***N*-(diphenylphosphanyl)-*N*-ethylpyridin-2-amin \equiv PN^{Et}-Ph (2c)**



This ligand was prepared analogously to **2b** with **1g** (1.00 eq; 37.98 mmol; 4.64 g), *n*-BuLi (1.05 eq; 39.88 mmol; 2.5 M; 16.0 mL) and PPh₂Cl (1.05 eq; 39.88 mmol; 8.80 g) as starting materials.

Yield: 8.80 g (76%) white solid

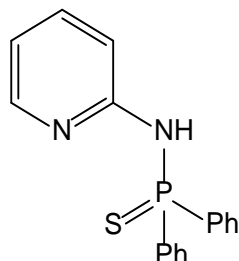
¹H-NMR (δ, CDCl₃, 20°C): 8.18 (ddd, ³*J*_{HH} = 5.0 Hz, ⁴*J*_{HH} = 2.0 Hz, ⁵*J*_{PH} = 0.9 Hz, 1H, py⁶), 7.43 – 7.37 (m, 5H, ph^{2,6}, py⁴), 7.31 – 7.29 (m, 7H, ph^{3,4,5}, py³), 6.64 (ddd, ³*J*_{HH} = 7.1 Hz, ³*J*_{HH} = 5.0 Hz, ⁴*J*_{HH} = 0.9 Hz, 1H, py⁵), 3.61 (qd, ³*J*_{HH} = 6.9 Hz, ³*J*_{PH} = 2.4 Hz, 2H, NCH₂CH₃), 0.61 (t, ³*J*_{HH} = 6.9 Hz, 3H, NCH₂CH₃).

¹³C{¹H}-NMR (δ, CDCl₃, 20°C): 160.13 (d, ²*J*_{CP} = 24.7 Hz, py²), 147.75 (d, ⁴*J*_{CP} = 1.6 Hz, py⁶), 137.13 (d, ¹*J*_{CP} = 15.3 Hz, ph¹), 136.97 (d, ⁴*J*_{CP} = 3.0 Hz, py⁴), 132.32 (d, ²*J*_{CP} = 20.8 Hz, ph^{2,6}), 128.98 (s, ph⁴), 128.44 (d, ³*J*_{CP} = 5.9 Hz, ph^{3,5}), 114.49 (d, ⁵*J*_{CP} = 1.0 Hz, py⁵), 111.06 (d, ³*J*_{CP} = 20.7 Hz, py³), 42.49 (d, ²*J*_{CP} = 5.8 Hz, NCH₂CH₃), 13.99 (s, NCH₂CH₃).

³¹P{¹H}-NMR (δ, CDCl₃, 20°C): 49.5.

5.5.2 SN ligands

P,P-diphenyl-*N*-(pyridine-2-yl)phosphinothiotic amide \equiv SN-Ph (2d)



2a (1.00 eq; 15.63 mmol; 4.35g) was stirred with elemental sulphur (1.10 eq; 17.19 mmol; 0.55 g) in 100 mL toluene at 80°C for 2 h. The solvent was evaporated and the crude product was purified by flash chromatography, using silica gel and EE as eluent.

Yield: 4.50 g (93%)

¹H-NMR (δ , CDCl₃, 20°C):

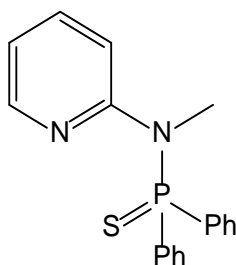
8.00 – 7.90 (m, 4H, ph^{3,5}), 7.84 (dd, ³J_{HH} = 5.0 Hz, ⁴J_{HH} = 1.0 Hz, 1H, py⁶), 7.48 – 7.35 (m, 6H, ph^{2,4,6}), 7.31 (ddd, ³J_{HH} = 8.4 Hz, ³J_{HH} = 7.3 Hz, ⁴J_{HH} = 1.9 Hz, 1H, py⁴), 6.85 (d, ³J_{HH} = 8.4 Hz, 1H, py³), 6.71 (bs, 1H, NH), 6.66 (ddd, ³J_{HH} = 7.3 Hz, ³J_{HH} = 5.0 Hz, ⁴J_{HH} = 0.8 Hz, 1H, py⁵).

¹³C{¹H}-NMR (δ , CDCl₃, 20°C):

153.52 (d, ²J_{CP} = 2.0 Hz, py²), 148.10 (s, py⁶), 137.63 (s, py⁴), 133.73 (s, ph¹), 132.70 (s, ph¹), 132.10 (d, ⁴J_{CP} = 3.0 Hz, ph⁴), 131.66 (d, ³J_{CP} = 11.6 Hz, ph^{3,5}), 128.72 (d, ²J_{CP} = 13.4 Hz, ph^{2,6}), 117.13 (s, py⁵), 112.16 (d, ³J_{CP} = 3.6 Hz, py³).

³¹P{¹H}-NMR (δ , CDCl₃, 20°C): 51.4.

***N*-methyl-*P,P*-diphenyl-*N*-(pyridine-2-yl)phosphinothiotic amide \equiv SN^{Me}-Ph (2e)**



This ligand was prepared analogously to **2d** with **2b** (1.00 eq; 17.58 mmol; 5.14 g) and elemental sulphur (1.10 eq; 19.34 mmol; 0.62 g) as starting materials.

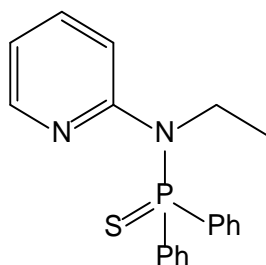
Yield: 5.49 g (96%) white solid

¹H-NMR (δ, CDCl₃, 20 °C): 8.11 (dd, ³J_{HH} = 4.8 Hz, ⁴J_{HH} = 1.6 Hz, 1H, py⁶), 7.94 – 7.85 (m, 4H, ph^{3,5}), 7.41 – 7.24 (m, 7H, ph^{2,4,6}, py⁴), 7.06 (dd, ³J_{HH} = 8.4 Hz, ⁴J_{HH} = 0.6 Hz, 1H, py³), 6.73 (ddd, ³J_{HH} = 7.3 Hz, ³J_{HH} = 4.9 Hz, ⁴J_{HH} = 0.8 Hz, 1H, py⁵), 3.15 (d, ³J_{PH} = 10.7 Hz, 3H, NCH₃).

¹³C{¹H}-NMR (δ, CDCl₃, 20 °C): 157.02 (d, ²J_{CP} = 4.8 Hz, py²), 147.66 (s, py⁶), 136.81 (s, py⁴), 134.09 (s, ph¹), 133.06 (s, ph¹), 132.08 (d, ³J_{CP} = 11.0 Hz, ph^{3,5}), 131.44 (d, ⁴J_{CP} = 3.0 Hz, ph⁴), 128.36 (d, ²J_{CP} = 13.4 Hz, ph^{2,6}), 117.88 (s, py⁵), 115.86 (d, ³J_{CP} = 4.2 Hz, py³), 35.95 (d, ²J_{CP} = 4.4 Hz, NCH₃).

³¹P{¹H}-NMR (δ, CDCl₃, 20 °C): 64.8.

***N*-ethyl-*P,P*-diphenyl-*N*-(pyridine-2-yl)phosphinothiotic amide \equiv SN^{Et}-Ph (2f)**



This ligand was prepared analogously to **2d** with **2c** (1.00 eq; 21.09 mmol; 6.46 g) and elemental sulphur (1.10 eq; 23.20 mmol; 0.74 g) as starting materials.

Yield: 6.98 g (98%) white solid

¹H-NMR (δ, CDCl₃, 20 °C):

8.12 (dd, ³J_{HH} = 4.8 Hz, ⁴J_{HH} = 1.6 Hz, 1H, py⁶), 7.93 – 7.85 (m, 4H, ph^{3,5}), 7.37 – 7.25 (m, 7H, ph^{2,4,6}, py⁴), 7.08 (dd, ³J_{HH} = 8.3 Hz, ⁴J_{HH} = 0.7 Hz, 1H, py³), 6.73 (ddd, ³J_{HH} = 7.3 Hz, ³J_{HH} = 4.9 Hz, ⁴J_{HH} = 0.8 Hz, 1H, py⁵), 3.79 (dq, ²J_{PH} = 14.0 Hz, ³J_{HH} = 7.0 Hz, 2H, NCH₂CH₃), 1.10 (t, ³J_{HH} = 7.0 Hz, 3H, NCH₂CH₃).

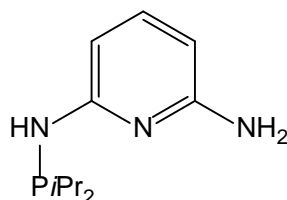
¹³C{¹H}-NMR (δ, CDCl₃, 20 °C):

155.52 (d, ²J_{CP} = 4.8 Hz, py²), 147.83 (s, py⁶), 136.86 (s, py⁴), 134.36 (s, ph¹), 133.32 (s, ph¹), 132.21 (d, ³J_{CP} = 11.1 Hz, ph^{3,5}), 131.29 (d, ⁴J_{CP} = 3.0 Hz, ph⁴), 128.19 (d, ²J_{CP} = 13.4 Hz, py^{2,6}), 118.23 (s, py⁵), 117.58 (d, ³J_{CP} = 4.1 Hz, py³), 43.09 (d, ²J_{CP} = 4.3 Hz, NCH₂CH₃), 14.65 (d, ³J_{CP} = 1.4 Hz, NCH₂CH₃).

³¹P{¹H}-NMR (δ, CDCl₃, 20 °C): 64.1.

5.5.3 PNP & PNN ligands

*N*²-(diisopropylphosphanyl)pyridin-2,6-diamin ≡ PN/NH₂-*i*Pr (3a)



2,6-Diaminopyridine (2.00 eq; 62.95 mmol; 6.87 g) was suspended in 150 mL toluene/THF 1:1, Et₃N (2.00 eq; 62.95 mmol; 8.7 mL) was added and the mixture was cooled to 0°C. P*i*Pr₂Cl (1.00 eq; 31.47 mmol; 4.80 g) was added dropwise and the reaction was stirred at 80°C for 12 h. After cooling down to r.t., the solution was washed with 50 mL sat. NaHCO₃ solution, followed by 50 mL brine. The organic phase was dried over Na₂SO₄, filtered and the solvent was removed under reduced pressure. The remaining yellow solid was purified via flash chromatography, using silica gel (conditioned with 5 Vol% Et₃N) and 2:1 EE/PE → EE as eluent.

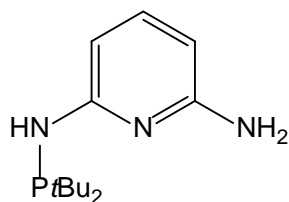
Yield: 4.32 g (61 %) white crystals

¹H-NMR (δ, CDCl₃, 20°C): 7.25 (t, ³J_{HH} = 7.9 Hz, 1H, py⁴), 6.46 (d, ³J_{HH} = 7.9 Hz, 1H, py³), 5.90 (d, ³J_{HH} = 7.7 Hz, 1H, py⁵), 4.40 (d, ²J_{PH} = 10.7 Hz, 1H, NH), 4.18 (s, 2H, NH₂), 1.77 (m, 2H, CH(CH₃)₂), 1.07 (m, 12H, CH(CH₃)₂).

¹³C{¹H}-NMR (δ, CDCl₃, 20°C): 159.86 (d, ²J_{CP} = 20.3 Hz, py²), 157.28 (s, py⁶), 139.42 (d, ⁴J_{CP} = 2.1 Hz, py⁴), 97.99 (d, ³J_{CP} = 18.3 Hz, py³), 97.99 (s, py⁵), 26.37 (d, ¹J_{CP} = 11.2 Hz, CH(CH₃)₂), 18.66 (d, ²J_{CP} = 19.7 Hz, CH(CH₃)₂), 17.05 (d, ²J_{CP} = 7.82 Hz, CH(CH₃)₂).

³¹P{¹H}-NMR (δ, CDCl₃, 20°C): 47.4.

***N*²-(ditertbutylphosphanyl)pyridin-2,6-diamin ≡ PN/NH₂-*t*Bu (3b)**



2,6-Diaminopyridine (2.00 eq; 47.37 mmol; 5.17 g) was dissolved in 120 mL THF and cooled to 0°C. After the addition of *n*-BuLi (1.02 eq; 24.16 mmol; 2.5 M; 9.6 mL) at 0°C, the solution was allowed to reach r.t. and was stirred for 3 h. P*t*Bu₂Cl (1.00 eq; 23.69 mmol; 4.28 g) was added and the reaction mixture was stirred at 80°C for 12 h. Workup was performed in the same way as for compound **2g**.

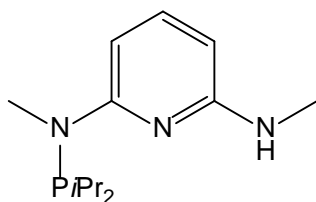
Yield: 2.70 g (45 %) white solid

¹H-NMR (δ, CDCl₃, 20°C): 7.25 (t, ³*J*_{HH} = 7.9 Hz, 1H, py⁴), 6.52 (dd, ³*J*_{HH} = 8.1 Hz, ⁴*J*_{PH} = 2.4 Hz, 1H, py³), 5.89 (d, ³*J*_{HH} = 7.7 Hz, 1H, py⁵), 4.67 (d, ²*J*_{PH} = 11.0 Hz, 1H, NH), 4.19 (s, 2H, NH₂), 1.16 (s, 9H, C(CH₃)₃), 1.13 (s, 9H, C(CH₃)₃).

¹³C{¹H}-NMR (δ, CDCl₃, 20°C): 160.25 (d, ²*J*_{CP} = 21.4 Hz, py²), 157.29 (d, ⁴*J*_{CP} = 1.5 Hz, py⁶), 139.39 (d, ⁴*J*_{CP} = 2.1 Hz, py⁴), 98.36 (d, ³*J*_{CP} = 18.8 Hz, py³), 97.96 (s, py⁵), 33.98 (d, ¹*J*_{CP} = 19.2 Hz, C(CH₃)₃), 28.08 (d, ²*J*_{CP} = 15.2 Hz, C(CH₃)₃).

³¹P{¹H}-NMR (δ, CDCl₃, 20°C): 58.2.

***N*²-(diisopropylphosphanyl)-*N*², *N*⁶-dimethylpyridine-2,6-amine ≡ PN/*N*^{Me}H-*i*Pr (3c)**



*N*²,*N*⁶-dimethylpyridine-2,6-diamine (1.00 eq; 22.96 mmol; 3.15 g) was dissolved in 100 mL toluene and cooled to 0°C. *n*-BuLi (1.05 eq; 24.11 mmol; 2.5 M; 9.6 mL) was added and the reaction was stirred at r.t. for 2 h. After cooling to 0°C, P*i*Pr₂Cl (1.00 eq; 22.96 mmol; 3.50 g) was added and the mixture was stirred at 80°C for 12 h. The reaction was quenched at r.t. by addition of 25 mL sat. NaHCO₃ solution, the organic phase was dried over Na₂SO₄, filtered and the solvent was removed under reduced pressure. The product was used without further purification for the next step.

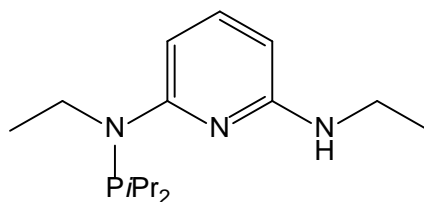
Yield: 5.26 g (90 %) yellow oil

¹H-NMR (δ, CDCl₃, 20°C): 7.22 (t, ³*J*_{HH} = 7.7 Hz, 1H, py⁴), 6.62 (bs, 1H, py³), 5.70 (d, ³*J*_{HH} = 8.0 Hz, 1H, py⁵), 4.27 (s, 1H, NH), 3.02 (s, 3H, N(H)CH₃), 2.82 (d, ³*J*_{PH} = 5.1 Hz, 3H, N(P)CH₃), 2.21 (m, 2H, CH(CH₃)₂), 1.08 (dd, ³*J*_{PH} = 17.0 Hz, ³*J*_{HH} = 7.0 Hz, 6H, CH(CH₃)₂), 0.97 (dd, ³*J*_{PH} = 12.1 Hz, ³*J*_{HH} = 7.0 Hz, 6H, CH(CH₃)₂).

¹³C{¹H}-NMR (δ, CDCl₃, 20°C): 160.45 (d, ²*J*_{CP} = 20.2 Hz, py²), 158.94 (s, py⁶), 137.07 (s, py⁴), 99.37 (d, ³*J*_{CP} = 21.4 Hz, py³), 93.99 (s, py⁵), 33.80 (bs, CH(CH₃)₂), 29.12 (s, N(H)CH₃), 26.21 (d, ²*J*_{CP} = 14.6 Hz, N(P)CH₃), 19.68 (s, CH(CH₃)₂), 19.40 (d, ²*J*_{CP} = 12.7 Hz, CH(CH₃)₂).

³¹P{¹H}-NMR (δ, CDCl₃, 20°C): 70.0.

***N*²-(diisopropylphosphanyl)-*N*², *N*⁶-diethylpyridine-2,6-amine ≡ PN/*N*^{Et}H-*i*Pr (3d)**



1e (1.00 eq; 21.60 mmol; 3.75 g) was dissolved in 200 mL toluene and *n*-BuLi (1.05 eq; 22.69 mmol; 2.5 M; 9.1 mL) was added at 0°C. After stirring at r.t. for 2 h, the mixture was cooled to 0°C and P*i*Pr₂Cl (1.00 eq; 21.60 mmol; 3.30 g) was added. The reaction was stirred at 80°C for 12 h. After quenching with 25 mL sat. NaHCO₃ solution, the organic phase was dried over Na₂SO₄, filtered and concentrated. The resulting yellow oil was used directly without further purification for subsequent reactions.

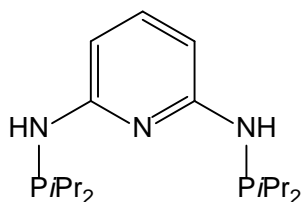
Yield: quantitative, yellow oil

¹H-NMR (δ, CDCl₃, 20°C): 7.20 (m, 1H, py⁴), 6.47 (bs, 1H, py³), 5.67 (d, ³J_{HH} = 7.9 Hz, 1H, py⁵), 4.14 (s, 1H, NH), 3.62 (m, 2H, N(P)CH₂CH₃), 3.19 (m, 2H, N(H)CH₂CH₃), 2.29 (m, 2H, CH(CH₃)₂), 1.13 – 0.82 (m, 18H, CH₂CH₃, CH(CH₃)₂).

¹³C{¹H}-NMR (δ, CDCl₃, 20°C): 159.11 (bs, py²), 158.26 (s, py⁶), 139.05 (s, py⁴), 102.04 (bs, py³), 94.28 (s, py⁵), 42.82 (bs, N(P)CH₂CH₃), 36.90 (s, N(H)CH₂CH₃), 26.20 (d, ¹J_{CP} = 15.1 Hz, CH(CH₃)₂), 19.87 (d, ²J_{CP} = 10.0 Hz, CH(CH₃)₂), 19.39 (s, CH(CH₃)₂), 14.93 (s, N(H)CH₂CH₃), 14.73 (s, N(P)CH₂CH₃).

³¹P{¹H}-NMR (δ, CDCl₃, 20°C): 78.8

***N*², *N*⁶-Bis(diisopropylphosphanyl)pyridin-2,6-diamin ≡ PNP-*i*Pr (4a)**



2,6-Diaminopyridine (1.00 eq; 34.26 mmol; 3.74 g) was suspended with Et₃N (3.00 eq; 102.77 mmol; 14.3 mL) in 300 mL toluene and cooled to 0°C. P*i*Pr₂Cl (2.02 eq; 69.20 mmol; 10.56 g) was added slowly via syringe and the reaction mixture was stirred for 12 h at 80°C. The white precipitate was filtered over Celite[®] and the solvent was removed under reduced pressure. The product crystallized as white solid after drying the oil for several hours under vacuum. If necessary, it can be purified by flash chromatography, using silica gel (conditioned with 5 Vol% Et₃N) and 3:1 PE/EE → EE as eluent.

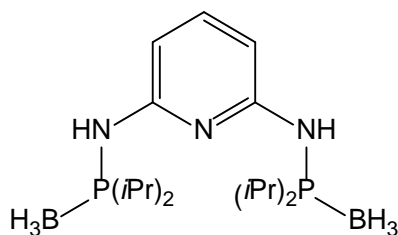
Yield: 10.60 g (91%) white solid

¹H-NMR (δ, CDCl₃, 20°C): 7.18 (t, ³*J*_{HH} = 7.9 Hz, 1H, py⁴), 6.38 (dd, ³*J*_{HH} = 7.9 Hz, ⁴*J*_{PH} = 2.2 Hz, 2H, py^{3,5}), 4.24 (d, ²*J*_{PH} = 11.1 Hz, 2H, NH), 1.68 (heptd, ³*J*_{HH} = 7.0 Hz, ²*J*_{PH} = 2.2 Hz, 4H, CH(CH₃)₂), 1.03 – 0.96 (m, 24H, CH(CH₃)₂).

¹³C{¹H}-NMR (δ, CDCl₃, 20°C): 159.54 (d, ²*J*_{CP} = 19.9 Hz, py^{2,6}), 139.10 (s, py⁴), 98.22 (d, ³*J*_{CP} = 18.4 Hz, py^{3,5}), 26.40 (d, ¹*J*_{CP} = 11.3 Hz, CH(CH₃)₂), 18.70 (d, ²*J*_{CP} = 19.6 Hz, CH(CH₃)₂), 17.13 (d, ²*J*_{CP} = 7.9 Hz, CH(CH₃)₂).

³¹P{¹H}-NMR (δ, CDCl₃, 20°C): 47.6.

***N*²,*N*⁶-bis(diisopropylphosphanyl)pyridine-2,6-diamine, borane adduct ≡ PNP-*i*Pr x2BH₃
(4b)**



4a (1.00 eq; 14.64 mmol; 5.00 g) was dissolved in 75 mL THF and cooled to 0°C. BH₃·THF (2.50 eq; 36.61 mmol; 1.0 M; 36.6 mL) was added slowly and the reaction was stirred at r.t. for 1h. After quenching with 10 mL sat. NaHCO₃ solution, the solvent was removed under reduced pressure. 100 mL water was added to the residue and extracted with 3x 100 mL CH₂Cl₂. The combined organic phases were washed with 50 mL brine, dried over Na₂SO₄, filtered, concentrated and dried under vacuum.

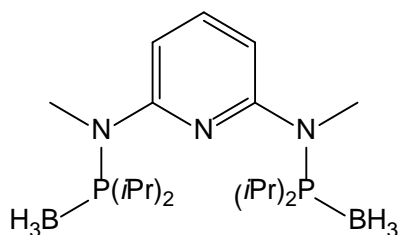
Yield: quantitative, white solid

¹H-NMR (δ, CDCl₃, 20°C): 7.36 (t, ³J_{HH} = 7.8 Hz, 1H, py⁴), 6.31 (d, ³J_{HH} = 7.9 Hz, 2H, py^{3,5}), 4.65 (d, ²J_{PH} = 7.6 Hz, 2H, NH), 2.65 (m, 4H, CH(CH₃)₂), 1.26 – 1.09 (m, 24H, CH(CH₃)₂), 0.58 – -0.15 (m, 6H, BH₃).

¹³C{¹H}-NMR (δ, CDCl₃, 20°C): 154.54 (d, ²J_{CP} = 4.4 Hz, py^{2,6}), 139.94 (s, py⁴), 103.16 (s, py^{3,5}), 24.48 (d, ¹J_{CP} = 36.5 Hz, CH(CH₃)₂), 16.92 (d, ²J_{CP} = 3.3 Hz, CH(CH₃)₂), 16.72 (s, CH(CH₃)₂).

³¹P{¹H}-NMR (δ, CDCl₃, 20°C): 76.6.

***N*²,*N*⁶-Bis(diisopropylphosphanyl)-*N*²,*N*⁶-dimethylpyridine-2,6-diamine, borane adduct ≡ PNP^{Me}-*i*Pr x2BH₃ (4c)**



To a solution of **4b** (1.00 eq; 20.18 mmol; 7.45 g) in 100 mL THF *n*-BuLi (2.05 eq; 41.38 mmol; 2.5 M; 17.0 mL) was added slowly at 0°C. The reaction mixture was allowed to reach room temperature and was stirred for 2 h. Methyl iodide (2.50 eq; 50.46 mmol; 3.15 mL) was then added slowly via syringe. After the mixture was stirred for 12 h at room temperature, the reaction was quenched with 100 mL sat. NH₄Cl solution and 5 mL conc. NH₃. The aqueous phase was extracted with 2x 100 mL CH₂Cl₂, the combined organic phases were washed with 50 mL brine, dried over Na₂SO₄, filtered and the solvent was removed under reduced pressure. The crude product was purified by flash chromatography, using silica gel and THF as eluent.

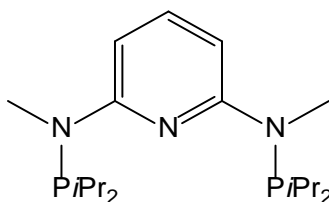
Yield: 5.05 g (63%) white solid

¹H-NMR (δ, CDCl₃, 20°C): 7.48 (t, ³J_{HH} = 8.0 Hz, 1H, py⁴), 6.49 (d, ³J_{HH} = 8.0 Hz, 2H, py^{3,5}), 3.17 (d, ³J_{PH} = 7.9 Hz, 6H, NCH₃), 2.80 (m, 4H, CH(CH₃)₂), 1.22 (dd, ³J_{PH} = 16.5 Hz, ³J_{HH} = 6.9 Hz, 6H, CH(CH₃)₂), 1.03 (dd, ³J_{PH} = 15.1 Hz, ³J_{HH} = 7.0 Hz, 6H, CH(CH₃)₂), 0.81 – -0.02 (m, 6H, BH₃).

¹³C{¹H}-NMR (δ, CDCl₃, 20°C): 156.89 (s, py^{2,6}), 139.08 (s, py⁴), 105.84 (s, py^{3,5}), 37.57 (d, ²J_{CP} = 5.1 Hz, NCH₃), 25.57 (d, ¹J_{CP} = 36.2 Hz, CH(CH₃)₂), 17.83 (d, ²J_{CP} = 2.8 Hz, CH(CH₃)₂), 17.17 (s, CH(CH₃)₂).

³¹P{¹H}-NMR (δ, CDCl₃, 20°C): 94.0

***N*²,*N*⁶-Bis(diisopropylphosphanyl)-*N*²,*N*⁶-dimethylpyridine-2,6-diamine ≡ PNP^{Me}-iPr (4d)**



Method A: **4c** (1.00 eq; 12.59 mmol; 5.00 g) was refluxed for 48 h in Et₂NH. After removal of the solvent under reduced pressure, the remaining oil was dissolved in 100 mL THF, filtered over a small pad of Celite[®], and obtained as a yellow oil after evaporation. The crude product was purified by recrystallization from hot acetonitrile.

Yield: 3.25 g (70 %) white solid

Method B: **3c** (1.00 eq; 20.25 mmol; 5.13 g) was dissolved in 100 mL toluene and cooled to 0°C. *n*-BuLi (1.05 eq; 21.26 mmol; 2.5 M; 8.5 mL) was added and the reaction was stirred at r.t. for 2 h. After cooling to 0°C, P*i*Pr₂Cl (1.00 eq; 20.25 mmol; 3.09 g) was added and the mixture was stirred at 80°C for 12 h. The reaction was quenched at r.t. by addition of 25 mL sat. NaHCO₃ solution, the organic phase was dried over Na₂SO₄, filtered and the solvent was removed under reduced pressure. The crude product was purified by recrystallization from hot acetonitrile.

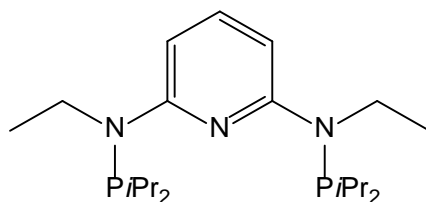
Yield: 5.39 g (72%) white solid

¹H-NMR (δ, CDCl₃, 20°C): 7.22 (t, ³*J*_{HH} = 8.0 Hz, 1H, py⁴), 6.64 (d, ³*J*_{HH} = 5.8 Hz, 2H, py^{3,5}), 3.04 (d, ³*J*_{PH} = 2.3 Hz, 6H, NCH₃), 2.22 (m, 4H, CH(CH₃)₂), 1.10 (dd, ³*J*_{PH} = 16.9 Hz, ³*J*_{HH} = 6.9 Hz, 12H, CH(CH₃)₂), 0.98 (dd, ³*J*_{PH} = 12.1 Hz, ³*J*_{HH} = 7.0 Hz, 12H, CH(CH₃)₂).

¹³C{¹H}-NMR (δ, CDCl₃, 20°C): 160.58 (d, ²*J*_{CP} = 20.2 Hz, py^{2,6}), 136.90 (s, py⁴), 99.07 (d, ³*J*_{CP} = 22.1 Hz, py^{3,5}), 33.66 (bs, CH(CH₃)₂), 26.16 (d, ²*J*_{CP} = 15.3 Hz, NCH₃), 19.40 (d, ²*J*_{CP} = 3.4 Hz, CH(CH₃)₂), 19.11 (d, ²*J*_{CP} = 10.7 hz, CH(CH₃)₂).

³¹P{¹H}-NMR (δ, CDCl₃, 20°C): 69.5.

***N*², *N*⁶-bis(diisopropylphosphanyl)-*N*², *N*⁶-diethylpyridine-2,6-amine ≡ PNP^{Et}-iPr (4e)**



3d (1.00 eq; 21.29 mmol; 5.99 g) was dissolved in toluene and *n*-BuLi (1.05 eq; 22.35 mmol; 2.5 M; 14.0 mL) was added slowly at 0°C. After stirring at r.t. for 2 h, the mixture was cooled to 0°C and P*i*Pr₂Cl (1.00 eq; 21.29 mmol; 3.25 g) was added. The reaction was stirred at 80°C for 12 h. After quenching with 25 mL sat. NaHCO₃ solution, the organic phase was dried over Na₂SO₄, filtered and concentrated. The product was purified by flash chromatography using silica (conditioned with 5 Vol% Et₃N) and 5:1 PE/EE as eluent.

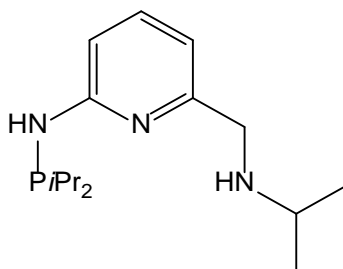
Yield: 6.87 g (81%) yellow oil

¹H-NMR (δ, CDCl₃, 20°C): 7.26 (t, ³*J*_{HH} = 8.0 Hz, 1H, py⁴), 6.50 (bs, 2H, py^{3,5}), 3.65 (qd, ³*J*_{PH} = 6.7 Hz, ³*J*_{HH} = 6.9 Hz, 4H, NCH₂), 2.36 (bs, 4H, CH(CH₃)₂), 1.18 – 0.98 (m, 30H, CH₃).

¹³C{¹H}-NMR (δ, CDCl₃, 20°C): 159.25 (d, ²*J*_{CP} = 10.5 Hz; py^{2,6}), 137.30 (s, py⁴), 102.02 (d, ³*J*_{CP} = 15.1 Hz, py^{3,5}), 43.56 (bs, NCH₂CH₃), 26.21 (d, ¹*J*_{CP} = 15.4 Hz, CH(CH₃)₂), 19.83 (d, ²*J*_{CP} = 15.4 Hz, CH(CH₃)₂), 19.33 (s, CH(CH₃)₂), 14.71 (s, NCH₂CH₃).

³¹P{¹H}-NMR (δ, CDCl₃, 20°C): 78.8.

***N*-(diisopropylphosphanyl)-6-(isopropylamino)methylpyridine-2-amine \equiv PNN-*i*Pr (4f)**



1k (1.00 eq; 14.28 mmol; 2.36 g) and Et₃N (1.50 eq; 21.42 mmol; 3.0 mL) were dissolved in 100 mL dry toluene and cooled to 0°C. *i*Pr₂PCl (1.02 eq; 14.57 mmol; 2.22 g) was added and the solution was stirred at 80°C for 12 h. The suspension was filtered over Celite[®] at r.t. and the solution was concentrated under reduced pressure.

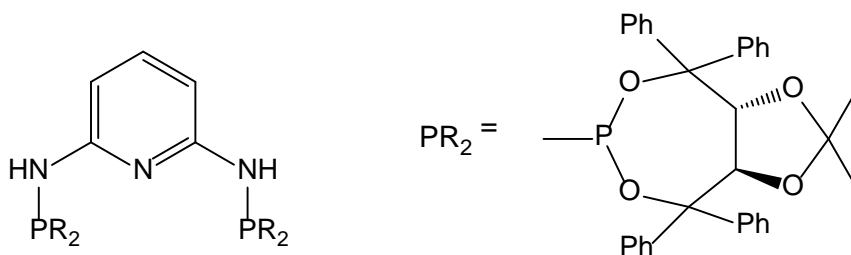
Yield: 3.63 (90%) white solid

¹H-NMR (δ, CDCl₃, 20°C): 7.40 (m, 1H, py⁴), 6.98 (dd, ³J_{HH} = 8.3 Hz, ⁴J_{PH} = 2.4 Hz, 1H, py³), 6.64 (d, ³J_{HH} = 7.0 Hz, 1H, py⁵), 4.68 (d, ²J_{PH} = 10.9 Hz, 1H, PNH), 3.74 (s, 2H, CH₂), 2.89 (hept, 1H, NCH(CH₃)₂), 2.46 (s, 1H, NH), 1.81 (m, 2H, PCH(CH₃)₂), 1.18 – 1.03 (m, 18H, PCH(CH₃)₂).

¹³C{¹H}-NMR (δ, CDCl₃, 20°C): 160.47 (d, ²J_{CP} = 19.7 Hz, py²), 157.72 (s, py⁶), 137.9 (d, ⁴J_{CP} = 2.2 Hz, py⁴), 112.49 (s, py⁵), 106.79 (d, ³J_{CP} = 18.5 Hz, py³), 52.61 (s, CH₂), 48.53 (s, NCH(CH₃)₂), 26.38 (d, ¹J_{CP} = 11.1 Hz, PCH(CH₃)₂), 22.82 (s, NCH(CH₃)₂), 18.66 (d, ²J_{CP} = 19.7 Hz, PCH(CH₃)₂), 17.11 (d, ²J_{CP} = 7.8 Hz, PCH(CH₃)₂).

³¹P{¹H}-NMR (δ, CDCl₃, 20°C): 48.4.

***N*²,*N*⁶-bis((3*aR*, 8*aR*)-2,2-dimethyl-4,4,8,8-tetraphenyltetrahydro-[1,3]dioxolo[4,5-*e*][1,3,2]dioxaphosphepin-6-yl)pyridine-2,6-diamin ≡ PNP-TAD (4g)**



To a solution of DAP (1.00 eq; 4.11 mmol; 415 mg) in 100 mL dry toluene NEt₃ (2.50 eq; 10.27 mmol; 1.1 mL) was added. After cooling to 0°C, a solution of **1c** (2.10 eq; 8.63 mmol; 4.58 g) in 30 mL toluene was added and the reaction mixture was stirred for 12 h at 80°C. The suspension was filtered over a small pad of Celite[®] and the solvent was removed under reduced pressure. The product was obtained as white powder in sufficient purity for subsequent reactions. It can be purified via flash chromatography, using silica (conditioned with 5 Vol% NEt₃) and 5:1 PE/EE as eluent.

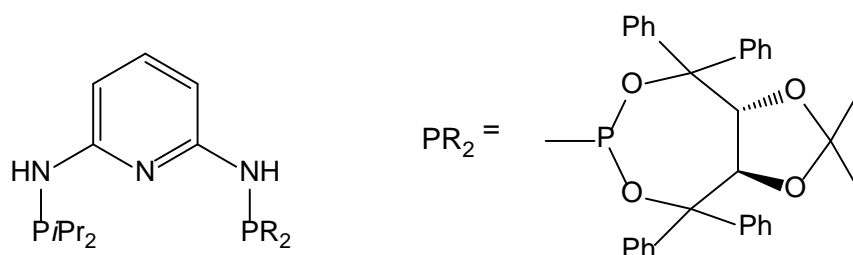
Yield: 3.61 g (80%) white solid

¹H-NMR (δ, CDCl₃, 20°C): 7.66 (m, 4H, ph), 7.58 (m, 4H, ph), 7.38 – 7.05 (m, 33H, ph, py⁴), 6.06 (d, ³J_{HH} = 8.0 Hz, 2H, py^{3,5}), 5.50 (d, ²J_{PH} = 3.9 Hz, 2H, NH), 5.26 (dd, ³J_{HH} = 8.4 Hz, ⁴J_{PH} = 2.8 Hz, 2H, CH^{TAD}), 4.86 (d, ³J_{HH} = 8.5 Hz, 2H, CH^{TAD}), 1.21 (s, 6H, CH₃^{TAD}), 0.23 (s, 6H, CH₃^{TAD}).

¹³C{¹H}-NMR (δ, CDCl₃, 20°C): 154.36 (d, ²J_{CP} = 17.3 Hz, py^{2,6}), 146.12 (s, ph¹), 145.53 (d, ³J_{CP} = 2.8 Hz, ph¹), 141.73 (d, ³J_{CP} = 1.9 Hz, ph¹), 140.95 (d, ³J_{CP} = 1.8 Hz, ph¹), 139.22 (s, py⁴), 129.02 (s, ph), 128.59 (d, J = 3.4 Hz, ph), 128.19 (s, ph), 127.80 (s, ph), 127.75 (s, ph), 127.53 (s, ph), 127.45 (s, ph), 127.36 (s, ph), 127.26 (s, ph), 127.15 (d, J = 3.2 Hz, ph), 112.17 (C(CH₃)₂^{TAD}), 100.75 (d, ³J_{CP} = 13.2 Hz, py^{3,5}), 82.95 (s, C(ph)₂), 82.67 (d, ³J_{CP} = 7.7 Hz, CH^{TAD}), 82.48 (d, ³J_{CP} = 6.0 Hz, CH^{TAD}), 82.24 (s, C(ph)₂), 27.49 (s, CH₃^{TAD}), 25.32 (s, CH₃^{TAD}).

³¹P{¹H}-NMR (δ, CDCl₃, 20°C): 134.0.

***N*'-(diisopropylphosphanyl)-*N*'-((3*aR*,8*aR*)-2,2-dimethyl-4,4,8,8-tetraphenyltetrahydro-[1,3]dioxolo[4,5-*e*][1,3,2]dioxaphosphepin-6-yl)pyridine-2,6-diamine \equiv PNP-*i*Pr/TAD (4h)**



To a solution of **3a** (1.00 eq; 8.84 mmol; 2.00 g) in 100 mL dry toluene NEt₃ (1.50 eq; 13.26 mmol; 1.9 mL) was added. After cooling to 0°C, a solution of **1c** (1.10 eq; 9.72 mmol; 5.16 g) in 30 mL toluene was added and the reaction mixture was stirred for 12 h at 80°C. The suspension was filtered over a small pad of Celite[®] and the solvent was removed under reduced pressure. The product was obtained as white powder in sufficient purity for subsequent reactions. It can be purified via flash chromatography, using silica (conditioned with 5 Vol% NEt₃) and 1:1:1 EE/PE/CH₂Cl₂ as eluent.

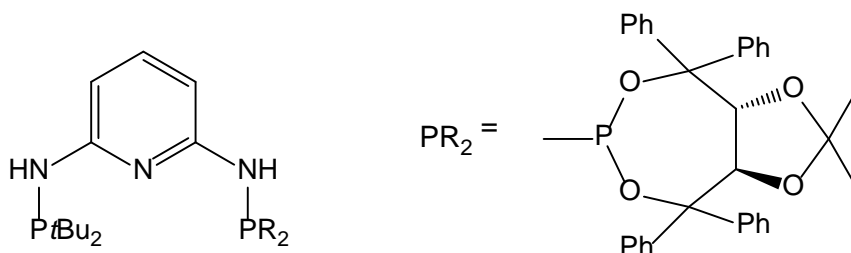
Yield: 3.48 g (63%) white solid

¹H-NMR (δ, CDCl₃, 20 °C): 7.74 – 7.63 (m, 4H, ph), 7.47 – 7.19 (m, 17H, ph, py⁴), 6.61 (dd, *J*₁ = 8.1 Hz, *J*₂ = 2.2 Hz, 1H, py³), 6.06 (d, *J* = 7.7 Hz, 1H, py⁵), 5.67 (d, *J* = 4.3 Hz, 1H, NH^{TAD}), 5.32 (dd, *J*₁ = 8.5 Hz, *J*₂ = 2.8 Hz, 1H, CH^{TAD}), 4.94 (d, *J* = 8.5 Hz, 1H, CH^{TAD}), 4.43 (d, *J* = 11.2 Hz, 1H, NH^{iPr}), 1.80 (m, 2H, CH(CH₃)₂^{iPr}), 1.39 (s, 3H, CH₃^{TAD}), 1.12 – 1.01 (m, 12H, CH(CH₃)₂^{iPr}), 0.34 (s, 3H, CH₃^{TAD}).

¹³C{¹H}-NMR (δ, CDCl₃, 20 °C): 159.96 (d, ²*J*_{CP} = 20.4 Hz, py²), 154.19 (d, ²*J*_{CP} = 16.2 Hz, py⁶), 146.42 (s, ph), 145.58 (s, ph), 141.62 (s, ph), 140.95 (s, ph), 139.12 (s, py⁴), 128.96 (s, ph), 128.52 (s, ph), 128.49 (s, ph), 128.15 (s, ph), 127.71 (s, ph), 127.67 (s, ph), 127.61 (s, ph), 127.37 (s, ph), 127.28 (s, ph), 127.16 (s, ph), 112.12 (s, C(CH₃)₂^{TAD}), 99.85 (d, ³*J*_{CP} = 18.8 Hz, py³), 99.03 (d, ³*J*_{CP} = 9.3 Hz, py⁵), 82.87 (bs, CH^{TAD}), 82.68 (s, C(ph)₂), 82.46 (bs, CH^{TAD}, C(ph)₂), 27.22 (s, CH₃^{TAD}), 26.37 (d, ¹*J*_{CP} = 10.8 Hz, CH(CH₃)₂^{iPr}), 26.27 (d, ¹*J*_{CP} = 9.9 Hz, CH(CH₃)₂^{iPr}), 24.89 (s, CH₃^{TAD}), 18.53 (d, ²*J*_{CP} = 3.6 Hz, CH(CH₃)₂^{iPr}), 18.33 (d, ²*J*_{CP} = 3.8 Hz, CH(CH₃)₂^{iPr}), 16.99 (d, ²*J*_{CP} = 8.3 Hz, CH(CH₃)₂^{iPr}), 16.90 (d, ²*J*_{CP} = 7.7 Hz, CH(CH₃)₂^{iPr}).

³¹P{¹H}-NMR (δ, CDCl₃, 20 °C): 134.6 (s, TAD), 47.9 (s, *i*Pr).

***N*²-(di-tert-butylphosphanyl)-*N*⁶-((3*aR*,8*aR*)-2,2-dimethyl-4,4,8,8-tetraphenyltetrahydro-[1,3]dioxolo[4,5-*e*][1,3,2]dioxaphosphepin-6-yl)pyridine-2,6-diamine ≡ PNP-*t*Bu/TAD (4i)**



This ligand was prepared analogously to **4h** with **3b** (1.00 eq; 3.39 mmol; 0.86 g) and **1c** (1.10 eq; 3.73 mmol; 1.98 g) as starting materials.

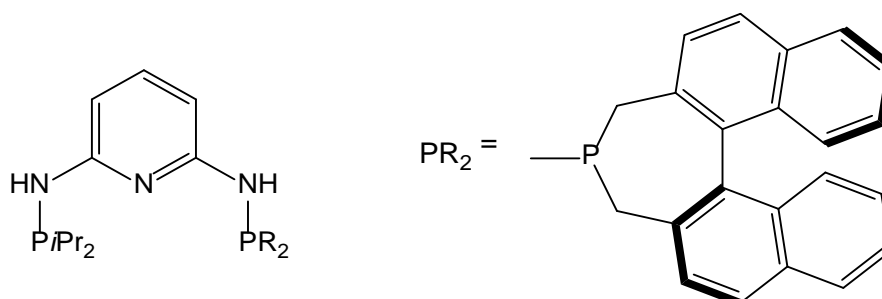
Yield: 2.39 g (94%) white solid

¹H-NMR (δ, CDCl₃, 20 °C): 7.73 (m, 2H, ph), 7.64 (m, 2H, ph), 7.50 – 7.16 (m, 17H, ph, py⁴), 6.63 (dd, ³J_{HH} = 8.0 Hz, ⁴J_{PH} = 2.2 Hz, 1H, py³), 6.10 (d, ³J_{HH} = 7.8 Hz, 1H, py⁵), 5.55 (d, ²J_{PH} = 2.4 Hz, 1H, NH^{TAD}), 5.32 (dd, ³J_{HH} = 8.4 Hz, ⁴J_{PH} = 2.4 Hz, 1H, CH^{TAD}), 4.99 (d, ³J_{HH} = 8.4 Hz, 1H, CH^{TAD}), 4.67 (d, ²J_{PH} = 11.2 Hz, 1H, NH^{tBu}), 1.22 (s, 3H, CH₃^{TAD}), 1.17 (d, ³J_{PH} = 4.7 Hz, 9H, C(CH₃)₃^{tBu}), 1.12 (d, ³J_{PH} = 4.7 Hz, 9H, C(CH₃)₃^{tBu}), 0.35 (s, 3H, CH₃^{TAD}).

¹³C{¹H}-NMR (δ, CDCl₃, 20 °C): 160.19 (d, ²J_{CP} = 21.8 Hz, py²), 153.90 (d, ²J_{CP} = 19.0 Hz, py⁶), 145.99 (s, ph¹), 145.52 (s, ph¹), 141.74 (s, ph¹), 140.95 (s, ph¹), 139.26 (s, py⁴), 128.93 (s, ph), 128.54 (s, ph), 128.19 (s, ph), 127.71 (s, ph), 127.47 (s, ph), 127.36 (s, ph), 127.15 (s, ph), 127.06 (s, ph), 126.65 (s, ph), 112.36 (C(CH₃)₂^{TAD}), 100.36 (d, ³J_{CP} = 19.2 Hz, py³), 99.07 (d, ³J_{CP} = 15.2 Hz, py⁵), 83.34 (s, C(ph)₂), 82.66 (d, ³J_{CP} = 7.6 Hz, CH^{TAD}), 82.27 (d, ³J_{CP} = 7.8 Hz, CH^{TAD}), 82.12 (s, C(ph)₂), 33.96 (d, ¹J_{CP} = 19.1 Hz, C(CH₃)₃^{tBu}), 28.19 (C(CH₃)₃^{tBu}), 27.95 (C(CH₃)₃^{tBu}), 27.33 (CH₃^{TAD}), 25.39 (CH₃^{TAD}).

³¹P{¹H}-NMR (δ, CDCl₃, 20 °C): 132.4 (s, TAD), 58.6 (s, tBu).

**(1*R*)-*N*²-(3,5-dihydro-4*H*-dinaphtho[2,1-*c*:1',2'-*e*]phosphhepin-4-yl)-*N*⁶-
(diisopropylphosphanyl)pyridine-2,6-diamine ≡ PNP-BIN/*i*Pr (4j)**



3a (1.00 eq; 6.55 mmol; 1.47 g) was dissolved in 100 mL toluene and Et₃N (1.50 eq; 9.83 mmol; 1.4 mL) was added. After cooling to 0°C, **1o** (1.10 eq; 7.21 mmol; 2.50 g) in 50 mL toluene was added and the reaction was stirred at 80°C for 12 h. The suspension was filtered over a small pad of Celite® and the solvent was removed under reduced pressure. The crude product was purified via flash chromatography, using silica gel (conditioned with 5 Vol% Et₃N) and 1:1 MC/EE as eluent.

Yield: 2.25 g (64%)

¹H-NMR (δ, CDCl₃, 20°C): 7.89 – 7.79 (m, 4H, naph), 7.47 (d, ³*J*_{HH} = 8.3 Hz, 1H, naph), 7.38 – 7.32 (m, 2H, naph), 7.31 (d, ³*J*_{HH} = 8.3 Hz, 1H, naph), 7.23 (m, 5H, py⁴, naph), 6.43 (dd, ³*J*_{HH} = 8.0 Hz, ⁴*J*_{PH} = 1.9 Hz, 1H, py⁵), 6.22 (d, ³*J*_{HH} = 8.4 Hz, 1H, py³), 4.31 (d, ²*J*_{PH} = 10.9 Hz, 1H, NH^{BIN}), 4.08 (d, ²*J*_{PH} = 10.7 Hz, 1H, NH^{iPr}), 3.03 (dd, ²*J*_{HH} = 17.0 Hz, ²*J*_{PH} = 11.9 Hz, 1H, CH₂), 2.70 (dd, ²*J*_{HH} = 14.3 Hz, ²*J*_{PH} = 2.8 Hz, 1H, CH₂), 2.50 (dd, ²*J*_{HH} = 18.2 Hz, ²*J*_{PH} = 14.3 Hz, 1H, CH₂), 2.29 (d, ²*J*_{HH} = 11.9 Hz, 1H, CH₂), 1.68 (m, 2H, CH(CH₃)₂), 1.04 – 0.95 (m, 12H, CH(CH₃)₂).

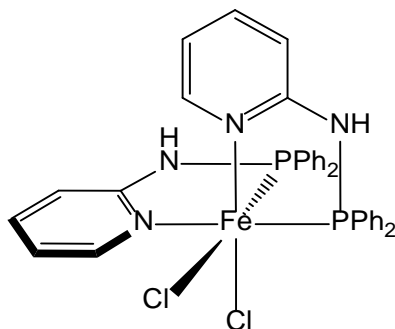
¹³C{¹H}-NMR (δ, CDCl₃, 20°C): 159.92 (d, ²*J*_{CP} = 20.0 Hz, py⁶), 157.01 (d, ²*J*_{CP} = 17.4, py²), 139.25 (s, py⁴), 133.79 (d, *J*_{CP} = 4.1Hz, naph), 133.43 (s, naph), 133.08 (s, naph), 132.82 (d, *J*_{CP} = 1.5 Hz, naph), 132.72 (s, naph), 132.38 (s, naph), 132.28 (d, *J*_{CP} = 1.8 Hz, naph), 132.15 (s, naph), 128.24 (s, naph), 127.58 (s, naph), 127.23 (d, *J*_{CP} = 2.1 Hz, naph), 126.69 (d, *J*_{CP} = 10.8 Hz, naph), 126.06 (d, *J*_{CP} = 11.5 Hz, naph), 125.09 (d, *J*_{CP} = 11.9 Hz, naph), 98.90 (d, ³*J*_{CP} = 18.4 Hz, py⁵), 98.73 (d, ³*J*_{CP} = 15.7, py³), 36.04 (d, ¹*J*_{CP} = 15.0 Hz, CH₂), 34.90 (d, ¹*J*_{CP} = 24.2 Hz, CH₂), 26.43 (d, ¹*J*_{CP} = 11.5 Hz, CH(CH₃)₂), 16.34 (d, ¹*J*_{CP} = 11.0 Hz, CH(CH₃)₂), 18.72 (d, ²*J*_{CP} = 19.8 Hz, CH(CH₃)₂), 17.22 (d, ²*J*_{CP} = 10.6 Hz, CH(CH₃)₂), 17.14 (d, ²*J*_{CP} = 10.4 Hz, CH(CH₃)₂).

³¹P{¹H}-NMR (δ, CDCl₃, 20°C): 48.6 (s, *i*Pr), 48.1 (s, BIN).

5.6 Iron (II) complexes

5.6.1 PN iron(II) complexes

cis-Fe(PN-Ph)₂Cl₂ (**5a**)

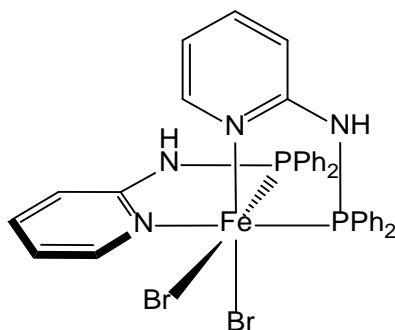


A solution of anhydrous FeCl₂ (1.00 eq; 0.88 mmol; 111 mg) and **2a** (2.05 eq; 1.80 mmol; 500 mg) was stirred in 15 mL THF at r.t. for 12 h. The solvent was then removed under reduced pressure. The remaining white solid was suspended in 20 mL toluene, collected on a glass frit, washed with 2x 15 mL toluene and 2x 15 mL *n*-pentane and dried at 50°C under vacuum for 3 h.

Yield: 510 mg (85%) white solid

ESI-MS (*m/z*, CH₃OH, NaCl) positive ion: 647.10 [M-Cl]⁺.

***cis*-Fe(PN-Ph)₂Br₂ (5b)**

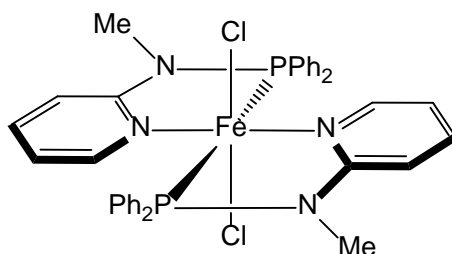


This complex was prepared analogously to **5a** with anhydrous FeBr₂ (1.00 eq; 0.88 mmol; 189 mg) and **2a** (2.05 eq; 1.80 mmol; 500 mg) as starting materials.

Yield: 510 mg (85%) white solid

ESI-MS (*m/z*, CH₃OH, NaBr) positive ion: 691.05 [M-Br]⁺.

***trans*-Fe(PN^{Me}-Ph)₂Cl₂ (5c)**

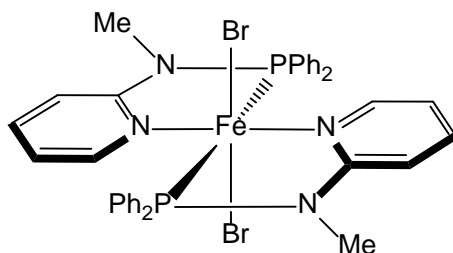


A solution of anhydrous FeCl₂ (1.00 eq; 0.79 mmol; 100 mg) and **2b** (2.05 eq; 1.62 mmol; 473 mg) was stirred in 15 mL THF at r.t. for 12 h. The solvent was then removed under reduced pressure. The residue was dissolved in 15 mL CH₂Cl₂, filtered, concentrated to 0.5 mL and precipitated with 40 mL *n*-pentane. The product was collected by filtration, washed with 2x 15 mL *n*-pentane and dried under vacuum.

Yield: 519 mg (92%) white solid

ESI-MS (*m/z*, CH₃OH, NaCl) positive ion: 675.13 [M-Cl]⁺.

***trans*-Fe(PN^{Me}-Ph)₂Br₂ (5d)**

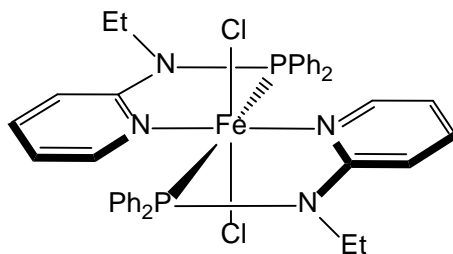


This complex was prepared analogously to **5c** with anhydrous FeBr₂ (1.00 eq; 0.81 mmol; 176 mg) and PN^{Me}-Ph (2.05 eq; 1.67 mmol; 488 mg) as starting materials.

Yield: 595 mg (91%) white solid

ESI-MS (*m/z*, CH₃OH, NaBr) positive ion: 719.08 [M-Br]⁺.

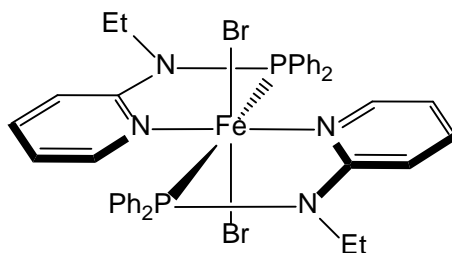
***trans*-Fe(PN^{Et}-Ph)₂Cl₂ (5e)**



This complex was prepared analogously to **5c** with anhydrous FeCl₂ (1.00 eq; 0.81 mmol; 103 mg) and **2c** (2.05 eq; 1.67 mmol; 510 mg) as starting materials.

Yield: 522 mg (87%) white solid

***trans*-Fe(PN^{Et}-Ph)₂Br₂ (**5f**)**

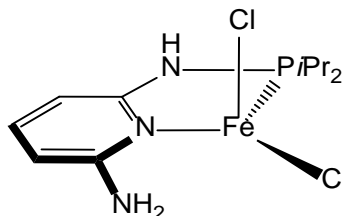


This complex was prepared analogously to **5c** with anhydrous FeBr₂ (1.00 eq; 0.72 mmol; 156 mg) and **2c** (2.05 eq; 1.48 mmol; 455 mg) as starting materials.

Yield: 515 mg (86%) white solid

5.6.2 PN/NH₂ iron(II) complexes

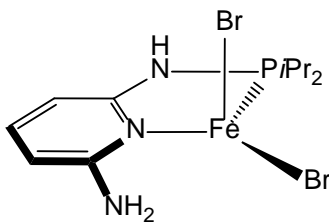
Fe(PN/NH₂-*i*Pr)Cl₂ (5g**)**



3a (1.05 eq; 1.33 mmol; 300 mg) was stirred with anhydrous FeCl₂ (1.00 eq; 1.27 mmol; 161 mg) in 15 mL THF₂ for 12 h. The yellow suspension was concentrated to 0.5 mL and the product was precipitated with 40 mL Et₂O. After filtration, the yellow solid was washed with 2x 10 mL Et₂O and dried under vacuum.

Yield: 352 mg (79%) yellow solid

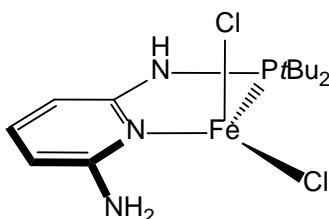
Fe(PN/NH₂-*i*Pr)Br₂ (**5h**)



This complex was prepared analogously to **5g** with **3a** (1.05 eq; 1.33 mmol; 300 mg) and anhydrous FeBr₂ (1.00 eq; 1.27 mmol; 274 mg) as starting materials.

Yield: 432 mg (77%) yellow solid

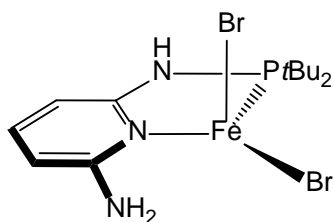
Fe(PN/NH₂-*t*Bu)Cl₂ (**5i**)



This complex was prepared analogously to **5g** with **3b** (1.05 eq; 1.18 mmol; 300 mg) and anhydrous FeCl₂ (1.00 eq; 1.13 mmol; 143 mg) as starting materials.

Yield: 349 mg (81%) yellow solid

Fe(PN/NH₂-*t*Bu)Br₂ (**5j**)

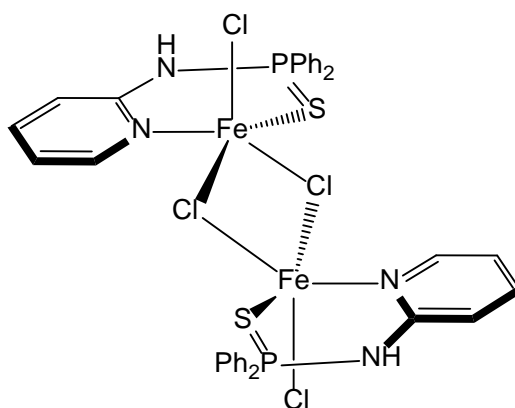


This complex was prepared analogously to **5g** with **3b** (1.05 eq; 1.18 mmol; 300 mg) and anhydrous FeBr₂ (1.00 eq; 1.13 mmol; 243 mg) as starting materials.

Yield: 425 mg (80%) yellow solid

5.6.3 SN iron(II) complexes

[Fe(SN-Ph)₂(μ-Cl)Cl]₂ (**5k**)

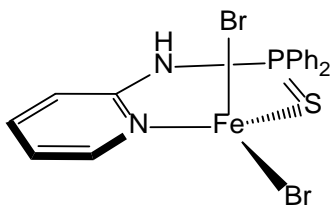


Anhydrous FeCl₂ (1.00 eq; 0.78 mmol; 97 mg) and **2d** (1.05 eq; 0.81 mmol; 250 mg) was stirred in 15 mL THF at r.t. for 12 h. The solvent was then evaporated to 0.5 mL and the product was precipitated by addition of 40 mL *n*-hexane. The white solid was filtered, washed with 2x 15 mL *n*-pentane and dried under vacuum.

Yield: 304 mg (83%) white solid

ESI-MS (*m/z*, *i*PrOH, NaCl) positive ion: 836.91 [M-Cl]⁺.

Fe(SN-Ph)Br₂ (**5l**)

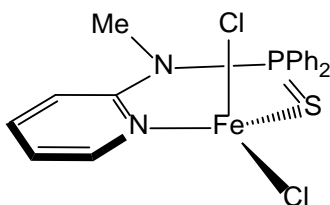


This complex was prepared analogously to **5k** with anhydrous FeBr₂ (1.00 eq; 0.61 mmol; 132 mg) and **2d** (1.05 eq; 0.64 mmol; 200 mg) as starting materials.

Yield: 304 mg (83%) white solid

ESI-MS (*m/z*, *i*PrOH, NaBr) positive ion: 546.83 [M+Na]⁺

Fe(SN^{Me}-Ph)Cl₂ (**5m**)

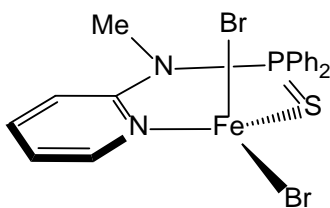


This complex was prepared analogously to **5k** with **2e** (1.05 eq; 0.77 mmol; 250 mg) and anhydrous FeCl₂ (1.00 eq; 0.73 mmol; 93 mg) as starting materials.

Yield: 256 mg (77%) white solid

ESI-MS (*m/z*, *i*PrOH, NaCl) positive ion: 472.95 [M+Na]⁺.

$\text{Fe}(\text{SN}^{\text{Me}}\text{-Ph})\text{Br}_2$ (**5n**)

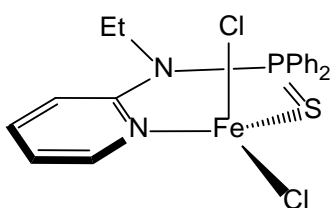


This complex was prepared analogously to **5k** with **2e** (1.05 eq; 0.62 mmol; 200 mg) and anhydrous FeBr_2 (1.00 eq; 0.59 mmol; 127 mg) as starting materials.

Yield: 240 mg (76%) white solid

ESI-MS (m/z , *i*PrOH, NaBr) positive ion: 560.85 $[\text{M}+\text{Na}]^+$.

$\text{Fe}(\text{SN}^{\text{Et}}\text{-Ph})\text{Cl}_2$ (**5o**)

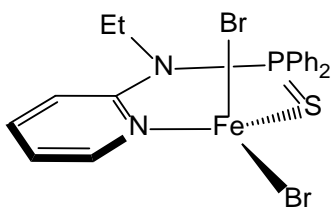


This complex was prepared analogously to **5k** with **2f** (1.05 eq; 74 mmol; 250 mg) and anhydrous FeCl_2 (1.00 eq; 0.70 mmol; 89 mg) and as starting materials.

Yield: 240 mg (81%) white solid

ESI-MS (m/z , *i*PrOH, NaCl) positive ion: 486.96 $[\text{M}+\text{Na}]^+$.

Fe(SN^{Et}-Ph)Br₂ (5p)



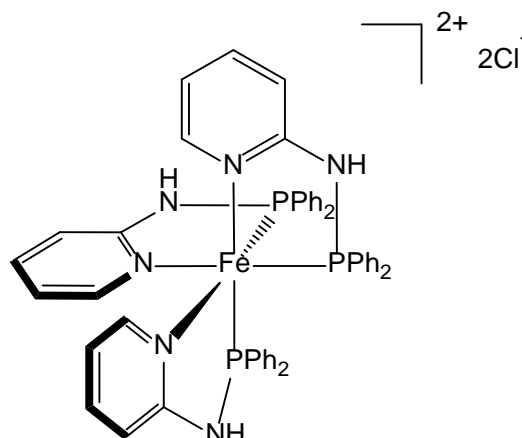
This complex was prepared analogously to **5k** with **2f** (1.05 eq; 59 mmol; 200 mg) and anhydrous FeBr₂ (1.00 eq; 0.56 mmol; 89 mg) and as starting materials.

Yield: 240 mg (85%) white solid

ESI-MS (*m/z*, *i*PrOH, NaBr) positive ion: 574.84 [M+Na]⁺.

5.6.4 (PN)₃ iron(II) complexes

cis-P,N-[Fe(PN-Ph)₃]Cl₂ (**5q**)



A solution of anhydrous FeCl₂ (1.00 eq; 0.35 mmol; 44 mg) and **2a** (3.10 eq; 1.08 mmol; 300 mg) was stirred in 15 mL MeOH at r.t. for 12 h. The red solution was filtered, the solvent was reduced to 0.5 mL and the product was precipitated by addition of 40 mL ether. The pink solid was filtered, washed with 2x 15 mL ether and dried under vacuum for 2h.

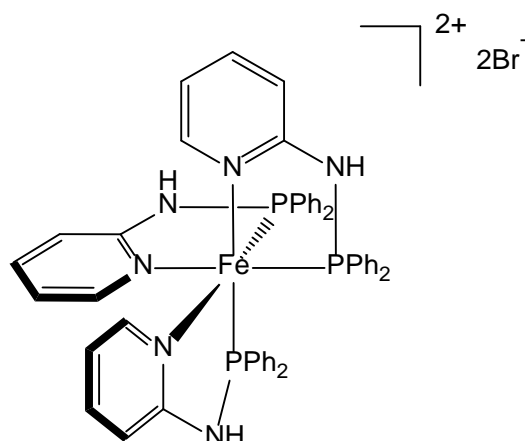
Yield: 301 mg (90%) pink solid

¹H-NMR (δ, CD₂Cl₂, 20°C): 7.62 (m, 6H), 7.41 – 7.10 (m, 24 H), 7.02 (bs, 6H), 6.64 (t, ³J_{HH} = 6.3 Hz, 3H, py⁵), 6.50 (d, ³J_{HH} = 5.7 Hz, 3H, py³), 4.88 (s, 3H, NH).

¹³C{¹H}-NMR (δ, CD₂Cl₂, 20°C): 163.91 (vdd, J_{CP} = 6.8 Hz, J_{CP} = 3.4 Hz, py²), 148.82 (s, py⁶), 140.09 (s, py⁴), 134.92 (vdd, J_{CP} = 31.6 Hz, J_{CP} = 16.1 Hz, ph¹), 133.87 (vdd, ¹J_{CP} = 27.5 Hz, ³J_{CP} = 14.5 Hz, ph¹), 131.62 (s, ph⁴), 131.29 (vdd, J_{CP} = 7.2 Hz, J_{CP} = 7.2, J_{CP} = 3.7 Hz, ph), 130.01 (s, ph), 129.27 (vdd, J_{CP} = 6.8, J_{CP} = 3.5 Hz, ph), 129.07 (vdd, J_{CP} = 6.6 Hz, J_{CP} = 3.3 Hz, ph), 128.20 (vdd, J_{CP} = 6.3 Hz, J_{CP} = 3.2 Hz, ph), 117.91 (s, py⁵), 112.22 (vdd, J_{CP} = 4.8 Hz, J_{CP} = 2.3 Hz, py³).

³¹P{¹H}-NMR (δ, CD₂Cl₂, 20°C): 104.6.

cis-P,N-[Fe(PN-Ph)₃]Cl₂ (**5r**)



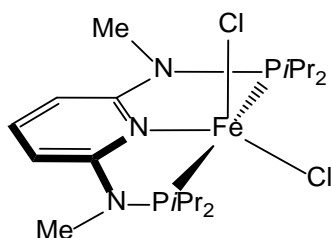
This complex was prepared analogously to **5q** with anhydrous FeBr₂ (1.00 eq; 0.35 mmol; 75 mg) and **2a** (3.10 eq; 1.08 mmol; 300 mg) as starting materials.

Yield: 343 mg (94%) pink solid

NMR-data were identically to **5q**.

5.6.5 PNP iron(II) complexes

Fe(PNP^{Me}-iPr)Cl₂ (6a)

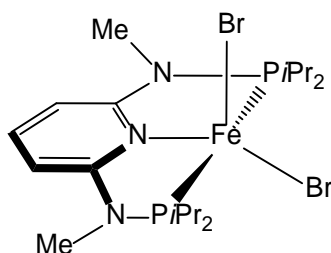


A suspension of anhydrous FeCl₂ (1.00 eq; 0.95 mmol; 120 mg) and **4d** (1.00 eq; 0.95 mmol; 350 mg) was stirred in 15 mL THF at r.t. for 12 h. The solvent was then removed under vacuum and the residue redissolved in 15 mL CH₂Cl₂ and filtered. The volume of the solvent was reduced to 0.5 mL and the product was precipitated by addition of 40 mL *n*-pentane. After filtration the product was washed with 2x 15 mL *n*-pentane and dried under vacuum.

Yield: 360 mg (77%) yellow solid

¹H-NMR (δ, CD₂Cl₂, 20°C): 183.51 (bs, 4H, CH(CH₃)₂), 68.66 (s, 2H, py^{3,5}), 24.79 (s, 6H, NCH₃), 9.44 (bs, 12H, CH(CH₃)₂), 3.00 (bs, 12H, CH(CH₃)₂), -17.37 (s, 1H, py⁴).

Fe(PNP^{Me}-iPr)Br₂ (6b)

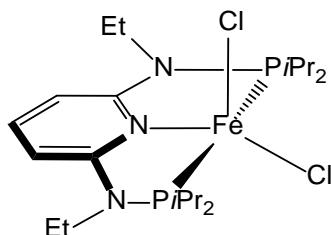


This complex was prepared analogously to **6a** with anhydrous FeBr₂ (1.00 eq; 0.81 mmol; 175 mg) and **4d** (1.00 eq; 0.81 mmol; 300 mg) as starting materials.

Yield: 406 mg (86%) yellow solid

¹H-NMR (δ, CD₂Cl₂, 20°C): 191.24 (bs, 4H, CH(CH₃)₂), 73.93 (s, 2H, py^{3,5}), 25.17 (s, 6H, NCH₃), 10.89 (bs, 12H, CH(CH₃)₂), 3.17 (bs, 12H, CH(CH₃)₂), -16.73 (s, 1H, py⁴).

Fe(PNP^{Et}-iPr)Cl₂ (6c)

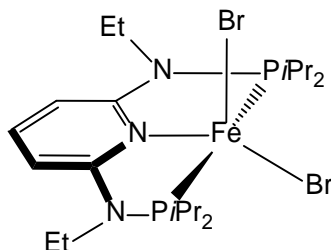


This complex was prepared analogously to **6a** with anhydrous FeCl₂ (1.00 eq; 0.88 mmol; 112 mg) and **4e** (1.00 eq; 0.88 mmol; 350 mg) as starting materials.

Yield: 346 mg (75%) yellow solid

¹H-NMR (δ, CD₂Cl₂, 20°C): 192.61 (bs, 4H, CH(CH₃)₂), 72.45 (s, 2H, py^{3,5}), 37.54 (s, 4H, NCH₂CH₃), 5.89 (bs, 12H, CH(CH₃)₂), 3.88 (bs, 12H, CH(CH₃)₂), 2.17 (bs, 6H, NCH₂CH₃), -19.67 (s, 1H, py⁴).

Fe(PNP^{Et}-iPr)Br₂ (6d)

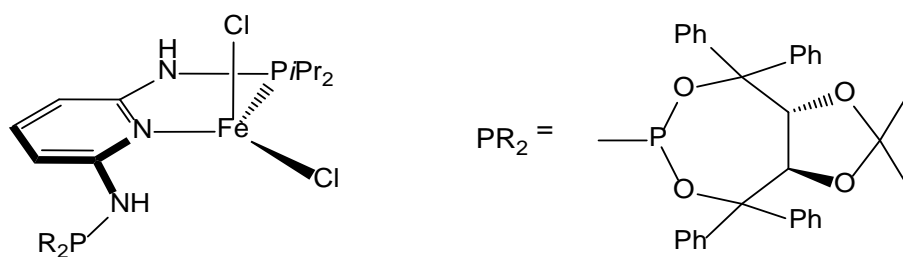


This complex was prepared analogously to **6a** with anhydrous FeBr₂ (1.00 eq; 0.75 mmol; 163 mg) and **4e** (1.00 eq; 0.75 mmol; 300 mg) as starting materials.

Yield: 396 mg (86%) yellow solid

¹H-NMR (δ, CD₂Cl₂, 20°C): 200.43 (bs, 4H, CH(CH₃)₂), 76.78 (s, 2H, py^{3,5}), 38.20 (s, 4H, NCH₂CH₃), 6.77 (bs, 12H, CH(CH₃)₂), 4.88 (bs, 12H, CH(CH₃)₂), 2.64 (bs, 6H, NCH₂CH₃), -20.43 (s, 1H, py⁴).

$\text{Fe}(\kappa^2\text{P},\text{N-PNP-}i\text{Pr/TAD})\text{Cl}_2$ (**6e**)



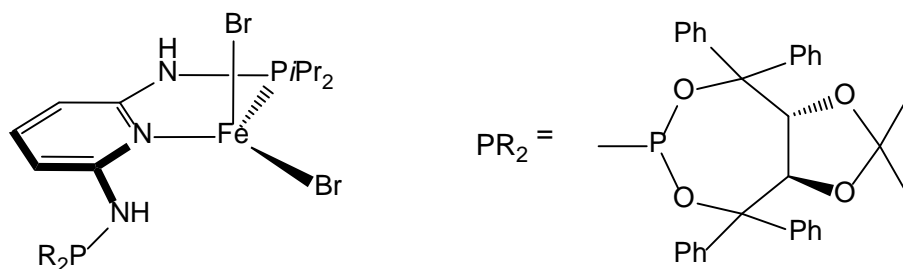
A suspension of anhydrous FeCl_2 (1.00 eq; 0.68 mmol; 86 mg) and **4h** (1.02 eq; 0.69 mmol; 500 mg) was stirred in 15 mL THF at r.t. for 12 h. The solvent was then removed under vacuum and the remaining solid redissolved in 15 mL CH_2Cl_2 . Insoluble materials were removed by filtration. The volume of the solution was reduced to 0.5 mL and the product was precipitated by addition of 40 mL *n*-pentane. After filtration the yellow product was washed with 2x 15 mL *n*-pentane and dried under vacuum.

Yield: 458 mg (79%) yellow solid

ESI-MS (m/z , $\text{CH}_3\text{CN}/\text{MeOH}$) positive ion: 868.2 $[\text{M}+\text{Na}]^+$, 842.3 $[\text{M}-\text{Cl}+\text{CH}_3\text{OH}]^+$, 810.2 $[\text{M}-\text{Cl}]^+$.

$\mu_{\text{eff}} = 4.95(1)\mu_{\text{B}}$.

$\text{Fe}(\kappa^2\text{P},\text{N-PNP-}i\text{Pr/TAD})\text{Cl}_2$ (**6f**)



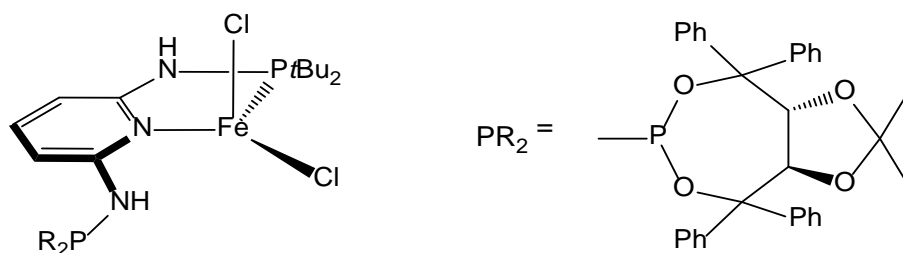
This complex was prepared analogously to **6e** with anhydrous FeBr_2 (1.00 eq; 0.82 mmol; 176 mg) and **4h** (1.02 eq; 0.83 mmol; 600 mg) as starting materials.

Yield: 678 mg (89%) yellow solid

ESI-MS (m/z , $\text{CH}_3\text{CN}/\text{MeOH}$) positive ion: 956.1 $[\text{M}+\text{Na}]^+$, 886.2 $[\text{M}-\text{Br}+\text{CH}_3\text{OH}]^+$, 854.2 $[\text{M}-\text{Br}]^+$, 806.3 $[\text{M}-\text{Br}-\text{HBr}+\text{CH}_3\text{OH}]^+$.

$\mu_{\text{eff}} = 4.97(1)\mu_{\text{B}}$.

$\text{Fe}(\kappa^2\text{P},\text{N-PNP-}i\text{Pr/TAD})\text{Cl}_2$ (**6g**)



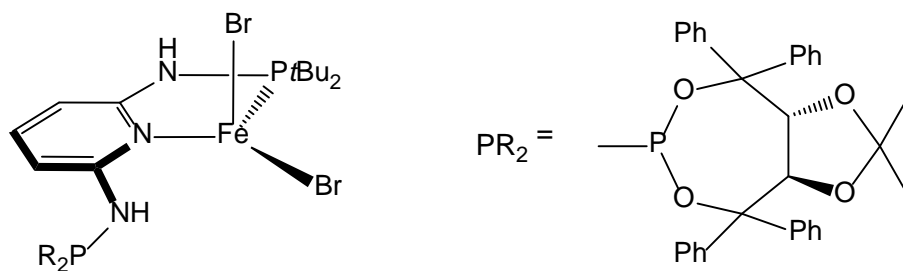
This complex was prepared analogously to **6e** with anhydrous FeCl_2 (1.00 eq; 0.38 mmol; 48 mg) and **4i** (1.02 eq; 0.40 mmol; 300 mg) as starting materials.

Yield: 263 mg (79%) yellow solid

ESI-MS (m/z , $\text{CH}_3\text{CN}/\text{MeOH}$) positive ion: 896.2 $[\text{M}+\text{Na}]^+$.

$\mu_{\text{eff}} = 4.98(1)\mu_{\text{B}}$.

Fe(κ^2 P,N-PNP-*i*Pr/TAD)Cl₂ (**6h**)



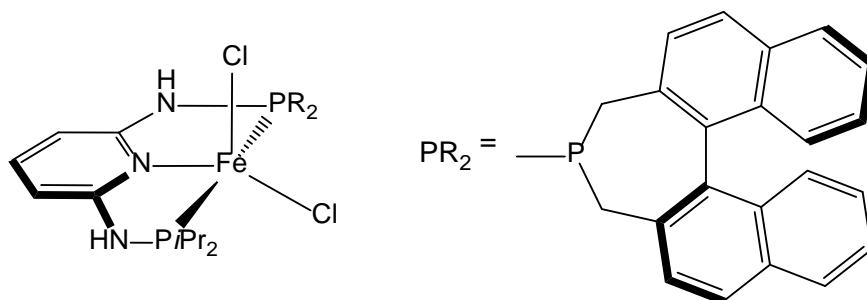
This complex was prepared analogously to **6e** with anhydrous FeBr₂ (1.00 eq; 0.38 mmol; 82 mg) and **4i** (1.02 eq; 0.40 mmol; 300 mg) as starting materials.

Yield: 305 mg (83%) yellow solid

ESI-MS (m/z , CH₃CN/MeOH) positive ion: 984.1 [M+Na]⁺, 882.2 [M-Br]⁺.

$\mu_{\text{eff}} = 5.00(1)\mu_{\text{B}}$.

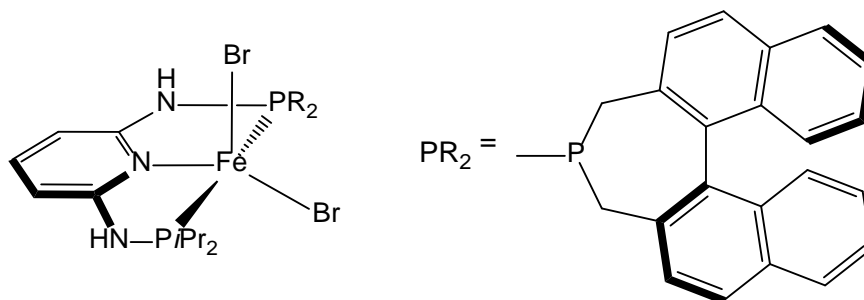
Fe(PNP-BIN/*i*Pr)Cl₂ (**6i**)



This complex was prepared analogously to **6a** with anhydrous FeCl₂ (1.00 eq; 0.56 mmol; 71 mg) and **4j** (1.00 eq; 0.56 mmol; 300 mg) as starting materials.

Yield: 324 mg (87%) yellow solid

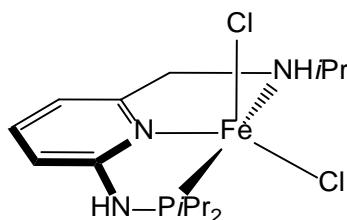
Fe(PNP-BIN/*i*Pr)Br₂ (6j)



This complex was prepared analogously to **6a** with anhydrous FeBr₂ (1.00 eq; 0.56 mmol; 121 mg) and **4j** (1.00 eq; 0.56 mmol; 300 mg) as starting materials.

Yield: 352 mg (84%) yellow solid

Fe(PNN-*i*Pr)Cl₂ (6k)

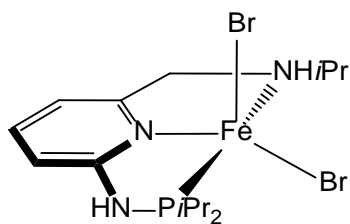


4f (1.00 eq; 0.71 mmol; 200 mg) was stirred with Fe(PMe₃)₂Cl₂ (1.00 eq; 0.71 mmol; 198 mg) in 15 mL CH₂Cl₂ for 12 h. The yellow solution was filtered, concentrated to 0.5 mL and the product was precipitated with 40 mL *n*-pentane. After filtration, the yellow solid was washed with 2x 10 mL *n*-pentane and dried under vacuum.

Alternatively, Fe[P(OMe)₃]₂Cl₂ can be used as an iron precursor.

Yield: 290 mg (88%) yellow solid

Fe(PNN-*i*Pr)Br₂ (6l)



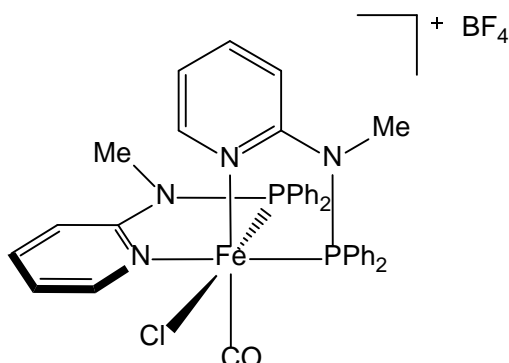
This complex was prepared analogously to **6k** with **4f** (1.00 eq; 0.71 mmol; 200 mg) and Fe(PMe₃)₂Br₂ (1.00 eq; 0.71 mmol; 261 mg) as starting materials.

Alternatively, Fe[P(OMe)₃]₃Br₂ can be used as an iron precursor.

Yield: 322 mg (91%) dark yellow solid

5.6.6 CO & CH₃CN iron(II) complexes

cis-[Fe(PN^{Me}-Ph)₂(CO)Cl](BF₄) (7a)



5c (1.00 eq; 0.70 mmol; 500 mg) was dissolved in 15 mL CH₂Cl₂ and NaBF₄ (1.20 eq; 0.84 mmol; 93 mg) was added. CO was bubbled through the solution for 5 min, whereupon the colour of the solution turned to dark red. The reaction mixture was then stirred under CO atmosphere for 12 h, filtered and concentrated to 0.5 mL. After precipitation with 40 mL *n*-pentane, the product was collected on a glas frit, washed with 2x 15 mL *n*-pentane and dried under vacuum for 2h.

Yield: 423 mg (76%) red solid

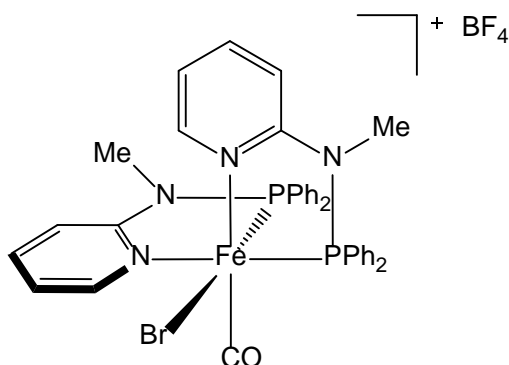
¹H-NMR (δ, CD₂Cl₂, 20 °C): 9.42 (d, *J*_{HH} = 5.3 Hz, 1H), 7.94 (s, 1H), 7.66 – 7.63 (m, 2H), 7.48 – 6.95 (m, 20 H), 6.67 (s, 2H), 6.56 (s, 2H), 3.13 (s, 3H, CH₃), 2.60 (d, ³*J*_{PH} = 3.8 Hz, 3H, CH₃).

¹³C{¹H}-NMR (δ, CD₂Cl₂, 20 °C): 215.88 (dd, ²*J*_{CP} = 28.7 Hz, ²*J*_{CP} = 23.5 Hz, CO), 162.73 (d, ²*J*_{CP} = 15.1 Hz, py²), 162.58 (d, ²*J*_{CP} = 11.9 Hz, py²), 152.68 (s, py⁶), 150.00 (s, py⁶), 142.89 (s, py⁴), 141.90 (s, py⁴), 133.37 (d, *J*_{CP} = 10.0 Hz, ph), 133.12 (d, *J*_{CP} = 2.4 Hz, ph), 132.73 (d, *J*_{CP} = 2.2, ph), 132.45 (d, *J*_{CP} = 10.9 Hz, ph), 132.17 (d, *J*_{CP} = 9.9 Hz, ph), 131.91 (d, *J*_{CP} = 1.8 Hz, ph), 131.64 (s, ph), 131.41 (d, *J*_{CP} = 2.8 Hz, ph), 131.20 (d, *J*_{CP} = 11.2 Hz, ph), 130.18 (d, *J*_{CP} = 10.6 Hz, ph), 129.94 (d, *J*_{CP} = 10.4 Hz, ph), 129.53 (d, *J*_{CP} = 5.8 Hz, ph), 129.06 (s, ph), 128.60 (d, *J*_{CP} = 6.6 Hz, ph), 128.07 (d, *J*_{CP} = 11.1 Hz, ph), 125.65 (s, ph), 125.18 (s, ph), 119.53 (s, py⁵), 118.26 (s, py⁵), 112.86 (d, ³*J*_{CP} = 7.2 Hz, py³), 112.05 (d, ³*J*_{CP} = 6.2 Hz, py³), 41.41 (d, ²*J*_{CP} = 5.9 Hz, CH₃), 38.61 (d, ²*J*_{CP} = 4.3 Hz, CH₃).

³¹P{¹H}-NMR (δ, CD₂Cl₂, 20 °C): 142.38 (d, ²*J*_{PP} = 49.2 Hz), 137.45 (d, ²*J*_{PP} = 49.1 Hz)

IR (ATR, cm⁻¹): 1978 (ν_{C=O}).

cis-[Fe(PN^{Me}-Ph)₂(CO)Br](BF₄) (7b)



This complex was prepared analogously to **7a** with **5d** (1.00 eq; 0.62 mmol; 500 mg) and NaBF₄ (1.20 eq; 0.75 mmol; 82 mg) as starting materials.

Yield: 412 mg (79%) red solid

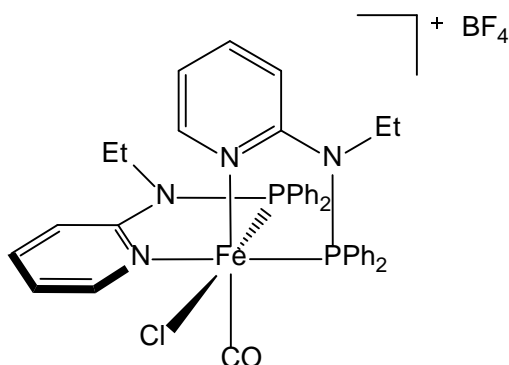
¹H-NMR (δ, CD₂Cl₂, 20 °C): 9.70 (s, 1H), 7.88 – 7.03 (m, 21H), 6.68 (m, 3H), 6.48 (s, 2H), 6.25 (s, 1H), 3.10 (s, 3H, CH₃), 2.53 (s, 3H, CH₃).

¹³C{¹H}-NMR (δ, CD₂Cl₂, 20 °C): 217.44 (dd, ²J_{CP} = 28.1 Hz, ²J_{CP} = 23.5 Hz, CO), 163.09 (d, ²J_{CP} = 16.5 Hz, py²), 162.53 (d, ²J_{CP} = 13.5 Hz, py²), 155.50 (s, py⁶), 150.84 (s, py⁶), 143.60 (s, py⁴), 142.80 (s, py⁴), 134.62 (d, J = 9.9 Hz, ph), 133.95 (s, ph), 133.68 (d, J = 9.8 Hz, ph), 133.21 (s, ph), 133.13 (s, ph), 133.10 (s, ph), 133.04 (s, ph), 132.96 (s, ph), 132.86 (s, ph), 132.56 (d, J = 9.2 Hz, ph), 132.25 (d, J = 9.5 Hz, ph), 131.72 (d, J = 11.1 Hz, ph), 131.37 (d, J = 10.7 Hz, ph), 130.54 (d, J = 6.8 Hz, ph), 130.44 (d, J = 7.2 Hz, ph), 129.82 (s, ph), 129.34 (d, J = 10.3 Hz, ph), 129.19 (d, J = 10.5 Hz, ph), 128.57 (s, ph), 128.09 (d, J = 11.2 Hz, ph), 120.72 (s, py⁵), 118.59 (s, py⁵), 114.13 (d, ³J_{CP} = 7.9 Hz, py³), 112.94 (d, ³J_{CP} = 6.2 Hz, py³), 43.39 (s, CH₃), 40.43 (s, CH₃).

³¹P{¹H}-NMR (δ, CD₂Cl₂, 20 °C): 146.86 (d, ²J_{PP} = 50.4 Hz), 138.90 (d, ²J_{PP} = 50.3 Hz).

IR (ATR, cm⁻¹): 1980 (ν_{C=O}).

***cis*-[Fe(PN^{Et}-Ph)₂(CO)Cl](BF₄) (7c)**



This complex was prepared analogously to **7a** with **5e** (1.00 eq; 0.68 mmol; 500 mg) and NaBF₄ (1.20 eq; 0.75 mmol; 89 mg) as starting materials.

Yield: 450 mg (81%) red solid

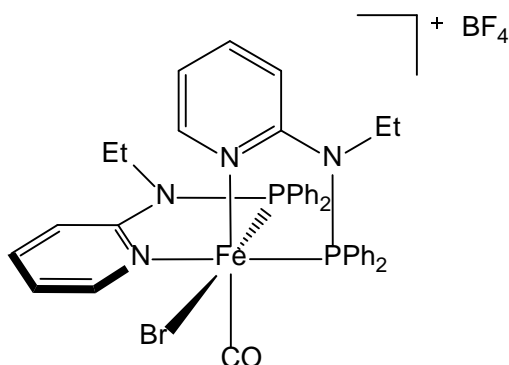
¹H-NMR (δ, CD₂Cl₂, 20 °C): 10.20 (s, 1H), 8.90 (s, 2H), 7.96 – 6.24 (m, 25H), 4.96 (bs, 4H, CH₂CH₃), 0.79 (bs, 6H, CH₂CH₃).

¹³C{¹H}-NMR (δ, CD₂Cl₂, 20 °C): 216.47 (bs, CO), 161.67 (bs, py²), 160.90 (bs, py²), 153.17 (s, py⁶), 152.50 (s, py⁶), 145.86 (s, py⁴), 144.68 (s, py⁴), 137.02 (d, J_{CP} = 9.9 Hz, ph), 135.31 (m, ph), 134.71 (m, ph), 134.32 (s, ph), 134.05 (m, ph), 133.39 (s, ph), 132.63 (d, J_{CP} = 10.8 Hz, ph), 131.27 (s, ph), 128.83 (d, J_{CP} = 10.1 Hz, ph), 120.25 (s, py⁵), 119.38 (s, py⁵), 116.07 (bs, py³), 103.90 (bs, py³), 48.62 (s, CH₂), 48.01 (s, CH₂), 16.24 (s, CH₃), 14.68 (s, CH₃).

³¹P{¹H}-NMR (δ, CD₂Cl₂, 20 °C): 147.70 (d, ²J_{PP} = 46.8 Hz), 130.90 (d, ²J_{PP} = 47.3 Hz).

IR (ATR, cm⁻¹): 1979 (ν_{C=O}).

cis-[Fe(PN^{Et}-Ph)₂(CO)Br](BF₄) (7d)



This complex was prepared analogously to **7a** with **5f** (1.00 eq; 0.60 mmol; 500 mg) and NaBF₄ (1.20 eq; 0.72 mmol; 80 mg) as starting materials.

Yield: 407 mg (78%) red solid

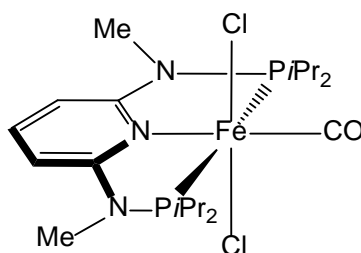
¹H-NMR (δ, CD₂Cl₂, 20 °C): 9.29 (d, *J* = 5.5 Hz, 1H), 7.99 (dd, *J* = 10.7 Hz, *J* = 8.1 Hz, 2H), 7.88 (bs, 1H), 7.61 (bs, 1H), 7.49 (m, 2H), 7.36 (m, 3H), 7.29 – 6.95 (m, 11H), 6.88 (m, 2H), 6.77 (m, 2H), 6.70 (d, *J* = 5.0 Hz, 1H), 6.40 (m, 1H), 6.35 (m, 1H), 3.68 (bs, 1H, CH₂), 3.62 (bs, 1H, CH₂), 3.32 (bs, 1H, CH₂), 2.91 (bs, 1H, CH₂), 0.79 (m, 6H, CH₃).

¹³C{¹H}-NMR (δ, CD₂Cl₂, 20 °C): 218.03 (dd, ²*J*_{CP} = 28.2 Hz, ²*J*_{CP} = 26.4 Hz, CO), 162.00 (d, ²*J*_{CP} = 15.8 Hz, py²), 160.81 (d, ²*J*_{CP} = 12.7 Hz, py²), 155.53 (s, py⁶), 150.53 (s, py⁶), 143.16 (s, py⁴), 141.91 (s, py⁴), 136.72 (s, ph), 136.61 (s, ph), 134.43 (d, *J*_{CP} = 2.5 Hz, ph), 133.95 (d, *J*_{CP} = 2.5 Hz, ph), 133.49 (d, *J*_{CP} = 2.3 Hz, ph), 133.15 (s, ph), 132.86 (d, *J*_{CP} = 2.3 Hz, ph), 132.47 (d, *J*_{CP} = 10.9 Hz, ph), 132.28 (d, *J*_{CP} = 10.2 Hz, ph), 132.08 (d, *J*_{CP} = 11.0 Hz, ph), 131.75 (d, *J*_{CP} = 8.4 Hz, ph), 130.32 (d, *J*_{CP} = 10.7 Hz, ph), 129.53 (d, *J*_{CP} = 10.1 Hz, ph), 128.21 (d, *J*_{CP} = 10.7 Hz, ph), 118.58 (s, py⁵), 118.05 (s, py⁵), 112.65 (d, ³*J*_{CP} = 10.8 Hz, py³), 112.18 (d, ³*J*_{CP} = 4.7 Hz, py³), 45.16 (s, CH₂), 44.42 (s, CH₂), 13.96 (s, CH₃), 13.21 (s, CH₃).

³¹P{¹H}-NMR (δ, CD₂Cl₂, 20 °C): 152.9 (d, ²*J*_{PP} = 48.1 Hz), 133.9 (d, ²*J*_{PP} = 47.9 Hz).

IR (ATR, cm⁻¹): 1970 (ν_{C=O}).

Fe(PNP^{Me}-iPr)COCl₂ (8a)



CO was bubbled through a solution of **6a** (1.00 eq; 0.50 mmol; 250 mg) in 15 mL CH₂Cl₂ for 5 min. An immediate colour change from yellow to dark red could be observed. The volume of the solvent was reduced to 0.5 mL and the product was precipitated by addition of 40 mL *n*-pentane. After filtration the red product was washed with 2x 15 mL *n*-pentane and dried under vacuum. A 28:72 mixture of the *cis/trans* isomers was obtained.

Yield: 226 mg (86%) red solid

cis-[Fe(PNP^{Me}-iPr)COCl₂]:

¹H-NMR (δ, CD₂Cl₂, 20°C): 7.26 (t, ³J_{HH} = 8.2 Hz, 1H, py⁴), 5.84 (d, ³J_{HH} = 8.3 Hz, 2H, py^{3,5}), 3.48 (m, 2H, CH(CH₃)₂), 3.01 (vt, ³J_{PH} = 1.6 Hz, 6H, NCH₃), 2.87 (m, 2H, CH(CH₃)₂), 1.60 – 1.46 (m, 18H, CH(CH₃)₂), 1.35 (dd, ²J_{PH} = 13.7 Hz, ³J_{HH} = 7.1 Hz, 6H, CH(CH₃)₂).

¹³C{¹H}-NMR (δ, CD₂Cl₂, 20°C): 220.30 (t, ²J_{CP} = 28.9 Hz, CO), 163.89 (vt, ²J_{CP} = 8.6 Hz, py^{2,6}), 138.85 (s, py⁴), 97.56 (vt, ³J_{CP} = 2.9 Hz, py^{3,5}), 35.98 (vt, ²J_{CP} = 2.3 Hz, NCH₃), 31.51 (vt, ¹J_{CP} = 8.6 Hz, CH(CH₃)₂), 29.01 (vt, ¹J_{CP} = 9.7 Hz, CH(CH₃)₂), 19.78 (s, CH(CH₃)₂), 18.65 (s, CH(CH₃)₂), 18.08 (vt, ²J_{CP} = 4.1 Hz, CH(CH₃)₂).

³¹P{¹H}-NMR (δ, CD₂Cl₂, 20°C): 128.2.

IR (ATR, cm⁻¹): 1937 (ν_{C=O}).

***trans*-[Fe(PNP^{Me}-*i*Pr)COCl₂]:**

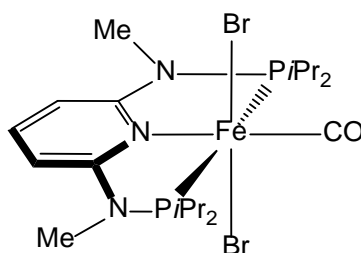
¹H-NMR (δ, CD₂Cl₂, 20°C): 7.66 (t, ³J_{HH} = 8.3 Hz, 1H, py⁴), 6.33 (d, ³J_{HH} = 8.3 Hz, 2H, py^{3,5}), 3.24 (vt, ³J_{PH} = 1.6 Hz, 6H, NCH₃), 2.87 (m, 4H, CH(CH₃)₂), 1.56 (dd, ²J_{PH} = 15.8 Hz, ³J_{HH} = 7.1 Hz, 12H, CH(CH₃)₂), 1.25 (dd, ²J_{PH} = 14.3 Hz, ³J_{HH} = 7.2 Hz, 12H, CH(CH₃)₂).

¹³C{¹H}-NMR (δ, CD₂Cl₂, 20°C): 223.91 (t, ²J_{CP} = 22.1 Hz, CO), 163.93 (vt, ²J_{CP} = 10.4 Hz, py^{2,6}), 140.04 (s, py⁴), 98.47 (vt, ³J_{CP} = 3.4 Hz, py^{3,5}), 36.78 (vt, ²J_{CP} = 2.5 Hz, NCH₃), 29.90 (vt, ¹J_{CP} = 10.5 Hz, CH(CH₃)₂), 20.96 (s, CH(CH₃)₂), 19.07 (vt, ²J_{CP} = 2.4 Hz, CH(CH₃)₂).

³¹P{¹H}-NMR (δ, CD₂Cl₂, 20°C): 143.7.

IR (ATR, cm⁻¹): 1960 (ν_{C=O}).

Fe(PNP^{Me}-*i*Pr)COBr₂ (8b)



This complex was prepared analogously to **8a** with **6b** (1.00 eq; 0.43 mmol; 250 mg) as starting material. A 50:18:32 mixture of the *cis/trans* isomers and Fe(PNP^{Me}-*i*Pr)(CO)₂Br]⁺ was obtained.

Yield: 232 mg (88%) red solid

***cis*-[Fe(PNP^{Me}-iPr)COBr₂]:**

¹H-NMR (δ, CD₂Cl₂, 20°C): 7.27 (t, ³J_{HH} = 8.3 Hz, 1H, py⁴), 5.87 (d, ³J_{HH} = 8.3 Hz, 2H, py^{3,5}), 3.71 (m, 2H, CH(CH₃)₂), 3.11 (m, 2H, CH(CH₃)₂), 3.03 (vt, ³J_{PH} = 1.7 Hz, 6H, NCH₃), 1.62 – 1.30 (m, 24H, CH(CH₃)₂).

¹³C{¹H}-NMR (δ, CD₂Cl₂, 20°C): 222.75 (t, ²J_{CP} = 28.9 Hz, CO), 163.86 (vt, ²J_{CP} = 8.7 Hz, py^{2,6}), 138.90 (s, py⁴), 97.78 (vt, ³J_{CP} = 2.9 Hz, py^{3,5}), 36.46 (s, NCH₃), 33.26 (vt, ¹J_{CP} = 9.3 Hz, CH(CH₃)₂), 29.12 (vt, ¹J_{CP} = 9.8 Hz, CH(CH₃)₂), 21.42 (s, CH(CH₃)₂), 19.47 (s, CH(CH₃)₂), 18.74 (s, CH(CH₃)₂).

³¹P{¹H}-NMR (δ, CD₂Cl₂, 20°C): 128.4.

IR (ATR, cm⁻¹): 1939 (ν_{C=O}).

***trans*-[Fe(PNP^{Me}-iPr)COBr₂]:**

¹H-NMR (δ, CD₂Cl₂, 20°C):

7.64 (t, ³J_{HH} = 8.3 Hz, 1H, py⁴), 6.34 (d, ³J_{HH} = 8.3 Hz, 2H, py^{3,5}), 3.25 (vt, ³J_{PH} = 1.5 Hz, 6H, NCH₃), 3.10 (m, 4H, CH(CH₃)₂), 1.62 – 1.30 (m, 24H, CH(CH₃)₂).

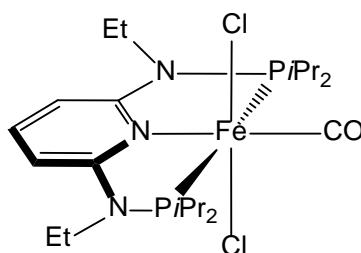
¹³C{¹H}-NMR (δ, CD₂Cl₂, 20°C):

226.37 (t, ²J_{CP} = 22.0 Hz, CO), 164.04 (vt, ²J_{CP} = 8.5 Hz, py^{2,6}), 139.87 (s, py⁴), 98.76 (vt, ³J_{CP} = 3.3 Hz, py^{3,5}), 37.61 (s, NCH₃), 30.06 (vt, ¹J_{CP} = 10.7 Hz, CH(CH₃)₂), 21.62 (s, CH(CH₃)₂), 18.50 (s, CH(CH₃)₂).

³¹P{¹H}-NMR (δ, CD₂Cl₂, 20°C): 144.4.

IR (ATR, cm⁻¹): 1939 (ν_{C=O}).

Fe(PNP^{Et}-iPr)COCl₂ (**8c**)



This complex was prepared analogously to **8a** with **6c** (1.00 eq; 0.48 mmol; 250 mg) as starting material. A 13:87 mixture of the *cis/trans* isomers was obtained.

Yield: 346 mg (75%) red solid

cis-[Fe(PNP^{Et}-iPr)COCl₂]:

¹H-NMR (δ , CD₂Cl₂, 20°C): 7.31 (t, ³J_{HH} = 8.3 Hz, 1H, py⁴), 5.93 (d, ³J_{HH} = 8.3 Hz, 2H, py^{3,5}), 3.84 – 3.75 (m, 6H, NCH₂CH₃, CH(CH₃)₂), 3.16 (m, 2H, CH(CH₃)₂), 1.60 (dd, ³J_{PH} = 14.5 Hz, ³J_{HH} = 7.1 Hz, 12H, CH(CH₃)₂), 1.45 (dd, ³J_{PH} = 15.8 Hz, ³J_{HH} = 7.4 Hz, 12H, CH(CH₃)₂), 1.31 (t, ³J_{HH} = 7.0 Hz, 6H, NCH₂CH₃).

¹³C{¹H}-NMR (δ , CD₂Cl₂, 20°C): 224.07 (t, ²J_{CP} = 22.5 Hz, CO), 163.02 (vt, ²J_{CP} = 10.3 Hz, py^{2,6}), 138.38 (s, py⁴), 97.96 (vt, ³J_{CP} = 3.0 Hz, py^{3,5}), 42.02 (vt, ²J_{CP} = 2.4 Hz, NCH₂CH₃), 30.22 (vt, ¹J_{CP} = 8.7 Hz, CH(CH₃)₂), 27.79 (vt, ¹J_{CP} = 9.5 Hz, CH(CH₃)₂), 21.89 (vt, ²J_{CP} = 4.1 Hz, CH(CH₃)₂), 19.16 (s, CH(CH₃)₂), 18.76 (s, CH(CH₃)₂), 17.54 (vt, ²J_{CP} = 4.0 Hz, CH(CH₃)₂), 13.00 (s, NCH₂CH₃).

³¹P{¹H}-NMR (δ , CD₂Cl₂, 20°C): 127.8.

IR (ATR, cm⁻¹): 1942 ($\nu_{C=O}$).

***trans*-[Fe(PNP^{Et}-*i*Pr)COCl₂]:**

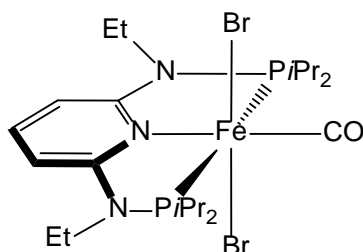
¹H-NMR (δ, CD₂Cl₂, 20°C): 7.70 (t, ³J_{HH} = 8.3 Hz, 1H, py⁴), 6.42 (d, ³J_{HH} = 8.3 Hz, 2H, py^{3,5}), 3.80 (m, 4H, NCH₂CH₃), 2.99 (m, 4H, CH(CH₃)₂), 1.60 (dd, ³J_{PH} = 14.5 Hz, ³J_{HH} = 7.1 Hz, 12H, CH(CH₃)₂), 1.45 (dd, ³J_{PH} = 15.8 Hz, ³J_{HH} = 7.4 Hz, 12H, CH(CH₃)₂), 1.35 (t, ³J_{HH} = 7.0 Hz, 6H, NCH₂CH₃).

¹³C{¹H}-NMR (δ, CD₂Cl₂, 20°C): 224.07 (t, ²J_{CP} = 22.5 Hz, CO), 163.02 (vt, ²J_{CP} = 10.3 Hz, py^{2,6}), 139.61 (s, py⁴), 98.66 (vt, ³J_{CP} = 3.5 Hz, py^{3,5}), 42.48 (vt, ²J_{CP} = 2.5 Hz, NCH₂CH₃), 27.08 (vt, ¹J_{CP} = 10.3 Hz, CH(CH₃)₂), 21.45 (s, CH(CH₃)₂), 18.35 (s, CH(CH₃)₂), 13.16 (s, NCH₂CH₃).

³¹P{¹H}-NMR (δ, CD₂Cl₂, 20°C): 142.8.

IR (ATR, cm⁻¹): 1950 (ν_{C=O}).

Fe(PNP^{Et}-*i*Pr)COBr₂ (8d)



This complex was prepared analogously to **8a** with **6d** (1.00 eq; 0.41 mmol; 250 mg) as starting material. A 24:43:33 mixture of the *cis/trans* isomers and Fe(PNP^{Et}-*i*Pr)(CO)₂Br]⁺ was obtained.

Yield: 232 mg (88%) red solid

***cis*-[Fe(PNP^{Et}-*i*Pr)COBr₂]:**

¹H-NMR (δ, CD₂Cl₂, 20°C): 7.22 (t, ³J_{HH} = 8.3 Hz, 1H, py⁴), 5.86 (d, ³J_{HH} = 8.3 Hz, 2H, py^{3,5}), 3.58 (m, 6H, NCH₂CH₃, CH(CH₃)₂), 3.20 (m, 2H, CH(CH₃)₂), 1.66 – 1.20 (m, 30H, NCH₂CH₃, CH(CH₃)₂).

¹³C{¹H}-NMR (δ, CD₂Cl₂, 20°C): 223.01 (t, ²J_{CP} = 28.4 Hz, CO), 163.06 (vt, ²J_{CP} = 5.4 Hz, py^{2,6}), 138.44 (s, py⁴), 98.07 (vt, ³J_{CP} = 2.9 Hz, py^{3,5}), 42.06 (s, NCH₂CH₃), 32.05 (vt, ²J_{CP} = 10.2 Hz, CH(CH₃)₂), 27.92 (vt, ¹J_{CP} = 9.6 Hz, CH(CH₃)₂), 23.17 (s, CH(CH₃)₂), 19.76 (s, CH(CH₃)₂), 18.01 (vt, ²J_{CP} = 4.0 Hz, CH(CH₃)₂), 12.92 (s, NCH₂CH₃)

³¹P{¹H}-NMR (δ, CD₂Cl₂, 20°C): 126.9.

IR (ATR, cm⁻¹): 1941 (ν_{C=O}).

***trans*-[Fe(PNP^{Et}-*i*Pr)COBr₂]:**

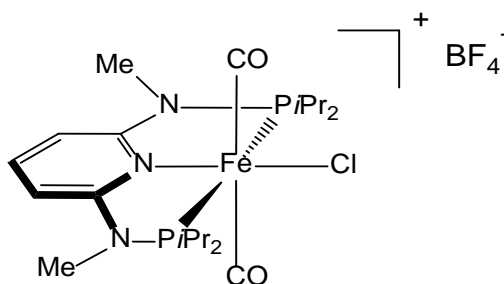
¹H-NMR (δ, CD₂Cl₂, 20°C): 7.59 (t, ³J_{HH} = 8.3 Hz, 1H, py⁴), 6.33 (d, ³J_{HH} = 8.3 Hz, 2H, py^{3,5}), 3.71 (qvt, ³J_{HH} = 7.0 Hz, ³J_{PH} = 2.3 Hz, 6H, NCH₃), 3.09 (m, 4H, CH(CH₃)₂), 1.66 – 1.20 (m, 30H, CH(CH₃)₂).

¹³C{¹H}-NMR (δ, CD₂Cl₂, 20°C): 226.54 (t, ²J_{CP} = 22.1 Hz, CO), 163.18 (vt, ²J_{CP} = 8.3 Hz, py^{2,6}), 139.54 (s, py⁴), 98.83 (vt, ³J_{CP} = 3.4 Hz, py^{3,5}), 42.57 (s, NCH₂CH₃), 28.42 (vt, ¹J_{CP} = 10.4 Hz, CH(CH₃)₂), 21.79 (s, CH(CH₃)₂), 18.70 (s, CH(CH₃)₂), 13.00 (s, NCH₂CH₃).

³¹P{¹H}-NMR (δ, CD₂Cl₂, 20°C): 143.7.

IR (ATR, cm⁻¹): 1941 (ν_{C=O}).

[Fe(PNP^{Me}-iPr)(CO)₂Cl]BF₄ (8e)



CO was bubbled through a solution of **6a** (1.00 eq; 0.30 mmol; 150 mg) and AgBF₄ (1.00 eq; 0.30 mmol; 59 mg) in 15 mL THF. The pink solution was stirred under CO atmosphere for 1 h, then the solvent was removed under reduced pressure. The residue was redissolved in 15 mL CH₂Cl₂, filtered and the volume of the solvent was reduced to 0.5 mL. The product was precipitated by addition of 40 mL *n*-pentane, collected on a frit, washed with 15 mL *n*-pentane and dried under vacuum.

Yield: 141 mg (78%) pink solid

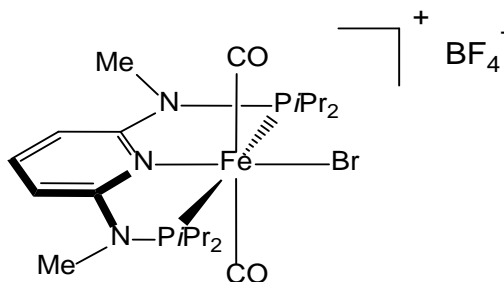
¹H-NMR (δ, CD₂Cl₂, 20°C): 7.53 (t, ³J_{HH} = 8.1 Hz, 1H, py⁴), 6.14 (d, ³J_{HH} = 8.2 Hz, 2H, py^{3,5}), 3.19 (m, 4H, CH(CH₃)₂), 3.08 (s, 6H, NCH₃), 1.53 – 1.42 (m, 24H, CH(CH₃)₂).

¹³C{¹H}-NMR (δ, CD₂Cl₂, 20°C): 211.58 (t, ²J_{CP} = 24.7 Hz, CO), 162.98 (vt, ²J_{CP} = 7.4 Hz, py^{2,6}), 142.17 (s, py⁴), 100.19 (vt, ³J_{CP} = 2.7 Hz, py^{3,5}), 35.40 (s, NCH₃), 31.98 (vt, ¹J_{CP} = 11.2 Hz, CH(CH₃)₂), 18.52 (s, CH(CH₃)₂), 17.69 (s, CH(CH₃)₂).

³¹P{¹H}-NMR (δ, CD₂Cl₂, 20°C): 130.6.

IR (ATR, cm⁻¹): 2002 (ν_{C=O}).

[Fe(PNP^{Me}-iPr)(CO)₂Br]BF₄ (8f)



This complex was prepared analogously to **8e** with **6b** (1.00 eq; 0.26 mmol; 150 mg) and AgBF₄ (1.00; 0.26 mmol; 50 mg) as starting materials.

Yield: 125 mg (79%) pink solid

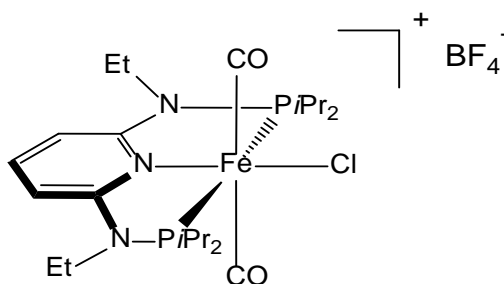
¹H-NMR (δ, CD₂Cl₂, 20°C): 7.56 (t, ³J_{HH} = 8.3 Hz, 1H, py⁴), 6.17 (d, ³J_{HH} = 8.3 Hz, 2H, py^{3,5}), 3.20 (m, 4H, CH(CH₃)₂), 3.07 (vt, ³J_{PH} = 2.1 Hz, 6H, NCH₃), 1.55 – 1.41 (m, 24H, CH(CH₃)₂).

¹³C{¹H}-NMR (δ, CD₂Cl₂, 20°C): 211.76 (t, ²J_{CP} = 24.5 Hz, CO), 162.94 (vt, ²J_{CP} = 7.5 Hz, py^{2,6}), 142.12 (s, py⁴), 100.14 (vt, ³J_{CP} = 2.7 Hz, py^{3,5}), 35.27 (s, NCH₃), 31.94 (vt, ¹J_{CP} = 11.4 Hz, CH(CH₃)₂), 18.55 (s, CH(CH₃)₂), 18.27 (s, CH(CH₃)₂).

³¹P{¹H}-NMR (δ, CD₂Cl₂, 20°C): 132.8.

IR (ATR, cm⁻¹): 1997 (ν_{C=O}).

[Fe(PNP^{Et}-iPr)(CO)₂Cl]BF₄ (8g)



This complex was prepared analogously to **8e** with **6c** (1.00 eq; 0.29 mmol; 150 mg) and AgBF₄ (1.00; 0.29 mmol; 56 mg) as starting materials.

Yield: 131 mg (75%) pink solid

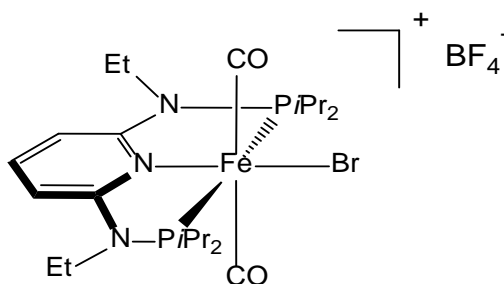
¹H-NMR (δ, CD₂Cl₂, 20°C): 7.54 (t, ³J_{HH} = 8.2 Hz, 1H, py⁴), 6.17 (d, ³J_{HH} = 8.2 Hz, 2H, py^{3,5}), 3.58 (m, 4H, NCH₂CH₃), 3.18 (m, CH(CH₃)₂), 1.49 – 1.10 (m, 30H, NCH₂CH₃, CH(CH₃)₂).

¹³C{¹H}-NMR (δ, CD₂Cl₂, 20°C): 211.77 (t, ²J_{CP} = 24.8 Hz, CO), 162.33 (vt, ²J_{CP} = 6.9 Hz, py^{2,6}), 142.42 (s, py⁴), 101.24 (vt, ³J_{CP} = 2.6 Hz, py^{3,5}), 43.30 (s, NCH₂CH₃), 31.40 (vt, ¹J_{CP} = 10.8 Hz, CH(CH₃)₂), 19.12 (s, CH(CH₃)₂), 17.81 (s, CH(CH₃)₂), 13.02 (s, NCH₂CH₃).

³¹P{¹H}-NMR (δ, CD₂Cl₂, 20°C): 132.8.

IR (ATR, cm⁻¹): 2005 (ν_{C=O}).

[Fe(PNP^{Et}-iPr)(CO)₂Br]BF₄ (8h)



This complex was prepared analogously to **8e** with **6d** (1.00 eq; 0.24 mmol; 150 mg) and AgBF₄ (1.00; 0.24 mmol; 48 mg) as starting materials.

Yield: 115 mg (73%) pink solid

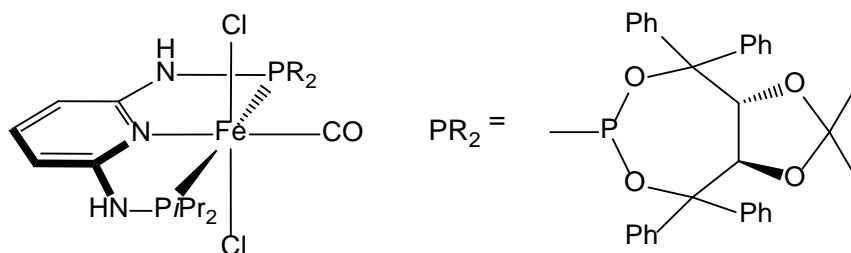
¹H-NMR (δ, CD₂Cl₂, 20°C): 7.55 (t, ³J_{HH} = 8.3 Hz, 1H, py⁴), 6.20 (d, ³J_{HH} = 8.3 Hz, 2H, py^{3,5}), 3.62 – 3.52 (m, 4H, NCH₂CH₃), 3.15 (m, 4H, CH(CH₃)₂), 1.51 (dd, ³J_{PH} = 10.3 Hz, ³J_{HH} = 5.9 Hz, 12H, CH(CH₃)₂), 1.46 (dd, ³J_{PH} = 11.4 Hz, ³J_{HH} = 5.9 Hz, 12H, CH(CH₃)₂), 1.30 (t, ³J_{HH} = 7.0 Hz, NCH₂CH₃).

¹³C{¹H}-NMR (δ, CD₂Cl₂, 20°C): 212.01 (t, ²J_{CP} = 24.4 Hz, CO), 162.30 (vt, ²J_{CP} = 7.1 Hz, py^{2,6}), 141.99 (s, py⁴), 101.28 (vt, ³J_{CP} = 2.8 Hz, py^{3,5}), 42.93 (s, NCH₂CH₃), 31.67 (vt, ¹J_{CP} = 11.0 Hz, CH(CH₃)₂), 19.19 (s, CH(CH₃)₂), 18.24 (s, CH(CH₃)₂), 13.09 (s, NCH₂CH₃).

³¹P{¹H}-NMR (δ, CD₂Cl₂, 20°C): 135.3.

IR (ATR, cm⁻¹): 1997 (ν_{C=O}).

trans-Fe(PNP-*i*Pr/TAD)COCl₂ (8i)



CO was bubbled through a solution of **6e** (1.00 eq; 0.24 mmol; 200 mg) in 5 mL THF for 3 min, whereupon the colour changed immediately from yellow to violet. This complex was difficult to manipulate and readily releases CO in solution under vacuum. The product crystallized by slow diffusion of *n*-pentane, the solvent was decanted off and the remaining solid was dried under vacuum for 30 min.

Yield: 152 mg (74%) violet powder

¹H-NMR (δ, d₆-acetone, 20°C): 8.09 (d, ²J_{PH} = 8.1 Hz, 1H, NH^{iPr}), 7.97 (m, 2H, ph), 7.82 (m, 2H, ph), 7.74 (d, ²J_{PH} = 3.1 Hz, 1H, NH^{TAD}), 7.56-7.47 (m, 4H, ph), 7.42-7.35 (m, 4H, ph), 7.29-7.19 (m, 9H, py⁴, ph), 6.56 (d, ³J_{HH} = 7.9 Hz, 1H, py³), 5.91 (d, ³J_{HH} = 8.0 Hz, 1H, CH^{TAD}), 5.87 (d, ³J_{HH} = 7.8 Hz, 1H, py⁵), 5.71 (d, ³J_{HH} = 8.0 Hz, 1H, CH^{TAD}), 3.14 (m, 1H, CH(CH₃)₂^{iPr}), 2.98 (m, 1H, CH(CH₃)₂^{iPr}), 1.55 (dd, ³J_{HH} = 7.0 Hz, ³J_{PH} = 13.7 Hz, 3H, CH(CH₃)₂^{iPr}), 1.54 (dd, ³J_{HH} = 7.0 Hz, ³J_{PH} = 13.9 Hz, 3H, CH(CH₃)₂^{iPr}), 1.45 (dd, ³J_{HH} = 7.3 Hz, ³J_{PH} = 16.0 Hz, 3H, CH(CH₃)₂^{iPr}), 1.36 (dd, ³J_{HH} = 7.3 Hz, ³J_{PH} = 15.9 Hz, 3H, CH(CH₃)₂^{iPr}), 0.75 (s, 3H, CH₃^{TAD}), 0.66 (s, 3H, CH₃^{TAD}).

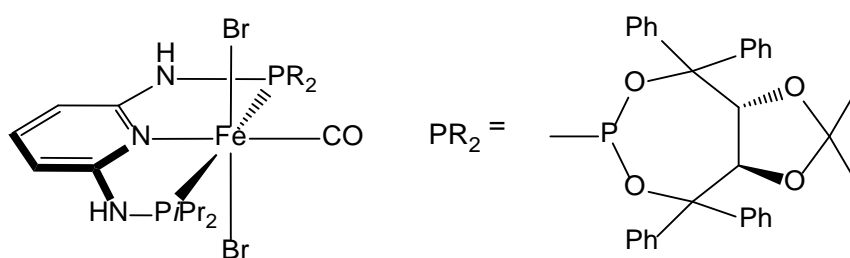
¹³C{¹H}-NMR (δ, d₆-acetone, 20°C): 220.32 (dd, ²J_{CP} = 22.3 Hz, ²J_{CP} = 35.1 Hz, CO), 162.58 (dd, ²J_{CP} = 8.0 Hz, ⁴J_{CP} = 12.9 Hz, py²), 157.81 (dd, ²J_{CP} = 3.3 Hz, ⁴J_{CP} = 23.5 Hz, py⁶), 144.07 (s, ph¹), 143.35 (s, ph¹), 141.75 (d, ³J_{CP} = 5.5 Hz, ph¹), 140.29 (d, ³J_{CP} = 8.2 Hz, ph¹), 139.46 (s, py⁴), 129.02 (s, ph), 128.84 (s, ph), 128.43 (s, ph), 128.36 (s, ph), 127.98 (s, ph), 127.68 (s, ph), 127.61 (s, ph), 127.34 (s, ph), 127.13 (s, ph), 127.05 (s, ph), 126.79 (s, ph), 126.66 (s, ph), 114.62 (s, C(CH₃)₂), 99.97 (d, ³J_{CP} = 7.3 Hz, py³), 98.65 (d, ³J_{CP} = 10.4 Hz, py⁵), 88.91 (d, ²J_{CP} = 8.3 Hz, C(ph)₂), 88.56 (d, ²J_{CP} = 19.9 Hz, C(ph)₂), 80.97 (d, ³J_{CP} = 2.5 Hz, CH^{TAD}), 79.98 (d, ³J_{CP} = 2.9 Hz, CH^{TAD}), 26.44 (s, CH₃^{TAD}), 26.01 (s, CH₃^{TAD}), 25.86 (d, ¹J_{CP} = 22.0 Hz, CH(CH₃)₂^{iPr}), 24.94 (d, ¹J_{CP} = 25.5 Hz, CH(CH₃)₂^{iPr}), 18.69 (d, ²J_{CP} = 4.3 Hz, CH(CH₃)₂^{iPr}), 18.61 (d, ²J_{CP} = 3.9 Hz, CH(CH₃)₂^{iPr}), 17.74 (s, CH(CH₃)₂^{iPr}), 17.28 (s, CH(CH₃)₂^{iPr}).

$^{31}\text{P}\{^1\text{H}\}$ -NMR (δ , d_6 -acetone, 20°C): 154.0 (d, $^2J_{\text{PP}} = 278.8$ Hz, TAD), 125.1 (d, $^2J_{\text{PP}} = 278.9$ Hz, $i\text{Pr}$).

IR (ATR, cm^{-1}): 1976 ($\nu_{\text{C}=\text{O}}$).

IR (CH_2Cl_2 , cm^{-1}): 1986 ($\nu_{\text{C}=\text{O}}$).

trans-Fe(PNP- $i\text{Pr}$ /TAD)COBr $_2$ (**8j**)



This compound was prepared analogously to **8i** with **6f** (1.00 eq; 0.21 mmol; 200 mg) as starting material.

Yield: 164 mg (80%) blue crystals

^1H -NMR (δ , d_6 -acetone, 20°C): 8.07 (d, $^2J_{\text{PH}} = 8.1$ Hz, 1H, $\text{NH}^{i\text{Pr}}$), 8.02 (m, 2H, ph), 7.89 (m, 2H, ph), 7.76 (dd, $^2J_{\text{PH}} = 6.5$ Hz, $^4J_{\text{PH}} = 3.0$ Hz, 1H, NH^{TAD}), 7.54 (m, 2H, ph), 7.48 (m, 2H, ph), 7.39 (m, 4H, ph), 7.34 (t, $^3J_{\text{HH}} = 7.9$ Hz, 1H, py^4), 7.29 – 7.18 (m, 8H, ph), 6.56 (d, $^3J_{\text{HH}} = 7.9$ Hz, 1H, py^3), 5.88 (d, $^3J_{\text{HH}} = 8.0$ Hz, 1H, CH^{TAD}), 5.82 (d, $^3J_{\text{HH}} = 7.8$ Hz, 1H, py^5), 5.72 (d, $^3J_{\text{HH}} = 8.0$ Hz, 1H, CH^{TAD}), 3.37 (m, 1H, $\text{CH}(\text{CH}_3)_2^{i\text{Pr}}$), 3.19 (m, 1H, $\text{CH}(\text{CH}_3)_2^{i\text{Pr}}$), 1.59 (dd, $^3J_{\text{HH}} = 7.2$ Hz, $^3J_{\text{PH}} = 13.6$ Hz, 3H, $\text{CH}(\text{CH}_3)_2^{i\text{Pr}}$), 1.53 (dd, $^3J_{\text{HH}} = 7.2$ Hz, $^3J_{\text{PH}} = 13.1$ Hz, 3H, $\text{CH}(\text{CH}_3)_2^{i\text{Pr}}$), 1.47 (dd, $^3J_{\text{HH}} = 7.4$ Hz, $^3J_{\text{PH}} = 16.0$ Hz, 3H, $\text{CH}(\text{CH}_3)_2^{i\text{Pr}}$), 1.37 (dd, $^3J_{\text{HH}} = 7.3$ Hz, $^3J_{\text{PH}} = 16.2$ Hz, 3H, $\text{CH}(\text{CH}_3)_2^{i\text{Pr}}$), 0.72 (s, 3H, CH_3^{TAD}), 0.65 (s, 3H, CH_3^{TAD}).

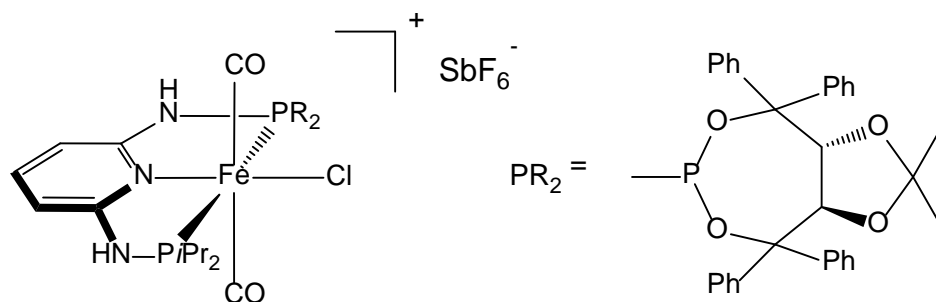
$^{13}\text{C}\{^1\text{H}\}$ -NMR (δ , d_6 -acetone, 20°C): 222.53 (dd, $^2J_{\text{CP}} = 22.2$ Hz, $^2J_{\text{CP}} = 34.9$ Hz, CO), 162.58 (dd, $^2J_{\text{CP}} = 12.5$ Hz, $^4J_{\text{CP}} = 7.3$ Hz, py^2), 157.81 (dd, $^2J_{\text{CP}} = 22.9$ Hz, $^4J_{\text{CP}} = 3.3$ Hz, py^6), 144.04 (s, ph^1), 143.27 (s, ph^1), 141.84 (d, $^3J_{\text{CP}} = 5.5$ Hz, ph^1), 140.10 (d, $^3J_{\text{CP}} = 8.2$ Hz, ph^1), 139.34 (s, py^4), 129.15 (s, ph), 129.06 (s, ph), 128.70 (s, ph), 128.40 (s, ph), 127.94 (s, ph), 127.72 (s, ph), 127.66 (s, ph), 127.53 (s, ph), 127.16 (s, ph), 127.09 (s, ph), 126.74 (s, ph), 126.65 (s, ph), 114.63 (s, $\text{C}(\text{CH}_3)_2$), 100.01 (d, $^3J_{\text{CP}} = 7.5$ Hz, py^3), 98.92 (d, $^3J_{\text{CP}} = 10.3$ Hz, py^5), 89.38 (d, $^2J_{\text{CP}} = 8.9$ Hz, $\text{C}(\text{ph})_2$), 89.27 (d, $^2J_{\text{CP}} = 12.6$ Hz, $\text{C}(\text{ph})_2$), 80.36 (d, $^3J_{\text{CP}} = 2.5$ Hz, CH^{TAD}), 79.74 (d, $^3J_{\text{CP}} = 2.9$ Hz, CH^{TAD}), 28.26 (d, $^1J_{\text{CP}} = 21.7$ Hz, $\text{CH}(\text{CH}_3)_2^{\text{iPr}}$), 26.89 (d, $^1J_{\text{CP}} = 26.8$ Hz, $\text{CH}(\text{CH}_3)_2^{\text{iPr}}$), 26.42 (s, CH_3^{TAD}), 26.07 (s, CH_3^{TAD}), 18.84 (d, $^2J_{\text{CP}} = 3.9$ Hz, $\text{CH}(\text{CH}_3)_2^{\text{iPr}}$), 18.50 (d, $^2J_{\text{CP}} = 4.3$ Hz, $\text{CH}(\text{CH}_3)_2^{\text{iPr}}$), 18.06 (s, $\text{CH}(\text{CH}_3)_2^{\text{iPr}}$), 17.42 (s, $\text{CH}(\text{CH}_3)_2^{\text{iPr}}$).

$^{31}\text{P}\{^1\text{H}\}$ -NMR (δ , d_6 -acetone, 20°C): 161.61 (d, $^2J_{\text{PP}} = 261.4$ Hz, TAD), 125.20 (d, $^2J_{\text{PP}} = 261.4$ Hz, iPr).

IR (ATR, cm^{-1}): 1967 ($\nu_{\text{C=O}}$).

IR (CH_2Cl_2 , cm^{-1}): 1980 ($\nu_{\text{C=O}}$).

***trans*-[Fe(PNP-*i*Pr/TAD)(CO)₂Cl]SbF₆ (8k)**



CO was bubbled through a solution of **6e** (1.00 eq; 0.24 mmol; 200 mg) and AgSbF₆ (1.00 eq; 0.24 mmol; 82 mg) in 15 mL THF for 5 min. The solvent was removed under vacuum and, the pink precipitate was redissolved in 15 mL CH₂Cl₂. Insoluble materials were removed by filtration and the volume of the solution was then reduced to 0.5 mL. The product was precipitated upon addition of 40 mL *n*-hexane and dried under vacuum for 2 h.

Yield: 210 mg (81%) red solid

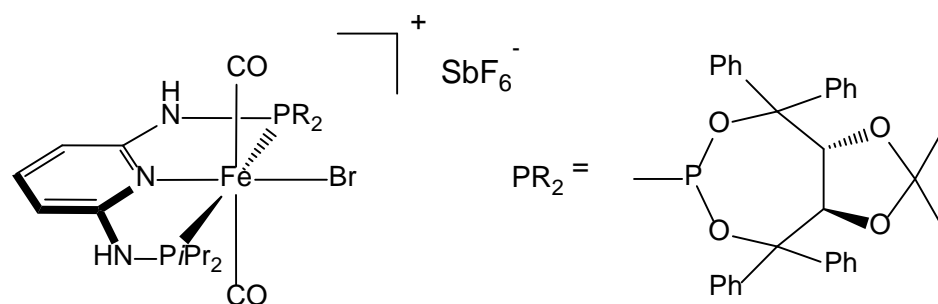
¹H-NMR (δ, CD₂Cl₂, 20 °C): 7.58 – 7.56 (m, 2H, ph), 7.50 – 7.48 (m, 2H, ph), 7.38 – 7.25 (m, 16H, ph), 7.18 (bs, 1H, py⁴), 6.37 (m, 2H, NH^{TAD}, py³), 5.67 (d, ²J_{PH} = 8.1 Hz, 1H, NH^{iPr}), 5.60 (d, ³J_{HH} = 7.2 Hz, 1H, py⁵), 5.52 (d, ³J_{HH} = 7.8 Hz, 1H, CH^{TAD}), 5.48 (d, ³J_{HH} = 7.8 Hz, 1H, CH^{TAD}), 3.05 – 2.83 (m, 2H, CH(CH₃)₂^{iPr}), 1.47 – 1.30 (m, 12H, CH(CH₃)₂^{iPr}), 0.78 (s, 3H, CH₃^{TAD}), 0.37 (s, 3H, CH₃^{TAD}).

¹³C{¹H}-NMR (δ, CD₂Cl₂, 20 °C): 207.44 (dd, ²J_{CP} = 23.8 Hz, ²J_{CP} = 36.6 Hz, CO), 207.08 (dd, ²J_{CP} = 24.4 Hz, ²J_{CP} = 38.0 Hz, CO), 161.78 (m, py²), 156.10 (dd, ²J_{CP} = 18.2 Hz, ⁴J_{CP} = 2.7 Hz, py⁶), 142.73 (py⁴), 141.95 (ph¹), 141.72 (d, ³J_{CP} = 2.3 Hz, ph¹), 139.19 (d, ³J_{CP} = 4.5 Hz, ph¹), 138.90 (d, ³J_{CP} = 8.7 Hz, ph¹), 129.52 (s, ph), 129.28 (s, ph), 129.07 (s, ph), 129.05 (s, ph), 128.57 (s, ph), 128.54 (s, ph), 128.42 (s, ph), 128.31 (s, ph), 128.20 (s, ph), 127.71 (s, ph), 127.67 (s, ph), 126.94 (s, ph), 115.79 (s, C(CH₃)₂), 102.54 (d, ³J_{CP} = 11.2 Hz, ⁵J_{CP} = 6.8 Hz, py³), 100.24 (d, ³J_{CP} = 9.0 Hz, ⁵J_{CP} = 3.3 Hz, py⁵), 93.68 (d, ²J_{CP} = 13.0 Hz, C(ph)₂), 93.12 (d, ²J_{CP} = 19.5 Hz, C(ph)₂), 79.47 (d, ³J_{CP} = 3.6 Hz, CH^{TAD}), 78.22 (d, ³J_{CP} = 3.2 Hz, CH^{TAD}), 32.16 (dd, ¹J_{CP} = 23.4 Hz, ³J_{CP} = 1.9 Hz, CH(CH₃)₂^{iPr}), 31.84 (d, ¹J_{CP} = 21.8 Hz, CH(CH₃)₂^{iPr}), 26.82 (CH₃^{TAD}), 25.80 (CH₃^{TAD}), 17.68 – 17.48 (m, ²J_{CP} = 1.1 Hz, CH(CH₃)₂^{iPr}).

³¹P{¹H}-NMR (δ, CD₂Cl₂, 20 °C): 144.66 (d, ²J_{PP} = 175.9 Hz, TAD), 111.87 (d, ²J_{PP} = 175.9 Hz, *i*Pr).

IR (ATR, cm⁻¹): 2026 (ν_{C=O}).

trans-[Fe(PNP-*i*Pr/TAD)(CO)₂Br]SbF₆ (8l)



This complex was prepared analogously to **8k** with **6f** (1.00 eq; 0.21 mmol; 200 mg) and AgSbF_6 (1.00 eq; 0.21 mmol; 74 mg) as starting materials.

Yield: 180 mg (73%) red solid

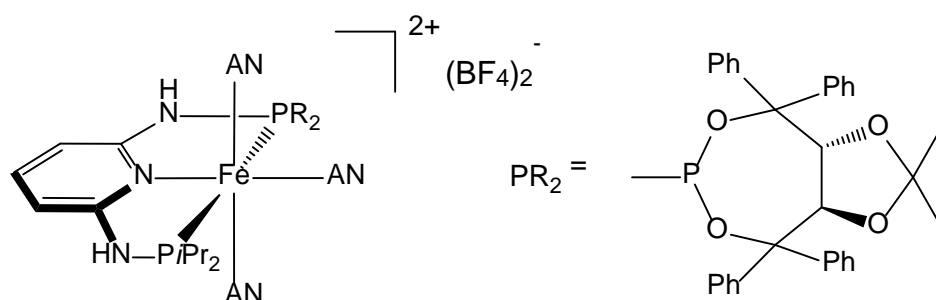
¹H-NMR (δ, CD₂Cl₂, 20°C): 7.57 - 7.55 (m, 2H, ph), 7.51 - 7.48 (m, 2H, ph), 7.41 - 7.25 (m, 16H, ph), 7.21 (d, ³J_{HH} = 8.1 Hz, 1H, py⁴), 6.44 (d, ²J_{PH} = 2.2 Hz, 1H, NH^{TAD}), 6.40 (d, ³J_{HH} = 8.1 Hz, 1H, py³), 5.66 (d, ²J_{PH} = 8.5 Hz, 1H, NH^{iPr}), 5.62 (d, ³J_{HH} = 8.0 Hz, 1H, py⁵), 5.50 (d, ³J_{HH} = 7.8 Hz, 1H, CH^{TAD}), 5.46 (d, ³J_{HH} = 7.8 Hz, 1H, CH^{TAD}), 3.00 - 2.84 (m, 2H, CH(CH₃)₂^{iPr}), 1.47 (dd, ³J_{HH} = 7.1 Hz, ³J_{PH} = 3.0 Hz, 3H, CH(CH₃)₂^{iPr}), 1.43 (dd, ³J_{HH} = 7.1 Hz, ³J_{PH} = 4.2 Hz, 3H, CH(CH₃)₂^{iPr}), 1.39 (dd, ³J_{HH} = 7.2 Hz, ³J_{PH} = 15.4 Hz, 3H, CH(CH₃)₂^{iPr}), 1.35 (dd, ³J_{HH} = 7.1 Hz, ³J_{PH} = 16.3 Hz, 3H, CH(CH₃)₂^{iPr}), 0.80 (s, 3H, CH₃^{TAD}), 0.37 (s, 3H, CH₃^{TAD}).

¹³C{¹H}-NMR (δ, CD₂Cl₂, 20°C): 207.76 (dd, ²J_{CP} = 21.2 Hz, ²J_{CP} = 37.9 Hz, CO), 207.38 (dd, ²J_{CP} = 23.8 Hz, ²J_{CP} = 42.3 Hz, CO), 161.75 (dd, ²J_{CP} = 8.1 Hz, ⁴J_{CP} = 6.2 Hz, py²), 156.14 (dd, ²J_{CP} = 18.5 Hz, ⁴J_{CP} = 2.9 Hz, py⁶), 142.77 (s, ph¹), 141.90 (s, py⁴), 141.87 (s, ph¹), 139.23 (d, ³J_{CP} = 4.3 Hz, ph¹), 138.91 (d, ³J_{CP} = 8.8 Hz, ph¹), 129.51 (s, ph), 129.28 (s, ph), 129.06 (s, ph), 129.00 (s, ph), 128.61 (s, ph), 128.54 (s, ph), 128.43 (s, ph), 128.35 (s, ph), 128.21 (s, ph), 127.69 (s, ph), 126.91 (s, ph), 115.77 (C(CH₃)₂), 102.50 (d, ³J_{CP} = 6.3 Hz, py³), 100.18 (d, ³J_{CP} = 9.2 Hz, py⁵), 94.01 (d, ²J_{CP} = 13.8 Hz, C(ph)₂), 93.02 (d, ²J_{CP} = 19.6 Hz, C(ph)₂), 79.52 (d, ³J_{CP} = 3.7 Hz, CH^{TAD}), 78.25 (d, ³J_{CP} = 3.3 Hz, CH^{TAD}), 32.44 (dd, ¹J_{CP} = 23.7 Hz, ³J_{CP} = 3.2 Hz, CH(CH₃)₂^{iPr}), 32.12 (dd, ¹J_{CP} = 22.4 Hz, ³J_{CP} = 3.2 Hz, CH(CH₃)₂^{iPr}), 26.85 (CH₃^{TAD}), 25.77 (CH₃^{TAD}), 18.01 (d, ²J_{CP} = 1.1 Hz, CH(CH₃)₂^{iPr}), 17.92 (bs, CH(CH₃)₂^{iPr}), 17.86 (CH(CH₃)₂^{iPr}), 17.84 (CH(CH₃)₂^{iPr}).

³¹P{¹H}-NMR (δ, CD₂Cl₂, 20°C): 144.66 (d, ²J_{PP} = 169.8 Hz, TAD), 113.36 (d, ²J_{PP} = 169.9 Hz, *i*Pr).

IR (ATR, cm⁻¹): 2021 (ν_{C=O}).

[Fe(PNP-*i*Pr/TAD)(AN)₃](BF₄)₂ (8m)



Method A: **6f** (1.00 eq; 0.16 mmol; 150 mg) was treated with NaBF₄ (2.10 eq; 0.34 mmol; 37 mg) in 15 mL CH₃CN and stirred at r.t. for 12 h. The solvent was removed under vacuum, the residue redissolved in CH₂Cl₂ and filtered. The volume of the solvent was removed to 0.5 mL and the product was precipitated by addition of 40 mL *n*-pentane. After filtration, the orange solid was washed with 2x 15 mL *n*-pentane and dried under vacuum for 2 h.

Yield: 122 mg (94%) orange solid

Method B: **4h** (1.00 eq; 0.14 mmol; 100 mg) was treated with [Fe(AN)₆](BF₄)₂ (1.00 eq; 0.14 mmol; 94 mg) in 15 mL CH₃CN and stirred at r.t. for 12 h. The workup was equal to method A.

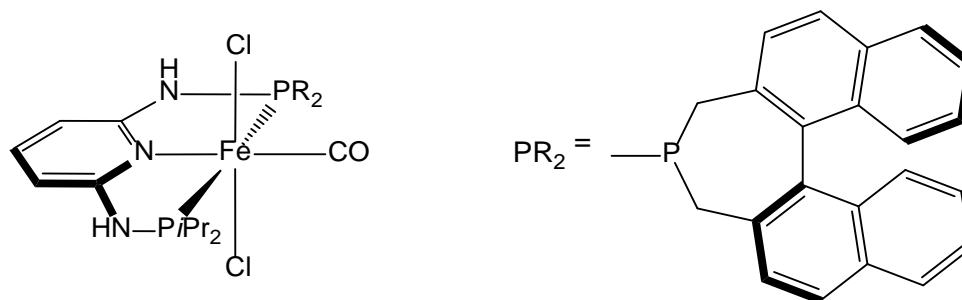
Yield: 141 mg (87%) orange solid

¹H-NMR (δ, CD₃CN, 20°C): 9.66 (d, ²J_{PH} = 3.4 Hz, 1H, NH^{TAD}), 8.35 (d, ²J_{PH} = 7.8 Hz, 1H, NH^{Pr}), 7.66 (m, 2H, ph), 7.58 (m, 2H, ph), 7.53 – 7.31 (m, 16H, ph), 7.28 (t, ³J_{HH} = 7.8 Hz, 1H, py⁴), 7.04 (d, ³J_{HH} = 8.0 Hz, 1H, py³), 5.97 (d, ³J_{HH} = 7.7 Hz, 1H, py⁵), 5.58 (s, 2H, CH^{TAD}), 3.04 (m, 1H, CH(CH₃)₂), 2.91 (m, 1H, CH(CH₃)₂), 1.97 (m, 9H, CH₃CN), 1.70 (dd, ³J_{HH} = 6.9 Hz, ³J_{PH} = 14.5 Hz, 3H, CH(CH₃)₂), 1.65 (dd, ³J_{HH} = 6.9 Hz, ³J_{PH} = 14.1 Hz, 3H, CH(CH₃)₂), 1.47 (dd, ³J_{HH} = 7.3 Hz, ³J_{PH} = 16.1 Hz, 3H, CH(CH₃)₂), 1.70 (dd, ³J_{HH} = 7.4 Hz, ³J_{PH} = 16.5 Hz, 3H, CH(CH₃)₂), 0.68 (s, 3H, CH₃^{TAD}), 0.62 (s, 3H, CH₃^{TAD}).

$^{13}\text{C}\{^1\text{H}\}$ -NMR (δ , CD_3CN , 20°C): 165.69 (dd, $^2J_{\text{CP}} = 11.2$ Hz, $^4J_{\text{CP}} = 6.7$ Hz, py^2), 158.99 (dd, $^2J_{\text{CP}} = 20.8$ Hz, $^4J_{\text{CP}} = 2.9$ Hz, py^6), 144.16 (s, ph), 142.90 (s, ph), 140.92 (s, ph), 140.51 (bs, py^4 , ph), 137.23 (d, $^3J_{\text{CP}} = 5.2$ Hz, CD_3CN), 136.35 (s, CD_3CN), 129.92 (s, ph), 129.86 (s, ph), 129.28 (s, ph), 129.18 (s, ph), 128.98 (s, ph), 128.86 (s, ph), 128.57 (s, ph), 128.47 (s, ph), 128.31 (s, ph), 128.25 (s, ph), 127.58 (s, ph), 127.33 (s, ph), 127.07 (s, ph), 115.80 (s, $\text{C}(\text{CH}_3)_2$), 102.19 (d, $^3J_{\text{CP}} = 7.0$ Hz, py^3), 99.68 (d, $^3J_{\text{CP}} = 9.5$ Hz, py^5), 90.71 (d, $^2J_{\text{CP}} = 20.37$ Hz, $\text{C}(\text{ph})_2$), 90.08 (d, $^2J_{\text{CP}} = 8.1$ Hz, $\text{C}(\text{ph})_2$), 80.34 (d, $^3J_{\text{CP}} = 3.1$ Hz, CH^{TAD}), 79.38 (d, $^3J_{\text{CP}} = 3.5$ Hz, CH^{TAD}), 28.06 (d, $^1J_{\text{CP}} = 16.8$ Hz, $\text{CH}(\text{CH}_3)_2^{\text{iPr}}$), 27.37 (d, $^1J_{\text{CP}} = 21.4$ Hz, $\text{CH}(\text{CH}_3)_2^{\text{iPr}}$), 26.58 (s, CH_3^{TAD}), 26.53 (s, CH_3^{TAD}), 19.58 (d, $^2J_{\text{CP}} = 13.4$ Hz, $\text{CH}(\text{CH}_3)_2^{\text{iPr}}$), 18.78 (bs, $\text{CH}(\text{CH}_3)_2^{\text{iPr}}$), 6.38 (m, CD_3CN).

$^{31}\text{P}\{^1\text{H}\}$ -NMR (δ , CD_3CN , 20°C): 154.1 (d, $^2J_{\text{PP}} = 243.6$ Hz, TAD), 114.8 (d, $^2J_{\text{PP}} = 243.6$ Hz, iPr).

trans-[Fe(PNP-BIN/*i*Pr)COCl₂ (8n)



CO was bubbled through a solution of **6i** (1.00 eq; 45.29 μ mol; 30 mg) in 0.6 mL CD₂Cl₂ for 2 min, whereupon the colour changed to dark violet.

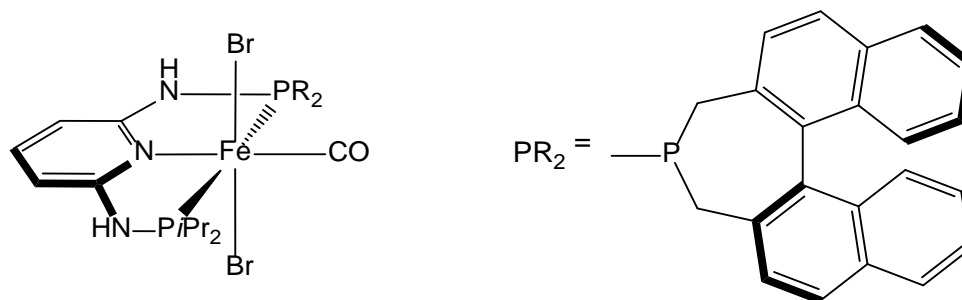
Yield: quantitative

¹H-NMR (δ , CD₂Cl₂, 20°C): 8.13 – 8.00 (m, 4H, naph), 7.79 (d, ³*J*_{HH} = 7.9 Hz, 1H, naph), 7.66 (d, ³*J*_{HH} = 7.5 Hz, 1H, naph), 7.41 (d, ³*J*_{HH} = 8.4 Hz, 1H, naph), 7.34 – 7.15 (m, 6H, naph, py⁴), 6.62 (bs, 1H, py⁵), 6.41 (bs, 1H, NH^{*i*Pr}), 6.03 (bs, 1H, py³), 5.56 (bs, 1H, NH^{BIN}), 4.35 (dd, ²*J*_{HH} = 12.3 Hz, ²*J*_{PH} = 4.1 Hz, 1H, CH₂), 3.76 (dd, ²*J*_{HH} = 15.1 Hz, ²*J*_{PH} = 9.1 Hz, 1H, CH₂), 3.20 (d, ²*J*_{HH} = 15.0 Hz, 1H, CH₂), 2.99 (m, 2H, CH(CH₃)₂), 2.71 (dd, ²*J*_{HH} = 17.0 Hz, ²*J*_{PH} = 13.0 Hz, 1H, CH₂), 1.62 – 1.37 (m, 12H, CH(CH₃)₂).

¹³C{¹H}-NMR (δ , CD₂Cl₂, 20°C): 220.73 (t, ²*J*_{CP} = 22.2 Hz, CO), 161.90 (dd, ²*J*_{CP} = 13.2 Hz, ³*J*_{CP} = 5.6 Hz, py⁶), 160.63 (dd, ²*J*_{CP} = 13.6 Hz, ³*J*_{CP} = 5.1 Hz, py²), 140.16 (s, py⁴), 134.67 (d, *J*_{CP} = 1.8 Hz, naph), 134.16 (d, *J*_{CP} = 4.9 Hz, naph), 133.21 (d, *J*_{CP} = 2.6 Hz, naph), 132.91 (d, *J*_{CP} = 1.6 Hz, naph), 132.82 (s, naph), 132.49 (s, naph), 132.24 (d, *J*_{CP} = 2.5 Hz, naph), 131.56 (d, *J*_{CP} = 3.0 Hz, naph), 129.03 (s, naph), 128.81 (d, *J*_{CP} = 2.1 Hz, naph), 128.45 (d, *J*_{CP} = 3.6 Hz, naph), 128.37 (d, *J*_{CP} = 8.0 Hz, naph), 127.53 (s, naph), 126.96 (s, naph), 126.79 (s, naph), 126.40 (s, naph), 126.08 (s, naph), 125.65 (s, naph), 125.51 (s, naph), 99.88 (d, ³*J*_{CP} = 7.7 Hz, py⁵), 99.52 (d, ³*J*_{CP} = 7.2 Hz, py³), 33.05 (d, ¹*J*_{CP} = 21.9 Hz, CH₂), 29.10 (d, ¹*J*_{CP} = 26.3 Hz, CH₂), 26.23 (d, ¹*J*_{CP} = 21.9 Hz, CH(CH₃)₂), 25.95 (d, ¹*J*_{CP} = 22.2 Hz, CH(CH₃)₂), 18.88 (d, ²*J*_{CP} = 4.1 Hz, CH(CH₃)₂), 18.86 (d, ²*J*_{CP} = 4.0 Hz, CH(CH₃)₂), 17.95 (d, ²*J*_{CP} = 3.5 Hz, CH(CH₃)₂).

³¹P{¹H}-NMR (δ , CD₂Cl₂, 20°C): 143.6 (d, ²*J*_{PP} = 189.7 Hz, BIN), 125.3 (d, ²*J*_{PP} = 189.7 Hz, *i*Pr).

trans-[Fe(PNP-BIN/*i*Pr)COBr₂ (8o)



This complex was prepared analogously to **8n** with **6j** (1.00 eq; 39.93 μ mol; 30 mg) as starting material.

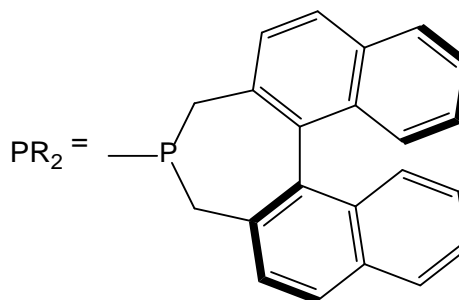
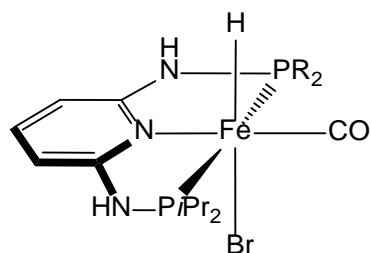
Yield: quantitative

¹H-NMR (δ , CD₂Cl₂, 20°C): 8.01 – 7.90 (m, 4H, naph), 7.80 (d, ³J_{HH} = 7.9 Hz, 1H, naph), 7.54 (d, ³J_{HH} = 7.5 Hz, 1H, naph), 7.41 – 7.36 (m, 3H, naph), 7.30 (d, ³J_{HH} = 8.4 Hz, 1H, naph), 7.25 – 7.03 (m, 3H, naph, py⁴), 6.50 (bs, 1H, py⁵), 6.32 (d, ²J_{PH} = 5.9 Hz, 1H, NH^{Pr}), 5.83 (bs, 1H, py³), 5.50 (d, ²J_{PH} = 6.0 Hz, 1H, NH^{BIN}), 4.67 (dd, ²J_{HH} = 12.5 Hz, ²J_{PH} = 3.9 Hz, 1H, CH₂), 3.94 (dd, ²J_{HH} = 15.1 Hz, ²J_{PH} = 8.8 Hz, 1H, CH₂), 3.10 (m, 3H, CH₂, CH(CH₃)₂), 2.73 (dd, ²J_{HH} = 17.3 Hz, ²J_{PH} = 13.3 Hz, 1H, CH₂), 1.49 (dd, ³J_{HH} = 5.8 Hz, ²J_{PH} = 12.1 Hz, 3H, CH(CH₃)₂), 1.45 (dd, ³J_{HH} = 6.8 Hz, ²J_{PH} = 15.3 Hz, 3H, CH(CH₃)₂), 1.41 (dd, ³J_{HH} = 7.2 Hz, ²J_{PH} = 16.9 Hz, 3H, CH(CH₃)₂), 1.32 (dd, ³J_{HH} = 7.2 Hz, ²J_{PH} = 16.6 Hz, 3H, CH(CH₃)₂),

¹³C{¹H}-NMR (δ , CD₂Cl₂, 20°C): 223.05 (t, ²J_{CP} = 21.9 Hz, CO), 161.97 (dd, ²J_{CP} = 12.6 Hz, ³J_{CP} = 5.3 Hz, py⁶), 160.60 (dd, ²J_{CP} = 13.3 Hz, ³J_{CP} = 5.1 Hz, py²), 140.11 (s, py⁴), 134.65 (s, naph), 134.12 (d, J_{CP} = 5.0 Hz, naph), 133.67 (d, J_{CP} = 10.9 Hz, naph), 133.18 (d, J_{CP} = 2.6 Hz, naph), 132.92 (d, J_{CP} = 1.3 Hz, naph), 132.44 (s, naph), 132.18 (d, J_{CP} = 2.4 Hz, naph), 131.61 (d, J_{CP} = 2.9 Hz, naph), 129.08 (s, naph), 128.80 (d, J_{CP} = 2.2 Hz, naph), 128.39 (d, J_{CP} = 6.2 Hz, naph), 128.22 (d, J_{CP} = 3.5 Hz, naph), 127.63 (d, J_{CP} = 1.6 Hz, naph), 126.92 (d, J_{CP} = 13.8 Hz, naph), 126.41 (s, naph), 126.10 (s, naph), 125.61 (d, J_{CP} = 13.5 Hz, naph), 100.17 (d, ³J_{CP} = 7.0 Hz, py⁵), 99.67 (d, ³J_{CP} = 7.2 Hz, py³), 36.23 (d, ¹J_{CP} = 23.3 Hz, CH₂), 31.39 (d, ¹J_{CP} = 27.9 Hz, CH₂), 28.48 (d, ¹J_{CP} = 22.6 Hz, CH(CH₃)₂), 28.01 (d, ¹J_{CP} = 23.3 Hz, CH(CH₃)₂), 18.97 (d, ²J_{CP} = 4.5 Hz, CH(CH₃)₂), 18.52 (m, CH(CH₃)₂).

³¹P{¹H}-NMR (δ , CD₂Cl₂, 20°C): 143.9 (d, ²J_{PP} = 176.6 Hz, BIN), 125.1 (d, ²J_{PP} = 176.5 Hz, *i*Pr).

Fe(PNP-BIN/*i*Pr)(H)COBr (8p)

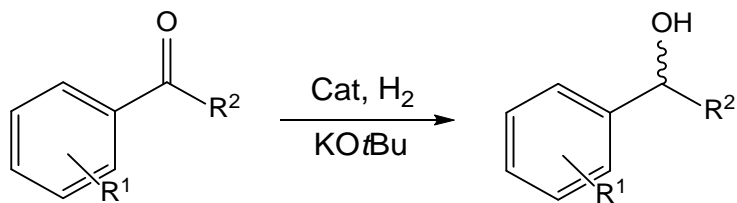


6j (1.00 eq; 0.40 mmol; 300 mg) was dissolved in 15 mL THF and CO was bubbled through the solution for 3 min, whereupon the colour changed to deep blue. The reaction mixture was then cooled to 0°C, Na[HBEt₃] (1.10 eq; 0.44 mmol; 0.44 mL) was added slowly via syringe and after stirring at 0°C the solvent was removed under reduced pressure. The residue was redissolved in 15 mL CH₂Cl₂, filtered and evaporated to 0.5 mL. The product was precipitated by addition of 40 mL *n*-petane, collected on a glas frit, washed with 10 ml *n*-pentane and dried under vacuum for 2 h. The product could not be isolated in pure form.

Yield: 154 mg (55%) yellow-brown solid

5.7 Hydrogenation reaction

General procedure for hydrogenation reactions



All hydrogenation reactions were performed at ambient temperature (25°C) under hydrogen atmosphere of 5 bar using a 90 mL Fisher-Porter tube, which was flushed several times with hydrogen gas prior to the addition of the reaction solution. For the preparation of the reaction solution a vial was charged with the specified amount of catalyst, substrate, and EtOH. Subsequently, KOtBu was added and the solution was taken up into a syringe and transferred to the Fisher-Porter tube. After stirring the solution for the stated time, pressure was carefully released, and the solvent was removed under reduced pressure. EE (20 mL) was added and the solution was filtered over a small pad of silica. The solvent was then again evaporated and the isolated product was characterized by NMR-spectroscopy in 0.5 mL CDCl₃.

5.8 Crystallographic data

	5c	5g^b	5k
formula	C ₃₆ H ₃₄ Cl ₂ FeN ₄ P ₂	C ₂₂ H ₄₀ Cl ₄ Fe ₂ N ₆ P ₂	C ₃₄ H ₃₀ Cl ₄ Fe ₂ N ₄ P ₂ S ₂
fw [g·mol ⁻¹]	711.39	704.04	874.18
cryst. size [mm]	0.20 x 0.10 x 0.05	0.71 x 0.32 x 0.22	0.50 x 0.26 x 0.05
color, shape	light-green plate	translucent yellow rod	colourless plate
crystal system	monoclinic	monoclinic	monoclinic
space group	<i>P</i> 2 ₁ / <i>c</i> (no. 14)	<i>P</i> 2 ₁ / <i>c</i> (no. 14)	<i>C</i> 2/ <i>c</i> (no. 15)
<i>a</i> [Å]	10.1491(3)	7.4720(5)	26.9244(7)
<i>b</i> [Å]	12.8821(3)	17.0774(11)	8.2404(3)
<i>c</i> [Å]	12.8714(3)	25.4250(16)	18.3309(5)
α [°]	90	90	90
β [°]	103.291(1)	92.110(2)	118.354(2)
γ [°]	90	90	90
<i>V</i> [Å ³]	1637.75(7)	3242.1(4)	3579.11(19)
<i>T</i> [K]	100(2)	100(2)	100(2)
<i>Z</i>	2	4	4
ρ_{calc} [g·cm ⁻³]	1.443	1.442	1.622
μ [mm ⁻¹] (MoK α)	0.755	1.346	1.348
<i>F</i> (000)	736	1456	1776
absorption corrections	multi-scan, 0.62-0.75	multi-scan, 0.22-0.71	multi-scan, 0.71-0.94
θ range [°]	2.27-30.04	1.44-32.64	1.72-30.00
no. of rflns measd	33383	107984	30624
<i>R</i> _{int}	0.042	0.034	0.029
no. of rflns unique	4749	11855	5221
no. of rflns <i>I</i> > 2 σ (<i>I</i>)	3686	10292	4722
no. of params / restraints	206 / 0	349 / 6	220 / 0
<i>R</i> ₁ (<i>I</i> > 2 σ (<i>I</i>)) ^a	0.0356	0.0323	0.0274
<i>R</i> ₁ (all data)	0.0576	0.0396	0.0319
<i>wR</i> ₂ (<i>I</i> > 2 σ (<i>I</i>))	0.0740	0.0419	0.0712
<i>wR</i> ₂ (all data)	0.0806	0.0430	0.0758
Diff.Four.peaks min/max [e·Å ⁻³]	-0.33 / 0.56	-0.48 / 1.45	-0.26 / 0.71

Table 11: Details for the crystal structure determinations of **5c**, **5g** and **5k**.

^a $R = \sum ||F_o| - |F_c|| / \sum |F_o|$, $wR = \sum w(|F_o| - |F_c|) / \sum w|F_o|$, ^b refined on F^2 with program JANA2006^[89]

	5l	5m	5n
formula	C ₁₇ H ₁₅ Br ₂ FeN ₂ PS	C ₁₈ H ₁₇ Cl ₂ FeN ₂ PS	C ₁₈ H ₁₇ Br ₂ FeN ₂ PS
fw [g·mol ⁻¹]	526.01	451.12	540.04
cryst. size [mm]	0.21 x 0.18 x 0.12	0.40 x 0.35 x 0.30	0.25 x 0.20 x 0.15
color, shape	colourless block	colourless block	colourless prism
crystal system	monoclinic	monoclinic	monoclinic
space group	<i>P</i> 2 ₁ / <i>c</i> (no. 14)	<i>P</i> 2 ₁ / <i>c</i> (no. 14)	<i>Cc</i> (no. 9)
<i>a</i> [Å]	14.9127(5)	12.2704(5)	16.3077(12)
<i>b</i> [Å]	8.7466(3)	11.2087(4)	8.3429(6)
<i>c</i> [Å]	14.9471(5)	15.4605(6)	15.7119(12)
α [°]	90	90	90
β [°]	96.386(2)	100.267(2)	105.028(2)
γ [°]	90	90	90
<i>V</i> [Å ³]	1937.53(11)	2092.32(14)	2064.5(3)
<i>T</i> [K]	100(2)	100(2)	100(2)
<i>Z</i>	4	4	4
ρ_{calc} [g·cm ⁻³]	1.803	1.432	1.737
μ [mm ⁻¹] (MoK α)	5.094	1.156	4.783
<i>F</i> (000)	1032	920	1064
absorption corrections	multi-scan, 0.56-0.75	multi-scan, 0.66-0.75	multi-scan, 0.38-0.53
θ range [°]	2.05–30.00	2.26–30.00	2.68–30.00
no. of rflns measd	49182	52157	21494
<i>R</i> _{int}	0.028	0.024	0.030
no. of rflns unique	5651	6044	5888
no. of rflns <i>I</i> > 2 σ (<i>I</i>)	5234	5767	5543
no. of params / restraints	221 / 0	227 / 0	227 / 2
<i>R</i> ₁ (<i>I</i> > 2 σ (<i>I</i>)) ^a	0.0163	0.0309	0.0212
<i>R</i> ₁ (all data)	0.0192	0.0323	0.0253
<i>wR</i> ₂ (<i>I</i> > 2 σ (<i>I</i>))	0.0400	0.0840	0.0414
<i>wR</i> ₂ (all data)	0.0409	0.0847	0.0430
Diff. Four. peaks min/max [e·Å ⁻³]	-0.42 / 0.48	-0.39 / 0.85	-0.40 / 0.64

Table 12: Details for the crystal structure determinations of **5l**, **5m** and **5n**.

$$^a R = \sum ||F_o| - |F_c|| / \sum |F_o|, wR = \sum w(|F_o| - |F_c|) / \sum w|F_o|$$

	5o	5p	5r
formula	C ₁₉ H ₁₉ Cl ₂ FeN ₂ PS	C ₁₉ H ₁₉ Br ₂ FeN ₂ PS	C ₅₁ H ₄₅ FeN ₆ P ₃
fw [g·mol ⁻¹]	465.14	554.06	1050.52
cryst. size [mm]	0.42 x 0.40 x 0.20	0.45 x 0.32 x 0.22	0.65 x 0.44 x 0.04
color, shape	colourless plate	colourless prism	clear yellow plate
crystal system	monoclinic	monoclinic	orthorhombic
space group	<i>P</i> 2 ₁ / <i>c</i> (no. 14)	<i>P</i> 2 ₁ / <i>c</i> (no. 14)	<i>F</i> dd2 (no. 43)
<i>a</i> [Å]	13.1363(3)	13.2029(3)	32.0762(14)
<i>b</i> [Å]	11.2803(3)	11.4860(2)	35.738(2)
<i>c</i> [Å]	15.2163(4)	15.7126(3)	19.252(2)
α [°]	90	90	90
β [°]	112.978(2)	114.157(2)	90
γ [°]	90	90	90
<i>V</i> [Å ³]	2075.87(9)	2174.12(7)	22070(3)
<i>T</i> [K]	100(2)	100(2)	100(2)
<i>Z</i>	4	4	16
ρ_{calc} , [g·cm ⁻³]	1.488	1.693	1.264
μ [mm ⁻¹] (MoK α)	1.167	4.545	1.845
<i>F</i> (000)	952	1096	8544
absorption corrections	multi-scan, 0.64-0.75	multi-scan, 0.29-0.44	multi-scan, 0.39-0.93
θ range [°]	2.32–30.00	2.27–30.00	2.11–30.00
no. of rflns measd	18508	54643	43656
<i>R</i> _{int}	0.026	0.029	0.042
no. of rflns unique	6010	6344	15186
no. of rflns <i>I</i> > 2 σ (<i>I</i>)	5143	5707	11710
no. of params / restraints	236 / 0	236 / 0	581 / 3
<i>R</i> ₁ (<i>I</i> > 2 σ (<i>I</i>)) ^a	0.0302	0.0187	0.0373
<i>R</i> ₁ (all data)	0.0394	0.0228	0.0512
<i>wR</i> ₂ (<i>I</i> > 2 σ (<i>I</i>))	0.0684	0.0470	0.0780
<i>wR</i> ₂ (all data)	0.0729	0.0490	0.0819
Diff.Four.peaks min/max [e·Å ⁻³]	-0.32 / 0.75	-0.31 / 0.61	-0.50 / 0.81

Table 13: Details for the crystal structure determinations of **5o**, **5p** and **5r**.

$$^a R = \sum ||F_o| - |F_c|| / \sum |F_o|, wR = \sum w(|F_o| - |F_c|) / \sum w|F_o|$$

	6a	6c ^b	6d ^b
formula	C ₂₃ H ₄₅ Cl ₂ FeN ₃ P ₂ O	C ₂₁ H ₄₁ Cl ₂ FeN ₃ P ₂	C ₂₁ H ₄₁ Br ₂ FeN ₃ P ₂
fw [g·mol ⁻¹]	1064.52	524.27	613.18
cryst. size [mm]	0.45 x 0.12 x 0.10	0.44 x 0.35 x 0.08	0.76 x 0.45 x 0.40
color, shape	yellow rod	translucent yellow, rhombic prism	dark yellow block
crystal system	monoclinic	monoclinic	Monoclinic
space group	C2/c (no. 15)	P2 ₁ /c (no. 14)	P2 ₁ /c (no. 14)
a [Å]	29.401(3)	9.6225(7)	9.7942(11)
b [Å]	14.7428(18)	18.6537(14)	18.937(2)
c [Å]	12.3624(15)	14.4955(10)	14.5593(17)
α [°]	90	90	90
β [°]	101.013(3)	93.547(2)	94.208(3)
γ [°]	90	90	90
V [Å ³]	5259.8(10)	2596.9(3)	2693.1(5)
T [K]	100(2)	100(2)	100(2)
Z	4	4	4
ρ _{calc.} [g·cm ⁻³]	1.334	1.341	1.5119
μ [mm ⁻¹] (MoKα)	0.914	0.923	3.659
F(000)	2232	1112	1256
absorption corrections	multi-scan, 0.66-0.90	multi-scan, 0.69-0.93	multi-scan, 0.15-0.23
θ range [°]	2.18-27.58	2.4-32.6	2.3-32.5
no. of rflns measd	43928	86108	165309
R _{int}	0.0603	0.024	0.061
no. of rflns unique	6061	9487	9871
no. of rflns I > 2σ(I)	4307	8295	7984
no. of params / restraints	282 / 0	262 / 0	262 / 0
R ₁ (I > 2σ(I)) ^a	0.0522	0.0213	0.0271
R ₁ (all data)	0.0883	0.0274	0.0413
wR ₂ (I > 2σ(I))	0.1210	0.0324	0.0318
wR ₂ (all data)	0.1412	0.0328	0.0332
Diff.Four.peaks min/max [e·Å ⁻³]	-0.72 / 2.29	-0.20 / 0.47	-0.42 / 0.95

Table 14: Details for the crystal structure determinations of **6a**, **6c** and **6d**.

^a $R = \sum ||F_o| - |F_c|| / \sum |F_o|$, $wR = \sum w(|F_o| - |F_c|) / \sum w|F_o|$, ^b refined on F^2 with program JANA2006^[89]

	6f ·THF	6g ·THF	6i ^b
formula	C ₄₆ H ₅₅ Br ₂ FeN ₃ O ₅ P ₂	C ₄₈ H ₅₉ Cl ₂ FeN ₃ O ₅ P ₂	C ₃₃ H ₃₅ Cl ₂ FeN ₃ P ₂
fw [g·mol ⁻¹]	1007.6	946.7	662.35
cryst. size [mm]	0.54 x 0.22 x 0.02	0.58 x 0.50 x 0.02	0.54 x 0.44 x 0.31
color, shape	yellow plate	yellow plate	translucent colourless, irregular shape
crystal system	triclinic	monoclinic	tetragonal
space group	<i>P</i> 1 (no. 1)	<i>P</i> 2 ₁ (no. 61)	<i>I</i> 4 ₁ /a (no. 88)
<i>a</i> [Å]	9.1105(5)	9.4904(9)	24.1896(7)
<i>b</i> [Å]	10.3931(6)	10.3270(9)	24.1896(7)
<i>c</i> [Å]	24.1374(14)	25.295(2)	28.4068(17)
α [°]	93.0205(19)	90	90
β [°]	93.3464(18)	98.334(3)	90
γ [°]	91.2982(19)	90	90
<i>V</i> [Å ³]	2277.7(2)	10227(3)	16621.9(12)
<i>T</i> [K]	100	100	100
<i>Z</i>	2,2	2,1	16
ρ_{calc} [g·cm ⁻³]	1.4691	1.2814	1.0587
μ [mm ⁻¹] (MoK α)	2.204	0.528	0.59
<i>F</i> (000)	1036	996	5504
absorption corrections	multi-scan, 0.56–0.96	multi-scan, 0.74–0.94	multi-scan, 0.74-0.83
θ range [°]	0.85–30.2	0.81–0.81	1.11-30.06
no. of rflns measd	55010	52964	219225
<i>R</i> _{int}	0.0406	0.0368	0.0465
no. of rflns unique	25848	14261	12180
no. of rflns <i>I</i> > 2 σ (<i>I</i>)	19167	12404	8658
no. of params / restraints	1064 / 0	551 / 0	370 / 0
<i>R</i> ₁ (<i>I</i> > 2 σ (<i>I</i>)) ^a	0.0327	0.0441	0.0763
<i>R</i> ₁ (all data)	0.0553	0.0529	0.0980
<i>wR</i> ₂ (<i>I</i> > 2 σ (<i>I</i>))	0.0347	0.0471	0.0947
<i>wR</i> ₂ (all data)	0.0379	0.0479	0.0967
Diff.Four.peaks min/max [e·Å ⁻³]	-0.33 / 0.34	-0.49 / 0.69	-1.10 / 1.72

Table 15: Details for the crystal structure determinations of **6f**·THF, **6g**·THF and **6i**.

^a $R = \sum(|F_o| - |F_c|) / \sum|F_o|$, $wR = \sum w(|F_o| - |F_c|) / \sum w|F_o|$, ^b refined on F^2 with program JANA2006^[89]

	6k ^b	6l ^b	8e ^b
formula	C ₁₂ H ₂₂ Cl ₂ FeN ₃ P	C ₁₆ H ₂₈ Br ₂ Cl ₂ D ₂ FeN ₃ P	C ₂₁ H ₃₇ BClF ₄ FeN ₃ O ₂ P ₂
fw [g·mol ⁻¹]	366.05	583.98	603.61
cryst. size [mm]	0.57 x 0.33 x 0.06	0.66 x 0.32 x 0.13	0.42 x 0.22 x 0.04
color, shape	translucent pale yellow plate	translucent yellow tabular	dark yellow plate
crystal system	monoclinic	monoclinic	monoclinic
space group	C2/c (no. 15)	C2/c (no. 15)	P2 ₁ /c
a [Å]	29.6937(19)	29.9135(19)	7.9758(4)
b [Å]	11.7217(7)	11.8868(7)	23.8910(13)
c [Å]	13.9499(9)	14.2796(9)	14.5351(8)
α [°]	90	90	90
β [°]	111.3638(18)	110.9847(18)	100.4173(16)
γ [°]	90	90	90
V [Å ³]	4521.8(5)	4740.7(5)	2724.0(3)
T [K]	100	100	100
Z	8	8	4
ρ _{calc.} [g·cm ⁻³]	1.4078	1.6364	1.4718
μ [mm ⁻¹] (MoKα)	1.174	4.306	0.821
F(000)	1989	2336	1256
absorption corrections	multi-scan, 0.63-0.93	multi-scan, 0.21-0.57	multi-scan, 0.80-0.97
θ range [°]	1.47-32.63	1.86-35.69	1.66-32.7
no. of rflns measd	109618	64390	54661
R _{int}	0.0309	0.0411	0.0553
no. of rflns unique	8255	10973	9991
no. of rflns I > 2σ(I)	7198	8086	6826
no. of params / restraints	250 / 0	248 / 2	316 / 0
R ₁ (I > 2σ(I)) ^a	0.0278	0.0278	0.0322
R ₁ (all data)	0.0339	0.0487	0.0632
wR ₂ (I > 2σ(I))	0.0510	0.0309	0.0345
wR ₂ (all data)	0.0518	0.0327	0.0365
Diff. Four. peaks min/max [e·Å ⁻³]	-0.38 / 1.15	-0.62 / 0.71	-0.48 / 0.51

Table 16: Details for the crystal structure determinations of **6k**, **6l** and **8e**.

^a $R = \sum ||F_o| - |F_c|| / \sum |F_o|$, $wR = \sum w(|F_o| - |F_c|) / \sum w|F_o|$, ^b refined on F^2 with program JANA2006^[89]

	8f ^b	8g ^b	8h ^b
formula	C ₂₁ H ₃₇ BBrF ₄ FeN ₃ O ₂ P ₂	C ₂₃ H ₄₁ BCIF ₄ FeN ₃ O ₂ P ₂	C ₂₃ H ₄₁ BBrF ₄ FeN ₃ O ₂ P ₂
fw [g·mol ⁻¹]	648.06	631.66	676.11
cryst. size [mm]	0.47 x 0.43 x 0.33	0.32 x 0.30 x 0.24	0.41 x 0.35 x 0.04
color, shape	dark red, irregular shape	dark red block	dark yellow plate
crystal system	monoclinic	monoclinic	orthorhombic
space group	<i>P</i> 2 ₁ / <i>c</i> (no. 14)	<i>P</i> 2 ₁ (no. 4)	<i>Pca</i> 2 ₁ (no.29)
<i>a</i> [Å]	8.0267(7)	8843(3)	26.2709(2)
<i>b</i> [Å]	23.671(2)	13.9759(6)	8.4711(3)
<i>c</i> [Å]	14.8427(12)	12.5318(5)	12.9569(5)
α [°]	90	90	90
β [°]	101.0101(18)	97*.8091(13)	90
γ [°]	90	90	90
<i>V</i> [Å ³]	2768.2(4)	1437.48(10)	2883.47(15)
<i>T</i> [K]	100	100	100
<i>Z</i>	4	2	4
ρ_{calc} , [g·cm ⁻³]	1.555	1.4593	1.5574
μ [mm ⁻¹] (MoK α)	2.155	0.781	2.072
<i>F</i> (000)	1328	660	1392
absorption corrections	multi-scan, 0.38-0.49	multi-scan, 0.78-0.83	multi-scan, 0.70-0.90
θ range [°]	1.64-35.13	1.64-35.09	1.55-30.10
no. of rflns measd	49889	53678	17126
<i>R</i> _{int}	0.0275	0.0213	0.0232
no. of rflns unique	12270	12700	7442
no. of rflns <i>I</i> > 2 σ (<i>I</i>)	10047	12003	6547
no. of params / restraints	316 / 0	335 / 0	335 / 0
<i>R</i> ₁ (<i>I</i> > 2 σ (<i>I</i>)) ^a	0.0299	0.0198	0.0234
<i>R</i> ₁ (all data)	0.0422	0.0217	0.0283
<i>wR</i> ₂ (<i>I</i> > 2 σ (<i>I</i>))	0.0364	0.0256	0.0268
<i>wR</i> ₂ (all data)	0.0377	0.0258	0.0276
Diff.Four.peaks min/max [e·Å ⁻³]	-0.73 / 0.54	-0.21 / 0.34	-0.18 / 0.28

Table 17: Details for the crystal structure determinations of **8f**, **8g** and **8h**.

^a $R = \sum ||F_o| - |F_c|| / \sum |F_o|$, $wR = \sum w(|F_o| - |F_c|) / \sum w|F_o|$, ^b refined on F^2 with program JANA2006^[89]

	8j·2THF ^b
formula	C ₅₁ H ₆₃ Br ₂ FeN ₃ O ₇ P ₂
fw [g·mol ⁻¹]	1107.7
cryst. size [mm]	0.72 x 0.24 x 0.24
color, shape	dark blue rod
crystal system	tetragonal
space group	<i>P</i> 4 ₁ (no. 76)
<i>a</i> [Å]	22.454(4)
<i>b</i> [Å]	22.454(4)
<i>c</i> [Å]	10.598(4)
α [°]	90
β [°]	90
γ [°]	90
<i>V</i> [Å ³]	5343(2)
<i>T</i> [K]	100
<i>Z</i>	4,1
ρ_{calc} [g·cm ⁻³]	1.3770
μ [mm ⁻¹] (MoK α)	1.888
<i>F</i> (000)	2288
absorption corrections	multi-scan, 0.59–0.78
θ range [°]	2.57–30.11
no. of rflns measd	138990
<i>R</i> _{int}	0.0628
no. of rflns unique	15648
no. of rflns <i>I</i> > 2 σ (<i>I</i>)	13207
no. of params / restraints	604 / 2
<i>R</i> ₁ (<i>I</i> > 2 σ (<i>I</i>)) ^a	0.0396
<i>R</i> ₁ (all data)	0.0487
<i>wR</i> ₂ (<i>I</i> > 2 σ (<i>I</i>))	0.0462
<i>wR</i> ₂ (all data)	0.0475
Diff. Four. peaks min/max [e·Å ⁻³]	-0.18 / 0.27

Table 18: Details for the crystal structure determinations of **8j·2THF**.

^a $R = \sum ||F_o| - |F_c|| / \sum |F_o|$, $wR = \sum w(|F_o| - |F_c|) / \sum w|F_o|$, ^b refined on F^2 with program JANA2006^[89]

6 Bibliography

1. Moulton, C. J.; Shaw, B. L., *J Chem Soc Dalton* **1976**, (11), 1020-1024.
2. (a) Peris, E.; Crabtree, R. H., *Coordination Chemistry Reviews* **2004**, *248* (21-24), 2239-2246; (b) Albrecht, M.; van Koten, G., *Angewandte Chemie International Edition* **2001**, *40* (20), 3750-3781; (c) Selander, N.; K, J. S., *Chem Rev* **2011**, *111* (3), 2048-76; (d) M. Jensen, C., *Chemical communications* **1999**, (24), 2443-2449; (e) Benito-Garagorri, D.; Kirchner, K., *Acc. Chem. Res.* **2008**, *41* (2), 201-213; (f) Langer, R.; Leitus, G.; Ben-David, Y.; Milstein, D., *Angewandte Chemie* **2011**, *50* (9), 2120-4.
3. (a) Guiry, P. J.; Saunders, C. P., *Advanced Synthesis & Catalysis* **2004**, *346* (5), 497-537; (b) Martin, R.; Buchwald, S. L., *Acc. Chem. Res.* **2008**, *41* (11), 1461-1473; (c) Surry, D. S.; Buchwald, S. L., *Angewandte Chemie* **2008**, *47* (34), 6338-61.
4. Yamanaka, M.; Mikami, K., *Organometallics* **2005**, *24* (19), 4579-4587.
5. Tolman, C. A., *Chem. Rev.* **1977**, *77* (3), 313-348.
6. (a) Streitwieser, A.; McKeown, A. E.; Hasanayn, F.; Davis, N. R., *Org. Lett.* **2005**, *7* (7), 1259-1262; (b) Henderson, W. A.; Streuli, C. A., *Journal of the American Chemical Society* **1960**, *82*, 5791-5794.
7. Morales-Morales, D.; Jensen, C. M., *The chemistry of pincer compounds*. 1st ed.; Elsevier: Amsterdam ; Boston, 2007; p xiii, 450 p.
8. van der Boom, M. E.; Milstein, D., *Chemical Reviews* **2003**, *103* (5), 1759-1792.
9. Brookhart, M.; Green, M. L. H., *Journal of Organometallic Chemistry* **1983**, *250* (1), 395-408.
10. Seebach, D., *Angewandte Chemie International Edition in English* **1979**, *18* (4), 239-258.
11. Leung, W.-P.; Ip, Q. W.-Y.; Wong, S.-Y.; Mak, T. C. W., *Organometallics* **2003**, *22* (22), 4604-4609.
12. Widhalm, M.; Kasák, P., *Synthesis* **2007**, *2007* (19), 2987-2994.
13. (a) Agbossou, F.; Carpentier, J.-F.; Mortreaux, A., *Chem. Rev.* **1995**, *95* (7), 2485-506; (b) Beller, M.; Cornils, B.; Frohning, C. D.; Kohlpaintner, C. W., *Journal of Molecular Catalysis A: Synthesis* **1995**, *104* (1), 17-85; (c) Breit, B.; Seiche, W., *Synthesis* **2000**, *1*, 1-36.
14. Paulik, F. E.; Roth, J. F., *Chem. Commun. (London)* **1968**, *24*, 1578.
15. Jones, J. H., *Platinum Metals Rev.* **2000**, *44* (3), 94-105.
16. (a) Masters, C., *Advances in Organometallic Chemistry* **1979**, *17*, 61-103; (b) Boudart, M.; McDonald, M. A., *J. Phys. Chem.* **1983**, *88*, 2185-2195.
17. (a) Volbeda, A.; Charon, M.-H.; Piras, C.; Hatchikian, C. E.; Frey, M.; Fontecilla-Camps, J. C., *Nature* **1995**, *373* (6515), 580-587; (b) Peters, J. W.; Lanzilotta, W. N.; Lemon, B. J.; Seefeldt, L. C., *Science* **1998**, *282* (5395), 1853-1858; (c) Lyon, E. J.; Shima, S.; Boecher, R.; Thauer, R. K.; Grevels, F.-W.; Bill, E.; Roseboom, W.; Albracht, S. P. J., *Journal of the American Chemical Society* **2004**, *126* (43), 14239-14248; (d) Tard, C.; Pickett, C. J., *Chem. Rev.* **2009**, *109* (6), 2245-2274.
18. Aubke, F.; Wang, C., *Coordination Chemistry Reviews* **1994**, *137* (0), 483-524.
19. Benito-Garagorri, D.; Lagoja, I.; Veiros, L. F.; Kirchner, K. A., *Dalton transactions* **2011**, *40* (18), 4778-92.
20. Blaser, H.-U.; Malan, C.; Pugin, B.; Spindler, F.; Steiner, H.; Studer, M., *Advanced Synthesis & Catalysis* **2003**, *345* (1-2), 103-151.

21. (a) Miyashita, A.; Yasuda, A.; Takaya, H.; Toriumi, K.; Ito, T.; Souchi, T.; Noyori, R., *Journal of the American Chemical Society* **1980**, *102* (27), 7932-7934; (b) Ohkuma, T.; Ooka, H.; Hashiguchi, S.; Ikariya, T.; Noyori, R., *Journal of the American Chemical Society* **1995**, *117* (9), 2675-2676.
22. (a) Sandoval, C. A.; Li, Y.; Ding, K.; Noyori, R., *Chem Asian J* **2008**, *3* (10), 1801-10; (b) Clapham, S. E.; Hadzovic, A.; Morris, R. H., *Coordination Chemistry Reviews* **2004**, *248* (21-24), 2201-2237.
23. (a) Gladiali, S.; Alberico, E., *Chem Soc Rev* **2006**, *35* (3), 226-36; (b) Matharu, D. S.; Martins, J. E. D.; Wills, M., *Chemistry – An Asian Journal* **2008**, *3* (8-9), 1374-1383; (c) Baratta, W.; Rigo, P., *European Journal of Inorganic Chemistry* **2008**, *2008* (26), 4041-4053.
24. Morris, R. H., *Chem Soc Rev* **2009**, *38* (8), 2282-91.
25. Gorgas, N.; Stöger, B.; Veiros, L. F.; Pittenauer, E.; Allmaier, G.; Kirchner, K., *Organometallics* **2014**, *33* (23), 6905-6914.
26. (a) Hazari, N., *Chem Soc Rev* **2010**, *39* (11), 4044-56; (b) Ingleson, M. J.; Layfield, R. A., *Chemical communications* **2012**, *48* (30), 3579-89; (c) Roy, A. K., A Review of Recent Progress in Catalyzed Homogeneous Hydrosilylation (Hydrosilylation). In *Advances in Organometallic Chemistry*, Robert West, A. F. H.; Mark, J. F., Eds. Academic Press: 2007; Vol. Volume 55, pp 1-59; (d) Junge, K.; Schroder, K.; Beller, M., *Chemical communications* **2011**, *47* (17), 4849-59; (e) Enthaler, S.; Junge, K.; Beller, M., *Angewandte Chemie International Edition* **2008**, *47* (18), 3317-3321; (f) Pospech, J.; Fleischer, I.; Franke, R.; Buchholz, S.; Beller, M., *Angewandte Chemie International Edition* **2013**, *52* (10), 2852-2872.
27. (a) Yang, X., *Inorganic chemistry* **2011**, *50* (24), 12836-43; (b) Prokopchuk, D. E.; Morris, R. H., *Organometallics* **2012**, *31* (21), 7375-7385; (c) Zhang, H.; Chen, D.; Zhang, Y.; Zhang, G.; Liu, J., *Dalton transactions* **2010**, *39* (8), 1972-8; (d) Yang, X., *ACS Catalysis* **2011**, *1* (8), 849-854.
28. Lagaditis, P. O.; Lough, A. J.; Morris, R. H., *Inorganic chemistry* **2010**, *49* (21), 10057-66.
29. Bhattacharya, P.; Krause, J. A.; Guan, H., *Organometallics* **2011**, *30* (17), 4720-4729.
30. (a) Jiao, H.; Junge, K.; Alberico, E.; Beller, M., *Journal of Computational Chemistry* **2015**, n/a-n/a; (b) Langer, R.; Iron, M. A.; Konstantinovski, L.; Diskin-Posner, Y.; Leitus, G.; Ben-David, Y.; Milstein, D., *Chemistry – A European Journal* **2012**, *18* (23), 7196-7209; (c) Lu, X.; Cheng, R.; Turner, N.; Liu, Q.; Zhang, M.; Sun, X., *The Journal of organic chemistry* **2014**, *79* (19), 9355-9364; (d) Qu, S.; Dai, H.; Dang, Y.; Song, C.; Wang, Z.-X.; Guan, H., *ACS Catalysis* **2014**, *4* (12), 4377-4388.
31. Benito-Garagorri, D.; Becker, E.; Wiedermann, J.; Lackner, W.; Pollak, M.; Mereiter, K.; Kisala, J.; Kirchner, K., *Organometallics* **2006**, *25* (8), 1900-1913.
32. (a) Oztöpcü, O.; Holzhaecker, C.; Puchberger, M.; Weil, M.; Mereiter, K.; Veiros, L. F.; Kirchner, K., *Organometallics* **2013**, *32* (10), 3042-3052; (b) de Aguiar, S. R.; Oztöpcü, O.; Stöger, B.; Mereiter, K.; Veiros, L. F.; Pittenauer, E.; Allmaier, G.; Kirchner, K., *Dalton transactions* **2014**, *43* (39), 14669-79; (c) de Aguiar, S. R.; Stöger, B.; Pittenauer, E.; Puchberger, M.; Allmaier, G.; Veiros, L. F.; Kirchner, K., *J Organomet Chem* **2014**, *760* (100), 74-83.
33. Bichler, B.; Holzhaecker, C.; Stöger, B.; Puchberger, M.; Veiros, L. F.; Kirchner, K., *Organometallics* **2013**, *32* (15), 4114-4121.
34. Mastalir, M. Modifizierung und Design neuer 2,6-Diaminopyridinsysteme für die Entwicklung neuer PNP-Pincer-Liganden. Diploma thesis, Vienna University of Technology, 2013.
35. Lloyd-Jones, G. C.; Taylor, N. P., *Chemistry* **2015**, *21* (14), 5423-8.
36. (a) Blaser, H. U., *Chemical Reviews* **1992**, *92* (5), 935-952; (b) Glueck, D. S., *Chemistry – A*

- European Journal* **2008**, *14* (24), 7108-7117; (c) Nugent, W. A.; RajanBabu, T. V.; Burk, M. J., *Science* **1993**, *259* (5094), 479-483.
37. Benito-Garagorri, D.; Bocokić, V.; Mereiter, K.; Kirchner, K., *Organometallics* **2006**, *25* (16), 3817-3823.
 38. Seebach, D.; Plattner, D. A.; Beck, A. K.; Wang, Y. M.; Hunziker, D.; Petter, W., *Helvetica Chimica Acta* **1992**, *75* (7), 2171-2209.
 39. Seebach, D.; Beck, A. K.; Heckel, A., *Angewandte Chemie International Edition* **2001**, *40* (1), 92-138.
 40. Kanger, T.; Kriis, K.; Paju, A.; Pehk, T.; Lopp, M., *Tetrahedron: Asymmetry* **1998**, *9* (24), 4475-4482.
 41. Teller, H.; Furstner, A., *Chemistry* **2011**, *17* (28), 7764-7.
 42. Kim, M., B.; Bae, S., J.; So, S. M.; Yoo, H. T.; Chang, S. K.; Lee, J. H.; Kang, J., *Org. Lett.* **2001**, *3* (15), 2349-2351.
 43. Bichler, B.; Glatz, M.; Stoger, B.; Mereiter, K.; Veiros, L. F.; Kirchner, K., *Dalton transactions* **2014**, *43* (39), 14517-14519.
 44. Junge, K.; Hagemann, B.; Enthaler, S.; Spannenberg, A.; Michalik, M.; Oehme, G.; Monsees, A.; Riermeier, T.; Beller, M., *Tetrahedron: Asymmetry* **2004**, *15* (17), 2621-2631.
 45. Holzhaecker, C.; Calhorda, M. J.; Gil, A.; Carvalho, M. D.; Ferreira, L. P.; Stoger, B.; Mereiter, K.; Weil, M.; Muller, D.; Weinberger, P.; Pittenauer, E.; Allmaier, G.; Kirchner, K., *Dalton transactions* **2014**, *43* (29), 11152-64.
 46. (a) Holzhaecker, C.; Standfest-Hauser, C. M.; Puchberger, M.; Mereiter, K.; Veiros, L. F.; Calhorda, M. J.; Carvalho, M. D.; Ferreira, L. P.; Godinho, M.; Hartl, F., *Organometallics* **2011**, *30* (24), 6587-6601; (b) Oztopcu, O.; Mereiter, K.; Puchberger, M.; Kirchner, K. A., *Dalton transactions* **2011**, *40* (26), 7008-21.
 47. Zhang, J.; Leitus, G.; Ben-David, Y.; Milstein, D., *Journal of the American Chemical Society* **2005**, *127* (31), 10840-10841.
 48. Fray, M. J.; Gillmore, A. T.; Glossop, M. S.; McManus, D. J.; Moses, I. B.; Praquin, C. F. B.; Keeves, K. A.; Thompson, L. R., *Organic Process Research & Development* **2010**, *14* (1), 263-271.
 49. Garcia, Y.; Ksenofontov, V.; Guetlich, P., *Hyperfine Interactions* **2002**, *139/140* (1-4), 543-551.
 50. Guetlich, P.; Gaspar, A. B.; Garcia, Y., *Beilstein J Org Chem* **2013**, *9*, 342-391.
 51. Neese, F. *an ab initio, Density Functional and Semi-empirical Program Package*, Version 2.9.0; Max-Planck-Institut für Bioorganische Chemie: Mülheim/Ruhr, 2012.
 52. (a) Neese, F., *Inorganica Chimica Acta* **2002**, *337*, 181-192; (b) Neese, F., *Coordination Chemistry Reviews* **2009**, *253* (5-6), 526-563.
 53. Benito-Garagorri, D.; Alves, L. G. a.; Puchberger, M.; Mereiter, K.; Veiros, L. F.; Calhorda, M. J.; Carvalho, M. D.; Ferreira, L. P.; Godinho, M.; Kirchner, K., *Organometallics* **2009**, *28* (24), 6902-6914.
 54. (a) Cecconi, F.; Di Vaira, M.; Midollini, S.; Orlandini, A.; Sacconi, L., *Inorganic chemistry* **1981**, *20* (10), 3423-3430; (b) Wu, C.-C.; Jung, J.; Gantzel, P. K.; Gütlich, P.; Hendrickson, D. N., *Inorganic chemistry* **1997**, *36* (23), 5339-5347; (c) Di Vaira, M.; Midollini, S.; Sacconi, L., *Inorganic chemistry* **1981**, *20* (10), 3430-3435.
 55. Holzhaecker, C.; Calhorda, M. J.; Gil, A.; Carvalho, M. D.; Ferreira, L. P.; Mereiter, K.; Stöger, B.; Pittenauer, E.; Allmaier, G.; Kirchner, K., *Polyhedron* **2014**, *81*, 45-55.

56. Nienkemper, K.; Kotov, V. V.; Kehr, G.; Erker, G.; Fröhlich, R., *European Journal of Inorganic Chemistry* **2006**, 2006 (2), 366-379.
57. (a) Malassa, A.; Herzer, N.; Gorls, H.; Westerhausen, M., *Dalton transactions* **2010**, 39 (22), 5356-5366; (b) O'Reilly, R. K.; Shaver, M. P.; Gibson, V. C.; White, A. J. P., *Macromolecules* **2007**, 40 (21), 7441-7452; (c) Raynaud, J.; Wu, J. Y.; Ritter, T., *Angewandte Chemie International Edition* **2012**, 51 (47), 11805-11808.
58. Harris, T. V.; Rathke, J. W.; Muetterties, E. L., *Journal of the American Chemical Society* **1978**, 100 (22), 6966-6977.
59. Holzhacker, C.; Stoger, B.; Carvalho, M. D.; Ferreira, L. P.; Pittenauer, E.; Allmaier, G.; Veiros, L. F.; Realista, S.; Gil, A.; Calhorda, M. J.; Muller, D.; Kirchner, K., *Dalton transactions* **2015**.
60. Bart, S. C.; Chłopek, K.; Bill, E.; Bouwkamp, M. W.; Lobkovsky, E.; Neese, F.; Wiegardt, K.; Chirik, P. J., *Journal of the American Chemical Society* **2006**, 128 (42), 13901-13912.
61. Fillman, K. L.; Bielinski, E. A.; Schmeier, T. J.; Nesvet, J. C.; Woodruff, T. M.; Pan, C. J.; Takase, M. K.; Hazari, N.; Neidig, M. L., *Inorganic chemistry* **2014**, 53 (12), 6066-6072.
62. DeRieux, W.-S. W.; Wong, A.; Schrodi, Y., *Journal of Organometallic Chemistry* **2014**, 772–773, 60-67.
63. Benito-Garagorri, D.; Alves, L. G. a.; Veiros, L. F.; Standfest-Hauser, C. M.; Tanaka, S.; Mereiter, K.; Kirchner, K., *Organometallics* **2010**, 29 (21), 4932-4942.
64. Lee, C.; Yang, W.; Parr, R. G., *Physical Review B* **1988**, 37 (2), 785-789.
65. Perrin, D. D.; Armarego, W. L. F., *Purification of Laboratory Chemicals*. 3rd ed.; Pergamon: New York, 1988.
66. Maurer, C.; Pittenauer, E.; Puchberger, M.; Allmaier, G.; Schubert, U., *ChemPlusChem* **2013**, 78 (4), 343-351.
67. Maurer, C.; Pittenauer, E.; Du, V. A.; Allmaier, G.; Schubert, U., *Dalton transactions* **2012**, 41 (8), 2346-53.
68. (a) APEX2, version 2009.9-0; Bruker AXS Inc.: Madison, WI; (b) SAINT, version 7.68 A; Bruker AXS Inc.: Madison, WI; (c) SADABS, version 2008/1; Bruker AXS Inc.: Madison, WI; (d) SHELXTL, version 2008/4; Bruker AXS Inc.: Madison, WI.
69. Sheldrick, G. M., *Acta Crystallogr A* **2008**, 64 (Pt 1), 112-22.
70. Spek, A. L., *Acta Crystallogr D Biol Crystallogr* **2009**, 65 (Pt 2), 148-55.
71. Frisch, M. J.; Trucks, G. W.; Schlegel, H. B.; Scuseria, G. E.; Robb, M. A.; Cheeseman, J. R.; Scalmani, G.; Barone, V.; Mennucci, B.; Petersson, G. A.; Nakatsuji, H.; Caricato, M.; Li, X.; Hratchian, H. P.; Izmaylov, A. F.; Bloino, J.; Zheng, G.; Sonnenberg, J. L.; Fox, D. J. *Gaussian 09*, Revision A.02; Gaussian, Inc.: Wallingford CT, 2009.
72. Hoe, W.-M.; Cohen, A. J.; Handy, N. C., *Chemical Physics Letters* **2001**, 341 (3–4), 319-328.
73. (a) Swart, M.; Groenhof, A. R.; Ehlers, A. W.; Lammertsma, K., *The Journal of Physical Chemistry A* **2004**, 108 (25), 5479-5483; (b) Swart, M.; Ehlers, A. W.; Lammertsma *, K., *Molecular Physics* **2004**, 102 (23-24), 2467-2474; (c) Swart, M., *Inorganica Chimica Acta* **2007**, 360 (1), 179-189; (d) Swart, M., *Journal of Chemical Theory and Computation* **2008**, 4 (12), 2057-2066; (e) Güell, M.; Luis, J. M.; Solà, M.; Swart, M., *The Journal of Physical Chemistry A* **2008**, 112 (28), 6384-6391; (f) Conradie, J.; Ghosh, A., *Journal of Chemical Theory and Computation* **2007**, 3 (3), 689-702.
74. (a) Bowman, D. N.; Jakubikova, E., *Inorganic chemistry* **2012**, 51 (11), 6011-6019; (b) Ye, S.; Neese, F., *Inorganic chemistry* **2010**, 49 (3), 772-774.

75. (a) Perdew, J. P.; Burke, K.; Ernzerhof, M., *Physical Review Letters* **1996**, *77* (18), 3865-3868; (b) Perdew, J. P.; Burke, K.; Ernzerhof, M., *Physical Review Letters* **1997**, *78* (7), 1396-1396.
76. Adamo, C.; Barone, V., *The Journal of Chemical Physics* **1999**, *110* (13), 6158-6170.
77. (a) Becke, A. D., *The Journal of Chemical Physics* **1993**, *98* (7), 5648-5652; (b) Miehlich, B.; Savin, A.; Stoll, H.; Preuss, H., *Chemical Physics Letters* **1989**, *157* (3), 200-206.
78. (a) Häussermann, U.; Dolg, M.; Stoll, H.; Preuss, H.; Schwerdtfeger, P.; Pitzer, R. M., *Molecular Physics* **1993**, *78* (5), 1211-1224; (b) Küchle, W.; Dolg, M.; Stoll, H.; Preuss, H., *The Journal of Chemical Physics* **1994**, *100* (10), 7535-7542; (c) Leininger, T.; Nicklass, A.; Stoll, H.; Dolg, M.; Schwerdtfeger, P., *The Journal of Chemical Physics* **1996**, *105* (3), 1052-1059.
79. (a) McLean, A. D.; Chandler, G. S., *The Journal of Chemical Physics* **1980**, *72* (10), 5639-5648; (b) Krishnan, R.; Binkley, J. S.; Seeger, R.; Pople, J. A., *The Journal of Chemical Physics* **1980**, *72* (1), 650-654; (c) Hay, P. J., *The Journal of Chemical Physics* **1977**, *66* (10), 4377-4384; (d) Raghavachari, K.; Trucks, G. W., *The Journal of Chemical Physics* **1989**, *91* (4), 2457-2460; (e) Curtiss, L. A.; McGrath, M. P.; Blaudeau, J. P.; Davis, N. E.; Binning, R. C.; Radom, L., *The Journal of Chemical Physics* **1995**, *103* (14), 6104-6113; (f) McGrath, M. P.; Radom, L., *The Journal of Chemical Physics* **1991**, *94* (1), 511-516.
80. (a) Peng, C.; Bernhard Schlegel, H., *Israel Journal of Chemistry* **1993**, *33* (4), 449-454; (b) Peng, C.; Ayala, P. Y.; Schlegel, H. B.; Frisch, M. J., *Journal of Computational Chemistry* **1996**, *17* (1), 49-56.
81. (a) Stratmann, R. E.; Scuseria, G. E.; Frisch, M. J., *The Journal of Chemical Physics* **1998**, *109* (19), 8218-8224; (b) Bauernschmitt, R.; Ahlrichs, R., *Chemical Physics Letters* **1996**, *256* (4-5), 454-464; (c) Casida, M. E.; Jamorski, C.; Casida, K. C.; Salahub, D. R., *The Journal of Chemical Physics* **1998**, *108* (11), 4439-4449.
82. Rassolov, V. A.; Pople, J. A.; Ratner, M. A.; Windus, T. L., *The Journal of Chemical Physics* **1998**, *109* (4), 1223-1229.
83. Wachters, A. J. H., *The Journal of Chemical Physics* **1970**, *52* (3), 1033-1036.
84. Schäfer, A.; Horn, H.; Ahlrichs, R., *The Journal of Chemical Physics* **1992**, *97* (4), 2571-2577.
85. (a) Eichkorn, K.; Treutler, O.; Öhm, H.; Häser, M.; Ahlrichs, R., *Chemical Physics Letters* **1995**, *240* (4), 283-290; (b) Eichkorn, K.; Weigend, F.; Treutler, O.; Ahlrichs, R., *Theor Chem Acta* **1997**, *97* (1-4), 119-124.
86. Bochevarov, A. D.; Friesner, R. A.; Lippard, S. J., *Journal of Chemical Theory and Computation* **2010**, *6* (12), 3735-3749.
87. Partridge, H., *The Journal of Chemical Physics* **1989**, *90* (2), 1043-1047.
88. (a) Dunning, T. H., *The Journal of Chemical Physics* **1989**, *90* (2), 1007-1023; (b) Woon, D. E.; Dunning, T. H., *The Journal of Chemical Physics* **1993**, *98* (2), 1358-1371.
89. Petříček, V.; Dušek, M.; Palatinus, L., *Zeitschrift für Kristallographie - Crystalline Materials* **2014**, *229* (5).